UNIVERSIDADE DE LISBOA
FACULDADE DE CIÊNCIAS
DEPARTAMENTO DE FÍSICA

Monte Carlo Simulation Applied to Dosimetry of Narrow High-Energy Photon Beams used in Radiosurgery

Adérito Barbosa Chaves

DOUTORAMENTO EM FÍSICA
(Física Tecnológica)

2004

UNIVERSIDADE DE LISBOA
FACULDADE DE CIÊNCIAS
DEPARTAMENTO DE FÍSICA

Monte Carlo Simulation Applied to Dosimetry of Narrow High-Energy Photon Beams used in Radiosurgery

Adérito Barbosa Chaves

Thesis oriented by: Professor Doutor Luis Filipe dos Santos Garcia Peralta
Professor Auxiliar c/Agregação
Faculdade de Ciências da Universidade de Lisboa

Doutor Carlos Manuel Azevedo de Sousa Oliveira
Investigador Principal
Instituto Tecnológico e Nuclear

DOUTORAMENTO EM FÍSICA
(Física Tecnológica)

2004

To Adriano, Maria de Fátima, Rose Marie and Maria.

"Que sais-je?"

Montaigne

Acknowledgments

First of all, I would like to express my endless gratitude to Doutora Maria do Carmo Lopes for the inestimable support in pedagogical aspects and also in theoretical and practical supports that she has always manifested along this work. I also want to thank for her friendship and the excellent working environment that she has provided without which this project would not have been possible to complete.

I would like to thank Prof. Doutor Luis Peralta and Doutor Carlos Oliveira for having oriented this thesis and for their endless support, inspiring ideas, understanding, trust and most of all their friendship.

I would like to express a very special thanks to Engª. Carla Alves, my colleague since my first day at IPOFG-CROC, S.A. Thanks for her great patience in listening the mountains of doubts that I had during this work. Thanks for the numerous fruitful discussions we had.

I also would like to express a special thanks to Engº. Miguel Capela for his great help in the measurement sessions and some of mathematical aspects of this work.

To my friends, with whom I started this work, Doutor João Seco and Dra. Margarida Fragoso for their scientific support.

To my colleagues, Engª. Armanda Matos, Engª. Josefina Mateus and Doutora Carmen Sousa, a great thanks for their support.

To Dr. Manuel António Leitão da Silva, Director of IPOFG-CROC, S.A., for always having encouraged medical physics research in his institution.

A thanks to Dr. Pedro Rodrigues and Dra. Andreia Trindade for their support in

the simulation of the accelerator head.

To *Laboratório de Instrumentação e Física Experimental de Partículas* for its financial and technological supports.

To *Fundação para a Ciências e Tecnologia* for its financial support through CERN project Nº CERN/PAL/43672/2001 and FEDER fund POCTI/PAL/43672/2002.

To *Liga Portuguesa Contra o Cancro, Núcleo Regional do Centro* for its financial support.

To Siemens AG Medical Engineering for having provided technical information about the accelerator head.

For all that have contributed more or less closely to this work, thank you.

Last but not least, I want first to thank my parents, Adriano e Maria de Fátima who worked hard and struggled in a foreign country to provide their children a good life. Thank you so much. To my sister, Rose Marie, for her inexhaustible advices and support. Finally, I want to thank my beloved Maria for all her love, for having given me so much joy and energy to conclude this project.

Contents

Abstract xv
Resumo xvii
List of Abbreviations and Symbols xxi
List of Figures xxiii
List of Tables xxxiii
List of Publications xxxv

Introduction **1**

Chapter 1 - Dosimetry of high-energy photon beams **5**
1.1 Photon interactions 6
1.1.1 Photoelectric effect 6
1.1.2 Rayleigh scattering 7
1.1.3 Compton effect 7
1.1.4 Pair and Triplet production 8
1.1.5 Total attenuation coefficient 9
1.2 Electron interactions 11
1.2.1 Inelastic collisions with atomic electrons 11
1.2.2 Inelastic collisions with nuclei 13
1.2.3 Elastic scattering 14
1.2.4 Total electron cross sections 15
1.3 Electron stopping powers 16
1.4 Absorbed dose determination 23
1.4.1 Kerma 23
1.4.2 Absorbed dose 25
1.4.3 Charged Particle Equilibrium 25
1.4.4 Bragg-Gray cavity theory 27
1.4.5 Spencer-Attix cavity theory 29

1.4.6 Basic dosimetric quantities 30
1.4.7 Dosimetry protocol 33

Chapter 2 - Stereotactic radiosurgery 39
2.1 Historical review 39
2.2 Typical radiosurgery treatment 40
2.3 SRS units 41
2.3.1 Gamma Knife 41
2.3.2 Linac 43
2.3.3 Stereotactic system 50
2.4 STP3 radiosurgery treatment planning system 52
2.4.1 Dosimetric STP3 database 53
2.4.2 Dose distribution calculation 55
2.4.3 Evaluation of treatment planning 56

Chapter 3 - Monte Carlo methods 59
3.1 Analog and condensed history Monte Carlo 60
3.2 Photon transport 61
3.3 Electron transport in MCNP4C 63
3.3.1 Electron step and substeps 63
3.3.2 Energy straggling 64
3.3.3 Angular deflections 65
3.3.4 Hard collision and radiative events 66
3.4 Electron transport in DPM 67
3.4.1 Multiple scattering with energy loss 67
3.4.2 The random hinge transport mechanism 68
3.4.3 Hard collision and radiative events 69
3.4.4 Transport across inhomogeneous voxel phantom 70

Chapter 4 - MC simulation of KD2 plus additional collimator 73
4.1 Phase Space Data generation 73
4.1.1 Simulation parameters 75
4.1.2 Characterization of the incident electron source 76
4.2 Phase Space Data analysis 78
4.2.1 Basic statistics 78
4.2.2 Particle creation and loss events 79

4.2.3 Particle characteristics in PSD 84
4.3 Phase Space Data validation 94
4.3.1 Dosimetric methods 94
4.3.2 Patient-dependent simulation 96
4.3.3 Validation criteria 98
4.3.4 Percent depth dose 103
4.3.5 Off-axis ratio 107
4.3.6 Output factor 111

Chapter 5 - Detailed study of depth of maximum dose 115
5.1 Experimental setup 115
5.2 Monte Carlo Simulation 116
5.3 Water dose components 119
5.4 Simplified source model 122
5.5 Results and discussion 125

Chapter 6 - Multiple source model for narrow photon beams 133
6.1 The multiple source model 135
6.1.1 Beam characterization 136
6.1.2 Definition of the relevant virtual sources 147
6.1.3 Beam reconstruction 150
6.2 Validation of RMSM 153
6.2.1 Number of histories in DPM simulations 154
6.2.2 Dose distributions 155

Chapter 7 - Clinical implementation of RMSM 169
7.1 CT-Interface 169
7.1.1 CT-number parametrization 170
7.1.2 Hounsfield units conversion into tissue parameters 171
7.1.3 Conversion of CT-pixel to DPM-voxel 174
7.1.4 Implementation of the CT-Interface 177
7.2 Stereotactic Transformation Interface 179
7.2.1 Fiducial points 179
7.2.2 Transformation 183
7.2.3 Implementation and validation 187

7.3 Source Interface 188
7.3.1 Rotation transformations 189
7.3.2 Implementation 191
7.4 Clinical cases 192

Conclusions 205

References 209

Abstract

The purposes of this work are, by one hand, the determination, the most accurately possible, of absorbed dose delivered by narrow photon beams used in radiosurgery and, on the other hand, the development of a fast and accurate Monte Carlo-based radiosurgery treatment planning for post-treatment verification. Included in the first purpose is the full understanding of the behavior of the depth of maximum dose (d_{max}) for narrow photon beams.

Monte Carlo methods were used to simulate the Siemens Mevatron linear accelerator in 6 MV photon mode with the additional collimator used to shape the narrow photon beams. The phase space data was analyzed and validated through comparisons between calculated and measured dose distributions. Great differences were found between calculated and measured output factors due to detectors characteristics. It was shown that primary photons were responsible for the shift in d_{max}. Secondary electrons originated from these photons were divided into two groups: those that deposit energy far away from their origin point and those that deposit energy locally. Finally, it was shown that the changes in the initial gradients of the depth dose curves for narrow photon beams were mainly due to electrons originated from the first photon collision in water.

A Monte Carlo radiosurgery treatment planning for post-treatment verification was developed based on a multiple source model. The dose engine accurately calculates dose distributions in the water phantom for all the additional collimators. In patient real cases, it was shown that differences between our model and a commercial treatment planning are significative when the target is localized near a high density region.

Key words: Monte Carlo simulation, Radiosurgery, narrow photon beams

Resumo

Os objectivos desta tese consistem, por um lado, na determinação exacta da dose absorvida devida a feixes finos de fotões utilizados em radiocirurgia e, por outro lado, no desenvolvimento de um sistema de planeamento de dose, rápido e exacto, baseado no método de Monte Carlo, para verificação pós tratamento. A total compreensão do comportamento em profundidade da dose máxima (d_{max}) para feixes finos de fotões é um pressuposto do primeiro objectivo.

Usando o código de Monte Carlo MCNP4C, simulou-se a cabeça do acelerador linear Siemens Mevatron KD2 no modo fotão 6 MV, tendo-se efectuado uma análise das características das partículas emergentes da cabeça do acelerador. Estas partículas foram guardadas num espaço de fase que constitui a fonte para as simulações dos feixes finos de fotões. A forma e o tamanho dos feixe finos de fotões utilizados para tratamentos de radiocirurgia praticados no IPOFG-CROC, S.A, são obtidos colocando colimadores adicionais logo à saída da cabeça do acelerador. Para cada colimador adicional foi executada uma simulação completa de Monte Carlo para calcular distribuições de dose num fantoma de água. Os dados registados no espaço de fase fonte foram validados através da comparação entre as distribuições de dose calculadas e medidas para cada colimador adicional. Devido à grande dificuldade em medir dose para campos pequenos, a metodologia seguida foi comparar as distribuições de dose calculadas para cada colimador adicional com os resultados obtidos a partir de diferentes métodos de medição e tentar encontrar uma consistência interna. Encontrou-se um bom acordo entre as curvas de dose em profundidade calculadas e medidas com o díodo, a câmara de Markus e a câmara PinPoint, para profundidades superior a 10 mm embora existisse uma tendência de sobre-resposta da câmara de Markus e de sob-resposta da câmara PinPoint para os colimadores adicionais mais pequenos e para grandes profundidades. Para perfis de dose, verificou-se que os resultados dos cálculos estavam em bom acordo com as medidas efectuadas com o díodo. A câmara PinPoint não é adequada para

resolver de maneira correcta a dose na penumbra devido ao seu efeito de volume. O filme radiográfico, embora melhor do que a câmara PinPoint na região de penumbra, sob-estima a dose nas região de baixa dose devido às dificuldades na calibração. Assim, pode-se concluir que o diodo é uma boa escolha para medir dose em profundidade e perfis para feixes finos de fotões. Devido à falta de equilíbrio lateral dos electrões, mostrou-se que o tipo e o tamanho dos detectores têm uma grande influência na determinação correcta dos factores de campo para os feixes finos de fotões. As maiores diferenças entre os valores calculados e medidos foram encontradas para os campos menores. Mostrou-se que os cálculos de Monte Carlo são o método mais exacto na determinação destes factores de campo.

Em radiocirurgia de feixes finos de fotões, a profundidade do máximo da dose (d_{max}), no eixo central do feixe, aumenta quando o tamanho do colimador adicional aumenta. Este comportamento é oposto ao que é observado em feixes convencionais usados em radioterapia. Para compreender este efeito, foram obtidas curvas experimentais de dose em profundidade para os vários colimadores adicionais. Foi observado um deslocamento de d_{max} entre os 11.0±0.6 milímetro para o colimador de 5 milímetros e os 14.5± 0.6 milímetro para o colimador de 23 milímetros. As simulações de Monte Carlo mostraram que os fotões que não tiveram nenhuma interacção nos colimadores adicionais, contribuem com mais de 90% para a dose total na água, e são responsáveis pelo deslocamento do d_{max}. As simulações de Monte Carlo mostraram também que os electrões originados a partir destes fotões e que contribuem para a dose na água, ao longo do eixo central do feixe, podem ser divididos em dois grupos: aqueles que depositam a sua energia longe do seu ponto de origem (o ponto da primeira colisão do fotão na água) e aqueles que depositam a sua energia localmente (originados a partir de mais de uma colisão do fotão na água). Aplicando um modelo simplificado baseado no facto que os fotões que originam electrões Compton (nas primeiras e subsequentes colisões) têm características similares no ar para todos os colimadores adicionais, mostrou-se que estes electrões são também responsáveis pelo deslocamento do d_{max}. Finalmente, mostrou-se que as mudanças nos gradientes iniciais nas curvas de dose em profundidade dos colimadores adicionais são principalmente devidas aos electrões originados a partir da primeira colisão do fotão na água.

A abordagem padrão para simular tratamentos em radioterapia, tem a vantagem de requerer somente uma vez a simulação completa da componente independente do pa-

ciente, seguida pela simulação da geometria do próprio paciente. Não obstante, alguns problemas limitam o uso desta abordagem para aplicações em radiocirurgia. A geometria de um fantoma ou de uma imagem de TAC é dividida em voxeis. O tamanho destes voxeis deve ser suficientemente pequeno para conseguir a exactidão requerida em tratamentos de radiocirurgia. Quando o tamanho dos voxeis diminui, é necessário aumentar o número das partículas para conseguir os mesmos valores de incerteza estatística. Em aplicações convencionais de radioterapia, são conseguidos bons resultados porque o número de partículas no espaço de fase (PSD) é estatisticamente relevante; este pode não ser o caso em aplicações de radiocirurgia. A principal técnica para aumentar o número das partículas que alcançam os voxeis é aumentar, nas simulações da componente independente do paciente, o número de histórias originais o que produz, por um lado, tempos de cálculo excessivamente longos, e, por outro lado, ficheiros de espaço de fases demasiado grandes. A outra opção é reciclar várias vezes o ficheiro fonte nas simulações da componente dependente do paciente. Um tratamento típico em radiocirurgia é composto por seis arcos. Para finalidades do cálculo, cada arco é dividido em pelo menos oito feixes de fotões. Em soma, devem ser simulados quarenta oito feixes de fotões para a componente dependente do paciente. Torna-se claro, que o tempo de cálculo e a capacidade de armazenamento são grandes factores limitativos.

A baixa eficiência da simulação de feixes finos de fotões produz espaços de fase cuja qualidade impede o cálculo da dose com a requerida exactidão. Para superar esta dificuldade, foi desenvolvido um modelo multi-fontes que realçasse a qualidade do espaço de fase reconstruído, reduzindo também as capacidades tempo de cálculo e armazenamento. Para desenvolver um modelo multi-fontes são necessárias três étapas principais. A primeira étapa é a caracterização completa do feixe, a segunda, a escolha das diferentes fontes virtuais e, finalmente a terceira, a reconstrução do feixe. Foram executadas, com o código de Monte Carlo MCNP4C, simulações completas da cabeça do acelerador e dos colimadores adicionais. Estas simulações permitiram a caracterização das partículas que vêm da cabeça do acelerador e dos colimadores adicionais. A sua análise identificou oito fontes virtuais relevantes de fotões. As distribuições espaciais e energéticas foram armazenadas em histogramas para as fontes virtuais que representam os componentes da cabeça do acelerador e dos colimadoras adicionais. Para as fontes virtuais que representam as componentes da cabeça do acelerador, foram calculadas as suas direcções; para as fontes virtuais que representam os colimadores adicionais, foram amostradas as direcções dos fotões a partir de histogramas. Todos estes his-

togramas foram incluídos no código Monte Carlo DPM e, usando um procedimento de amostragem que reconstroi os espaços de fases, foram calculadas distribuições de dose num fantoma da água dividido em 20000 voxeis de $1\times1\times5$ mm^3. Foi utilizado um teste baseado no índice gama para comparar os valores calculados com os valores medidos. De acordo com este teste, o modelo calcula com exactidão as distribuições de dose no fantoma de água para todos os colimadores adicionais. Este modelo multi-fontes representa o motor de cálculo de dose num sistema de planeamento.

Como em qualquer sistema de planeamento de tratamento em radiocirurgia, o nosso sistema deve incluir ferramentas tais como a conversão de dados de imagens de TAC em tecido humano, a transformação geométrica estereotáxica e uma transformação geométrica da fonte para simular os arcos. Para a conversão imagens de TAC em tecido humano, cada pixel da imagem, que contem a informação da composição do material e da densidade em valores de Hounsfield, é transformado num voxel de dimensões $1.37\times1.37\times2$ mm^3 onde a composição do material e a densidade foram calculados. A transformação estereotáxica é calculada usando uma rotina que busca, em cada imagem de TAC, os pontos fidúcias e calcula a posição desses pontos no referencial estereotáxico. A matriz de transformação é calculada usando restrições geométricas. As inclinações do anel estereotáxico no referencial DPM, são calculadas usando a transformação estereotáxica. Finalmente, a posição e direcção de cada fotão, extraído do modelo multi-fontes, são calculadas de acordo com a posição da mesa e do braço do acelerador, simulando dessa maneira um arco. O nosso sistema de planeamento foi aplicado em dois casos reais e comparado com um sistema comercial de planeamento computadorizado. Quando o alvo está situado em regiões de baixa densidade, as diferencias entre as distribuições de dose calculadas pelo nosso sistema e o sistema comercial são mínimas. Quando o alvo está situado perto de regiões de elevada densidade, o nosso sistema de planeamento revelou diferenças nas distribuições de dose, comparado com o sistema comercial.

Palavras Chave: Simulação de Monte Carlo, Radiocirurgia, feixes finos de fotões

List of Abbreviations and Symbols

AVM	arteriovenous malformation
CAX	beam central axis
CBI	Convergent Beam Irradiation
CF	Collimator Factor
CPE	Charged Particle Equilibrium
CRP	calibration dose point
CSDA	Continuous Slowing Down Approximation
CT	Computorized Tomography
$CTMR$	Calibrated Tissue-Maximum Ratio
D	absorbed dose
DDC	Depth Dose Curve
d_{max}	depth of maximum dose
DPM	Dose Planning Method
DTA	Distance-To-Agreement
φ_c	couch angle according to DIN-6847 standard norm
γ	gamma evaluation quality index
H	Hounsfield unit
IAEA	International Atomic Energy Agency
ICRU	International Commission On Radiation Units and Measurements
IPOFG-CROC, S.A.	Instituto Português de Oncologia Francisco Gentil - Centro Regional de Oncologia de Coimbra, Sociedade Anónima
(L_Δ/ρ)	restricted mass collisional stopping power
linac	linear accelerator
PDF	Probability Distribution Function
MC	Monte Carlo
MCNP	Monte Carlo N-Particle
MCNP4C	MCNP version 4C

MFP	Mean Free Path
MU	Monitor Unit
MV	MegaVolt
N_{D,w,Q_0}	dose calibration factor in water
OAR	Off-Axis Ratio
OF	Output Factor
(ψ_x, ψ_y, ψ_z)	ring tilts in the x-, y- and z-axis
PAC_net	Photon Additional Collimator net component
PAC_trans	Photon Additional Collimator transmitted component
PDD	Percent Depth Dose
P_r	prescribed dose
PSD	Phase Space Data
Rc	additional collimator radius
RMSM	Radiosurgery Multiple Source Model
S/ρ	mass stopping power
$(S/\rho)^{medium_1}_{medium_2}$	collisional mass stopping power ratio medium 1 to medium 2
SAD	Source Axis Distance
SID	Source Isocenter Distance
SRS	stereotactic radiosurgery
SSD	Source Surface Distance
STP3	Fisher-Liebinger TPS version 3
θ_g	gantry angle according to DIN-6847 standard norm
TCPE	Transient Charged Particle Equilibrium
TMR	Tissue-Maximum Ratio
TPR	Tissue-Phantom Ratio
$TPR_{20,10}$	beam quality index
TPS	Treatment Planning System
$\overline{W}_{air}$	mean energy required to create an ion pair in air (33.97 J/C)
(x^{ct}, y^{ct}, z^{ct})	point coordinates in the CT referential
$(x^{dpm}, y^{dpm}, z^{dom})$	point coordinates in the DPM referential
(x^{st}, y^{st}, z^{st})	point coordinates in the stereotactic referential
$\overline{zl}$	average cote along the z-axis of the point of origin of the unscattered photons

List of Figures

1.1 Example of sigmoidal shape of dose response curves for tumor control probability (TCP) and normal tissue complication probability (NCTP). 5

1.2 Total mass attenuation coefficient μ/ρ and the partial contribution of the various effects for water. 10

1.3 Total mass attenuation coefficient μ/ρ and the partial contribution of the various effects for tungsten. 10

1.4 Parameters for an electron collision with the atom where a is the classical radius of the atom and b is the classical impact parameter. 12

1.5 Total cross section for the carbon (Z=6) representing ionizations in three atomic shells (Møller scattering), excitation and Bremsstrahlung processes. Elastic scattering is also represented. 16

1.6 Mass collision stopping power versus electron kinetic energy for air and water. 18

1.7 Ratios of mass collision stopping powers, medium to water, for various substances of medical interest. 19

1.8 A comparison between radiative mass collision stopping powers for compact bone (ICRU) and water. 21

1.9 The energy and material dependence of the ratio radiative stopping power and collisional stopping power, S_{rad}/S_{col}, for the various media of interest in medical dosimetry. 22

1.10 Collision, radiation and total mass stopping powers for electrons in water. 23

1.11 Illustration of energy transferred in a medium of mass dm by a photon of energy $h\nu$. The photon interacts in the medium at point P and transfers some of its energy in the form of electron's kinetic energy. The electron, in turn, transfers its energy to the medium through small collisions between point P and P'. The energy transferred per unit mass in P is designated by *kerma*. One of the δ-ray carries energy out of the volume with mass dm. 24
1.12 Quantities kerma (K), absorbed dose (D) and collision kerma (K_{coll}) plotted as function of depth in *Charged Particle Equilibrium* condition. 26
1.13 Quantities kerma (K), absorbed dose (D) and collision kerma (K_{coll}) plotted as function of depth in *Transient Charged Particle Equilibrium* condition. 27
1.14 A Bragg-Gray cavity in a medium traversed by electron tracks. 27
1.15 Diagram illustrating the definition of the percent depth dose in a water phantom. 30
1.16 Diagram illustrating the definition of the off-axis ratio in a water phantom. 31
1.17 Diagram illustrating the definition of the tissue-phantom ratio in a water phantom. 32
1.18 Calculated value of the beam quality correction factor, k_Q, for the PTW 30013 Farmer chamber as a function of the photon beam quality Q obtained from Andreo [And92]. 36

2.1 Simplified diagram of a radiosurgery treatment. 41
2.2 The Leksell's Gamma Knife (Elekta). 42
2.3 Schematic view of a LGK unit (University Neurosurgery LSU Health Sciences Center). 42
2.4 Schematic view of convergent Cobalt beams (University of Kentucky, Chandler Medical Center). 42
2.5 Leksell's stereotactic frame with a collimator helmet (Elekta). 43
2.6 View of the Siemens Mevatron KD2 linear accelerator. 44
2.7 View of main components of the Siemens Mevatron KD2 linear accelerator in photon mode. 44
2.8 Isocenter definition. 45
2.9 Illustration of linac multiple non-coplanar arcs used in radiosurgery treatments. 46

2.10 (a) Additional collimators used to shape the narrow photon beams and (b) their localization in the Siemens Mevatron KD2 linac. 47
2.11 Couch immobilization device used in radiosurgery. 47
2.12 Adjustment of the geometrical isocenter using two pointers. 48
2.13 Needle hole placed at the isocenter. 49
2.14 *Star* of various beams on the film resulting of irradiations at various gantry angle. 49
2.15 Stereotactic ring fixed at the patient. 51
2.16 Stereotactic ring with localizers used in angiography or verification procedures. 51
2.17 Localizer used to setup the patient in the linac. 52
2.18 Calibrated Tissue Maximum Ratio for all the additional collimators. . . 54
2.19 Geometrical configuration used for dose calculation in STP3. 55
2.20 Dose volume histogram calculated by STP3. Dose: 100%=20 Gy, volume 100%=2.4 cm^3. 57

4.1 (a) First simulation block: Siemens Mevatron KD2 linear accelerator head components in 6 MV photon mode, (b) second simulation block: additional collimator, air column and water phantom. 74
4.2 Type of events for photons in block 1 simulation. W_t represents the number of particles for one type of event per incident electrons. 80
4.3 Type of events for electrons in block 1 simulation. W_t represents the number of particles for one type of event per incident electron. 81
4.4 Type of events for photons for each accelerator head component in block 1 simulation. W_t represents the number of particles for one type of event per incident electron. 82
4.5 Type of events for photons for each accelerator head component in block 1 simulation. W_t is normalized for each component to the sum of the total weight of that component. 82
4.6 Type of events for electrons for each accelerator head component in block 1 simulation. W_t represents the number of particles for one type of event per incident electron. 83
4.7 Type of events for electrons for each accelerator head component in block 1 simulation. W_t is normalized for each component to the sum of the total weight of that component. 84

4.8 Point of origin or last interaction along the z-axis of the photons reaching the scoring plane for a 10×10 cm^2 field size. 85
4.9 Point of origin or last interaction in the yz-plane of the photons reaching the scoring plane for a 10×10 cm^2 field size. 86
4.10 Radial distributions of particles at the scoring plane for each accelerator head component. Results are normalized to the total number of particles per unit of area. The right scale is applied to the target component and to the total number of particles. 87
4.11 Calculated energy spectra at the scoring plane for particles coming from each accelerator head component. Results were normalized to the total number of particles in the scoring plane. 88
4.12 Radial average energy distributions for particles coming from the most important accelerator head components. 89
4.13 Radial energy fluence distributions for particles coming from the accelerator head components. Results are normalized to the total energy fluence. 90
4.14 Angle distributions for particles in the scoring plane coming from the various accelerator head components. Results were normalized to the total number of particles in the scoring plane inside a radius ≤ 5 cm. . 91
4.15 Radial average angle for particles coming from the accelerator head components. 92
4.16 Radial average energy vs. polar angle for particles coming from the accelerator head components. 93
4.17 Simplified schematic view of the scoring cells for two different setups: (a) depth dose calculation, (b) off-axis dose calculation. The different geometrical components are not properly scaled. 97
4.18 Geometric representation of dose distribution evaluation criterion using the combined ellipsoidal dose-difference and distance-to-agreement test. 100
4.19 Geometric representation, for one-dimensional case, of the gamma criterion for discrete dose distributions. (a) Some calculated points are within the ellipsoid of tolerances. (b) No calculated points in the ellipsoid of tolerances. (c) Representation of interpolated points between two calculated points that are not within the ellipsoid of tolerances. 102
4.20 Measured percent depth dose for the 10×10 cm^2 square field. Results are normalized at 50 mm depth. 103

4.21 A comparison between calculated and measured percent depth dose (Source Surface Distance 100 cm). Each graphic represents the results for one additional collimator: (a) col5, (b) col7, (c) col9, (d) col11, (e) col 13, (f) col15, (g) col17, (h) col20, (i) col23. Results are normalized to value of dose at 50 mm depth for each additional collimator. The γ quality index is also plotted for each measurement point with the diode. 105

4.22 Measured depth of the maximum point dose d_{max} for each additional collimator. A trendline was added to show easier the shift of d_{max} as the size of the additional collimator increases. 107

4.23 A comparison between calculated and measured off-axis ratios. The setup is the following: Source Surface Distance 95 cm, depth of calculation and measurement 5 cm. Each graphic represents the results for one additional collimator: (a) col5, (b) col7, (c) col9, (d) col11, (e) col 13, (f) col15, (g) col17, (h) col20, (i) col23. For each additional collimator, the results to the value of maximum dose. The γ quality index is also plotted for each measurement point. 110

4.24 A relationship between the beam profiles of three additional collimators (D_a>D_b>D_c) with the cylindrical chamber dimension. 111

4.25 A comparison between calculated and measured output factors for all the additional collimators. 112

5.1 Measured off-axis ratios at different depths for the 5 mm additional collimators. Measurements were performed with a PTW-Freiburg diode (type TM60008) in the PTW-MP3 water phantom. Normalization was performed at the maximum dose at each depth. 118

5.2 Calculated from full Monte Carlo simulations 5 mm (a) and 23 mm (b) additional collimator depth doses in the buildup region in water. Primary dose, additional collimator scatter dose components and total dose are obtained using the MCNP4C col-option. Relative errors calculated by MCNP4C associated to simulation results are less than 1.5% for the total dose, less than 2% for the primary dose, and less than 5% for the scattered dose. 120

5.3 Measured depth of the maximum point dose d_{max} for each additional collimator. A trendline was added to show easier the shift of d_{max} as the size of the additional collimator increases. 121

5.4 Calculated deposited energy from full Monte Carlo simulations. The total beam is composed by both scattered and unscattered photons and electrons. Relative errors associated to Monte Carlo calculations are lower than 1%. 122

5.5 Radial spatial distributions of the unscattered photons in air. 123

5.6 Radial average angle distributions of the unscattered photons in air. . . 123

5.7 Energy distributions of the unscattered photons in air for the 5 and 23 mm additional collimators. 124

5.8 Equivalent 5 mm and 20 mm additional collimator fields in the 23 mm additional collimator PSD_2. The 20 mm additional collimator can be represented by the 5 mm additional collimator plus the annulus of internal diameter 5 mm and external diameter 20 mm. 125

5.9 Deposited energy versus depth (a) due to electrons from one photon collision for the 5 mm and the 23 mm additional collimator. (b) Contribution of electrons from one photon collision for each annulus. Errors bars were added. 127

5.10 Deposited energy due to electrons from more one photon collision as a function of depth (a) for the 5 mm and the 23 mm additional collimator. (b) Contribution of electrons from more one photon collision for 3 different annuli. 128

5.11 Deposited energy as a function of depth in four cases. Results of χ^2 test are the following: (1) χ^2=7.36 and P=0.599; (2) χ^2=9.46 and P=0.396; (3) χ^2=9.07 and P=0.431; (4) χ^2=7.26 and P=0.478. 129

5.12 Initial average kinetic energy for electrons that reach all the scoring cells for one and more than one photon collisions. The unscattered photons are coming from annuli representing each additional collimator. The inner diameter of the annuli was fixed to 5 mm and the outer diameter was increased from 7 mm (7 mm additional collimator) to 23 mm (23 mm additional collimator). 130

6.1 Simplified diagram of the Mevatron KD2 accelerator head components plus the additional collimator. 136

6.2 Relative number of unscattered photons that reach the scoring plane 2 for all the components of the accelerator head and for each additional collimator. The right scale is only applied to the target component. Normalization was performed to the total number of particles that reach the scoring plane 2 for each additional collimator. 138

6.3 Radial fluence distributions of the unscattered photons from target component of the accelerator head at the scoring plane 2 for the 5, 11, 17 and 23 mm additional collimators. 139

6.4 Radial distributions of the unscattered photons at origin for the primary collimator component of the accelerator head for the 5, 11, 17 and 23 mm additional collimator. The peaks in the curves are simply due to the geometry of the primary collimator. 140

6.5 Average unscattered photon angle in air for the most relevant accelerator head components and for all additional collimators. For all the additional collimators, calculated relative errors at 1σ are lower than 0.4% for the target component, 1.5% for the primary collimator and target assembly components, 2% for the flattening filter component and finally 3% for the flattening filter component. 141

6.6 Average energy of the unscattered photons that reach the scoring plane 2 from each the relevant accelerator head component. For all the additional collimators, calculated relative errors at 1σ are lower than 0.4% for the target component, 2.5% for the primary collimator and target assembly components, 3% for the flattening filter component and finally 5% for the flattening filter component. 142

6.7 Radial average energy distributions of each accelerator head component for photons reaching the scoring plane 2 and for the 23 mm additional collimator. 142

6.8 Energy spectra for unscattered photons from the flattening filter component for all the additional collimators (the penumbra region was excluded). Normalization was performed to the total number of unscattered photons for this component and for each additional collimator. . . 143

6.9 Additional collimator subdivided into four equal layers. 145

6.10 Average scattered photon angle in air for the PAC_net and PAC_trans components and for all the additional collimators. Errors bars were added. 145

6.11 Average scattered photon energy in air for the PAC_net and PAC_trans components and for all the additional collimators. Errors bars were added. 146

6.12 Scattered photon energy spectra for the PAC_net component. For each additional collimator, the energy spectrum is normalized to the total number of photons from this component. 147

6.13 Spatial distribution for unscattered photons coming from the target component reaching the scoring plane 2 for the 23 mm additional collimator. 151

6.14 Reconstructed spatial distribution for target unscattered photons at scoring plane 2 for the 23 mm additional collimator after applying the circular symmetry optimization. 152

6.15 Beam reconstruction process. 153

6.16 A comparison between calculated with RMSM and measured percent depth dose (SSD = 100 cm). Each graphic represents the results for one additional collimator: (a) col5, (b) col7, (c) col9, (d) col11, (e) col 13, (f) col15, (g) col17, (h) col20, (i) col23. Results are normalized to value of dose at 50 mm depth for each additional collimator. The γ quality index is plotted for each measurement point with the diode. Percent depth dose calculated with MCNP4C is also plotted. 157

6.17 A comparison between calculated (RMSM) and measured (diode) off-axis ratios (OAR) at various depths in water along (1) the x-axis and (2) the y-axis for the 5 mm additional collimator. In each axis, the γ-index is calculated. 158

6.18 A comparison between calculated (RMSM) and measured (diode) off-axis ratios (OAR) at various depths in water along (1) the x-axis and (2) the y-axis for the 7 mm additional collimator. In each axis, the γ-index is calculated. 159

6.19 A comparison between calculated (RMSM) and measured (diode) off-axis ratios (OAR) at various depths in water along (1) the x-axis and (2) the y-axis for the 9 mm additional collimator. In each axis, the γ-index is calculated. 160

6.20 A comparison between calculated (RMSM) and measured (diode) off-axis ratios (OAR) at various depths in water along (1) the x-axis and (2) the y-axis for the 11 mm additional collimator. In each axis, the γ-index is calculated. 161

6.21 A comparison between calculated (RMSM) and measured (diode) off-axis ratios (OAR) at various depths in water along (1) the x-axis and (2) the y-axis for the 13 mm additional collimator. In each axis, the γ-index is calculated. 162
6.22 A comparison between calculated (RMSM) and measured (diode) off-axis ratios (OAR) at various depths in water along (1) the x-axis and (2) the y-axis for the 15 mm additional collimator. In each axis, the γ-index is calculated. 163
6.23 A comparison between calculated (RMSM) and measured (diode) off-axis ratios (OAR) at various depths in water along (1) the x-axis and (2) the y-axis the 17 mm additional collimator. In each axis, the γ-index is calculated. 164
6.24 A comparison between calculated (RMSM) and measured (diode) off-axis ratios (OAR) at various depths in water along (1) the x-axis and (2) the y-axis for the 20 mm additional collimator. In each axis, the γ-index is calculated. 165
6.25 A comparison between calculated (RMSM) and measured (diode) off-axis ratios (OAR) at various depths in water along (1) the x-axis and (2) the y-axis for the 23 mm additional collimator. In each axis, the γ-index is calculated. 166

7.1 Conversion of CT-number into density of 61 defined materials for Siemens Somatom Plus 4. 173
7.2 Representation of the pixels in two CT consecutive images. 174
7.3 Representation of the voxel (i', j', k') in the DPM reference system. . . 175
7.4 Simplified diagram of DPM material pre-process procedure. 178
7.5 Coordinate system of the stereotactic head ring. 179
7.6 Stereotactic localizers mounted on the stereotactic head ring. 180
7.7 Fiducial points in a CT-image. 180
7.8 Positions of the fiducial points 1-3 as seen (a) on the CT-slice and (b) in the anterior localizer. 181
7.9 Stereotactic transformation results in two patient cases. 187
7.10 Angle definitions of the linear accelerator according to the DIN-6847 standard. The DPM reference system is also represented. 188
7.11 Angle definitions of the gantry (θ_g) and couch (φ_c) of the accelerator according to the DPM reference system. 189

7.12 Simplified diagram of the Source Interface implementation. 192
7.13 Dose distribution calculated by STP3 for case 1 in the axial plane. . . 195
7.14 Dose distribution calculated without heterogeneities by RMSM for case 1.a in the axial plane. 196
7.15 Dose distribution calculated with heterogeneities by RMSM for case 1.b in the axial plane. 196
7.16 Dose distribution calculated by STP3 for case 1 in the coronal plane. . 197
7.17 Dose distribution calculated without heterogeneities by RMSM for case 1.a in the coronal plane. 197
7.18 Dose distribution calculated with heterogeneities by RMSM for case 1.b in the coronal plane. 198
7.19 Dose distribution calculated by STP3 for case 1 in the sagittal plane. . 198
7.20 Dose distribution calculated without heterogeneities by RMSM for case 1.a in the sagittal plane. 199
7.21 Dose distribution calculated with heterogeneities by RMSM for case 1.b in the sagittal plane. 199
7.22 Dose distribution calculated by STP3 for case 2 in the axial plane. . . 200
7.23 Dose distribution calculated with heterogeneities by RMSM for case 2 in the axial plane. 200
7.24 Dose distribution calculated by STP3 for case 2 in the coronal plane. . 201
7.25 Dose distribution calculated with heterogeneities by RMSM for case 2 in the coronal plane. 201
7.26 Dose distribution calculated by STP3 for case 2 in the sagittal plane. . 202
7.27 Dose distribution calculated with heterogeneities by RMSM for case 2 in the sagittal plane. 202

List of Tables

1.1 Values of $< Z/A >_{med}$ / $< Z/A >_{w}$ for various substances of medical interest. 20

1.2 Reference conditions for the determination of the calibration factor N_{D,w,Q_0} in Cobalt-60 according to IAEA TRS-398 *Code of Practice*. 34

4.1 Relative contributions of the accelerator head components for the 10×10 cm^2 radiation field. Average energy of particles coming from each component. All data are calculated at the scoring plane placed at 45 cm from the source. 85

4.2 Calculation time needed to achieve an uncertainty of 1.5% in all calculated points for depth dose simulations. 103

4.3 Calculation time needed to achieve an uncertainty of 1.5% in all calculated points for off axis dose simulations. 108

4.4 Value of calculated output factor for all the additional collimators. δ is the relative difference between the calculated output factor OF_c and the measured output factor OF_m: $\delta_m = (OF_c - OF_m)/OF_m$ in %. 113

6.1 Values of $\overline{zl}$ for the different accelerator head components. $\overline{zl}$ represents the average cote along the z-axis of the point of origin of the unscattered photons for different accelerator head components. 139

6.2 Percentage intensities of the relevant virtual sources representing the accelerator head plus the additional collimator. 150

6.3 Relative number of original histories for each additional collimator based on output factors calculated by MCNP4C (OF_{4C}). Results are normalized to the number of original histories $n_{RM}(23) = 7.2 \times 10^8$. OF calculated by RMSM are also presented. 155

7.1 Conversion of CT-number to elemental weights according to Schneider *et al.* [SBS00] of 61 defined materials for Siemens Somatom Plus 4. . . 173
7.2 Tilts of the ring in the CT-reference system for two cases compared with ones calculated by the commercial TPS STP3. 188
7.3 Plan characterization for two patient cases. The reference isodose Pr is the isodose that involves at least 90% of the volume the target. 193
7.4 Average CPU time per fixed beam and dose associated error at isocenter for simulations performed with 2.1×10^8 histories (per fixed beam) using the 11 mm additional collimator. 193
7.5 Comparison between maximum dose points calculated by STP3 and RMSM for cases 1.a and 1.b. 194
7.6 Comparison between maximum dose points calculated by STP3 and RMSM for case 2. 194

List of Publications

Journal Publications

C.Oliveira, I.F.Gonçalves, A.Chaves, M.C.Lopes, N.Teixeira, B.Matos, I.C.Gonçalves, A.Ramalho and J.Salgado, "Monte Carlo method applied to medical physics", *Radioproteção* **1(6-7)**:37–42, 1999/2000.

A.Chaves, M.C.Lopes and C.Oliveira, "Monte Carlo simulation applied to radiosurgery narrow beams using MCNP4C", *Radioproteção* **1**:149–157, 2000/2001.

M.C.Lopes, F.Sánchez-Doblado, K.Theodorou, A.Mazal, L.Nuñez, A.Chaves, C.Kappas, M.Bazioglou and P.Lassalete, "A proposed method for beam measurements in stereotactic radiotherapy", *Phys. Medica* **16**:91–94, 2000.

A.Chaves, M.C.Lopes, C.Oliveira, C.Alves, L.Peralta, P.Rodrigues and A.Trindade, "Basic dosimetry of radiosurgery narrow beams using Monte Carlo simulations - A detailed study of depth of maximum dose", *Med. Phys.* **30**:2904–2911, 2003.

A.Chaves, M.C.Lopes, C.Oliveira, C.Alves, L.Peralta, P.Rodrigues and A.Trindade, "A Monte Carlo multiple source model applied to radiosurgery narrow photon beams", *Med. Phys.* **31**:2192–2204, 2004.

Conference Publications

Grupo de Radiocirurgia de Coimbra, "Radiocirurgia: procedimentos de controlo de qualidade e aferição da técnica", III Congresso Nacional de Radiologia, 22th to 25th May 1996, European week against cancer, 9th October 1996 Coimbra, Portugal, IV Encontro da Sociedade Portuguesa de Neurocirurgia, 22th to 23th November 1996, Porto, Portugal.

M.C.Lopes and A.Chaves, "Dosimetria de feixes finos em Radiocirurgia", V Jornadas Portuguesas de Protecção Contra as Radiações, 28th March 1998, Évora, Portugal.

A.Chaves, M.Fragoso, M.C.Lopes, C.Oliveira, L.Peralta and J.Seco, "Simulação por Monte Carlo da cabeça de um acelerador linear de electrões para a Radioterapia", 11^{a} Conferência Nacional de Física, 7th to 10th September 1998, Porto, Portugal .

A.Chaves, C.Oliveira, M.C.Lopes and J.Salgado, "A Monte Carlo study of a linear accelerator head. Optimization of the running time to obtain the phase space source", 5th Biennial ESTRO Meeting on Physics for Clinical Radiotherapy, 8th to 11th April 1999, Göttingen, Germany, *Rad. and Onc.* **51(S1)**:S62, 1999.

M.Fragoso, A.Chaves, C.Alves, C.Oliveira, J.Seco, L.Peralta and M.C.Lopes, "MC simulation of a linear accelerator treatment head-EGS4 and MCNP-4B intercomparison", 5th Biennial ESTRO Meeting on Physics for Clinical Radiotherapy, 8th to 11th April 1999, Göttingen, Germany, *Rad. and Onc.* **51(S1)**:S62, 1999.

M.Fragoso, A.Chaves, C.Alves, M.C.Lopes, C.Oliveira, L.Peralta L and J.Seco, "MC simulation of a linear accelerator treatment head -EGS4 and MCNP-4B intercomparison", *in Proc. 8th Int. Conf. On Calorimetry in High Energy Physics (Lisboa)*, Edited by G.Barreira, B.Tomé, A.Gomes, A.Maio and M.J.Varanda, pp 697-702, World Scientific, Singapore, 1999.

C.Alves, A.Chaves, M.Fragoso, M.C.Lopes, L.Peralta, P.Rodrigues, C.Oliveira and A.Trindade, "Simulação por Monte Carlo em Radioterapia Externa", 12^{a} Conferência Nacional de Física, 27th to 30th de September 2000, Figueira da Foz, Portugal.

A.Chaves, M.C.Lopes, C.Oliveira, P.Rodrigues, A.Trindade and L.Peralta, "Monte Carlo Calculations for Output Factors of Radiosurgery Narrow Beams", MC2000 - Advanced Monte Carlo on Radiation Physics, Particle Transport Simulation and Applications, 23th to 26th October 2000, Lisbon, Portugal.

C.Alves, M.C.Lopes, A.Chaves, L.Peralta, P.Rodrigues, A.Trindade, C.Oliveira, "Buildup measurements and calculations for photon beams", *in Proc. of the Topical Meeting on Medical Radiation Physics and Engineering (Lisbon)*, *Phys. Medica*, **17(4)**:23–25, 2001.

A.Chaves, M.C.Lopes, C.Oliveira, L.Peralta, P.Rodrigues and A.Trindade, "Monte Carlo Simulation of Radiosurgery Photons Beams", 6th Portuguese Conference On Biomedical Engineering, BioEng'2001, 11th to 12th June 2001, Universidade do Algarve, Portugal.

A.Chaves, M.C.Lopes and C.Oliveira, "Basic dosimetry of radiosurgery narrow beams using Monte Carlo simulations - a detailed study of depth of dose maximum", International Symposium on Standards and Codes of Practice in Medical Radiation Dosimetry, 25th to 28th November 2002, Viena, Austria.

A.Chaves, M.C.Lopes, C.Oliveira and L.Peralta, "Problems and solutions to face radiosurgery dosimetry and calculations", Bioeng'2003: 7th Portuguese Conference on Biomedical Engineering, 26th to 27th June 2003, Lisboa, Portugal.

A.Chaves, C.Oliveira, M.C.Lopes and L.Peralta, "Development and validation of a multiple source model for radiosurgery", 7th Biennal ESTRO Meeting on Physics in Clinical Radiotherapy, 13th to 18th September 2003, Genève, Suisse, *Rad. and Onc.* **68(S1)**:S42, 2003.

Note

Technical information regarding the Siemens Mevatron KD2 linear accelerator treatment head is propriety of Siemens AG Medical Engineering and cannot be used outside this thesis without previous consent.

Introduction

The discovery of x-rays by Röntgen in 1895 marked the beginning of a new physics branch: medical physics. Traditionally, medical physics deals with applications of ionizating radiation: nuclear medicine, radiology, and radiotherapy, the field of interest of this thesis. Radiotherapy is divided into two main areas: external radiotherapy which deals with radiation produced outside the patient and brachytherapy which deals with radioactive sources placed inside the patient. The aim of radiotherapy is to deliver a prescribed amount of radiation dose to the tumor, whilst sparing, as much as possible, the surrounding normal tissues.

Radiation sources used in external radiotherapy are usually radioactive Cobalt-60 sources in Cobalt units, and the large majority, high energy x-rays photons and electrons sources produced by medical electron linear accelerators (linac). The increase of interest in hadronic therapy leaded to the use of hadronic radiation sources, such as protons. Unfortunately due to the high cost of such therapy, only few centers in the world have these kind of facilities. The first high energy x-rays beams for radiotherapy treatments became available in the 50's and 60's. The appearance of new image modalities such as the computed tomography, allowed a better definition of the volumes to irradiate but also a more reliable computation of the absorbed dose in the patient using sophisticated calculation tools. Since those days, great efforts were done to accurately deliver the dose to the patient involving more and more sophisticated linacs using dynamic techniques such as *Intensity Modulated Radiation Therapy* (IMRT).

A precise dose delivery to the tumor site in the patient implies quantitative measurements. Radiation dosimetry is the branch of medical physics that deals with the measurement of the dose and is based on the understanding of the nature of ionizing radiation used in radiotherapy and the radiation detection methods. The determination of the absorbed dose is a complex process composed by various steps conducting

from the knowledge of the basic particles interaction processes in matter, to the use of dosimetry protocols to accurately determine the absorbed dose in water. This will be the aim of **Chapter 1**.

Radiosurgery is a highly-specialized external radiotherapy procedure that uses narrow photon beams produced by a linear accelerator or a Gamma-Knife. Using linear accelerators, narrow photon beams are shaped through the interposition of additional collimators at the beam exit. This technique, clinically available since 1996 at Instituto Português de Oncologia Francisco Gentil - Centro Regional de Oncologia de Coimbra (IPOFG-CROC) nowadays IPOFG-CROC, S.A., is applied to the treatment of tumors and arteriovenous malformations (AVMs) of small dimensions located in the brain, where conventional surgery can not access. Combining several arcs, couch positions and secondary collimators, patients are treated in one single session with a delivered dose approximately 10 times higher than that administrated in a conventional radiotherapy treatment fraction. A high degree, of both geometrical and dosimetrical accuracy, must be achieved in this kind of treatment. **Chapter 2** will present some basic physical aspects of radiosurgery.

Dose measurement with narrow photon beams used in radiosurgery is not an easy task. The reduced field dimensions and the corresponding high dose gradients in the penumbra region, make the dose measurement very complex and results remain inaccurate for the very narrow photon beams. This is mainly due to three factors:

1. the relationship between the detector size and the field dimension,
2. the lack of lateral electron equilibrium which leads to steep dose gradients in the penumbra region,
3. the material of the detector.

Monte Carlo techniques are suitable to study difficult radiation transport problems as much as simple energy degradation processes. They are in fact a powerful tool to assess the details of the dose deposit process that accounts for all aspects of primary and secondary radiation transport inside the treatment machine head, and also within the patient. Medical physics, in general, and radiotherapy in particular, are nowadays privileged Monte Carlo simulation application fields. This was achieved through the great improvement in the photon-electron transport and the great increase of CPU

capabilities. This increase of interest for radiotherapy applications leads to the development of very suitable specific codes, although general codes continue to be very useful in understanding the details of dose deposit. **Chapter 3** will present the electron-photon transport for a general and a specific Monte Carlo code used in this thesis.

In **Chapter 4**, the accelerator head of the Siemens Mevatron KD2 linear accelerator in 6 MV photon mode with the 10×10 cm^2 radiation beam and the additional collimators, used in radiosurgery treatments performed at IPOFG-CROC, S.A., are simulated through the general Monte Carlo code MCNP4C. The aim of this chapter, is to describe the process of simulation, to characterize the 10×10 cm^2 radiation beam and, the first goal of this thesis, to compare and validate the Monte Carlo results with several dosimetric methods.

In radiosurgery narrow photon beams, the depth of maximum dose in water, d_{max}, in the beam central axis increases as the size of the additional collimator increases. This behavior is the opposite of what is observed in radiotherapy conventional beams. But the details of such phenomenon regarding narrow photon beams still remain quite unknown like the characteristics of the photons producing electrons contributing to d_{max} and the details of the scattered photon and electron processes in the water. MC simulation is a privileged tool to assess such type of information. The purpose of **Chapter 5**, is to fully understand the behavior of d_{max} for narrow photon beams using MC simulations performed by MCNP4C.

In radiotherapy, sophisticated dose calculation tools called treatment planning systems are used to compute the dose distribution according to a determined treatment plan. Unfortunately, in some complex setups (irregular fields, air/bone interfaces, heterogeneities), current commercial treatment planning systems do not accurately calculate dose distributions. Once again, Monte Carlo methods can be applied to overcome this difficulty. In radiosurgery applications, MC calculation time and data storage are strong limitation factors. In fact, radiosurgery arcs are simulated using fixed beams. In a standard treatment, at least 48 fixed beams have to be taken into account. Therefore, because the patient geometry must be divided into small voxels, the overall simulation time has to be increased dramatically in order to achieve the required dose accuracy with very large source particle files. To solve the problem, a new approach called multiple source model, produces radiation beams having the same dosimetric effect than

the full Monte Carlo simulation of real radiation beams. This model, coupled with the specific Monte Carlo code DPM, will be developed in **Chapter 6**. The development of this very fast dose calculation engine enables a Monte Carlo based radiosurgery treatment planning for real patient cases. Like any radiosurgery treatment planning system, it must include tools such as CT-image data conversion to human tissues and stereotactic geometrical transformation. A source transformation to simulate the arcs must also be included. All these features will be treated in **Chapter 7** where comparisons with the commercial treatment planning currently used at IPOFG-CROC, S.A., will also be performed. The development of a fast and accurate MC treatment planning system based on a multiple source model represents the second goal of this thesis.

Chapter 1

Dosimetry of high-energy photon beams

In radiotherapy, the accurate determination of the dose delivered to the tumor and the healthy tissues surrounding the lesion is of primary importance for the outcome of a treatment. Brahme [Bra88] has discussed uncertainties in the absorbed dose to lesions influences the *tumor control probability* (TCP). He showed that the dose response (TCP) is correlated with the uncertainty levels on absorbed dose (D) by:

$$DRG = \frac{\Delta(TCP)}{\Delta D/D}, \tag{1.1}$$

where DRG is the normalized dose response gradient extracted from a dose response curve to control a tumor using the sigmoidal shape model (see Fig. 1.1).

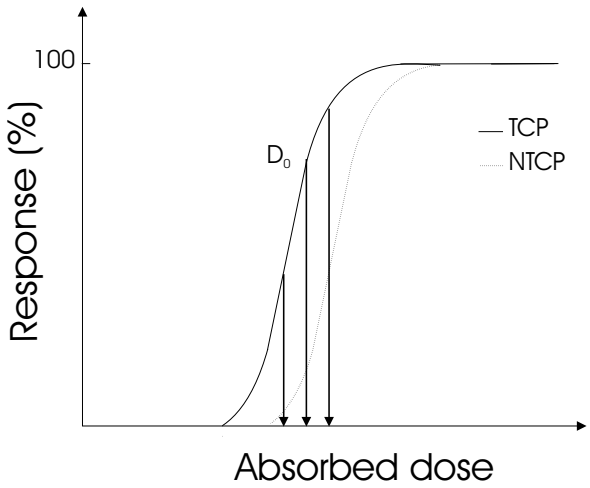

Figure 1.1: Example of sigmoidal shape of dose response curves for tumor control probability (TCP) and normal tissue complication probability (NCTP).

Figure 1.1 also shows the influence of an uncertainty in the delivered dose D_0 to the *normal tissue complication probability* (NTCP): higher doses can produce undesirable (and sometimes unacceptable) secondary effects in the healthy tissues. A complication-free cure is the desired goal of treatment. That is, an optimal treatment dose will produce the maximal TCP with a reasonably low incidence of NTCP [Ste97]. The inaccuracy in the absorbed dose was fixed at 5% [ICR93].

The determination of the absorbed dose in water is a complex process composed by various steps conducting from the knowledge of the basic particles interaction processes in matter, to the application of dosimetry protocols to accurately determine the absorbed dose in water. The goal of this chapter is to present these various steps.

1.1 Photon interactions

The main photon interactions which take place when a megavoltage x-ray beam interacts with matter (namely human tissues) are photoelectric, Compton and pair production effects. The mechanism by which the photons interact with the matter without an appreciable transfer of energy is the Rayleigh-Thompson scattering.

1.1.1 Photoelectric effect

The photoelectric effect is dominant at low photon energies and involves the absorption of the photon by an orbital electron when ejected from the atom. The kinetic energy of the emitted photoelectron, T_{e^-}, is equal to the incident photon energy $k_0 = h\nu_0$ minus the binding energy E_b of the electron, i.e, $T_{e^-} = k_0 - E_b$. The photoelectric interaction is most probable when the photon energy k_0 is only slightly larger than the electron binding energy in the particular atomic shell. Above the energy of the atomic K-shell, the probability per atom of photon absorption with an energy sufficiently high to eject an electron with non-relativist energy is approximately given by:

$$\sigma_p^a \approx \sqrt{2}\frac{32\pi r_e^2 \alpha^4}{3}\left(\frac{3m_0c^2}{k_0}\right)^m Z^n, \tag{1.2}$$

where $\alpha = 1/137$ is the fine structure constant, m_0 and r_e are respectively the mass and classical electron radius and Z the atomic number of the material. The exponent n varies between 4 ($k_0 < 100$ keV) and 4.6 ($k_0 > 500$ keV), and m varies between 3 ($k_0 <$ 100 keV) and 1 ($k_0 > 500$ keV) [Bie00]. In the region $k_0 \leq 0.1$ MeV, photoeffect is

important with energies greater than the atomic binding energy of the atomic electrons of the absorber, and the atomic cross section varies roughly as Z^4 and $(k_0)^{-3}$. The photoelectric mass attenuation coefficient, μ_p/ρ, varies as Z^3 and $(k_0)^{-3}$. After the ejection of the atomic electron, the atom is left in an excited state with an electron vacancy in one of the electron shells. The exceed atomic energy will be released by one of several possible processes such as characteristics x-rays or Auger electron.

1.1.2 Rayleigh scattering

Rayleigh scattering, or coherent scattering, is the elastic interaction of a photon with an atom. Photons are scattered by the bound electrons of the atom without energy transfer to the atom. This process mainly occurs with low energy photons in high-Z materials. The differential cross section in solid angle Ω for coherent scattering is given by:

$$\frac{d\sigma_r^a}{d\Omega} = \frac{r_e^2}{2}\left(1+\cos^2\theta\right)[F(q,Z)]^2 \qquad (\mathrm{cm^2 sr^{-1} atom^{-1}}), \tag{1.3}$$

where $q = 2ksin(\theta/2)$ (with $k = h\nu/c$) is the transferred momentum at angle θ and $F(q,Z)$ is the atomic form factor [HØ79]. When $q \to 0$ because $\theta \to 0$ then $F(q,Z) \to Z$.

1.1.3 Compton effect

The process is due to the interaction of a photon of energy k_0 with an essentially free electron. The electron is considered free as long as its binding energy is much less than the photon energy. In this interaction, the initial photon is scattered, transferring some of its initial energy to an ejected electron. The collision process of the Compton interaction is described by applying the relativistic laws of conservation of momentum and energy. Thus, the kinetic energy T_{e^-} of the Compton recoil electron, scattered at angle φ, is given by:

$$T_{e^-} = h\nu_0 \frac{\varepsilon(1-\cos\theta)}{1+\varepsilon(1-\cos\theta)}, \tag{1.4}$$

where θ is the angle of the scattered photon with:

$$\cot\theta = \left(1+\frac{k_0}{m_0c^2}\right)\tan(\theta/2). \tag{1.5}$$

The energy of the scattered photon, k, at angle θ is given by:

$$k = \frac{k_0}{1+\varepsilon(1-\cos\theta)}, \tag{1.6}$$

where $\varepsilon = k_0/m_0c^2$ with $m_0c^2 = 0.511$ MeV, the mass of the electron. The Klein-Nishina (K-N) [KN29] expression for the differential cross section per unit solid angle per electron for a photon scattered at an angle θ is:

$$\frac{d\sigma_c^e}{d\Omega} = \frac{1}{2}r_e^2\left(\frac{k}{k_0}\right)\left(\frac{k}{k_0} + \frac{k_0}{k} - \sin^2\theta\right) \qquad (\text{cm}^2\text{sr}^{-1}\text{electron}^{-1}). \tag{1.7}$$

The total cross section per electron σ_c^e is obtained by integrating Eq. 1.7 over all scattering angles θ:

$$\sigma_c^e = 2\pi r_e^2\left\{\frac{1+\varepsilon}{\varepsilon^2}\left[\frac{2(1+\varepsilon)}{1+2\varepsilon} - \frac{ln(1+2\varepsilon)}{2\varepsilon}\right] + \frac{ln(1+2\varepsilon)}{2\varepsilon} - \frac{1+3\varepsilon}{(1+2\varepsilon)^2}\right\} \ (\text{cm}^2\text{electron}^{-1}). \tag{1.8}$$

For incident photons with $h\nu_0 \leq 0.01$ MeV, the K-N electron cross section is almost equal to the Thompson scattering cross section but then it gradually decreases at higher photon energies and becomes proportional to $(h\nu_o)^{-1}$. In the Thompson scattering, no energy is retained by the electron as a result of this elastic event. For very low energy incident photons, the K-N cross section must be corrected to take into account the energy binding of the electrons. The atomic K-N cross section, σ_c^a, is proportional to atomic number Z of the material since the K-N theory assumes the electron to be unbound turning the electron cross section independent of Z. Thus, $\sigma_c^a = Z.\sigma_c^e$ (cm^2/atom). The Compton mass attenuation coefficient, μ_c/ρ, is approximately independent of Z, since $\mu_c/\rho = [N_A.(Z/A)]\sigma_c^e$ (cm^2/g), where the ratio Z/A is equal to 1 for hydrogen and may be averaged to 0.45 ± 0.05 for all other elements.

1.1.4 Pair and Triplet production

When the incident photon energy is larger than 1.02 MeV, an interaction with the coulombian nuclear field can occur. Then, the photon disappears and an electron/positron (e^+,e^-) pair is created. Because of the large nuclear mass, essentially no energy is transferred to the nucleus and part of the energy of the photon $h\nu_0$ is converted into electron and positron rest mass (1.022 MeV) while the remaining energy is distributed between the electron and the positron kinetic energies T_{e^-} and T_{e^+} respectively. The screening by atomic electrons surrounding the nucleus plays an important role in pair production. The cross section is dependent on a parameter ξ defined as:

$$\xi = \frac{100m_0c^2h\nu_0}{E_+E_-Z^{1/3}}, \tag{1.9}$$

where E_+ and E_- are, respectively, the total energy of outgoing positron and electron. At extreme relativistic energies and arbitrary screening, the Born approximation gives:

$$\frac{d\sigma^a_{pp}}{dE_+} = \frac{4Z^2 r_e^2 \alpha}{(h\nu_0)^3}\left\{(E_+^2+E_-^2)\left[\frac{\phi_1(\xi)}{4}-\frac{1}{3}\ln Z - f(Z)\right]+\frac{2}{3}E_+E_-\left[\frac{\phi_2(\xi)}{4}-\frac{1}{3}\ln Z - f(Z)\right]\right\}, \tag{1.10}$$

where $\alpha = 1/137$ is the fine structure constant, $\phi_1(\xi)$ and $\phi_2(\xi)$ are screening functions and $f(Z)$ a Coulomb correction function. To obtain the total pair production cross section at arbitrary screening, an integration of the above equation must be performed. It has been shown that this total cross section is proportional to Z^2 and increases as the logarithm of the incident photon energy [Bie00]:

$$\sigma^a_{pp} \propto Z^2 \ln\left(\frac{2k}{m_0c^2}\right). \tag{1.11}$$

Pair production may also occur in the atomic electron field. In this case, the interaction yields three particles; the electron-positron pair and the ejected orbital electron. This process is refereed as the triplet production. To approximately account for this interaction, Z^2 must be replaced by $Z(Z+1)$ in the above formulae. The pair production mass attenuation coefficient, μ_{pp}/ρ, is proportional to Z, since $\mu_{pp}/\rho = \sigma^a_{pp}[N_A.(Z/A)]$ and Z/A is almost constant as shown earlier (cf. Compton effect).

1.1.5 Total attenuation coefficient

The *total mass attenuation coefficient*, μ/ρ, is the sum of the mass attenuation coefficients of all the effects. Thus, the total mass attenuation coefficient (in $\mathrm{cm^2 g^{-1}}$) is given by:

$$\frac{\mu}{\rho} = \frac{\mu_p}{\rho} + \frac{\mu_c}{\rho} + \frac{\mu_r}{\rho} + \frac{\mu_{pp}}{\rho}, \tag{1.12}$$

where μ_p/ρ, μ_r/ρ, μ_c/ρ and μ_{pp}/ρ represent respectively the photoelectric, Rayleigh, Compton and pair-production mass attenuation coefficients. Figures 1.2 and 1.3 show respectively the cross sections of the different effect for water and tungsten. This experimental data were extracted from the XCOM library [BHS$^+$99].

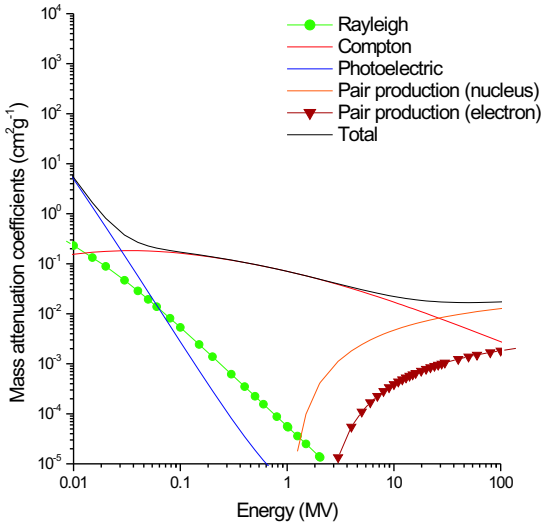

Figure 1.2: Total mass attenuation coefficient μ/ρ and the partial contribution of the various effects for water.

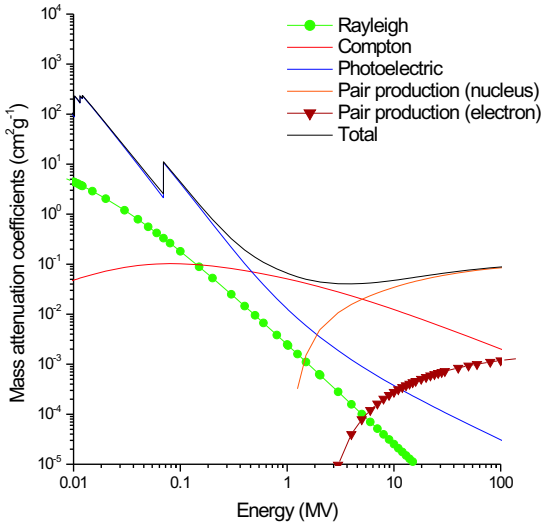

Figure 1.3: Total mass attenuation coefficient μ/ρ and the partial contribution of the various effects for tungsten.

The total mass attenuation coefficient is high for low energy photons due to the predominant photoelectric effect. It can be also noticed that, for low energy photons, μ/ρ is higher for tungsten than for water due to the Z^3 dependence of the photoelectric mass attenuation coefficient. At high energies, we clearly see that pair production process is dominant. Finally, in the range of photon energies used in radiotherapy applications (up to few MeV), where tissues are almost water equivalent ($\overline{Z} \simeq 7.6$), we clearly see that Compton effect is dominant. In this energy region, water and tungsten total mass attenuation coefficients do not differ significantly since the Compton mass attenuation coefficient is almost independent of Z.

Nuclear inelastic interactions were not taken into account since they only take place for photon energies above 10 MeV. At these energies, (γ, n) and (γ, p) photonuclear interactions start to appear [Kno89].

1.2 Electron interactions

The mechanisms by which an electron loses its kinetic energy or is deflected from its path are inelastic and elastic collisions in the Coulomb field of bound atomic electrons or nuclei [Kha84].

1.2.1 Inelastic collisions with atomic electrons

Coulomb interactions with the bound atomic electrons are the principal way by which electrons lose energy. Excitations and ionizations occur along the electron path. Occasionally, the energy transferred to the atomic electron is sufficient to create a secondary electron with a sufficient energy to proceed in the medium. These secondary electrons are called δ-rays. The electron Coulomb-force interactions can be described in terms of the relative size of the classical impact parameter b with respect to the size of the classical atomic radius a as illustrated in Fig. 1.4.

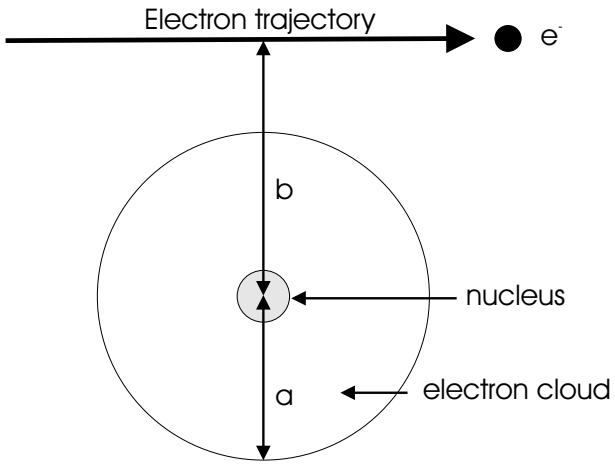

Figure 1.4: Parameters for an electron collision with the atom where a is the classical radius of the atom and b is the classical impact parameter.

In the excitation process, the electron energy is transferred by collision to the atom. During the excitation, an electron from an inner shell is moved to an outer orbit. The required energy is on the range 10-100 eV and consequently the energy loss of the impinging electron is small. The excited atom dissipates the excess energy by emitting visible light if the medium is gas or in form of heat in a condensed material. These kind of collisions, called soft collisions, takes place when the classical impact parameter b is much larger than the atom radius a and is the most probable interaction of an energetic electron with an absorbing medium, since b has a high probability to be greater than a. When the impact parameter b is of the order of the atomic radius a, the electron most likely interacts with a single atomic electron which receives most of the incident electron's kinetic energy. This kind of collisions are called hard collisions. If the incident electron has enough energy to overcome the binding energy of the orbital electron, this electron is removed from the shell and the atom becomes ionized. In general, the interaction can be treated as a free electron collision. This type of collision is often divided into two groups: small energy transfer and, more frequent, large energy transfer to the ejected orbital electron [Kle84]. The removed electron is called δ-ray if it carries energy in excess of about 100 eV and the collision is described as a catastrophic event. The direct knock-on collisions with orbital electrons with large energy transfer to the target electron are relatively rare compared to soft collisions. These knock-on electrons do not have much influence in the energy loss of the incident electron.

In the physics model of the Coulomb interaction between the primary fast electron and the bound electron in the medium (electron-electron collision), the primary elec-

tron imparts a net impulse to the bound electron, assumed free and at rest, and the energy transfer w is given by [Leo86]:

$$w = \frac{2e^4}{m_0 b^2 v^2}, \tag{1.13}$$

where e is the electron charge, b the classical impact parameter and v the velocity of the primary electron. Møller derived the relativistic cross-section for Coulomb interactions between free electrons and obtained the differential cross section for electron-electron scattering differential in the kinetic energy T of the scattered electron which is initially at rest, which is:

$$\frac{d\sigma_{col}}{dT} = \frac{2\pi r_e^2 m_0}{\beta^2}\frac{1}{T^2}\left[1 + \frac{T^2}{(T_0 - T)^2} + \frac{\tau^2}{(\tau+1)^2}\left(\frac{T}{T_0}\right)^2 - \frac{2\tau+1}{(\tau+1)^2}\frac{T}{T_0 - T}\right], \tag{1.14}$$

where $\beta = v/c$, T_0 the incident electron kinetic energy and $\tau = T_0/m_0c^2$ the electron kinetic energy in units of electron mass. Because the two electrons are indistinguishable, Eq. 1.14 is symmetric with respect to exchange of the energies of the two scattered particles and the maximum energy transfer is $T_0/2$. By definition, the electron with the higher energy after the collision is considered to be the primary. Møller cross section is valid for primary electrons with kinetic energy much greater than the binding energies of the atom in the medium and must be modified for electron kinetic energies close to the binding energies. This also sets a lower limit to the possible energy transfer. Thus, the total cross section for Møller interactions is obtained through integration of Eq. 1.14 from a threshold kinetic energy above which Møller events can occur up to $T_0/2$.

1.2.2 Inelastic collisions with nuclei

When the incident electron is close to the atomic nucleus, interactions with the nuclear Coulomb-field take place. Most of the interactions are quasi-elastic collisions with no modification in the electron energy. Occasionally, hard bremsstrahlung interactions take place and are called radiative collisions. Under the influence of the nuclear Coulomb field, the incident electron is deflected from its trajectory with a loss of energy. The loss of energy will be emitted in the form of radiation energy and the resulting photon can carry away up to 100% of the kinetic energy of the electron. This means that losses due to radiative collisions can be larger than for electron-electron collisions. The bremsstrahlung cross section for an incident electron with a total energy E_0 on an atom with atomic number Z, differential in the photon energy $k = h\nu$, corresponding

to the angular integration of the photon and electron emission directions, is given by Koch and Motz equation:

$$\frac{d\sigma_{brem}}{dk} = \frac{4Z^2 r_e^2 \alpha}{k}\left\{(1+\epsilon^2)\left[\frac{\phi_1(\xi)}{4} - \frac{1}{3}\ln Z - f(Z)\right] - \frac{2}{3}\epsilon\left[\frac{\phi_2(\xi)}{4} - \frac{1}{3}\ln Z - f(Z)\right]\right\}, \quad (1.15)$$

where $\alpha = 1/137$ is the fine structure constant, $\epsilon = E/E_0$ where E is the total scattered electron energy, $f(Z)$ the Coulomb correction factor for $\beta \gg \alpha Z$ (with β the incident electron velocity in units of the speed of light). The functions $\phi_1(\xi)$ and $\phi_2(\xi)$ account for screening effects with $\xi = (100 m_0 c^2 k)/(E_0 E Z^{1/3})$. Equation 1.15 is the result of the Born approximation calculation and is not valid for low incident electron energies. The bremsstrahlung cross section $d\sigma_{brem}/dk$ varies approximately in $1/k$. Due to the dependence in Z^2 of $d\sigma_{brem}/dk$, radiative collisions are more important for high-Z materials than for low-Z materials. The angular distribution of the bremsstrahlung photons is important. For low incident electron energy, the maximum intensity of the produced x-rays is in the direction perpendicular to the direction of the electron motion. At relativistic electron energies, the angular distribution of the emitted photons is strongly peaked forward. The mean value of the angular distribution of the emitted photons is $\overline{\theta} \approx m_0 c^2/E_0$.

1.2.3 Elastic scattering

In elastic nuclear scattering, the incident electron is deflected without radiating or exciting the nucleus, losing only the required kinetic energy for conservation of the momentum between the two particles [Eva55]. In elastic scattering with atomic electrons, the incident electron interacts really with the atom as a whole and is elastically deflected. These collisions with atoms are significant only for the case of low energy incident electrons ($<$ 100 eV) [Eva55]. Ignoring spin effects and screening, collisions with atoms are individually governed by the Rutherford formula [Rut11]:

$$\frac{d\sigma_{SR}}{d\Omega} = \frac{r_e^2 Z^2 e^4 m_0 c/\beta p}{4\sin^4(\theta/2)}, \quad (1.16)$$

where p is the incident electron momentum and θ the scattering polar angle. Because of its $1/\sin^4(\theta/2)$ dependence, the vast majority of these collisions result, therefore, in a small angular deflection of the electron. As the nucleus is much more massive than the electron, it is then assumed that the energy transfer to the nucleus is negligible. The cumulative effect of these small angle scatterings is a net deflection from the original

electron direction. In general, the treatment of Coulomb scattering is divided into three regions:

1. *single scattering* when the absorber is so thin that the probability of one or more than one Coulomb scattering is small. In that case Eq. 1.16 is used to calculate the angular distribution,

2. *plural scattering* when the number of collision N is lower than 20,

3. *multiple scattering* when $N > 20$ and energy loss is small or negligible. The problem can be treated statistically to obtain a probability distribution for the net deflection angle as a function of the thickness of the traversed material. The developed multiple scattering theories are included in Monte Carlo codes and will be discussed in Chapter 3.

1.2.4 Total electron cross sections

Figure 1.5 shows the total cross sections for the different elastic and inelastic processes. Data for carbon were extracted from the data library EEDL97 [CPS91]. Figure 1.5 shows clearly that, for carbon, between 10 eV and 5 MeV, the elastic process is the most probable with no contribution for electron energy loss. Between 10 eV and 10 GeV, the excitation process is the dominant inelastic interaction. The total cross section for ionizations is higher for the outer atomic shells than for the inner atomic shells due the lower binding energy of these orbital electrons. For energies of interest in radiotherapy field (a few MeV), the excitation process is the major mechanism of electron energy degradation due to its high cross section in this energy region, with small electron energy losses. It has to be noticed that as expected, the bremsstrahlung process in carbon is rare due to the low interaction cross section shown in Fig. 1.5.

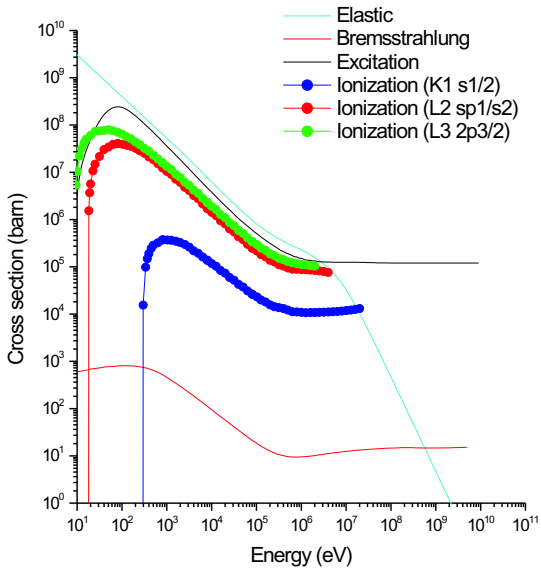

Figure 1.5: Total cross section for the carbon (Z=6) representing ionizations in three atomic shells (Møller scattering), excitation and Bremsstrahlung processes. Elastic scattering is also represented.

1.3 Electron stopping powers

In radiation physics and dosimetry, it is necessary to have the information about how the charged particles, such as the electrons, lose their energy along their tracks through matter. Energy losses usually take place in small steps and an electron must therefore suffer many collisions before it loses all its energy which is in marked contrast to the way in which photons transfer energy. Inelastic collisions occur with a certain quantum mechanical probability. However, because their number per macroscopic pathlength is generally large, the fluctuations in the total energy loss are small. Then, the electron penetration into a medium can be described by the *continuous slowing down approximation* (CSDA) which assumes that particles lose their energy linearly and continuously as they penetrate into medium. Thus, one can meaningfully work with the average energy loss per unit pathlength along the track of the electron called *stopping power*, $S = -dE/dx$, expressed in MeVcm^{-1}. The quotient S/ρ called the *mass stopping power* expressed in MeVcm^{2}g^{-1}, greatly reduces, but does not eliminate, the dependence on the density ρ of the medium [ICR84]. As mentioned earlier, electrons lose energy by inelastic collisions. The evaluation of S/ρ should then include losses due

to all these inelastic collisions and is divided in two components [ICR99]:

$$\left(\frac{S}{\rho}\right)_{total} = \left(\frac{S}{\rho}\right)_{col} + \left(\frac{S}{\rho}\right)_{rad}, \tag{1.17}$$

where $(S/\rho)_{col}$ represents the losses by ionization and excitation collisions and $(S/\rho)_{rad}$ represents the losses by radiative collisions. This distinction between losses is important since the absorbed dose in the medium will be different: energy is deposited along the area surrounding the ionization track of the electron due to inelastic collisions with the atomic electrons, whereas energy irradiated is carried away from the point of interaction by bremsstrahlung and does not contribute locally to the dose.

The *collision mass stopping power* expresses the average linear energy loss by a charged particle in very numerous soft and few hard collisions. In general, the mass collision stopping power can be expressed as [BS82]:

$$\left(\frac{S}{\rho}\right)_{col} = \frac{N_A Z}{A} \int_{w_{min}}^{w_{max}} w \frac{d\sigma}{dw} dw, \tag{1.18}$$

where $d\sigma/dw$ is the cross section (per electron) for ionization and excitation with energy transfer of magnitude w. w_{max} for an electron with kinetic energy T_0 is equal to $T_0/2$, w_{min} a minimum value below which no excitation or ionization can happen. That is, the result of the interaction is an energy loss w between a minimum value w_{min} and an maximum possible value w_{max}. Bethe-Bloch have developed a theory to compute $(S/\rho)_{col}$ for electrons and they gave the following formula [Leo86]:

$$\left(\frac{S}{\rho}\right)_{col} = \frac{2\pi r_e^2 m_0 c^2}{\beta^2} \left(\frac{N_A Z}{A}\right) \left[\ln \frac{\tau^2(\tau+2)}{2(I/m_0c^2)} + F(\tau) - \delta - 2\frac{C}{Z}\right], \tag{1.19}$$

with

$$F(\tau) = 1 - \beta^2 + \left[\frac{\tau^2}{8} - (2\tau+1)\ln 2\right]/(\tau+1)^2, \tag{1.20}$$

where $\beta = v_0/c$, v the speed of the electron, $\tau = T_0/(m_0c^2)$, N_AZ/A the number of electrons per gram of medium, I the *mean excitation energy*, δ the *density-effect correction* parameter and C/Z the *shell correction*. The mean excitation energy, I, is an average of the transition energies E_i weighted by their oscillator strengths f_i according to:

$$Z \ln I = \Sigma_i f_i \ln E_i. \tag{1.21}$$

The most recent values of I are given by ICRU report 37 [ICR84]. For water, the best current estimate of I-value is 75.0 eV. The ratio of I/Z is approximately constant for absorbers with Z greater than 13. For smaller atoms, the electrons play a more important role in influencing the value of I. The stopping power varies slowly with particle energy and is proportional to the atomic number Z of the absorber material. Thus the general behavior of $(S/\rho)_{col}$ can be inferred from the residual multiplicative factor. It can be seen that $(S/\rho)_{col}$ varies as $(1/v^2)$, or inversely with particle energy. The Bethe-Bloch formula validates the intuitive assumption that the higher Z and the more dense the absorber, the greater the stopping power. Figure 1.6 shows the behavior of the mass collision stopping power with electron kinetic energy for air and water. The

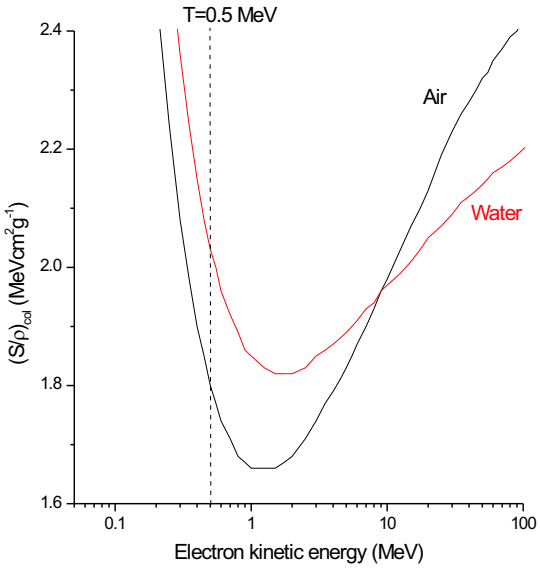

Figure 1.6: Mass collision stopping power versus electron kinetic energy for air and water.

rise at low energies is due to the $(1/v^2)$ factor. This is simply due to the fact that slow electrons spend more time passing through an atom than fast ones and hence lose more energy. The density-effect factor correction term, δ, arises from the fact that the electric field of the particle also tends to polarize the atoms along its path. This effect becomes more important as the particle energy increases and depends on the density of the material. The density effect reduces the value of $(S/\rho)_{col}$ at relativistic energies in condensed media [ICR84, Nah85]. The relativistic rise in the stopping power is connected to δ and Fig. 1.6 shows that the relativistic rise in the collision stopping power in the condensed medium (water) is much less pronounced compared to that in the

gas (air). The shell corrections account for the effects which arise when the velocity of the incident particle is comparable or smaller than the orbital velocity of the bound electrons. At such energies, the assumption that the electron is stationary with respect to the incident particle is no longer valid.

For ionization chamber dosimetry, it is useful to define the *collisional stopping power ratios* as:

$$\frac{\left(\frac{S}{\rho}\right)_{col}^{medium1}}{\left(\frac{S}{\rho}\right)_{col}^{medium2}} = \left(\frac{S}{\rho}\right)_{medium2}^{medium1}. \tag{1.22}$$

This quantity is of primary importance in the Bragg-Gray [Bra10, Gra29] and Spencer-Attix [SA55] cavity theories for the determination of the dose. Figure 1.6 shows clearly that the ratio of mass stopping powers, air to water, fundamental in the absorbed dose determination with an ionization chamber, is strongly energy dependent above around 0.5 MeV. This energy region is precisely the relevant one for megavoltage beams used in radiotherapy. Figure 1.7 shows the mass stopping power ratios, medium to water, for various substances of interest in radiotherapy in the megavoltage region. Once again,

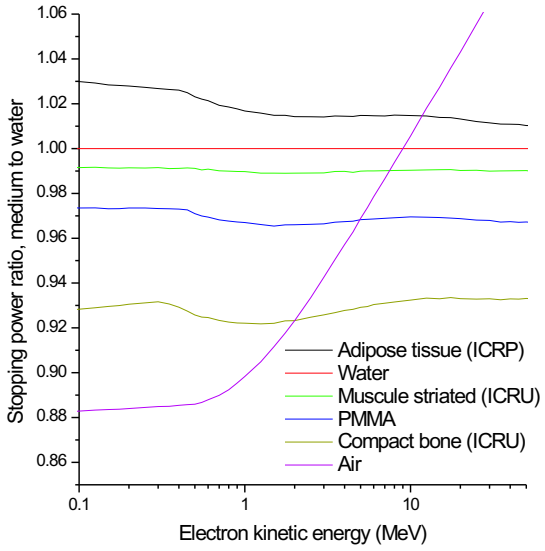

Figure 1.7: Ratios of mass collision stopping powers, medium to water, for various substances of medical interest.

the strong energy dependence of $(S/\rho)_{water}^{air}$ is observed for electron kinetic energies

greater than 0.5 MeV. Finally, it can be shown that for all the substances presented in Fig. 1.7 except bone, where the atomic number is appreciably higher, and air where the density effect plays a dominant role, we have $[(S/\rho)_{col}]_{med} \propto < Z/A >_{med}$ (see Table 1.1 for values of $< Z/A >_{med} / < Z/A >_w$).

	Adipose tissue	Muscle striated	PMMA	Compact bone	Air
$< Z/A >_{med} / < Z/A >_w$	1.006	0.990	0.971	0.955	0.899

Table 1.1: Values of $< Z/A >_{med} / < Z/A >_w$ for various substances of medical interest.

The concept of *restricted mass collisional stopping power*, (L_Δ/ρ), is introduced to calculate the energy transfer to a localized region of interest and expressed by:

$$\frac{L_\Delta}{\rho} = \left(\frac{S}{\rho}\right)_{col} - \frac{dE_{ke,\Delta}}{\rho dx}, \tag{1.23}$$

where $dE_{ke,\Delta}$ is the sum of the kinetic energies, greater than Δ, of all the electrons released by charged particle traversing a distance dx. (L_Δ/ρ) can also be calculated by setting $w_{max} = \Delta$ in Eq. 1.18. By limiting the energy transfer to secondary charged particles (δ-rays) to a threshold Δ, highly energetic secondary particles are allowed to escape the region of interest. That is, (L_Δ/ρ) includes collisions that produce secondary electrons having a kinetic energy less than the cutoff value Δ. The definition of (L_Δ/ρ) presented in Eq. 1.23 expresses an energy balance: energy lost by primary charged particle in collisions with electrons, along a track segment dx, minus energy carried away by secondary electrons having kinetic energies greater than Δ, equals energy considered as locally transferred. The choice of Δ depends on the problem. For problems involving ionization chambers, a frequently used threshold value is 10 keV (the range of a 10 keV electron in air is on order of 2 mm). The restricted mass stopping power (L_Δ/ρ) for electrons is given by [ICR84]:

$$\frac{L_\Delta}{\rho} = \frac{2\pi r_e^2 m_0 c^2}{\beta^2}\left(\frac{N_A Z}{A}\right)\left[\ln(T_0/I^2) + \ln(1+\tau/2) + G(\tau,\eta) - \delta\right], \tag{1.24}$$

where $\eta = T_0/\Delta$. The G factor is:

$$G(\tau,\eta) = -1-\beta^2+\ln(4(1-\eta)\eta)+\frac{1}{1-\eta}+(1-\beta^2)\left[\frac{\tau^2\eta^2}{2}+(2\tau+1)\ln(1-\eta)\right]. \tag{1.25}$$

It has been shown that for water and for $\Delta < 10$ keV, there is only a slight reduction in (S_{col}/ρ) which emphasizes the predominance of very small losses [ICR70].

The *mass radiative stopping power* $(S/\rho)_{rad}$ gives the rate in $\mathrm{MeVcm^2g^{-1}}$ of the bremsstrahlung production by electrons and is given by:

$$\left(\frac{S}{\rho}\right)_{rad} = \sigma_0 \frac{N_A Z^2}{A}(T_0 + m_0c^2)\overline{B_r}, \tag{1.26}$$

with $\sigma_0 = (1/137)(e^2/(m_0c^2))$, T_0 the kinetic energy of the incident electron and $\overline{B_r}$ a very slowly varying function of Z and T_0. Extensive tables of radiative stopping powers are given by Berger and Seltzer. For $T \gg m_oc^2$ (highly relativistic energies), Eq. 1.26 becomes:

$$\left(\frac{S}{\rho}\right)_{rad} \propto \frac{Z^2}{A} T_0 \overline{B_r}. \tag{1.27}$$

This implies that $(S/\rho)_{rad}$ increases with electron kinetic energy T_0 in an almost linear way above 0.5 MeV. Figure 1.8 compares the radiative mass stopping powers for compact bone (ICRU) and water. The radiative stopping power for compact bone is larger than for water due to the Z^2/A dependency.

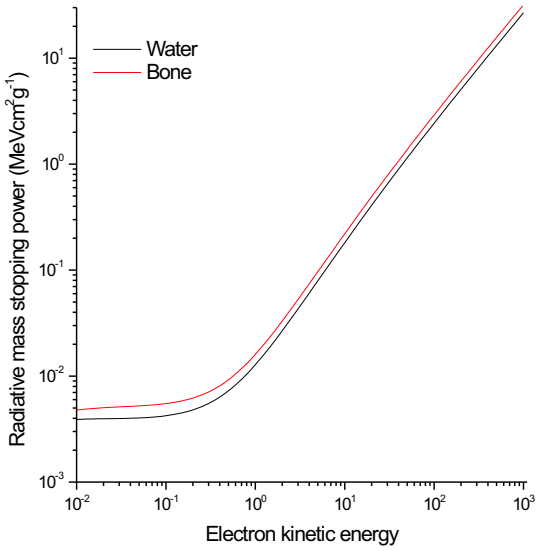

Figure 1.8: A comparison between radiative mass collision stopping powers for compact bone (ICRU) and water.

From the ratio S_{rad}/S_{col} shown in Fig. 1.9 for the various media of interest in radiotherapy, we have $S_{rad}/S_{col} \propto ZT_0$. A useful quantitative approximation is given by:

$$\frac{\left(\frac{S}{\rho}\right)_{rad}}{\left(\frac{S}{\rho}\right)_{col}} = \frac{ZT_0}{1600 m_0 c^2}. \tag{1.28}$$

The critical energy T_c is the energy at which collision and radiative losses are equal.

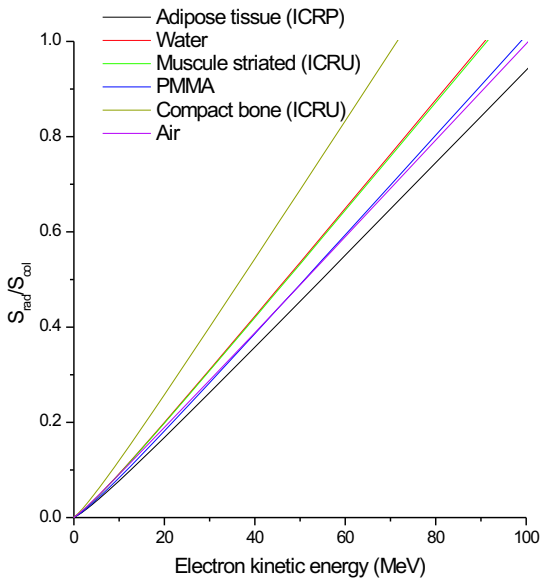

Figure 1.9: The energy and material dependence of the ratio radiative stopping power and collisional stopping power, S_{rad}/S_{col}, for the various media of interest in medical dosimetry.

For low atomic number materials, such as water, T_c lies about 90 MeV and above. For high Z material like Pb, T_c is about 7 MeV.

Finally, Fig. 1.10 shows the total mass stopping power for water. It is clear, according to Fig. 1.10, that the collision losses are dominant in the energy range of interest in radiotherapy. Radiation losses only become important above $T_c \backsimeq 93$ MeV. In the range of energies used in radiotherapy, it can be seen from Fig. 1.10 that $(S/\rho)_{total}$ varies slowly with T_0. The minimum value of $(S/\rho)_{total}$ is around $T_0 = 2$ MeV which is almost the same value for the various media of interest.

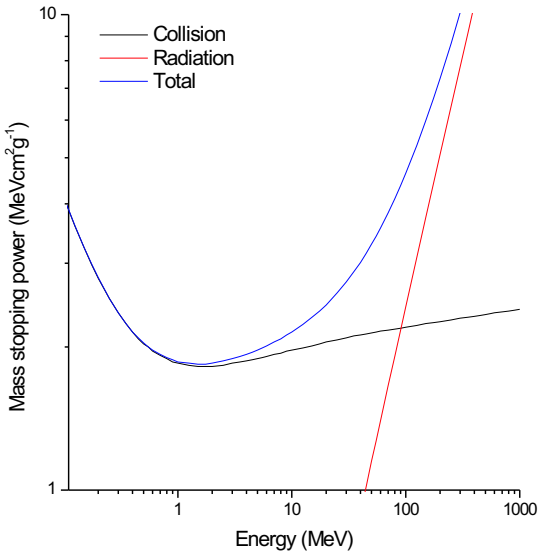

Figure 1.10: Collision, radiation and total mass stopping powers for electrons in water.

It showld be noticed that some more complex models also include losses due to positron interactions (Bhabha scattering and annihilation). In terms of stopping powers, the formalism is the same as for electrons with a different $F(\tau)$ function in Eq. 1.19 and $G(\tau, \eta)$ function in Eq. 1.26.

1.4 Absorbed dose determination

The International Commission on Radiological Units and Measurements (ICRU) defined some fundamental units in dosimetry such as *kerma* and *absorbed dose*, which will now be discussed.

1.4.1 Kerma

The quantity called *kerma* (Kinetic Energy Released in Material), K, is define as:

$$K = \frac{d\overline{E}_{tr}}{dm}, \tag{1.29}$$

where $d\overline{E}_{tr}$ is the sum of the initial kinetic energies of all charged ionizing particles released by uncharged ionizing particles in a material of mass dm. Kerma is expressed

in Gray (Gy) with 1Gy=1J/kg. The photon fluence ϕ defined as:

$$\phi = \frac{dN}{da}, \tag{1.30}$$

where dN is the number of photons incident on a sphere of cross-sectional area da, can be used to expressed Kerma. Thus,

$$K = \phi \frac{\mu}{\rho} \overline{E}_{tr}, \tag{1.31}$$

where μ/ρ is the photon mass attenuation coefficient of the medium. The product $\phi(\mu/\rho)$ represents the number of photon interactions per unit mass. Equation 1.31 is valid for a monoenergetic photon beam. For realistic beams composed by a spectrum of photon energies, Eq. 1.31 becomes:

$$K = \int_0^{h\nu_{max}} \frac{d\phi(h\nu)}{(h\nu)} \left(\frac{\mu(h\nu)}{\rho} \right) \overline{E}_{tr}(h\nu).d(h\nu). \tag{1.32}$$

Figure 1.11 illustrates the concepts of kerma.

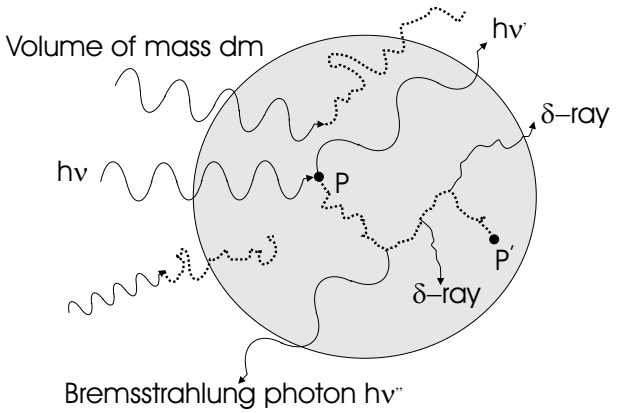

Figure 1.11: Illustration of energy transferred in a medium of mass dm by a photon of energy $h\nu$. The photon interacts in the medium at point P and transfers some of its energy in the form of electron's kinetic energy. The electron, in turn, transfers its energy to the medium through small collisions between point P and P'. The energy transferred per unit mass in P is designated by *kerma*. One of the δ-ray carries energy out of the volume with mass dm.

1.4.2 Absorbed dose

The *absorbed dose* is the most important quantity in radiation dosimetry and is defined by the ICRU as:

$$D = \frac{d\overline{E}_{ab}}{dm}, \tag{1.33}$$

where $d\overline{E}_{ab}$ is the mean energy absorbed in the medium element of mass dm from ionizing energy. As kerma, the absorbed dose is expressed in Gy. Using Fig. 1.11, the absorbed dose is the energy given to the medium by the secondary electron along the path P to P', excluding all energy that escapes the volume, i.e, excluding the energy of the scattered photon $h\nu'$, the energy of the bremsstrahlung photon $h\nu''$ and part of the energy of the δ-ray which escapes from the volume. The size of dm has to be small enough to represent the dose value at a point, however, not too small to avoid significant statistical fluctuations from the energy deposition process. That is, if dm is too small, due to the random energy deposition process, fluctuations are so large that the energy deposition process becomes stochastic. The absorbed dose defined in Eq. 1.33 is a non-stochastic quantity i.e, it is assumed that the fluctuations are negligible in the mass element dm.

1.4.3 Charged Particle Equilibrium

The concept of *Charged Particle Equilibrium* (CPE) is very important in radiation dosimetry. Since kerma and absorbed dose do not occur at the same point, a similar relation to Eq.1.31 cannot be applied to calculate the absorbed dose unless electronic equilibrium exists at the point of calculation. That is using Fig. 1.12, the number of secondary electrons entering and stopping inside the volume of mass dm must be equal to the number of secondary electrons created and escaping the same volume. Figure 1.12 is also useful to introduce some definitions. The point d_{max} represents the depth of the maximum dose. The buildup region represents the region between the surface and d_{max}. Under the CPE condition, kerma and absorbed dose are linked by the following relation:

$$D = \phi\frac{\mu}{\rho}\overline{E}_{ab} = K(1-g) = K_{col}, \tag{1.34}$$

where g is the fraction of electron's energy lost in radiative processes and K_{col} called the *collision kerma*.

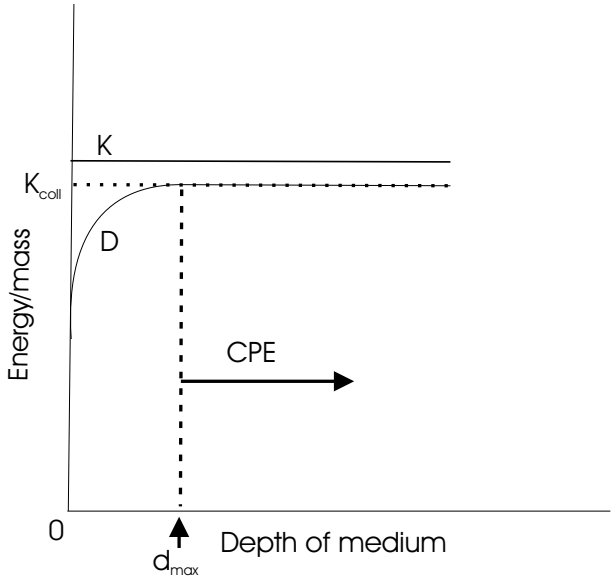

Figure 1.12: Quantities kerma (K), absorbed dose (D) and collision kerma (K_{coll}) plotted as function of depth in *Charged Particle Equilibrium* condition.

True CPE is virtually impossible to achieve in practice. In photon beams, attenuation means that the photon fluence does not remain constant and therefore the number of secondary electrons starting at different depths cannot either be constant. Even if true CPE does not exists, there are situations when we have:

$$D \propto K_{col}. \tag{1.35}$$

In these particular situations we have the so-called *Transient Charged Particle Equilibrium* (TCPE). Figure 1.13, where the quantities K, D and K_{coll} are plotted as function of depth, shows an example of TCPE region [Att86]. In the TCPE conditions, we have the curves representing K, D and K_{coll} parallels to each other and if the radiative interactions and scattered photons are ignored, we have at a depth d [Gre81]:

$$D(d) = K_{col}(d)e^{\mu\overline{x}}, \tag{1.36}$$

$$D(d) \approx K_{col}(d)[1 + \mu\overline{x}] = \beta K_{col}(d), \tag{1.37}$$

where μ is the common slope of D, K and K_{col} curves and $\overline{x}$ is the mean distance the secondary charged particles carry their kinetic energy in the direction of primary rays while depositing it as dose [Att86].

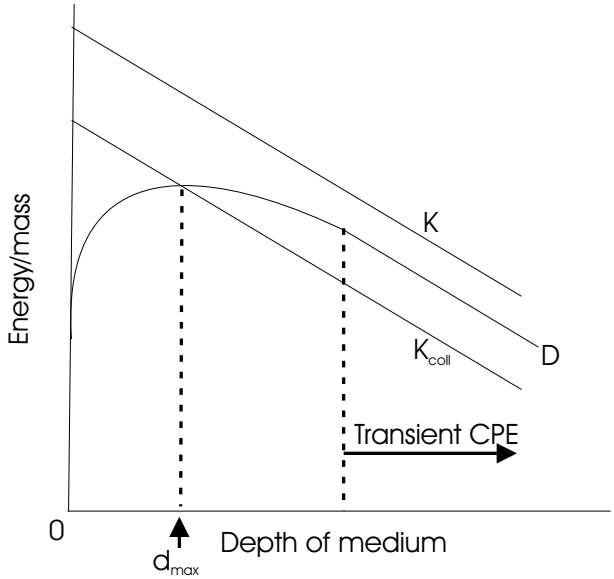

Figure 1.13: Quantities kerma (K), absorbed dose (D) and collision kerma (K_{coll}) plotted as function of depth in *Transient Charged Particle Equilibrium* condition.

1.4.4 Bragg-Gray cavity theory

The determination of the absorbed dose to water is usually based on a measurement of ionization followed by calculations involving a number of correction factors. These factors are derived from the Bragg-Gray cavity theory [Bra10, Gra29]. The Bragg-Gray theory was the first cavity theory developed to provide a relationship between absorbed dose in a dosimeter and the absorbed dose in the medium containing the dosimeter. This theory considers a homogeneous medium containing a small gas-filled cavity traversed by electron tracks (see Fig. 1.14). To apply the theory, two conditions

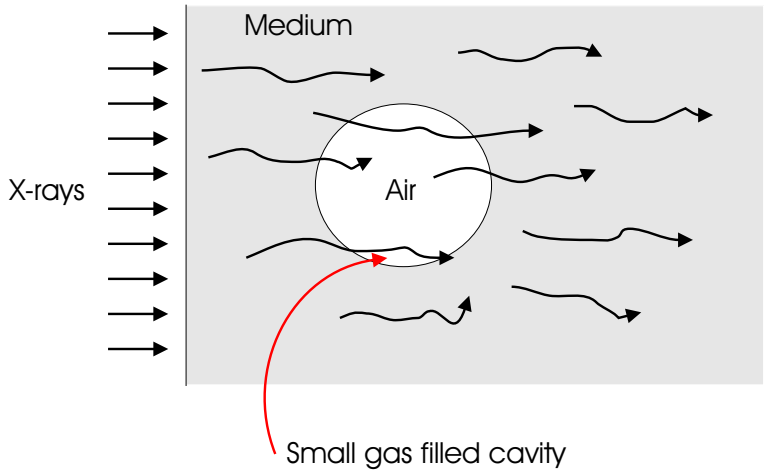

Figure 1.14: A Bragg-Gray cavity in a medium traversed by electron tracks.

must be fulfilled. First, the dimension of the cavity must be small in order to not change the electron fluence in the medium i.e the fluence of electrons traversing the cavity is assumed to be identical to that existing at the point of interest in the medium in absence of the cavity. Second, the absorbed dose in the cavity must be deposited by the electrons released by photons in the surrounding medium and passing through this cavity.

Assuming that CPE conditions exist, the dose D_m to the medium m is equal to a quantity called CEMA (Converted Energy per unit Mass) [ICR98] given by :

$$D_m = \Phi_T \Big(\frac{S_T}{\rho}\Big)^m_{col}, \tag{1.38}$$

where $(S_T/\rho)^m_{col}$ is the collisional stopping power for the medium for electrons with kinetic energy T and Φ_T the fluence of the primary electrons of kinetic energy T. The collisional stopping power is used because we are interested in energy locally deposited rather than the total stopping power which includes the energy lost in the form of bremsstrahlung which would escape. Under the Bragg-Gray cavity theory conditions, the dose deposited in the medium D_m is related to the dose in the cavity D_c as follows:

$$\frac{D_c}{D_m} = \frac{(S_T/\rho)^c_{col}}{(S_T/\rho)^m_{col}} = \Big(\frac{S}{\rho}\Big)^c_m, \tag{1.39}$$

where $(S/\rho)^c_m$ is the ratio of mass collisional stopping powers in media c and m for electrons of kinetic energy T. For realistic beams composed by a spectrum of electron energies, $(S_T/\rho)^m_{col}$ is replaced by the average mass collision stopping power given by:

$$\left(\frac{\overline{S}}{\rho}\right)^m_{col} = \frac{\displaystyle\int_0^{T_{max}} \Phi(T)\Big(S(T)/\rho\Big)^m_{col} dT}{\displaystyle\int_0^{T_{max}} \Phi(T) dT} = \frac{D}{\Phi}, \tag{1.40}$$

and Eq. 1.39 becomes:

$$\frac{D_c}{D_m} = \frac{(\overline{S}/\rho)^c_{col}}{(\overline{S}/\rho)^m_{col}} = \Big(\frac{\overline{S}}{\rho}\Big)^c_m. \tag{1.41}$$

The absorbed dose in an air cavity D_c can be determined by measuring the charge Q produced in the gas using the following relation:

$$D_c = \frac{Q}{m_{air}} \overline{W}_{air}, \tag{1.42}$$

where $\overline{W}_{air} = 33.97$ J/C is the mean energy required to create an ion-pair in air [IAE00] and m_{air} the mass of air in the cavity in which the charge Q is produced. Using the

Bragg-Gray cavity theory (Eq.1.41), the dose in a medium D_m is thus given by:

$$D_m = \frac{Q}{m_{air}} \overline{W}_{air} \left(\frac{\overline{S}}{\rho} \right)_{air}^{m}. \tag{1.43}$$

1.4.5 Spencer-Attix cavity theory

In Bragg-Gray cavity theory, the cavity is assumed to be so small so as not to perturb the radiation field that passes through it. In other words, no interactions occur in the cavity at all. For electrons, this is a difficult condition to achieve unless the wall and gas media are close in atomic number. In Spencer-Attix theory, δ-ray production is taken into account. This helps correct for the inadequacy of the Bragg-Gray theory with air-filled cavities, especially those with walls of high atomic number. This theory attempts to incorporate δ-rays in such a way that the observed variation of ionization density with cavity size may be accounted for, at least for cavities small enough to satisfy Bragg-Gray conditions. It is indeed an improvement over Bragg-Gray theory as it gives somewhat better agreement with experimental observations for small cavities. However, as it still relies on Bragg-Gray conditions, it is not valid when those conditions are violated. The secondary electron fluence in Spencer-Attix cavity theory is divided into two components based on a user-defined energy threshold Δ. The parameter Δ is closely related to the size of the cavity. Secondary electrons with kinetic energies T less than Δ are considered slow electrons that deposit their energy locally; secondary electrons with energies larger than or equal to Δ are considered fast electrons and are part of the electron spectrum. Consequently, this spectrum has a low energy threshold of Δ and a high energy threshold of T_0, where T_0 represents the initial electron kinetic energy. Hence, energy deposition is calculated as the product of the restricted mass collision stopping power, L_Δ/ρ, and the fast electron fluence with electrons ranging in energy from Δ to T_0. The two electron components leads to:

$$\frac{D_m}{D_c} = \frac{\int_\Delta^{T_{max}} \Phi^\delta(T)[L_\Delta(T)/\rho]_m dT + \Phi^\delta(\Delta)[S(\Delta)/\rho]_{col}^m \Delta}{\int_\Delta^{T_{max}} \Phi^\delta(T)[L_\Delta(T)/\rho]_c dT + \Phi^\delta(\Delta)[S(\Delta)/\rho]_{col}^c \Delta} = \left(\frac{\overline{L}_\Delta}{\rho} \right)_c^m, \tag{1.44}$$

where Φ^δ is the electron fluence in the medium including the δ-rays. The second terms of the numerator and denominator of Eq. 1.44 accounts for energy deposition by those electrons falling bellow Δ in energy and are the so-called track-end terms approximated by Nahum [Nah78, Nah88].

1.4.6 Basic dosimetric quantities

Before measuring the absorbed dose, it is necessary to define some basic quantities which will be useful in the absorbed dose determination but also in the determination of the basic input data of any treatment planning system. The *basic dosimetry* consists in obtaining a great amount of dose distributions in function of the size of radiation beams with and without beam modifiers, for all the available photon and electron energies of the accelerator. These dose distributions are obtained using an ionization chamber in a water phantom. All this information allows a 3D-characterization of the dose distribution for each type of radiation, each energy and each setup. All the measured dose distributions are relative and it is only necessary to determine once the absorbed dose to water in reference conditions. The passage from relative to absolute dose distributions for any setup is performed using field factors relative to the reference conditions. The first basic quantity is called the *Percent Depth Dose* (PDD) and is defined as:

$$PDD(z) = \frac{D(z)}{D(z_{ref})} 100\%, \tag{1.45}$$

where $D(z)$ is the measured dose along the beam central axis at a depth z and $D(z_{ref})$ the measured dose along the beam central axis at a point considered as reference as shown in Fig. 1.15. PDD measurements are performed at a fixed *Source-Surface-*

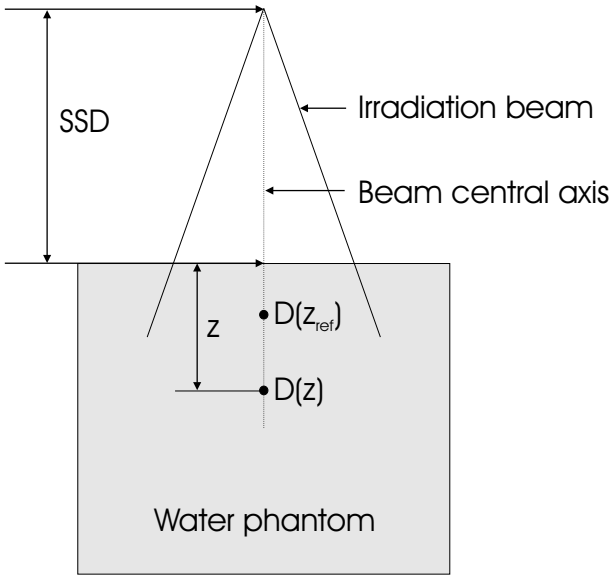

Figure 1.15: Diagram illustrating the definition of the percent depth dose in a water phantom.

Distance (SSD) which is the distance between the radiation beam source and the surface patient or the surface of the water phantom for example. The 1D-representation

of all the PDD points is called the *Depth Dose Curve* (DDC).

The *Off-Axis Ratio* (OAR) is defined as the ratio between a measured dose point located in a perpendicular plane to the central beam axis and a dose point chosen as reference in that same plane as shown in Fig. 1.16. The reference point can be located or not in the beam central axis. Generalizing Eq. 1.45, OAR is then defined as:

$$OAR(r,z) = \frac{D(r,z)}{D(r_{ref},z_{ref})}100\%. \tag{1.46}$$

The 1D-representation of all the OAR points in a determinate direction in a plane perpendicular to the beam central axis is called a *dose profile*.

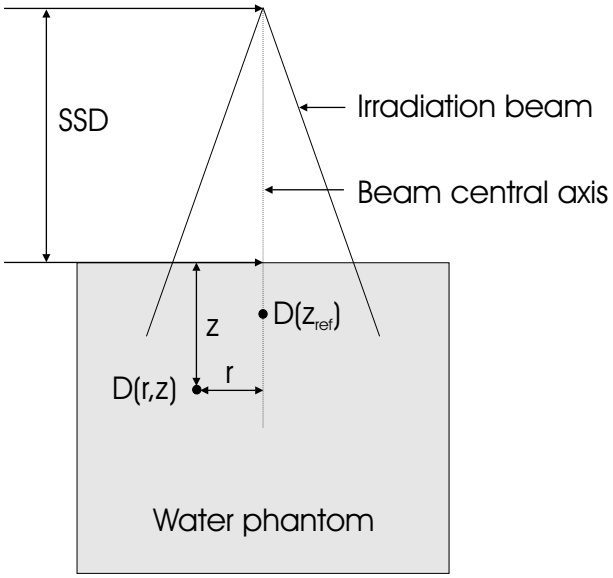

Figure 1.16: Diagram illustrating the definition of the off-axis ratio in a water phantom.

The *Tissue-Phantom Ratio* (TPR) is defined as the ratio of the dose at a given point along the beam central axis in phantom to the dose at the same point at a fixed reference depth. This is illustrated in Fig. 1.17 where the *Source-Axis-Distance* (SAD) is the distance between the x-rays beam source and the isocenter of the linac. According to Fig. 1.17, we have $SAD = SSD_z + z = SSD_{ref} + z_{ref}$. Thus, TPR at a depth z is given by:

$$TPR(z) = \frac{D(z)}{D(z_{ref})}. \tag{1.47}$$

When z_{ref} is the reference depth of maximum dose, then TPR becomes by definition the *Tissue-Maximum Ratio* (TMR).

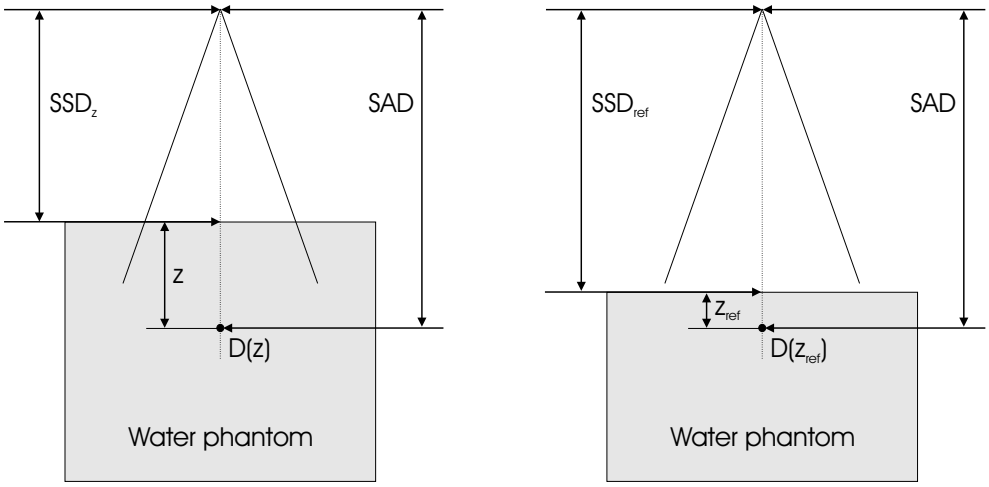

Figure 1.17: Diagram illustrating the definition of the tissue-phantom ratio in a water phantom.

An important quantity used in dosimetry is the *quality index* Q. This quality index is directly linked to the energy of the irradiation beam. By definition, the quality index is given by [IAE00]:

$$Q = \frac{TPR(20)}{TPR(10)}, \tag{1.48}$$

where $TPR(10)$ and $TPR(20)$ are respectively the $TPRs$ measured at 10 and 20 cm depth in a water phantom for a 10×10 cm^2 irradiation field size. Usually, we denotes $Q = TPR_{20,10}$. The Q value of a radiation beam is used to select the proper correction factors that are provide in dosimetry protocols. The most important characteristics of the beam quality index $TPR_{20,10}$ is its independence on the electron contamination in the incident beam. It is also a measure of the effective attenuation coefficient describing the approximately exponential decrease of the photon depth dose curve beyond the depth of maximum [IAE00].

Since the experimental measurements of $TPRs$ is difficult and very time consuming, PPD curves are measured and the conversion of the PDD data to TPR is performed taking into account the inverse square low factor i.e:

$$TPR(z,s) = \frac{PDD(z,c')}{100\%}\left(\frac{f+z}{f+z_{ref}}\right)^2, \tag{1.49}$$

where z is the depth of measurement, z_{ref} the normalization depth of the TPR, f the SSD in the acquisition of the PDD, c' is the field size on the surface and $s = c'.(f+z)/f$

the field size at depth z.

The quantity called *Output Factor* (OF) [LST+00] gives the relation between the dose of an arbitrary open field in a determinate depth at $SSD = SAD$ in a large water phantom and the dose at the same point and SSD of a reference open field (in our case the 10×10 cm^2 irradiation field). Thus, the output factor in our case is given by:

$$OF(c) = \frac{D(z,c)}{D(z, 10 \times 10 \text{ cm}^2)}, \tag{1.50}$$

where $D(z,c)$ is the dose at depth z for the additional collimator c and $D(z, 10{\times}10$ cm$^2)$ the dose at depth z for the 10×10 cm^2 reference field. Usually, OF measurements are performed at 5 cm depth and doses are normalized to maximum. In these conditions, the output factor is given by:

$$OF(c) = \frac{D(z,c)}{D(z, 10 \times 10 \text{ cm}^2)} \times \frac{PDD(z, 10 \times 10 \text{ cm}^2)}{PDD(z,c)}, \tag{1.51}$$

where $PDD(z,c)$ and $PDD(z, 10 \times 10$ cm$^2)$ were normalized to the maximum dose for respectively the additional collimator c and 10×10 cm^2 reference field.

1.4.7 Dosimetry protocol

In this section, we will present how dose is determined in water using the IAEA TRS-398 *Dosimetry Protocol* or *Code of Practice* [IAE00]. This *Code of Practice* is based upon a *calibration factor* in terms of absorbed dose to water N_{D,w,Q_0} for a reference beam of quality Q_0 and is applied to photon beams generated by electrons with energies in the range of 1 MeV to 50 MeV. Only cylindrical ionization chambers are recommended for reference dosimetry in high-energy photon beams.

Before determining the absorbed dose to water for our high-energy photon beam, it is necessary to define some reference conditions for the N_{D,w,Q_0} determination and shown in Table 1.2 according to IAEA TRS-398. The calibration factor N_{D,w,Q_0} given in Gy/C is denoted by $N_{D,w}$ when the reference quality Q_0 is Cobalt-60. The calibration factor is obtained for the cylindrical chamber but also for the entire dosimetric system composed by the cylindrical chamber and the electrometer. The absorbed dose in water for a megavoltage beam is given by:

$$D_{w,Q} = M_Q N_{D,w,Q_0} k_{Q,Q_0}, \tag{1.52}$$

where M_Q is the reading of the electrometer in Coulombs and k_{Q,Q_0} is the chamber-specific factor which corrects for the difference between the Cobalt-60 quality Q_0 and the actual quality being used, Q. The reading M_Q was corrected for the influence quantities temperature and pressure, polarity effect and ion recombination.

Influence quantity	Reference value or reference characteristics
Phantom material	water
Chamber type	cylindrical
Measurement depth z_{ref}	5 cm for cobalt-60 beam
SSD	75 cm
Field size	10×10 cm^2

Table 1.2: Reference conditions for the determination of the calibration factor N_{D,w,Q_0} in Cobalt-60 according to IAEA TRS-398 *Code of Practice*.

The *beam quality correction factor* k_{Q,Q_0} is defined as the ratio, at beam quality Q and Q_0, of the calibration factors in terms of absorbed dose to water of the ionization chamber as:

$$k_{Q,Q_0} = \frac{N_{D,w,Q}}{N_{D,w,Q_0}} = \frac{D_{w,Q}/M}{D_{w,Q_0}/M_{Q_0}}. \tag{1.53}$$

The beam quality correction factors should be measured directly for each ionization chamber at the same beam quality of the local clinical beams. In practice, this is not possible and the factors are calculated from the Bragg-Gray theory. Under the validity of the theory, the correction factor is given by:

$$k_{Q,Q_0} = \frac{\left[\left(\frac{S}{\rho}\right)_{air}^{water}\right]_Q [\overline{W}_{air,Q}]p_Q}{\left[\left(\frac{S}{\rho}\right)_{air}^{water}\right]_{Q_0} [\overline{W}_{air,Q_0}]p_{Q_0}}, \tag{1.54}$$

where p_Q and p_{Q_0} are respectively, overall perturbation factors for beam quality Q and Q_0. The overall perturbation factor includes all departures from the behavior of an ideal Bragg-Gray detector and is given for an ionization chamber by:

$$p = p_{dis}p_{wall}p_{cav}p_{cel}, \tag{1.55}$$

where p_{dis} is the displacement factor that accounts for the facts that a cylindrical chamber cavity with its center at z_{ref} samples electron fluence at a point which is closer to

the radiation source than z_{ref}, p_{wall} is the factor that accounts for differences in photon mass energy-absorption coefficients and electron stopping powers of the chamber wall material and medium, p_{cav} is the factor that corrects for the perturbation of the electron fluence due to the scattering between air cavity and medium and finally p_{cel} is a factor that corrects the lack of air equivalence of the central electrode for cylindrical ionization chambers. The IAEA TRS-398 assumes that $[\overline{W}_{air,Q}] = [\overline{W}_{air,Q_0}] = 33.97$ J/C if Q_0 is referred to Cobalt-60, and k_{Q,Q_0} is denoted k_Q. Equation 1.54 then becomes:

$$k_Q = \frac{\left[\left(\frac{S}{\rho}\right)_{air}^{water}\right]_Q p_Q}{\left[\left(\frac{S}{\rho}\right)_{air}^{water}\right]_{Co60} p_{Co60}}. \tag{1.56}$$

Values of k_Q were calculated by Andreo [And92] for various cylindrical chambers.

As mentioned earlier, the reading M_Q was corrected for various influence factors. The temperature and pressure correction factor, k_{TP}, must be used because the chamber is open to the air ambient and thus, the mass of air inside the cavity volume is subjected to atmospheric variations. The correction factor for temperature and pressure is given by:

$$k_{PT} = \frac{273.2 + T}{273.2 + T_0}.\frac{P_0}{P}, \tag{1.57}$$

were T_0 and P_0 are the reference values (generally 20 ^{o}C and 1013 kPa). The effect on a chamber reading using polarizing potential of opposite polarity must always be checked in chamber commissioning. The polarity effect factor, k_{pol} is given by:

$$k_{pol} = \frac{|M_+| + |M_-|}{2M}, \tag{1.58}$$

where $|M_+|$ and $|M_-|$ are the electrometer readings obtained at positive and negative polarity, respectively, and M is the electrometer reading with the polarity used routinely. The incomplete collection of charge in an ionization chamber cavity due to the recombination of ions requires the use of a correction factor k_s. The method recommended by the IAEA TRS-398 assumes a linear dependence of $1/M$ and $1/V$ and uses the measured values of collected charges M_1 and M_2 at polarizing voltages V_1 and V_2 respectively. Thus the recombination factor k_s at the normal operating voltage V_1 and for a pulsed beam is given by:

$$k_s = a_0 + a_1\left(\frac{M_1}{M_2}\right) + a_2\left(\frac{M_1}{M_2}\right)^2, \tag{1.59}$$

where the constants a_i are function of the ratio V_1/V_2 [WM84]. The last correction factor is the electrometer calibration factor, k_{elec}, when the ionization chamber and the electrometer are calibrated separately. Typically, if the electrometer readout is in terms of charge, k_{elec} is a dimensionless factor very closed to unity. With all the correction factors defined, Eq. 1.52 can be rewritten as:

$$D_{w,Q} = M_Q N_{D,w} k_Q = k_{PT} k_{pol} k_s k_{elec} M_U N_{D,w} k_Q, \tag{1.60}$$

where M_U is the direct reading in the electrometer in Coulombs.

The aim of calibrating a linac is to determine a relationship between the signal from the beam monitor system (*Monitor Unit*, MU) and the absorbed dose in water delivered under chosen reference conditions. The adjustments in the Siemens Mevatron KD2 linear accelerator for the 6 MV photon mode were performed in such way that the absorbed dose at the depth of d_{max} for a 10×10 cm^2 and for a $SSD = 100$ cm is equal to 1 cGy for 1 MU. The value of $N_{D,w}$ obtained from a Secondary Standards Laboratory for our reference chamber which is the PTW 30013 Farmer chamber is $N_{D,w} = 5.301 \times 10^7$ Gy/C. The value of $k_Q = 0.9956$ for our reference chamber and for

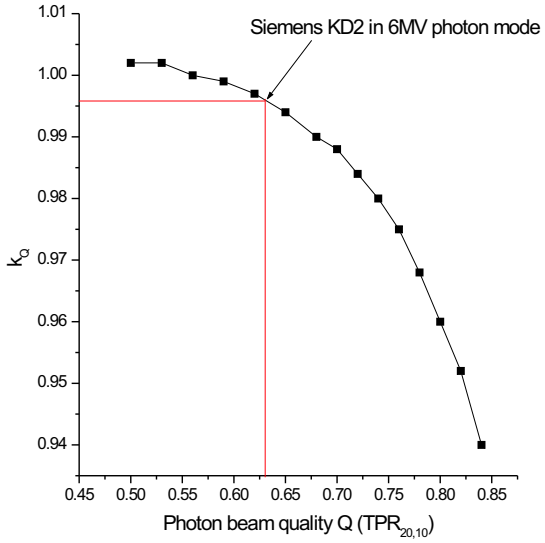

Figure 1.18: Calculated value of the beam quality correction factor, k_Q, for the PTW 30013 Farmer chamber as a function of the photon beam quality Q obtained from Andreo [And92].

the 6 MV photon beam of the Siemens KD2 linac with $Q = 0.6266$ was obtained by

interpolation of k_Q values calculated by Andreo [And92] (Fig. 1.18 shows the variation of factor k_Q as a function of Q for our reference chamber).

Chapter 2

Stereotactic radiosurgery

2.1 Historical review

The term *radiosurgery* was first introduced by the Swedish neurosurgeon Lars Leksell [Lek51] in 1951 to describe a therapeutic procedure where lesions in the brain were treated in one single session using external narrow beam radiation. This procedure differs from conventional radiotherapy in that the volume of the lesion is usually smaller, the delivered dose is much higher and it is delivered in an unique fraction. The term *stereotactic* derives from the use of a well-defined, 3-dimensional coordinate system to locate accurately in space any point in the brain. Nowadays, the stereotactic localization is also used outside the brain in fractionated treatments. When patients are treated in multiple fractions, the therapeutic procedure is called *stereotactic radiotherapy* (SRT). The designation of *stereotactic radiosurgery* (SRS) is thus applied when one single fraction is used to treat brain lesions.

In 1951, Leksell used a conventional 200 kVp x-rays and a stereotactic frame attached to a ring. In 1968, he designed together with Borje Larsson the first Gamma Knife unit containing 179 Cobalt-60 sources to treat patients with functional disorders. In 1972, the first case of arteriovenous malformation (AVM) treated with a Gamma Knife was reported by Ladislau Steiner [SLG$^+$72]. This became the main application of SRS with Gamma Knife during the following years. Some kind of brain tumors have also been treated with Gamma Knife. The concept of performing SRS treatments using medical linear accelerators appeared in 1983 when Betti and Derechinsky [BD83] have demonstrated that linear accelerators could deliver narrow photon beams similar to Gamma Knifes. Nowadays, most of the SRS treatments are performed using medical

linear accelerators. The IPOFG-CROC, S.A., has performed its first SRS treatment in June 1996.

2.2 Typical radiosurgery treatment

A typical radiosurgery treatment involves a multi-disciplinary team composed usually by neurosurgeons, neuroradiologists, radiotherapists and physicists. The treatment begins with the fixation of the stereotactic ring in the patient head. The head ring is fitted tightly to prevent movement during the procedure. This is necessary to locate the exact area of the brain or lesion being targeted using complex measurements taken in relation to the head ring. Then, images of the head are acquired using a Computed Tomography (CT) scanner. This diagnostic device is used mainly because there is no image distortion and the images contain information about the tissue density. CT-images will be used to precisely plan the delivery of radiation to the tumor. In some instances, a Magnetic Resonance (MRI) scan may also be necessary in order to fully visualize the tumor and adjacent critical anatomy. For AVM treatments, it is necessary to acquire two orthogonal images using digital angiography with contrast injection. This is due to the fact that the CT-contrast is not sufficient to visualize the vascularization in the arteriovenous malformation region.

Once the patient images are acquired, they are sent to a treatment planning system. Treatment planning is the process through which physicians and medical physicists plan the details of radiation delivery to a tumor or other lesion. The goal is to deliver a therapeutic dose of radiation to the lesion while sparing the adjacent healthy tissue. The tumor volume is delineated using the CT-images whereas AVM volume is delineated in the angiography images and then exported into CT-images for dose calculation. Volumes can also be delineated in images acquired by other diagnostic devices. In that case, image fusion is performed and the volumes are exported into CT-images.

Finally, the patient is accurately positioned in the treatment device and radiation beams are delivered according to the treatment plan. Narrow photon beams from many different angles and intersecting at one point are delivered to confine the dose to the lesion. This is the so-called *Convergent Beam Irradiation* (CBI) technique. Figure 2.1 resumes the radiosurgery treatment procedure.

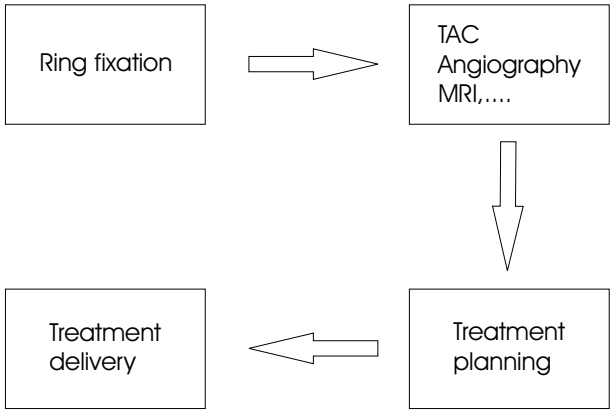

Figure 2.1: Simplified diagram of a radiosurgery treatment.

2.3 SRS units

In this section, we will present the two main SRS units mainly used in clinical applications: the Gamma Knife and the medical linear accelerator (linac). Strictly speaking, the Gamma Knife is a dedicated SRS unit whereas the same linac used in conventional radiotherapy can be adapted to performed SRS treatments. A brief description of the Gamma knife (due to its historical interest) and the linac used for SRS treatments will be performed. For the linac, the modifications needed for SRS treatment will also be presented.

2.3.1 Gamma Knife

The major components of the Gamma Knife unit, commonly called the Leksell's Gamma Knife (LGK) (see Fig. 2.2), are the radiation unit, the collimator helmets, the patient's treatment table, the hydraulic system and the control panel. Figure 2.3 shows the schematic view of a LGK unit. Within the central body of the Gamma Knife there is an array of 201 separated cobalt sources. Each of these sources produces a fine beam of gamma radiation. The sources are evenly distributed over the surface of the hemispherical source core so that each beam is directed to a common focal spot at the center (see Fig. 2.4). The resultant intensity of radiation at the focus is extremely high and this intensity at only a short distance from the focus is very low. This enables a high dose of radiation to be delivered to the abnormal tissues, sparing the adjacent healthy brain tissue. The total nominal activity of the Gamma Knife is around 222×10^{12} Bq $\pm$ 10% [Arn93].

Figure 2.2: The Leksell's Gamma Knife (Elekta).

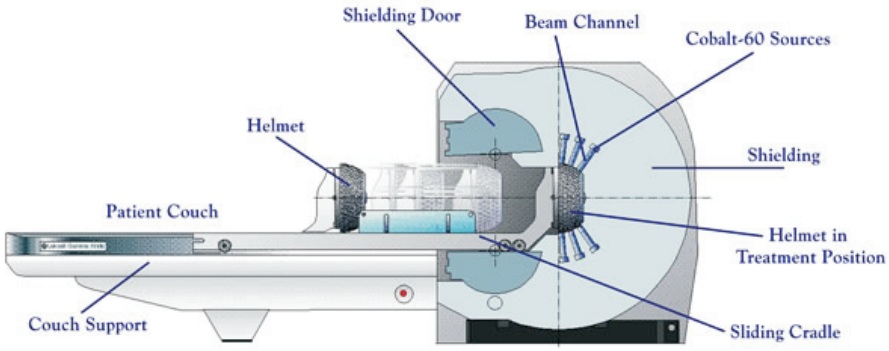

Figure 2.3: Schematic view of a LGK unit (University Neurosurgery LSU Health Sciences Center).

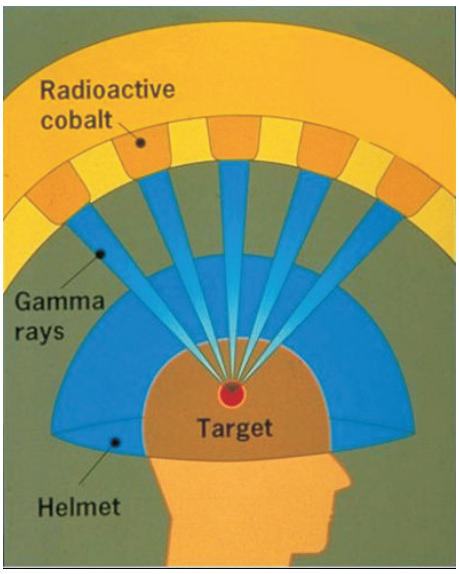

Figure 2.4: Schematic view of convergent Cobalt beams (University of Kentucky, Chandler Medical Center).

The final collimation is accomplished with one of the four collimator helmets (see Fig. 2.5). The 201 channels are drilled in each helmet. They have apertures that produce 4, 8, 14 and 18 mm diameter fields at the focus. The great advantage of using the LGK

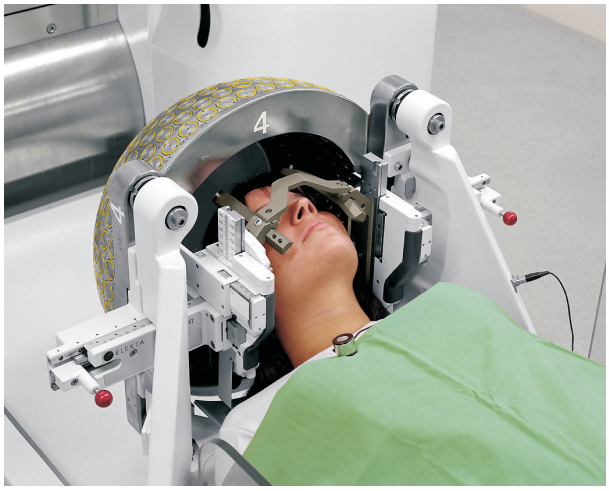

Figure 2.5: Leksell's stereotactic frame with a collimator helmet (Elekta).

system is its ability to treat in a short time complex geometrical target volumes using multiple focus points.

2.3.2 Linac

Description of the accelerator head

The linac used for SRS treatment at IPOFG-CROC, S.A., is the Siemens Mevatron KD2 which is a dual linear accelerator (see Fig. 2.6). Two photons modes (6 and 18 MV) and six electrons modes (6, 8, 10, 12, 15 and 18 MeV) are available. For SRS treatments, the 6 MV photon mode was chosen because it is the most commonly used [HHB96, SMH+98, MT99, RC99, WAN+00, HFL+02]. The production of the linac beams is a quite complex process. Figure 2.7 shows the main components of the linac. First, microwaves are produced in a klystron which is basically a microwave amplifier. The klystron is composed by resonant cavities where a continuous initial current is transformed into electrons bunches by applying microwaves of low amplitude. When electrons reach the last cavity, a strong interaction occurs between them and the resonant cavity producing microwaves of high energy. These microwaves are transported through a wave guide to the accelerator structure where they are injected simultaneous with electrons (produced by an electron gun).

Figure 2.6: View of the Siemens Mevatron KD2 linear accelerator.

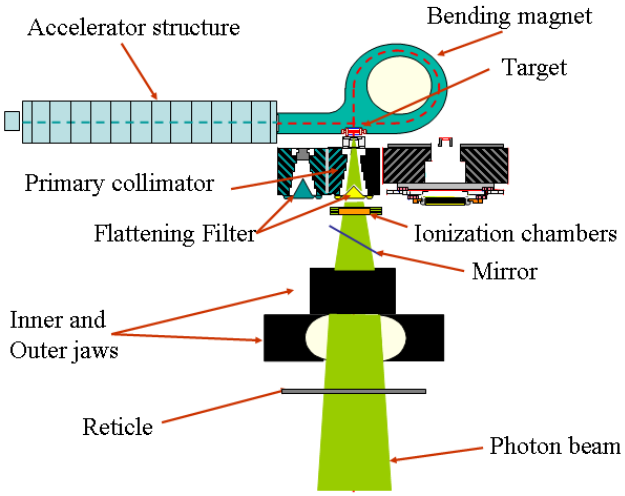

Figure 2.7: View of main components of the Siemens Mevatron KD2 linear accelerator in photon mode.

The electrons are accelerated up to the desired energy and then suffer a deviation caused by a bending magnet to orient the beam to a convenient direction. In the photon mode, the accelerated electrons impinge into a high-Z target and high energy x-rays are produced. In the KD2 accelerator, the beam is then collimated through a primary collimator. In order to produce irradiation fields with homogeneous dose in the patient, a flattening filter is placed just after the primary collimator. The emerging beam from the flattening filter passes through the ionization chambers that monitor the photon fluence. The signals (expressed in MU) delivered by these ionization chambers are used to control a number of beam parameters in addition to radiation dose, such as symmetry and uniformity of the radiation beam. Accelerators have two independent chamber systems to monitor the delivered radiation: a primary and secondary (back-up) channel. After leaving the ionization chambers, the beam passes through a mirror (used for visualizing the light field on the patient surface). At this level, moveable jaws of high-Z material are used to define the dimensions of the beam. In conventional radiotherapy, field sizes vary between 3×3 cm^2 and 40×40 cm^2. The dimension of the radiation beam is defined at the isocenter of the machine which is located at 100 cm from the target. The isocenter of a medical accelerator is the intersection point of the axes of rotation of the treatment couch, the gantry, the collimator and the radiation beam central axis (see Fig. 2.8). Positioning lasers located at the wall of the treatment

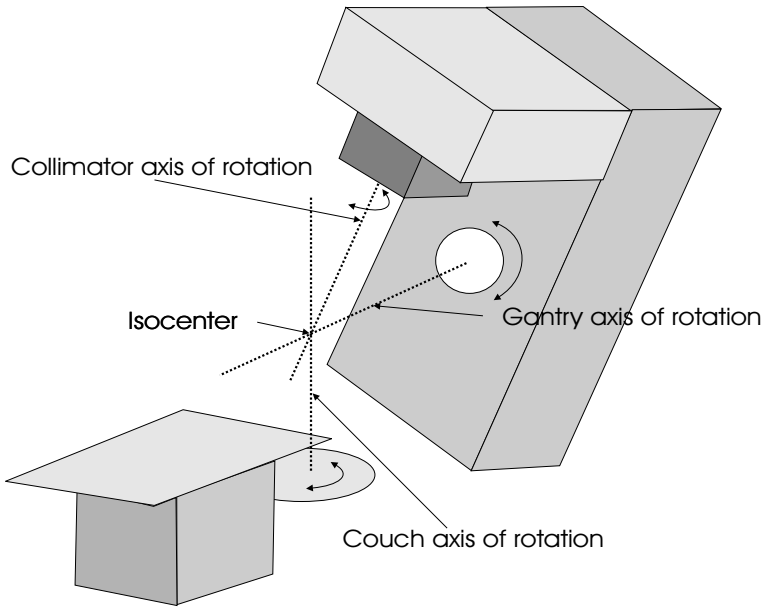

Figure 2.8: Isocenter definition.

room are adjusted in a such way that their intersection point is coincident with the

isocenter. Finally, the radiation beam passes through a reticle used to project a scale in the patient surface. The jaws aperture used for radiosurgery treatments corresponds to the 10×10 cm^2 field size at isocenter.

Linac modifications for SRS treatments

The technique for stereotactic linac irradiation has been originally designed in order to simulate the LGK treatment in terms of the conformity of the dose distribution to the target volume as well as the accuracy of head immobilization and target localization. The dynamic capacities of the linac (rotations of the couch and the gantry) are used to produce the multiple non-coplanar arcs resulting from the combinations of several gantry and couch positions. These arcs converge at the isocenter (see Fig. 2.9). Thus, the center of the target is placed stereotactically at the linac isocenter.

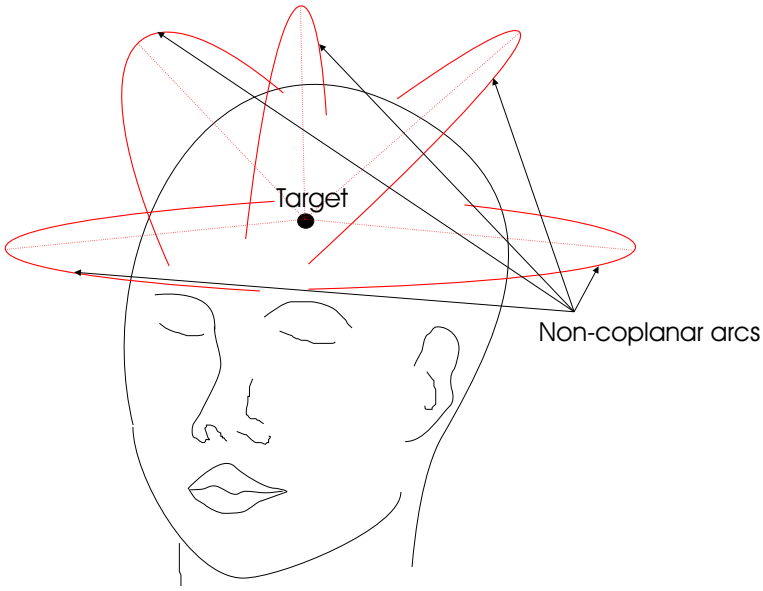

Figure 2.9: Illustration of linac multiple non-coplanar arcs used in radiosurgery treatments.

As mentioned earlier, some modifications in the linacs have to be performed, since they are originally designed for conventional radiotherapy treatments. The SRS narrow photon beams are shaped through the interposition of an additional collimator system which is placed just below the reticle. The additional collimators used at IPOFG-CROC, S.A., are from Fisher-Liebinger and are made of tungsten. Their geometrical internal diameters are 2, 5, 7, 9, 11, 13, 15, 17, 20 and 23 mm. The 2 mm additional collimator is just used for quality control procedures. Figure 2.10 shows

these additional collimators and their localization in the Siemens Mevatron KD2 head.

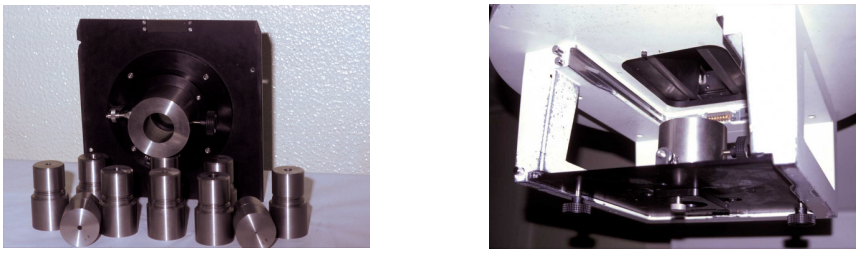

Figure 2.10: (a) Additional collimators used to shape the narrow photon beams and (b) their localization in the Siemens Mevatron KD2 linac.

The second main modification concerns the couch treatment. During the positioning and treatment procedures, we have to warrant the stability of the couch. For that purpose, a special device was created that blocks all the couch movements except the rotation around the couch axis rotation where the isocenter is located. Figure 2.11 shows the couch immobilization device used at IPOFG-CROC, S.A.

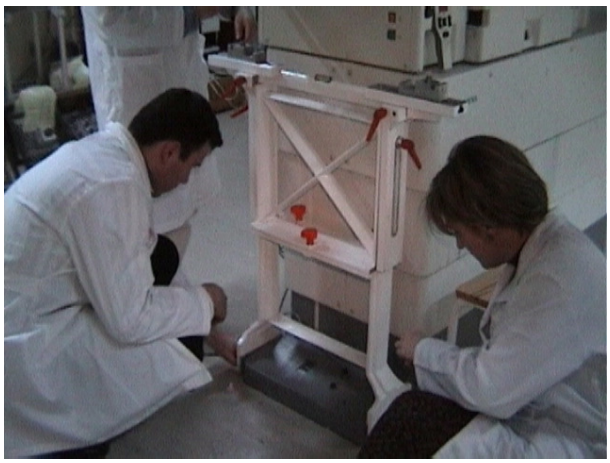

Figure 2.11: Couch immobilization device used in radiosurgery.

SRS linac quality control

A geometrical quality control procedure must be implemented to warrant the machine geometrical isocenter is coincident with the machine radiation isocenter within a tolerance of 1 mm [Har95]. To determine the mechanical isocenter, the isocenter pointer and a target point for the linac couch are used (see Fig. 2.12). These devices determine the mechanical isocenter and measure the mechanical stability of the isocenter. The laser cross is adjusted to this mechanical isocenter. The determination of the isocen-

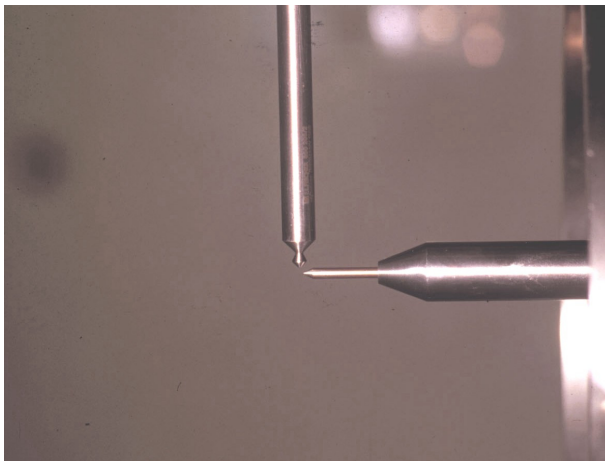

Figure 2.12: Adjustment of the geometrical isocenter using two pointers.

tric accuracy is performed using the 2 mm additional collimator. The accuracy of the gantry rotation is checked using a verification film placed in a vertical plan containing the isocenter. The isocenter given by the lasers is marked with a needle hole on the film (see Fig. 2.13). Then, the gantry is set at various rotation angles and the film is irradiated. In this test, the couch is fixed at 0 degree. This produces a *star* on the film as shown in Fig. 2.14. The distance between the center of the star and the needle hole is smaller than 1 mm.

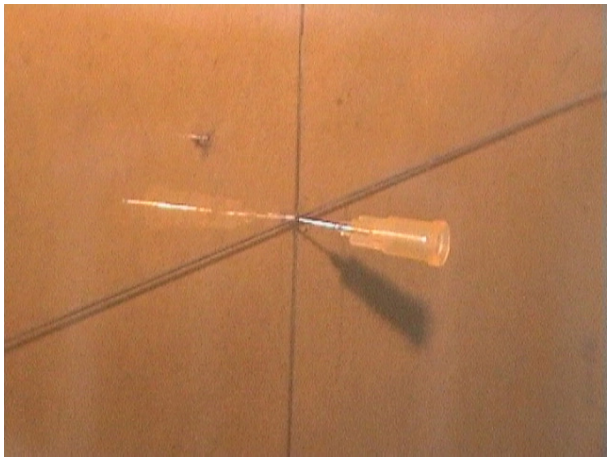

Figure 2.13: Needle hole placed at the isocenter.

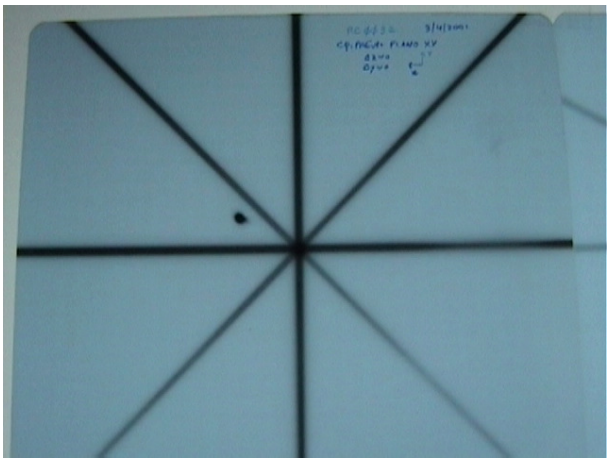

Figure 2.14: *Star* of various beams on the film resulting of irradiations at various gantry angle.

The same kind of test is performed to check the accuracy of the couch rotation. A film is placed parallel to the table, and the isocenter given by the lasers is marked with a needle on the film which is irradiated for different couch positions. In this test, the gantry is set to 90 degrees (horizontal beam direction). The distance between the center of the resulting star and the needle hole is also less than 1 mm.

The determination of the center of the dose distribution was performed using the head of an anthropomorphic Alderson-Rando phantom. A small piece of film was marked with a needle and placed inside the phantom head. A complete SRS treatment procedure was performed. The pinhole cross-section on the film was chosen as the target for planning. The deviation between the needle hole and the center of the multiple arcs distribution was less than 1 mm. To validate the dose calculation, a diode was placed in the phantom head and once again the hole SRS treatment procedure was performed. The difference between the dose at the target point and the measured dose by the diode at the same target point was less than 1%.

2.3.3 Stereotactic system

An accurate definition of the target volume (localization and shape) obtained through CT, Magnetic Resonance (MRI) and/or Angiography images is required in SRS treatments. It is why a stereotactic system must be defined.

The basic requirements for such system are [Phi93]:

1. to provide a unique and fixed reference frame relative to the brain,
2. to provide the means by which this reference frame can be applied to radiological images of the brain and surrounding structures,
3. and finally, to provide precise and accurate positioning of the patient.

The precision and accuracy of the target localization is the purpose of the stereotactic system. There exists a wide range of stereotactic systems and frames for use in SRS. We will just present the system used at IPOFG-CROC, S.A.

It is the modified Riechert-Mundinger stereotactic frame, first used in Heidelberg, Germany. This system is composed by a titanium ring fixed at the patient skull using usually 4 pins as shown in Fig. 2.15. In this system, the ring is attached through an

interface device directly to the linac couch.

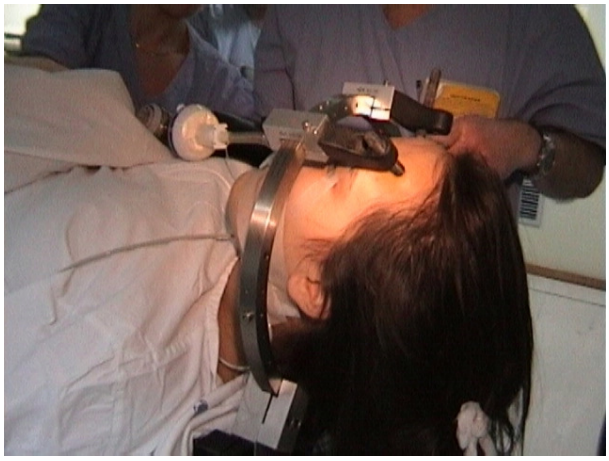

Figure 2.15: Stereotactic ring fixed at the patient.

By definition, the center of this stereotactic system is the center of the titanium ring. Special accessories are attached to the ring to accurately determine the target position in the stereotactic frame. Two sets of such accessories are used. The first one is composed by 4 localizing plates used during the CT scan procedure and the second is composed by localizing plates used during the angiography, quality control and patient localization verification procedures (see in Fig. 2.16 for angiography localizers).

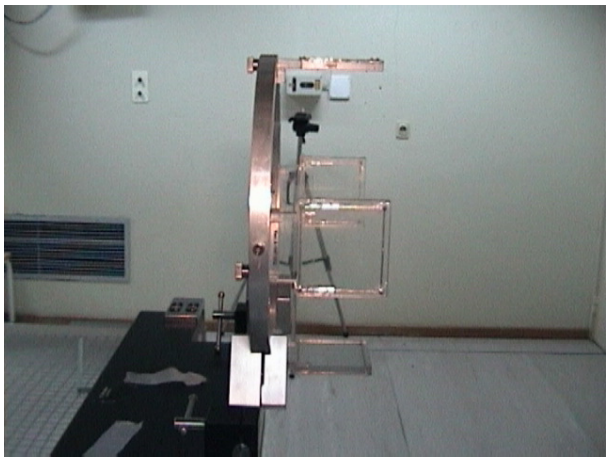

Figure 2.16: Stereotactic ring with localizers used in angiography or verification procedures.

Finally, a special accessory also attached to the ring is used to accurately setup the position of the defined target in the stereotactic frame in correlation with the linac referential defined by the lasers (see Fig. 2.17). It enables the localization of the target

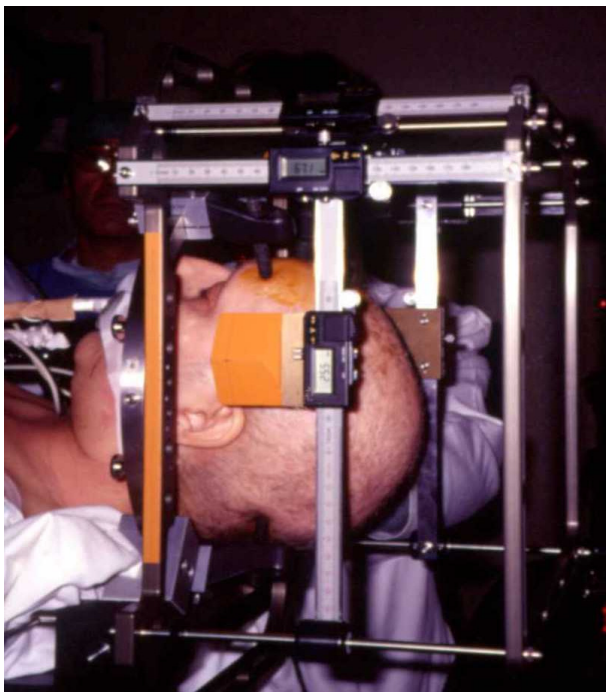

Figure 2.17: Localizer used to setup the patient in the linac.

point within tenth of a millimeter. The point defined as the target in the stereotactic frame is the isocenter of the linac. Thus, the localizer frame of Fig. 2.17 must be perfectly aligned with the laser system of the linac.

2.4 STP3 radiosurgery treatment planning system

Radiosurgery calculations performed by the Fisher-Liebinger Treatment Planning System (TPS) STP3 are based on measured dose data. The dose distribution, using the CBI technique, is calculated by the superposition of single stationary beams. For complex 3-D dose calculations, a compromise must be found between exactness and calculation time. Due to the fact that the gross anatomic structure of the brain is relatively simple, tissue inhomogeneities are ignored in STP3 and therefore dose calculation becomes very fast. In this section, we will present the dose calculation engine implemented in STP3.

2.4.1 Dosimetric STP3 database

The database in STP3 includes basic dosimetric data determined in water which are $TMRs$, $OARs$ (see Chapter 1) and the *calibration dose point* (CRP). This calibration dose point is determined in a phantom at the equilibrium depth ($x = d_{max}$) for a field reference field (usually the 10×10 cm^2) at a *Source-Isocenter Distance* SID. For our accelerator, we found $CRP = 0.0103$ Gy/MU for SID=100 cm and $x = d_{max} = 1.5$ cm. The basic data used by STP3 for dose calculation is the *Calibrated Tissue-Maximum Ratio* ($CTMR$) which is defined by:

$$CTMR(B, d) = CF(B, A) \times TMR(B, d), \tag{2.1}$$

where B is an additional collimator field, A the reference field, d the depth of measurement and CF the collimator factor. It has to be notice that the definition of CF is the same that for OF defined in Chapter 1.

Obtaining the basic dosimetric data used in STP3 is not an easy task. The choice of the detector size is an important criteria in narrow photon beam dosimetry. The size of the detector must be small enough to minimize perturbation of the particle fluence. A non appropriate detector size can cause great complication in the interpretation of dose distributions. Hartmann *et al.* [Har95] suggest that for central axis measurements, the detector should be less than 1/3 of the field diameter. Moreover, Rice *et al.* [RHS$^+$87] have reported that for off axis measurements, a detector with a non appropriate size might not able to resolve correctly the existent steep dose gradients. The effect of the detector size in the penumbra region is particulary important.

The problem of lateral electronic disequilibrium emerges whenever the x-rays energy is so high or the beam radius is so small that the latter becomes comparable to the maximum electron range in the irradiated medium [Maz90, BTR89]. That is, the beam diameter is less than the maximum range of the primary electron leading to lack of lateral electron equilibrium. Heydarian *et al.* [HHB96] have shown that the lateral disequilibrium has an effect on measurements when the detector is not tissue equivalent and therefore any change in photon or electron spectrum causes a change in response relative to a tissue equivalent detector. Wu *et al.* [WZK$^+$93] have shown that in no-lateral equilibrium situations and for the very small beams, there is a lack of the lower-energy electrons which otherwise could have reached the central axis from points at distances approaching the maximum electron range. This causes an increase of the

average electron energy spectrum at the central axis and consequently a decrease of the stopping power ratio of water to air [HHB+93]. The impact of this change is very important in the determination of the output factors for narrow photon beams. Finally, it was shown that the electron spectra vary with depth for narrow photon beams [HHB96].

It is recommended to use a detector whose material is the most similar to the medium in which dose is measured in order to reduce the perturbation of the particle fluence [DB85]. If the detector is an air cavity, its introduction into the field causes an increase of lateral electronic disequilibrium and a subsequent lower dose to the air in the cavity than would exist in tissue at that position [HHB96]. On the other hand, a detector like a diode, a TLD or a film, will cause a reduction in the lateral electronic disequilibrium and a subsequent overestimation of the dose [BMO94].

The common approach to perform dose measurements for narrow photon beams is to combine different measurements techniques obtaining an internal self-consistency [AAP95, HHB96, MT99, WAN+00]. Monte Carlo method is another tool in order to determine the most accurately as possible the dose for such narrow photon beams. Figure 2.18 shows the CTMR curves introduced in STP3 for each additional collimator.

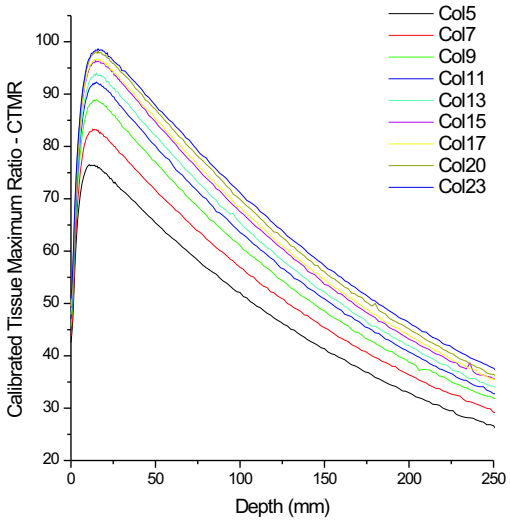

Figure 2.18: Calibrated Tissue Maximum Ratio for all the additional collimators.

2.4.2 Dose distribution calculation

The theory of dose calculation implemented in STP3 was developed by Hartmann *et al.* [HSS+84]. The underlying idea for his beam model is that a very accurate description of the dose is just necessary in the vicinity of the isocenter, where the dose is concentrated due to the intersection of a great number of beam orientations. It is then a good approximation to treat the radiation field of the narrow beam like a pencil beam, especially for CBI techniques using a great number of non-coplanar arcs. In this case and for the additional collimator c, the dose of the *single beam* in cylindrical coordinates $D_{SB}(P)$ at point P (see Fig. 2.19) is given by:

$$D_{SP}(P) = \left(\frac{SID}{SID+b}\right)^2 CTMR(c,d)OAR(c,q), \tag{2.2}$$

where $OAR(c,q)$ is the off-axis ratio at the lateral distance q from the beam central axis at the depth of the isocenter, b is the distance along the beam central axis between the isocenter and the plane perpendicular to the beam central axis where the point P is located and finally, d is the distance between the entry point of the radiation beam in the beam central axis and the plane perpendicular to the beam central axis where the point P is located. This simplified beam model does not take into account the beam divergence.

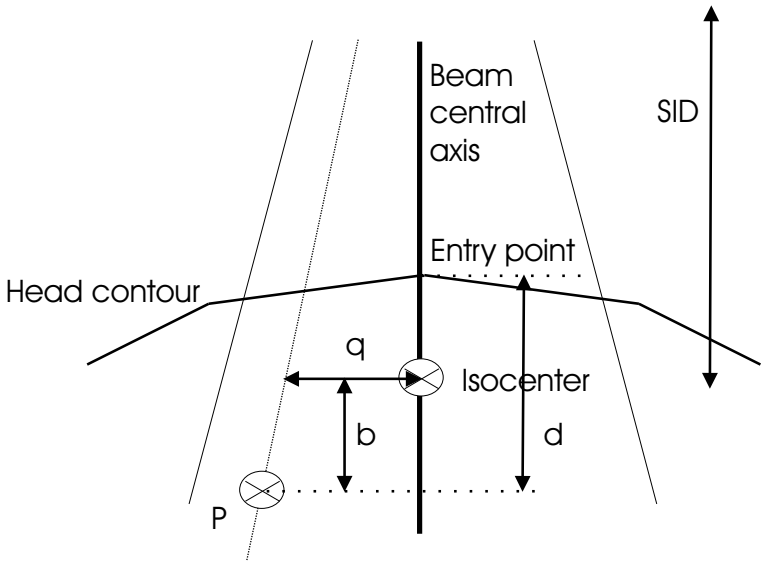

Figure 2.19: Geometrical configuration used for dose calculation in STP3.

The total dose $D_{CBI}(P)$ at point P which is generated by an isocentric convergent beam irradiation is:

$$D_{CBI}(P) = CRP \times \sum_{t=1}^{m} \left(\frac{m}{n(t)} \times MU(t) \times D_{SP}(P) \right), \tag{2.3}$$

where $n(t)$ is the number of individual fields simulating arc t, m is the number of table positions, i.e. arcs and $MU(t)$ are the precalculated monitor units of arc t. In STP3, the monitor units MU delivered per arc are:

$$MU(t) = \frac{D_{iso}}{CRP \times \overline{CTMR}(iso)} \times \frac{w(t)}{\sum_{k=1}^{m} w(t)}, \tag{2.4}$$

where D_{iso} is the dose in Gy at isocenter, $\overline{CTMR}(iso)$ is the average $CTMR$ at the isocenter, m is the number of couch positions and $w(t)$ is the relative weight of arc t.

2.4.3 Evaluation of treatment planning

Treatment planning process often results in different treatment plans. It is necessary to have some defined criteria that help us to decide if a plan is acceptable or not and what is the optimal plan for that case. The criteria used and proposed by the Radiation Therapy Oncology Group (RTOG) [SKG+93] are relative to dose homogeneity and conformity in the target volume. Following the RTOG recommendations, the value of the prescribed isodose which corresponds to the minimum dose in the lesion should be between 70% and 90% with isocenter normalized to 100%. The homogeneity index defined by *MDPD=(maximum dose)/(prescribed dose)*, should be:

$$MDPD \leq 2.$$

The percentage of volume covered by the prescribed isodose should be greater than 90%. The conformity index defined as the *prescribed isodose volume to target volume*, $PITV$, should satisfy:

$$1 \leq PITV \leq 2.$$

Finally, the analysis of the dose gradients expressed in %/mm (linear approximation obtained from dose profiles in the axial, coronal and sagittal planes) should conclude that the dose gradient between the reference isodose and the 50% isodose is greater than 10%/mm and should be greater than 5%/mm between the 50% isodose and 20% isodose.

Parameters are calculated using the two-dimensional isodose contours and others using a *Dose-Volume Histogram* (DVH). Two kinds of DVHs can be used. The frequency DVH which represents the number of calculation points in a volume for each dose value and the integral DVH which represents the percentage of a volume enclosed by a defined dose level. In STP3, only the integral DVH is available. Figure 2.20 shows an of STP3 output integral DVH. The information has to be analyzed like in the example of Fig. 2.20: 95% of the volume is at least covered by the 75% isodose.

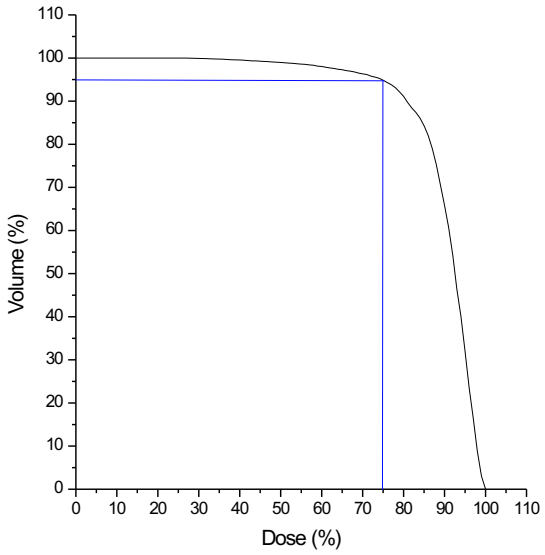

Figure 2.20: Dose volume histogram calculated by STP3. Dose: 100%=20 Gy, volume 100%=2.4 cm^3.

Chapter 3

Monte Carlo methods

In the past few years, some important improvements in Monte Carlo (MC) codes, especially regarding the implementation of electron multiple scattering theories [Sel88, AB84, SAB+97, BR87, BS01, HKM+92, KR00], made these codes powerful tools to understand all the processes involved in the radiation energy deposition in materials. Radiotherapy is a field where MC codes such as EGS4, MCNP4C give great contributions to accurately determine basic dosimetric data [MT99, HHB96, WAN+00, CLO+03]. Nowadays, MC methods are also the basis of some in-house treatment planning systems due to the emergence of specific geometrical packages such as BEAM [RFD+95], and more recently due to the improvement of fast MC codes such as DPM [SWB00] or VMC [KFF96].

MC methods are very different from deterministic transport methods. Deterministic methods, the most common of which is the discrete ordinates method, solve the transport equation for the average particle behavior. By contrast, Monte Carlo does not solve an explicit equation, but rather obtains answers by simulating individual particles and recording some characteristics of their average behavior.

The two MC code systems used in this thesis were: the *Monte Carlo N-Particle* code version 4C (MCNP4C) [Bri00] and the *Dose Planning Method* code (DPM) [SWB00]. MCNP4C is a Monte Carlo code which can handle continuous energy, generalized geometry, coupled or de-coupled neutron/photon/electron problems. This code is widely used in medical physics applications [CDS00, DSC+98, SCB+99, YSS01, JKO99, LRS+00]. It belongs to the ETRAN MC codes family. MCNP uses continuous-energy nuclear and atomic data libraries. The primary sources of nuclear data are evaluations

from the Evaluated Nuclear Data File (ENDF) system [Kin79], the Evaluated Nuclear Data Library (ENDL) [HCH+75] and the Activation Library (ACTL) [GH78]. The geometry of MCNP treats any three-dimensional configuration of user-defined materials in geometric cell bounded by first- and second-degree surfaces and fourth-degree elliptical tori. A great improvement in the transport of electrons is the use of the Integrated TIGER Series (ITS 3.0) in the continuous-slowing down approximation physics [HKM+92].

MC code DPM has been designed to deal with radiotherapy-class problems. More specifically, it is optimized for the calculation of the dose distribution delivered by high energy (∼1 MeV up to ∼20 MeV) electron and photon beams in patients, whose geometries are defined in terms of a (usually) large number of small volume elements, or *voxels*. Tables and cross sections for given materials are produced from raw physics data from PENELOPE's library of constants [SFB+96]. The gains in CPU speed, compared to generalist MC codes such as MCNP4C, are essentially due to a new transport mechanism which is associated with a new multiple scattering formalism for electrons, and allows the use of large step sizes. Photon and electron transport is performed along different material regions without taking into account the existence of borders.

3.1 Analog and condensed history Monte Carlo

The simplest MC model for particle transport problems is the *analog* MC model. In this model, particles are followed from event to event, and the next event is always sampled (using the random number generator) from a number of possible next events according to the events probabilities. This model is adequate for the transport of particles, such as photons, with large mean free pathlengths.

Because of the strength and long range of the Coulomb interaction, the number of collisions in a typical charged particle history is enormous (of the order of 10^6). Thus, the analog simulation is not adequate because it would be too time consuming. In order to reduce the required amount of computation time, Berger [Ber63] introduced the *condensed history technique* or *condensed random walk*. In each step, the angular deflection and the energy loss from the combined effect of many collisions are accounted for through random sampling from multiple scattering theories (Goudsmit and Saunderson [GS40a, GS40b], Lewis [Lew50], Molière [Mol47, Mol48]) and stopping

powers, respectively. Berger [Ber63] also defined two different implementations of the condensed history technique, known as Class I and Class II schemes. In the Class I scheme, or complete grouping, all electron interactions are grouped together, using a predetermined set of pathlengths or average energy loss fractions and the random sampling of the interactions is performed at the end of the step. MCNP4C is a Class I scheme. In the Class II scheme, or mixed procedure, collisions with small energy losses and deflections are grouped, but occasional catastrophic collisions occur and they are treated separately using single scattering cross sections. Catastrophic events generate bremsstrahlung photons and δ-rays that are able to interact with matter in a relevant way, i.e. producing secondary particles. Classe II algorithms simulate the inelastic collisions with production of secondary particles above an energy threshold Δ in an analog way. For energy transfer below Δ, the collisions are grouped with the energy loss estimated from restricted stopping power, L_Δ, distributions. MC code DPM is a Class II scheme.

In the following sections, we will briefly present how the photon transport is treated by MCNP4C and DPM (version 1.1) and in more detail how the electron condensed history is treated by these two codes. The terminology employed in MCNP4C and DPM will be respected.

3.2 Photon transport

An important component of Monte Carlo techniques is the numerical sampling of random variables with a given probability distribution function (PDF). The random sampling algorithms are based on the use of random numbers uniformly distributed in the interval]0,1]. In general, photon analog MC simulation can be performed in four main steps basically used by MCNP4C and DPM:

1. random choice of the *distance to the next interaction*, according to the total photon cross section σ_{total}. The distance to the next interaction is randomly sampled from the exponential attenuation law, i.e. the distance, t, to the next interaction is governed by the following PDF:

$$p(t)dt = \mu e^{-\mu t} dt, \tag{3.1}$$

where μ is the linear attenuation coefficient for the medium. In that case, the

distance t is determined by:

$$t = -\frac{1}{\mu}\ln(\xi) = -\lambda\ln(\xi) = -\frac{A}{N_a\rho\sigma_{total}}\ln(\xi), \tag{3.2}$$

where A, N_a and ρ are respectively the atomic mass, Avogadro's number and density of the material, σ_{total} the total photon cross section, ξ a pseudo-random number sampled in]0,1], and λ the total *mean free path* (MFP).

2. *transport to the interaction site*, taking into account the geometry constraints;

3. random choice of the *interaction mechanism*, according to the total photon cross section σ_{total}. The interaction mechanism's choice is based upon the relative magnitudes of the photon cross sections of the competing processes σ_i, i.e. a random number is generated and the interaction mechanism, i, is chosen according to its probability, σ_i/σ_{total};

4. random choice of the *outcome of the interaction*, in terms of the scattering angle and energy, according to the corresponding differential photon cross section. The probability distribution function, defined by the differential photon cross section of the interaction mechanism previously chosen, is randomly sampled to give the scattering angle. The energy is then obtained from the energy - scattering angle relationship. For the details of photon interactions, see Chapter 1.

The analog simulation requires that the distance to the next interaction has to be recalculated when the photon crosses an interface between two distinct materials, which occurs very frequently in a small-voxel based geometry and induces a significative loss in transport process efficiency. To overcome this difficulty, DPM uses the δ-scattering method of Woodcock *et al.* [WMH$^+$65], which avoids calculating intersections with the interfaces of all the visited voxels. The method is implemented by first determining the energy dependent minimum total MFP, $\lambda_\gamma^{(min)}(E)$, in the entire geometry. A distance to the next interaction t is then sampled using $\lambda_\gamma^{(min)}(E)$, and the photon is transported through t, ignoring all boundary crossing. Next, the material of the current voxel is determined and an interaction is simulated at t only with a probability equal to:

$$P = \frac{\lambda_\gamma^{(min)}(E)}{\lambda_\gamma^{(vox)}(E)}, \tag{3.3}$$

where $\lambda_\gamma^{(vox)}(E)$ represents the total MFP in the current voxel. If an interaction does not occur, the transport is continued. If an interaction i does occur, its type is sampled

according to the correspondent probability P_i, which is:

$$P_i = \frac{\lambda_\gamma^{(vox)}(E)}{\lambda_i^{(vox)}(E)}, \tag{3.4}$$

where $\lambda_i^{(vox)}(E)$ represents the MFP of the interaction i in the current voxel.

The detailed physics treatment is used in MCNP4C. It includes the photoelectric effect, the Compton scattering, the Thomson scattering, the pair production and accounts for fluorescence photons after photoelectric absorbtion. In DPM code, only the photoelectric absorption, the Compton scattering and pair production are considered.

3.3 Electron transport in MCNP4C

3.3.1 Electron step and substeps

The condensed random walk for electrons can be considered in terms of a sequence of sets of values:

$$(0, E_0, t_0, u_0, r_0), (s_1, E_1, t_1, u_1, r_1), (s_2, E_2, t_2, u_2, r_2), \ldots \tag{3.5}$$

where s_n, E_n, t_n and r_n are the total pathlength energy, time, direction and position of the electron at the end of n steps. On the average, the energy and pathlength are related by:

$$E_{n-1} - E_n = -\int_{s_n-1}^{s_n} \frac{dE}{ds} ds, \tag{3.6}$$

where $-dE/ds$ is the total stopping power. The electron steps with pathlengths $s = s_n - s_{s-1}$ are called *the major steps* or *energy steps*. The condensed random walk of the electrons is structured in terms of these energy steps. Class I ETRAN-based codes such as MCNP4C usually choose the sequence of pathlengths $\{s_n\}$ such that:

$$\frac{E_{n-1}}{E_n} = k, \tag{3.7}$$

for a k constant. The most commonly used value is $k = 2^{-1/8}$, which results in an average energy loss per step of 8.3%. In MCNP4C, to accurately represent the electron trajectory, a major step s is divided into m substeps, each of pathlength s/m. The integer number m depends only on the material (average atomic number Z). Angular deflections and the production of secondary particles are sampled at the level of these substeps.

3.3.2 Energy straggling

In Class I codes such as MCNP, all electron interactions are grouped together. Thus, the distribution for energy loss sampling must include values of losses due to secondary electrons. That is why MCNP uses the collisional stopping power calculated in Chapter 1 without the shell correction factor, treating all the collisional events in an uncorrelated, probabilistic way. Because an energy step represents the cumulative effect of many individual random collisions, fluctuation in energy loss rate will occur. Thus, the energy loss will not be a simple average $\overline{\Delta}$ but a probability function $f(s,\Delta)d\Delta$. Landau [Lan44] developed a theory to calculate this distribution and found that the energy loss distribution can be expressed as:

$$f(s,\Delta)d\Delta = \phi(\lambda)d\lambda, \tag{3.8}$$

where $\phi(\lambda)$ is an universal function of a single scaled variable

$$\lambda = \frac{\Delta}{\xi} - ln\left[\frac{2\xi mv^2}{(1-\beta^2)I^2}\right] + \delta + \beta^2 - 1 + \gamma, \tag{3.9}$$

where m and v are the mass and speed of the electron, δ the density effect correction, $\beta = v/c$, I the mean excitation energy of the medium, and γ is the Euler's constant. The parameter ξ is defined by:

$$\xi = \frac{2\pi e^4 NZ}{mv}s. \tag{3.10}$$

Landau's theory is valid if the mean energy loss for a energy step s is small compared with the electron energy and if the parameter ξ is large compared with the mean excitation energy of the medium. The Rutherford cross section [Rut11] is used to compute the energy loss.

Blunck *et al.* [BL50] have extended Landau's result to include the second moment of expansion of the cross section. Their result can be expressed as a convolution of Landau's distribution with a Gaussian distribution:

$$f^*(s,\Delta) = \frac{1}{\sqrt{2\pi}\sigma}\int_{-\infty}^{+\infty} f(s,\Delta')exp\left[\frac{(\Delta-\Delta')^2}{s\sigma^2}\right]d\sigma. \tag{3.11}$$

Blunck *et al.* [BW51] provided a simple form for the variance of the Gaussian:

$$\sigma_{BW}^2 = 10eV.Z^{4/3}\overline{\Delta}, \tag{3.12}$$

and Seltzer [Sel91] recommends a correction to σ_{BW} which is used in MCNP4C:

$$\sigma = \frac{\sigma_{BW}}{1 + 3\epsilon_{CE}}, \tag{3.13}$$

where ϵ_{CE} is the an estimate for the relative error found by Chechin *et al.* [CE76]:

$$\sigma_{CE} \approx \left[\frac{10\xi}{I} \left(1 + \frac{\xi}{10I} \right)^{-1/2} \right]. \tag{3.14}$$

3.3.3 Angular deflections

In all condensed history MC programs, the effect of the large number of elastic interactions, which occur over a given pathlength, is modelled by means of multiple scattering theories. The MCNP code relies on the Goudsmit-Saunderson theory for the probability distribution of angular deflection [GS40a, GS40b]. This theory is an exact solution for the angular distribution of charged particles traversing a given distance, assuming a constant cross section over the path. The Goudsmit-Saunderson distribution for angle deflections is given by:

$$F_{GS}(s/m, \mu) = \sum_{l=0}^{\infty} \left(l + \frac{1}{2} \right) e^{-s/mG_l} P_l(\mu), \tag{3.15}$$

where s/m is the length of the substep, $\mu = \cos\theta$ the angular deflection from the direction at the beginning of the substep, $P_l(\mu)$ the l^{th} Legendre polynomial, and G_l is:

$$G_l = 2\pi N \int_{-1}^{+1} \frac{d\sigma}{d\Omega} [1 - P_l(\mu)] d\mu, \tag{3.16}$$

in terms of microscopic cross section $d\sigma/d\Omega$, and the atomic density N of the medium. In MCNP, the microscopic cross section is taken from numerical tabulations from Riley *et al.* [RMB75] for electron energies below 0.256 MeV, and, for higher electron energies, a combination of the Mott [Mot29] and Rutherford cross sections, with screening correction given by [Sel88]:

$$\frac{d\sigma}{d\Omega} = \frac{Z^2 e^2}{p^2 v^2 (1 - \mu + 2\eta)^2} \left[\frac{(d\sigma/d\Omega)_{Mott}}{(d\sigma/d\Omega)_{Rutherford}} \right], \tag{3.17}$$

where e, p and v are the charge, momentum and speed of the electron respectively. MCNP uses the recommendation of Seltzer [Sel88] for the value of the screening correction η given by:

$$\eta = \frac{1}{4} \left(\frac{\alpha mc}{0.855p} \right)^2 Z^{2/3} \left[1.13 + 3.76(\alpha Z/\beta)^2 \sqrt{\frac{\tau}{\tau + 1}} \right], \tag{3.18}$$

where α is the fine structure constant, m is the rest mass of the electron, $\beta = v/c$ and τ is the electron energy in units of electron rest mass.

3.3.4 Hard collision and radiative events

Using the differential Møller cross section, the probability of energy transfer greater than some ϵ_c representing an energy cutoff, below which secondary particles will not be followed is given by:

$$\sigma(\epsilon_c) = \int_{\epsilon_c}^{1/2} \frac{d\sigma}{d\epsilon} d\epsilon. \tag{3.19}$$

Then the normalized probability distribution for generation of secondary electrons with $\epsilon > \epsilon_c$ is given by:

$$g(\epsilon, \epsilon_c)d\epsilon = \frac{1}{\sigma(\epsilon_c)} \frac{d\sigma}{d\epsilon} d\epsilon. \tag{3.20}$$

At each electron substep, MCNP uses $\sigma(\epsilon_c)$ to determine randomly whether knock-on electrons will be generated. If so, the distribution of Eq. 3.20 is used to sample the energy of each secondary electron. Once an energy has been sampled, the angle between the primary direction and the direction of the newly generated secondary particle is determined by momentum conservation. This angular deflection is used for subsequent transport of the secondary particle. The energy and direction of the primary electron are not changed by the sampling of secondary particles. On average, both the energy loss and the angular deflection of the primary electron have been taken into account by the multiple scattering theories.

For the sampling of bremsstrahlung photons, MCNP uses the Bethe-Heitler Born-formalism. In MCNP, all the data including bremsstrahlung production probabilities, photon energy distributions and photon angular distributions are converted into tables. At each substep, according to the bremsstrahlung production probabilities table, MCNP determines if a photon is created or not. If created, a sampling in the photon energy distribution tables is performed and finally a sampling in the photon angular distribution table is performed. The direction of the primary electron is unaffected by the generation of the photon, because the angular deflection of the electron is controlled by the multiple scattering theory. However, the energy of the electron at the end of the substep is reduced by the energy of the sampled photon because the treatment of the electron energy loss is based only on nonradiative processes.

3.4 Electron transport in DPM

3.4.1 Multiple scattering with energy loss

The first major innovation introduced in DPM to speed up calculations, is the use of a new step-size independent multiple-scattering theory. This method is a robust implementation of the Lewis's formulation of Goudsmit-Saunderson theory. In the continuous slowing down approximation, the pathlength can be expressed in terms of the energy loss as:

$$s = \int_{E-\Delta E}^{E} \frac{dE}{S(E)} = R(E) - R(E - \Delta E), \tag{3.21}$$

where $S(E)$ is the CSDA stopping power and $R(E)$ the CDSA range. The average energy loss ΔE for an electron with initial energy E travelling a distance s can be determined by inverting the CSDA range:

$$\Delta E = E - R^{-1}(R(E) - s). \tag{3.22}$$

Lewis [Lew50] introduced the energy dependence in the Goudsmit-Saunderson multiple scattering theory and obtained the angular distribution:

$$F_L(\omega) = \sum_{l=0}^{\infty} \Big(l + \frac{1}{2}\Big) P_l(w) exp\Big[- \int_{E-\Delta E}^{E} dE \frac{G_l}{S} \Big], \tag{3.23}$$

where $\omega = \cos\theta$, $G_l = g_l/\lambda$ with λ the MFP of the inelastic interactions and the coefficients g_l given by the expansion of the angular differential elastic cross section using Legendre polynomials. Kawrakow *et al.* [KB98] have shown that Eq. 3.23 can be accurately expressed by:

$$F_L(\omega) = q(u, E) \frac{2B(1 + B)}{(1 + 2B - \omega)^2}, \tag{3.24}$$

where B is a free parameter, u a angular variable calculated from ω. They have shown that the function $q(u, E)$ depends only on the dynamic variable u and E. This function is pre-calculated by DPM from Rutherford cross section corrected for spin and screening. This formalism allows a very fast determination of the polar angle θ due to the fact that the problem of sampling F_L has been reduced to interpolating $q(u, E)$.

3.4.2 The random hinge transport mechanism

The second major innovation introduced in DPM lies in the use of a new transport mechanism. The no-dependency on the stability of the angular distributions calculated in 3.23, allows the use of a new mechanism of transport called the *random hinge mechanism* [FMB+93, BS01]. MC code PENELOPE's random hinge model provides an excellent compromise between speed and accuracy, and is therefore well suited for a fast MC code. In this model, the energy loss along a step is disregarded. The random hinge model splits the pathlength s in two sub-steps of lengths: $s_A = \xi s$ and $s_B = s - s_A$ where ξ is a random number between 0 and 1. A first sub-step s_A is taken in the electron initial direction, after which the particle is deflected according to any multiple scattering law which provide polar and azimuthal deflection determined over the entire step s. A second substep is then taken over the remaining distance s_B in the new direction.

Unfortunately, the inclusion of the energy losses along s reduces the accuracy of the random hinge model: PENELOPE model overestimates the scattering for very large pathlengths. Using the same concept of random hinge model, DPM uses a variable called *scattering strength*, K_1, where sampling is performed rather than the distance s, i.e:

$$K_1^{(A)} = \xi K_1(s), \tag{3.25}$$

where $K_1(s)$ is given by:

$$K_1(s) \equiv \int_0^s ds' G_1(s') \simeq s G_1\Big(\frac{s}{2}\Big), \tag{3.26}$$

with $G_1 = g_1/\lambda$. The electron is then transported until it "accumulates" a scattering equal to $K_1^{(A)}$, where a deflection is imposed. The electron is then moved the pathlength required to exhaust the scattering strenght $K_1(s) - K_1^{(A)}$. This formalism corrects the overestimation of the scattering and more important, provides a basis for simulating the scattering across material density boundaries. This new transport mechanism allows to accurately describe the trajectories of the electrons until complete absorption with only 8-10 steps in the condensed history compared to the required multiple steps for the generalistic codes in each crossed voxel [SWB00].

3.4.3 Hard collision and radiative events

As DPM is a Class II algorithm, hard interactions are simulated discretely using an analog (event-by-event) model. DPM uses the Møller cross section to treat the inelastic collisions of electrons with atomic electrons. Integrating the differential Møller cross section, the inverse MFP, λ_M^{-1} for hard collisions events (those above the cutoff W_M) in homogeneous media is given by:

$$\lambda_M^{-1} = \frac{2\pi e^4}{mv^2}\frac{Zn_m}{E}\left[\frac{1-2k_M}{k_M(1-k_M)} + \left(\frac{\gamma-1}{\gamma}\right)^2\left(\frac{1}{2}-k_M\right) + \left[\left(\frac{\gamma-1}{\gamma}\right)^2 - 1\right]\ln\frac{1-k_M}{k_M}\right], \tag{3.27}$$

where n_m is the number of molecules per unit of volume and

$$k_M = \frac{W_M}{E}. \tag{3.28}$$

In the limit that $mc^2 \ll E$ and $k_M \ll 1$, Eq. 3.27 can be approximated by:

$$\lambda_M \simeq \frac{A}{Z\rho}\frac{mc^2 W_M}{N_A 2\pi e^4}. \tag{3.29}$$

By default, DPM sets W_M =200 keV, as knock-on electrons with less than that energy have ranges much smaller than the minimum 1 mm voxel size. For water, we have $\lambda_M \simeq 2$ cm with W_M =200 keV and it is practically independent of E as shown in Eq. 3.29. When a Møller interaction takes place, the fraction k of energy lost is sampled from the normalized probability distribution function based on the total Møller cross section. A knock-on electron is generated and its energy, direction an position stored for later transport. If the knock-on electron has a kinetic energy W, the direction of the movement will be determined according to the momentum conservation and the angle, θ_2 formed between this direction and the velocity of the primary electron is given by:

$$\cos\theta_2 = \sqrt{\frac{W(E+2mc^2)}{E(W+2mc^2)}}. \tag{3.30}$$

For bremsstrahlung events, from the data tables given by Seltzer *et al.* [SB85], it can be shown that for materials and energies typically seen in radiotherapy, the bremsstrahlung cross section implemented in DPM is given by:

$$\sigma_B = \frac{Z^2}{\beta k}a(1-bk), \tag{3.31}$$

where $W = kE$ (W the energy of the produced photon), β the electron velocity in units of the speed of light, and (a, b) energy and material independent constants of a linear function fitting the tabulated data. For a given cutoff energy for bremsstrahlung production, W_B, the inverse MFP resulting from Eq. 3.31 is given by:

$$\lambda_B^{-1} = \frac{Z^2 n_m a}{\beta^2}\left[\ln\frac{1}{k_B} - b(1-k_B)\right], \tag{3.32}$$

where $k_B = W_B/E$. In the limit $mc^2 \ll E$ and $k_M \ll 1$, Eq. 3.32 can be approximated by:

$$\lambda_B \simeq \frac{A}{Z^2 \rho N_A a}\left(\ln\frac{E}{W_B} - b\right)^{-1}. \tag{3.33}$$

The analog simulation of hard bremsstrahlung events are performed using a random sampling on the PDF corresponding to the normalized σ_B. The angular deflection of the incoming electron is small and can be neglected and the scattering angle of the secondary photon is set equal to its mean value, approximately given by Heitler [Hei54]:

$$\langle\theta\rangle \simeq \frac{mc^2}{E + mc^2}. \tag{3.34}$$

3.4.4 Transport across inhomogeneous voxel phantom

In typical mixed class II electron transport MC models, electrons are created with an initial direction, an initial energy and are transported in a series of steps until they exit the problem geometry or their energies fall below a user defined absorption cutoff. In this section, we will present how the transport is performed in a voxel based geometry.

For catastrophic events, the distance to a catastrophic collision is sampled according to:

$$t_{ca} = -\lambda_{ca}\ln\xi, \tag{3.35}$$

where λ_{ca} is the catastrophic collision MFP for a reference material which is water, and ξ a random number uniformly distributed in]0,1]. A lookup table with values of $\lambda_{ca} = \lambda_M$ for Møller event and $\lambda_{ca} = \lambda_B$ for bremsstrahlung event, based on Eqs. 3.29 and 3.33 respectively, are read from input files during the initialization of DPM. When an electron travels a distance t inside a voxel, t_{ca} is decreased an amount Λt_{ca} given by:

$$\Lambda t_{ca} = \Delta t_M = t\frac{(Z\rho/A)_{vox}}{(Z\rho/A)_{water}}, \tag{3.36}$$

for Møller events, and

$$\Lambda t_{ca} = \Delta t_B = t\frac{(Z^2\rho/A)_{vox}}{(Z^2\rho/A)_{water}}, \tag{3.37}$$

for bremsstrahlung events. At that point, a catastrophic event is simulated, in which the secondary particle is generated with its phase sampling according to the interaction process (Møller or bremsstrahlung event) and placed in a secondary stack.

The total scattering strength K_1 is obtained for water at the initial electron energy. Values of K_1 as a function of energy and a preset pathlength s are precalculated for water and read by DPM during its initialization. Using the DPM random hinge mechanism, the scattering strength prior to simulation of a multiple scattering event is given by:

$$t_S = K_1^{(A)} = \xi K_1. \tag{3.38}$$

At each step t inside a voxel, t_S is decreased by an amount equal to:

$$\Delta t_S = \int_0^t dt' G_1^{vox}(t') \approx \frac{t}{2}\left[G_1^{vox}(t'=0) + G_1^{vox}(t'=t)\right]. \tag{3.39}$$

Once t_S exhausted, the angular deviation is sampled from the Lewis PDF, using the $q(u, E)$ surface corresponding to water. After rotating through the scattering angle to determine the new electron direction, the linear transport is resumed until a new quantity of scattering strength, given by:

$$t_S = K_1^{(B)} = K_1 - K_1^{(A)}, \tag{3.40}$$

is spent. A new Δt_S is calculated and after the distance to t_S is traversed, the process is repeated with a new total scattering strength K_1 determined according to the lookup tables and a new t_S is sampled according to Eq. 3.38.

Apart from discrete events the continuous energy loss of electrons is computed at each step and given by:

$$\Delta E = \int_0^t dt' S_r^{(vox)}(t'), \tag{3.41}$$

where t is the distance traversed in a given voxel prior to a hard collisions or existing the voxel and $S_r^{(vox)}$ is the restricted collision stopping power for energy transfer below Møller and bremsstrahlung production thresholds for the problem. For large t, $S_r^{(vox)}$ can vary over the step, and so the integral is approximated by first estimating the energy loss over t assuming that $S_r^{(vox)}$ is constant, and then averaging the stopping

power over the step. Values of $S_r^{(vox)}$ are precalculated for a dense grid of energies and read by DPM during its initialization.

Chapter 4

MC simulation of KD2 plus additional collimator

Dose measurements for the narrow photon beams used in radiosurgery are complicated by the lack of electron equilibrium which is a requirement namely for ionometric methods. To overcome this difficulty the use of different dosimetric supports is strongly recommended in order to appreciate the influence of each type of detector. MC simulation is another kind of tool to assess the details of the energy deposition phenomena in such narrow photon beams. In this chapter, we will simulate the head of the accelerator used for radiosurgery treatments at IPOFG-CROC, S.A., and analyze the subsequent created Phase Space Data (PSD). The validation of the PSD will be done comparing calculated $DDCs$, $OARs$ and OFs with experimental ones obtained from various detectors.

4.1 Phase Space Data generation

A very detailed geometry of the accelerator head plus the additional collimator is modelled in MC code MCNP4C using cells constructed by Boolean combinations of first and second-degree surfaces. For instance, a complex component such as the flattening filter is composed by various cells. In each cell, the user has to provide the type of material, its density, and two additional parameters controlling, for photons and electrons respectively, the geometry splitting with the variance reduction technique Russian Roulette [Bri00].

Since the internal geometry of the accelerator head remains unchanged in a radiosurgery treatment, it has to be simulated just once. In this first block the following components are included: target, target assembly, primary collimator, flattening filter, ionization chambers, mirror, jaws and reticle (see Fig. 4.1 (a)). The second block includes the additional cylindrical collimator, the water phantom and the air column between the additional collimator and the water phantom (see Fig. 4.1 (b)). This approach is commonly used in medical accelerator simulations and is called the standard approach [SKL+99]. The simulation of the first block will be called the patient-independent simulation. Since the dose deposition in the water phantom is calculated in the second block, this phase will be called the patient-dependent simulation.

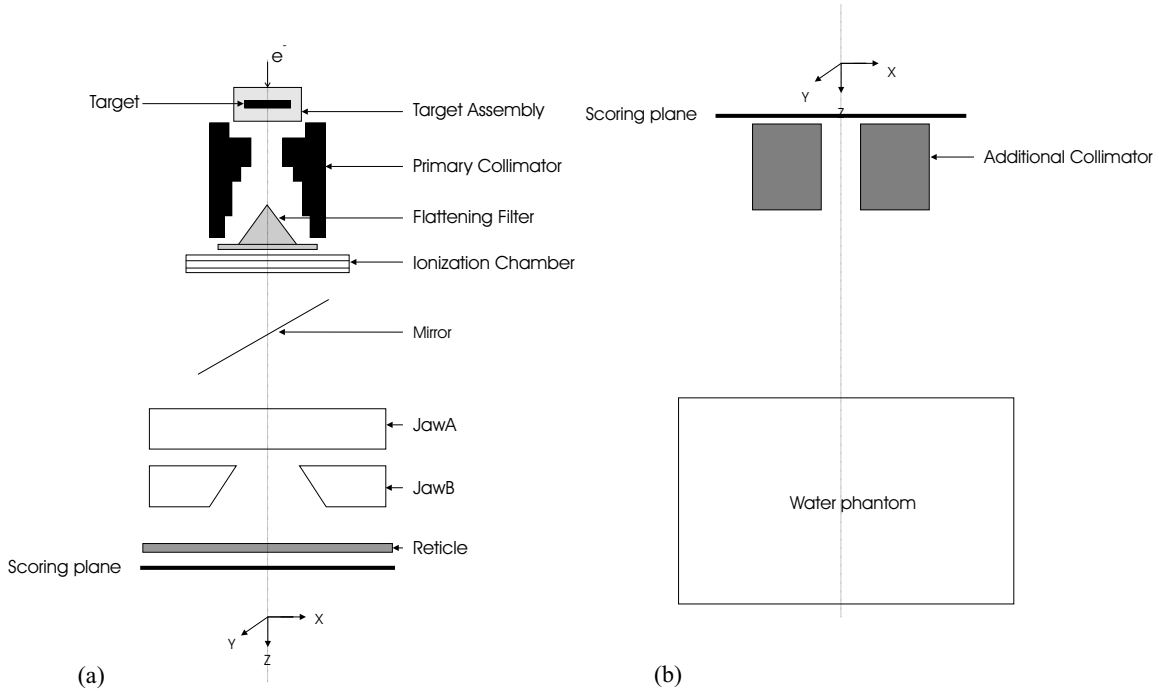

Figure 4.1: (a) First simulation block: Siemens Mevatron KD2 linear accelerator head components in 6 MV photon mode, (b) second simulation block: additional collimator, air column and water phantom.

A PSD is recorded at the scoring plane into a binary file *wssa* which is the source for the next simulation block (patient-dependent simulation). In this PSD, the characteristics of the particles are stored. A dedicated code, MCNP-STRIP, is used in order to transform the binary *wssa*-file into an ascii readable file. This code originates from the LAHET Monte Carlo code and was adapted to MCNP and improved by Siebers [Sie]. For photons, an in-house code XYZLAST was developed in order to determine

where the photon that reach the scoring plane was generated or suffered its last interaction. This code is based on the zl parameter (coordinate along the z-axis of the point of origin) recorded in the wssa-file.

4.1.1 Simulation parameters

The interactions in the MCNP simulations can be described by two physics models: the simple and the detailed one. The simple model is intended for high-energy photons where little coherent scattering occurs, but it is inadequate for high-Z materials. Due to this fact, the detailed model has been used and it accounts for fluorescent photons after photoelectric absorbtion. Electron binding effect is also accounted by inclusion of form factors.

A crucial issue is the generation process of bremsstrahlung photons. In the previous MCNP version 4B, some authors such as Siebers *et al.* [SKL+99] advised against the use of bremsstrahlung splitting. The problem consisted in output photons, after the splitting having identical phase space coordinates. This problems was solved in MCBP4C and the bremsstrahlung splitting was used in this work (parameter $BNUM = 4$). In the patient-independent simulation, no other particle splitting procedure was used.

According to the CSDA theory implemented in MCNP4C, the condensed random walk is structured in terms of energy steps. However, the representation of the electron trajectory will be more accurate if the major step s is divided in multiple substeps. The integer entry m of the *estep* card of MCNP4C divides the major step s in m substeps. By default, the value of m varies from $m = 2$ for materials with $Z < 6$ to $m = 15$ for materials with $Z > 91$. In the simulation of the accelerator, the target material plays the crucial role and this is why the trajectory of the electrons must be as accurate as possible. This can be critical in the case of a thick target. The default value ($m = 13$) given by MCNP4C may not be sufficient to sample correctly the electron trajectory. But the value of m can change drastically the running time of the simulation. The greater the value of m, the better is the sampling of the electron trajectory but the greater is the running time. Simulations of the target alone were performed to check if the default value of m was adequate. An analysis of the characteristics of the particles was performed and the results were compared for different values of m larger than the default value. For incident electrons of 6.15 MeV, no significant changes were found

in the characteristics of the emergent particles from the slab for the different values of m, but the running time increased by a factor 2.4 for $m = 40$ compared to $m = 13$. According to the results of these simulations, the default value of m for the target material was used.

Following some authors [RFD+95, LSM99, SKL+99, MMK+99, LRS+00], the kinetic electron energy cutoff was set to 0.189 MeV in the first block and 50 keV in the second block. The photon energy cutoff was set to 10 keV in both blocks. The electron energy indexing algorithm used was the ITS-style with nearest group boundary treatment. The upper energy limit for electron interactions ($EMAX$) was set to 6.2 MeV for the two blocks. A total of $nps = 10^9$ incident electrons were used in the first block. Electron cross sections and related data are generated on a logarithmic energy grid from $EMAX$ to an energy at least as low as the global energy cutoff for electrons. The data library for materials used in the simulations are the improved ENDF/B-VI data library with EL03 electron data library [Bri00].

In the overall simulation process, some particles created in the first block, whose tracks cross the scoring plane, do not interact in the water phantom or patient; it is thus unnecessary to follow the history of such particles. This is why, in the simulation of the patient independent block, only particles that cross the surface which defines the scoring plane within a radius equal to 20 cm were kept. In the simulation of the patient dependent block, particles whose tracks enter an annular cell placed between the planes which define the top and the bottom of the additional collimator and with an internal diameter equal to the external diameter of the additional collimator are eliminated by the cell importance mechanism.

4.1.2 Characterization of the incident electron source

The determination of the characteristics of the incident electrons impinging in the target is a crucial step in the overall simulation process. The calculated dose distributions depend to a certain extent on the characteristics of the incident electrons. The energy and spatial distributions of these incident electrons can vary for the same accelerator depending on the adjustments made in-situ. This is why values given by the manufactor are only indicative values of the real characteristics of the incident electrons of the accelerator that we want to simulate.

The direct measurement of the spot size of the photon beam or the primary electron beam is a very difficult task due to the very high beam intensities produced by linear accelerators. Different experimental methods have been used to measure such characteristic [MR88, LMB88, LLB$^+$92, JBF$^+$93, SLR02]. Detailed studies on the influence of the linac components and the characteristics of the primary electron beam using MC simulations were done by Sheik-Bagheri *et al.* [SR02]. They concluded that the calculated DDC in water is relatively insensitive to relative small changes in the primary electron energy, whereas the lateral dose profile is a good indicator for the exact value of the primary electron energy, also confirmed by the work of Lovel *et al.* [LCM95] and Lin *et al.* [LCL01]. They have also shown that, for different modelled linear accelerators, the energy spread of the electron primary beam has a very weak effect on the calculated dose distributions and can be ignored. According to these authors, the procedure to tune the energy and spot size of the incident electrons is based on DDC and OAR calculations. First, the primary energy of the incident electrons is set according to the manufactory specification. This energy is tuned until the calculated DDC matches the measured one for the 10×10 cm^2 field. Second, with that energy, the incident electron spot size is changed until calculated profiles match the measured ones. Finally, once the spot size is defined, another DDC is calculated to verify if the incident electrons energy has to be changed or not.

The procedure to tune the energy and spot size of the incident electron can be very time consuming especially if the electron energy has to be changed again after the tuning of the spot size. It is clear for conventional radiotherapy, that the spot size plays a crucial role (especially for the larger field sizes) and must be taken into account to calculate with a good accuracy the profiles and the geometry size of the radiation fields [SRR$^+$00]. But for the narrow photon beams used in radiosurgery, it may be not so important to take into account this parameter. For radiation fields smaller than 10×10 cm^2, Fix *et al.* [FKR00] have shown that models taking into account no radial variation of photon energy and fluence gave the same dose distribution results that those taking into account these variations. That is, for field sizes lower than 10×10 cm^2, the electron spot and the flattening filter have a weak effect on the radial variation of fluence and energy of the photons (emerging from the flattening filter) scored after the jaws. These variations are expected to be even smaller after the interposition of the additional collimators. This is why, for this particular application (simulation of

narrow photon beams), the electron source spot size is replaced by an electron source point. As refereed before, the electron energy spread can be ignored. In our simulation, the electron source is then an unidirectional electron source point of 6.15 MeV [CLO00, FCA+99]. Finally, Rodrigues [Rod02] has shown that for our linear accelerator, the dose distribution for the 10×10 cm^2 using the defined electron point source is in good agreement with measurements.

4.2 Phase Space Data analysis

4.2.1 Basic statistics

During the simulation process, the weight of the particles is adjusted depending on various factors. The understanding of the weight mechanism is crucial in analyzing all the physics processes involved in simulation. Some variables have to be defined. Let us consider a population of n particles. A subpopulation i of n_i particles has the same weight w_i. The total weight of the population of n particles is defined as:

$$W_t = \sum_i n_i w_i. \tag{4.1}$$

MCNP4C writes in the output file for each cell this variable for the corresponding particle creation or capture process. The average weight of the population is given by:

$$\overline{w} = \frac{\sum_i n_i w_i}{\sum_i n_i}. \tag{4.2}$$

Combining Eqs. 4.1 and 4.2 we obtain:

$$W_t = \overline{w} \sum_i n_i = \overline{w} n. \tag{4.3}$$

If we consider that the population has an average weight equal to 1, Eq. 4.3 becomes: $W_t = n'$. That means n particles with an average weight $\overline{w}$ are equivalent to n' particles with an average weight equal to 1. The mean energy of the population is given by:

$$\overline{E} = \frac{\sum_i E_i n_i w_i}{\sum_i n_i w_i}. \tag{4.4}$$

Combining Eqs. 4.1 and 4.4, the mean energy of the population is related to the total weight of the population by the equation:

$$\overline{E}W_t = \sum_i E_i n_i w_i. \tag{4.5}$$

Let us consider a simple example to understand how these variables can be useful to represent a population of particles. A population is composed of 10 particles: 5 particles of 1 MeV and 0.25 of weight, 3 particles of 2 MeV and 0.5 of weight and 2 particles of 3 MeV and 1 of weight. In theses conditions and using Eq. 4.1, the total weight is equal to $W_t = 4.75$. From Eq. 4.4, the mean energy of the population is $\overline{E} = 2.16$ MeV. This population is equivalent to a population of 4.75 particles with a mean energy of 2.16 MeV. To turn W_t independent of the number of incident particles, we normalize W_t to the number of incident electrons (nps). In this case, W_t represents the number of particle (from a population) per incident electron.

The distributions of the particles that reach the scoring plane are represented by histograms, the statistical error for one channel of N entries is given by $\sqrt{N}$. For mean distributions such radial mean energy distribution, the error associated to the mean value in each channel with N entries is given by [Lyo89]:

$$s_m = \frac{\sigma_E}{\sqrt{N}} = \sqrt{\frac{1}{(N)(N-1)}\sum_{i=1}^{N}(E_i - \overline{E})^2}. \tag{4.6}$$

If N is the number of particles in a channel and A the area where the N particles are counted, then the associated error of the value N/A is given by $\sqrt{N}/A$.

4.2.2 Particle creation and loss events

Before analyzing the PSD, it is interesting to have a global perspective of the particles creation and loss events occurring in all the components in the simulation block 1. Figure 4.2 shows the photon processes in block 1. Clearly, the bremsstrahlung interaction is the main photon creation process, followed by fluorescence. Electron x-ray and electron-positron annihilation (p-annihilation) processes are secondary creation photon processes in terms of importance. Figure 4.2 also shows that most of the photons are eliminated by capture processes (photoelectric events). Pair production process is quite marginal compared to capture processes. It has to be notice that a small fraction of photons are eliminated because they escape in the sense that these

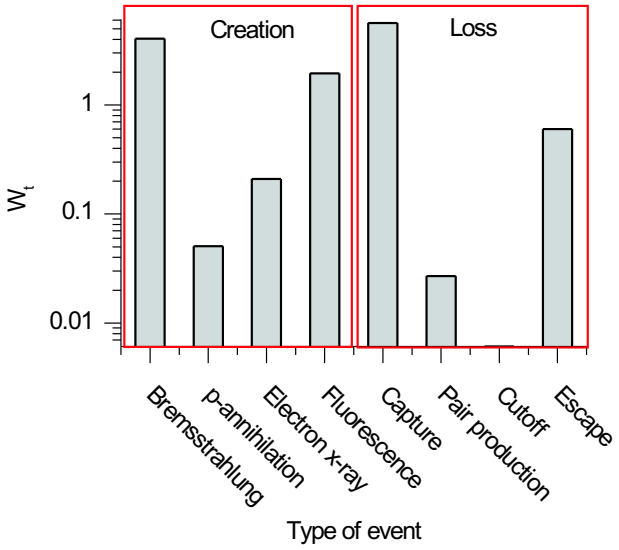

Figure 4.2: Type of events for photons in block 1 simulation. W_t represents the number of particles for one type of event per incident electrons.

photons go out the region of interest. Finally, the type of event *energy cutoff* is negligible ($W_t = 1.5 \times 10^{-5}$). For electrons, results presented in Fig. 4.3 show that the knock-on collisions are dominant for electron creation (strictly speaking, the knock-on process does not create electrons, energy is transferred from one electron to another). The photoelectric and Compton processes have the same order of importance in creating electrons in block 1. Finally, the pair production process weakly contributes to electron creation. Relatively few electrons escape, most of them are eliminated by the bremsstrahlung process (most significative) and energy cutoff events.

The average weight $\overline{w}$ of the particles (photons and electrons) created or eliminated in block 1 is $\overline{w} = 0.2603$. This value is not equal to 0.25 because not all the incident electrons suffer bremsstrahlung process as first interaction. Simulations show that characteristic x-ray photons have a weight equal to 1: only incident electrons produce characteristic photons. For the p-annihilation process $\overline{w} = 0.9467$ meaning that most of these photons are produced by the incident electrons. For the fluorescence process, simulations show that most of these photons are produced by secondary electrons that were originated themselves by bremsstrahlung photons ($\overline{w} = 0.2572$ for 1^{st} fluorescence and $\overline{w} = 0.2503$ for 2^{nd} fluorescence). Concerning photon losses, for all the events, $\overline{w} \approx 0.26$ indicating that the origin of most of these photons is the bremsstrahlung

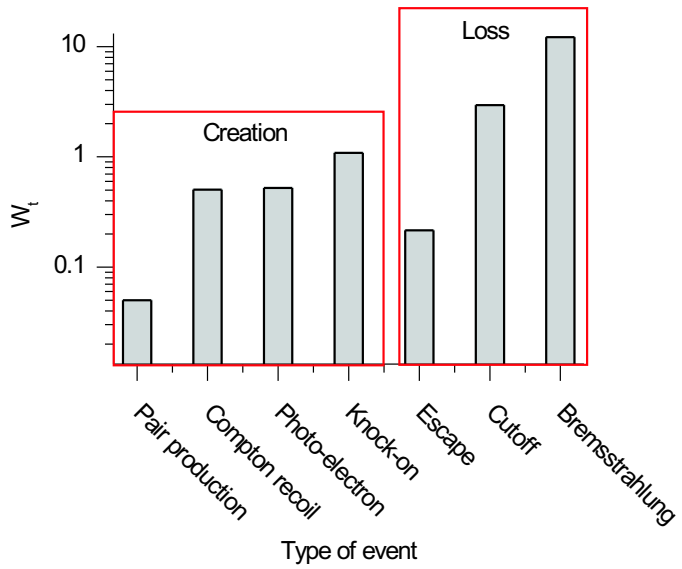

Figure 4.3: Type of events for electrons in block 1 simulation. W_t represents the number of particles for one type of event per incident electron.

interaction. For electrons, it is not relevant to perform the same analysis since most of the capture photons have $\overline{w} = 0.26$. It is expected that the weight of the created electrons does not differ from this value.

If we analyze the events in each component, we can conclude that most of the bremsstrahlung interactions take place in the target as expected but also in the primary collimator, as shown in Fig. 4.4. In fact, high energy electrons produced in the target or incident electrons can reach the high-Z primary collimator located very close to the target. The bremsstrahlung process is the main photon creation process in most of the components, as shown in Fig. 4.5. Simulation results also show that the fluorescence process is the second main photon creation process and mostly takes place in the target and primary collimator. Photons are essentially captured in the target and primary collimator, as shown in Fig. 4.4, and is the main photon loss process in most of the components, as shown in Fig. 4.5.

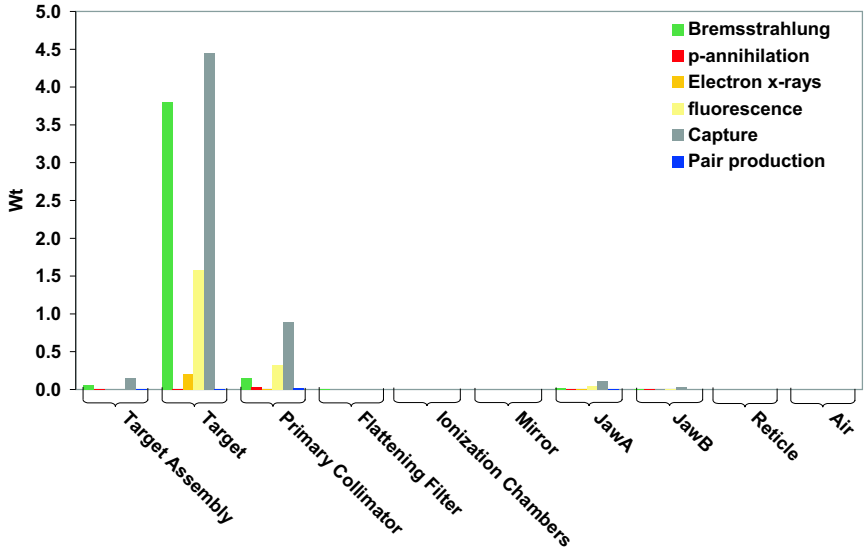

Figure 4.4: Type of events for photons for each accelerator head component in block 1 simulation. W_t represents the number of particles for one type of event per incident electron.

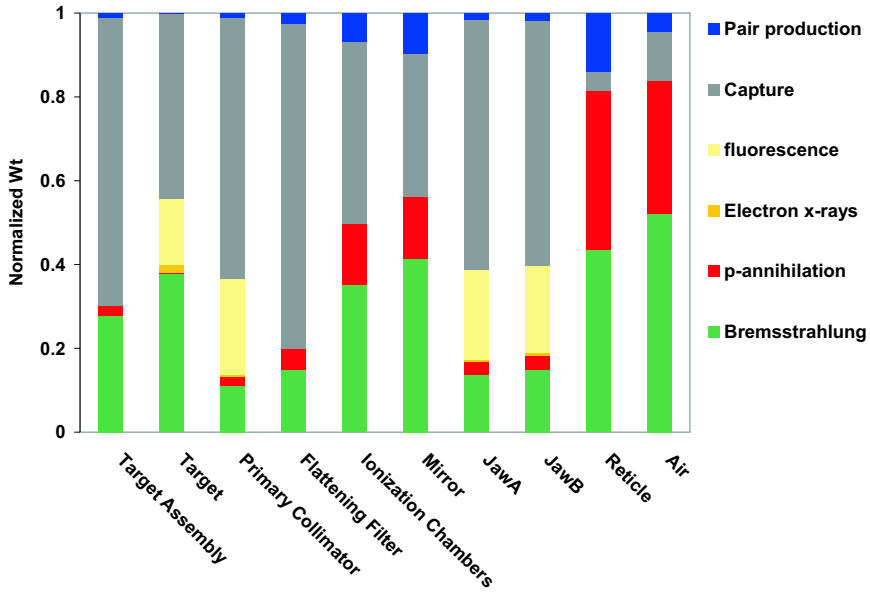

Figure 4.5: Type of events for photons for each accelerator head component in block 1 simulation. W_t is normalized for each component to the sum of the total weight of that component.

For electrons, most of the processes occur in the target as shown in Fig. 4.6. As it happens with photons, the primary collimator is the second source of electron creation due to its proximity to the target. Figure 4.6 also shows that the Compton and photoelectric processes are an important source of electron creation. Figure 4.7 shows that the Compton process is the relative main electron creation process in most of the components. As expected, most of the electrons are eliminated by the bremsstrahlung process and energy cutoff in the target and primary collimator. Except in the target, the energy cutoff mechanism is responsible for most of the eliminated electrons as shown in Fig. 4.7.

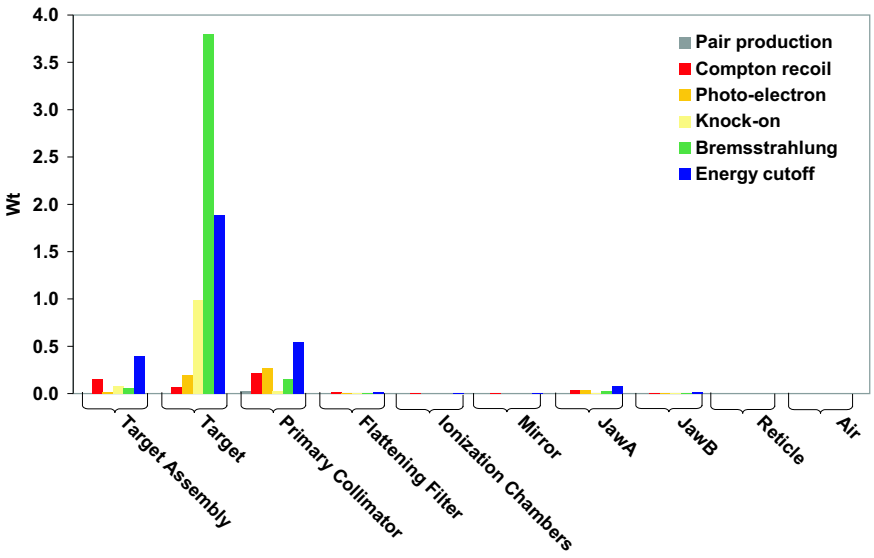

Figure 4.6: Type of events for electrons for each accelerator head component in block 1 simulation. W_t represents the number of particles for one type of event per incident electron.

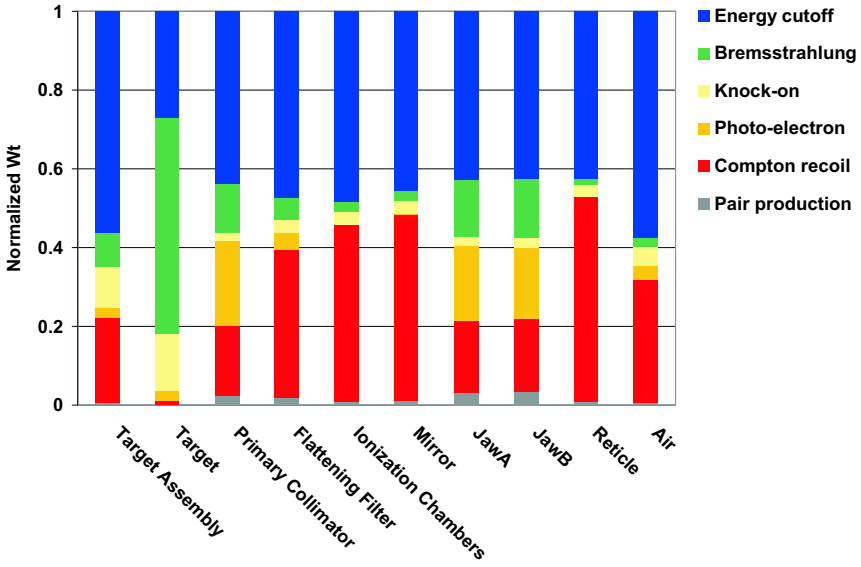

Figure 4.7: Type of events for electrons for each accelerator head component in block 1 simulation. W_t is normalized for each component to the sum of the total weight of that component.

4.2.3 Particle characteristics in PSD

In this section, we will focus on identifying the sources of the particles reaching the scoring plane and then we will analyze the characteristics of these particles. It is not our purpose to analyze the characteristics of the particles at different levels in the accelerator head which for our accelerator has already been performed by Rodrigues [Rod02]. Results of block 1 simulation show that the number of electrons reaching the scoring plane is a small fraction of the total number of particles stored in the PSD. They represent 0.9% of the total number of particles (photons and electrons) reaching the scoring plane. This result is of course machine dependent but it is of the same order of the results reported by other authors [ZW99, CDS00, FHD$^+$03] for a 10×10 cm^2 field size. Using XYZLAST, the origin or last interaction point of photons was found. Unfortunately, this point can not be calculated for electrons since the variable zl represents for electrons the starting point of the last substep and not the point of origin. Some studies have shown that these contaminant electrons were mostly originated by Compton interactions (see Fig. 4.7), in the flattening filter [SK96, ZP98]. In this characterization, electrons will be globally analyzed. Figure 4.8 shows the point of origin or last interaction of the photons along the z-axis and Table 4.1 resumes the relative contribution of each accelerator head component for the 10×10 cm^2 at the

scoring plane.

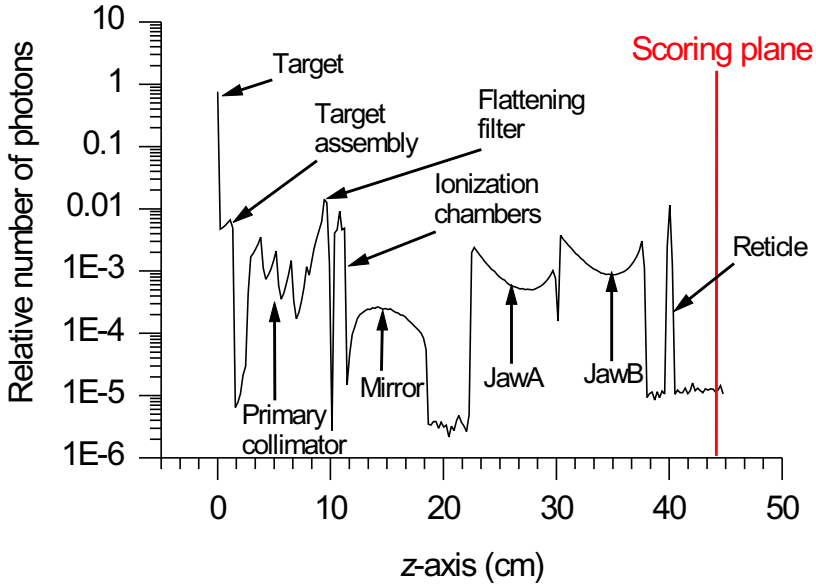

Figure 4.8: Point of origin or last interaction along the z-axis of the photons reaching the scoring plane for a 10×10 cm^2 field size.

Component	Relative intensity (%)	Average energy (MeV)	Average polar angle (degrees)
Target	75.27	1.8710 ± 0.0005	2.101 ± 0.002
Target Assembly	3.36	0.8239 ± 0.0013	1.9552 ± 0.0003
Primary Collimator	2.81	1.310 ± 0.0014	3.903 ± 0.004
Flattening Filter	4.48	1.1333 ± 0.0017	3.890 ± 0.004
Ionization Chambers	2.70	1.033 ± 0.0020	5.468 ± 0.006
Mirror	0.56	1.0912 ± 0.0043	7.398 ± 0.017
JawA	3.09	1.491 ± 0.0016	12.199 ± 0.017
JawB	5.21	1.292 ± 0.0012	18.089 ± 0.022
Reticle	1.51	0.7880 ± 0.0019	25.922 ± 0.045
Air	0.09	0.9031 ± 0.0091	17.859 ± 0.232
Total photons	99.08	1.6990 ± 0.0004	2.916 ± 0.001
Electrons	0.92	1.321 ± 0.0070	23.456 ± 0.112

Table 4.1: Relative contributions of the accelerator head components for the 10×10 cm^2 radiation field. Average energy of particles coming from each component. All data are calculated at the scoring plane placed at 45 cm from the source.

As expected, most of the photons reaching the scoring plane came from the target. These photons constitute the primary radiation according to Ahnesjö nomenclature [AA99]. Particles from all other components represent about 25% of the total number of particles in the scoring plane and constitute in the same terminology the scatter radiation. According to the simulation, the photons coming from the air, the mirror and the reticle are almost negligible. Figure 4.9 shows the point of origin or last interaction of the photons in the yz-plane. The various components of the accelerator head are clearly identifiable. According to this figure, the photons coming from the flattening filter interact or are originated in the flattening filter as a whole. Also from Fig. 4.9, most of the photons coming from the jaws have suffered their last interaction or have been originated in the inner border of the jaws and especially near from their top. Figure 4.9 also shows clearly the function of the primary collimator: first collimation of the radiation beam. It has to be noticed that jawB contributes more than jawA. This is of course due to the fact that some particles originated in jawA are absorbed in jawB.

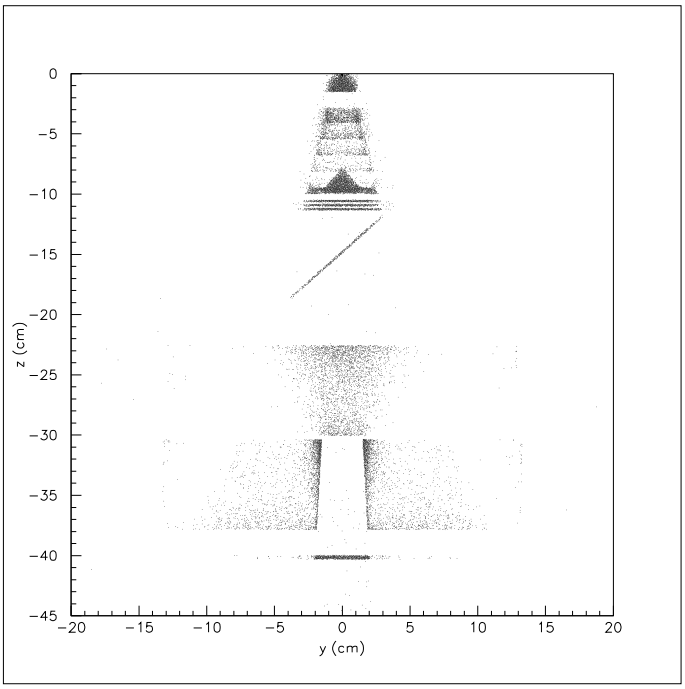

Figure 4.9: Point of origin or last interaction in the yz-plane of the photons reaching the scoring plane for a 10×10 cm^2 field size.

Although the geometry does not present a cylindrical symmetry due to the jaws, we will calculate radial distributions. Only particles inside a radius equal to 5 cm in the scoring plane will be analyzed. This value is very conservative since the distance in

the scoring plane between the center and a corner of 10×10 cm^2 field size (defined at isocenter) is less than 3.2 cm. Also, in this disk, more than 93% of the particles recorded in the PSD are present. Figure 4.10 shows particles radial distributions for each component.

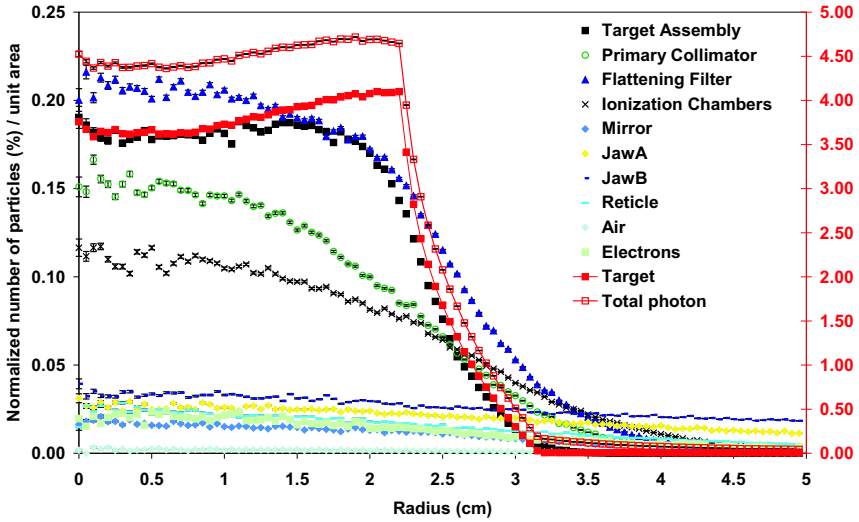

Figure 4.10: Radial distributions of particles at the scoring plane for each accelerator head component. Results are normalized to the total number of particles per unit of area. The right scale is applied to the target component and to the total number of particles.

Some authors found that, for a Siemens accelerator and a 10×10 cm^2 field size, *i)* the jaws contribution is negligible and *ii)* the flattening filter is the second most important source of particles [CCG94, DJK$^+$00], which seem to be in contradiction with results presented in Table 4.1. If we define a circular light field which almost represents the 10×10 cm^2 field size at isocenter, the radius of this light field in the scoring plane is 2.2 cm. Thus, if we just take into account the photons present in the light field (particles inside a radius $\leq$ 2.2 cm in Fig. 4.10), we would see that the jaws contribution represents a small fraction of the total of the particles reaching the scoring plane, which is in agreement with the cited later studies. According to the results also presented in Fig. 4.10, in the light field, the photons coming from the flattening filter are the second main source of particles followed by the photons coming from target assembly, the primary collimator and the ionization chambers respectively (in most of the studies, the target assembly is not modelled or is included in the target component). All these results are also in agreement with the previous cited studies. The effect of the flattening filter is perfectly visible in the shape of the curve representing the total number of particles in

Fig. 4.10: as the radius increases, more particles can reach the scoring plane. Finally, Fig. 4.10 shows that outside the light field, the jaws contribution becomes more important and predominant for radius > 3.6 cm.

Energy spectra were calculated for all the particles coming from each accelerator head component. The results of such calculations are presented in Fig. 4.11. Values of average energy are also presented in Table 4.1. The average energy of all the photons in the scoring plane for a 10×10 cm^2 field size is 1.6990 ± 0.0004 MeV which is close to the value calculated by Rodrigues [Rod02] for our accelerator. He calculated a value equal to 1.7832 ± 0.0008 MeV. The small difference between the two values comes from the different incident electron source models used in both simulations and the use of two different MC codes.

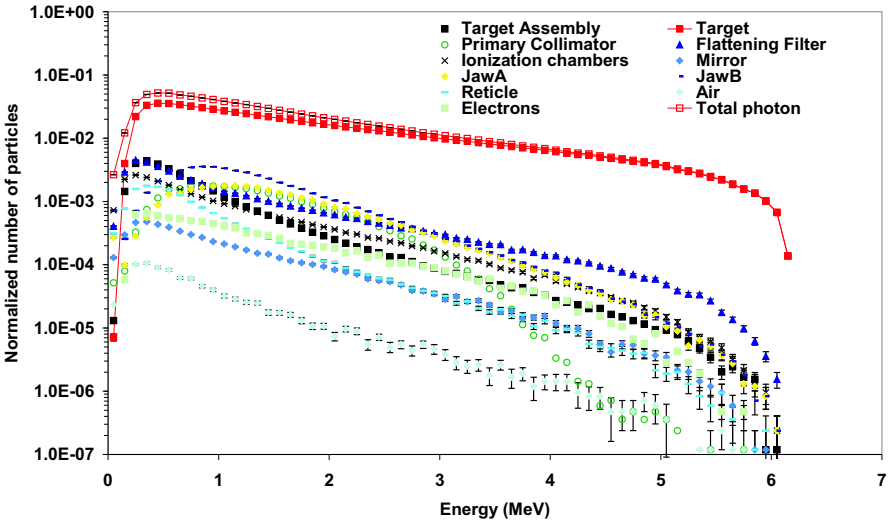

Figure 4.11: Calculated energy spectra at the scoring plane for particles coming from each accelerator head component. Results were normalized to the total number of particles in the scoring plane.

Figure 4.12 shows the radial average energy of the particles at the scoring plane for the components that contribute more in the light field. The decrease of the average energy as the radius increases is small in the light field. For the target component, this decrease is lower than 0.15 MeV between radius equal 0 cm and radius equal 3.1 cm. This decrease can be explained by the presence of the flattening filter. Outside the light field, the radial average energy of the photons coming from the target increases abruptly. In this region, photons with high energy are able to go through the jaws whereas the

photons with low energies are absorbed by these structures. Outside the light field, the average energy for all the photons increases and becomes closer to the values for photons from the jaws because these components are predominant as the radius increases.

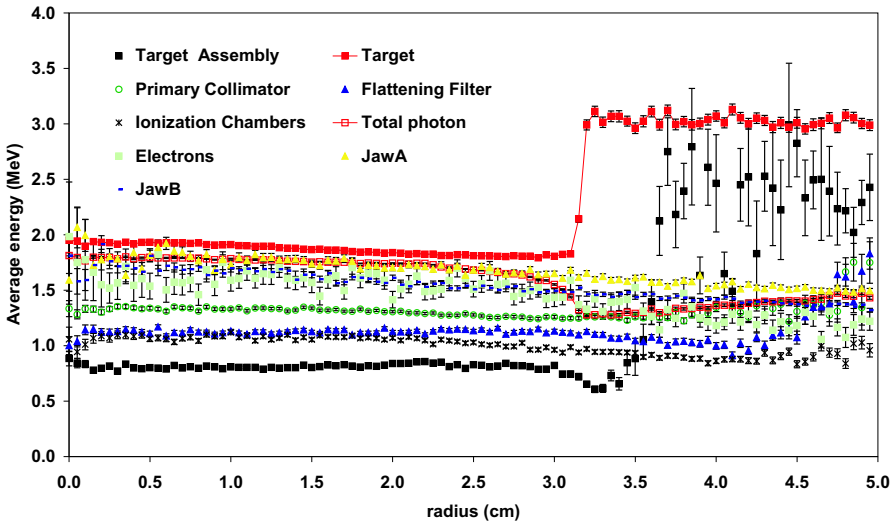

Figure 4.12: Radial average energy distributions for particles coming from the most important accelerator head components.

If we calculate the radial energy fluence which represents the amount of the transported energy (see Fig 4.13), the effect of the flattening filter is perfectly explained: for the target component, photons with low energy are absorbed in the center of the flattening filter but as the radius increases, these photons can pass through the flattening filter increasing the photon fluence but decreasing its average energy. The flattening filter is designed in such a way that the dose profile in a reference field at a reference depth in water must be homogeneous. For the other components, there is no compensation since the number of particles of each component decreases (see Fig. 4.10) and the average energy also decreases or remains almost constant (see Fig. 4.11).

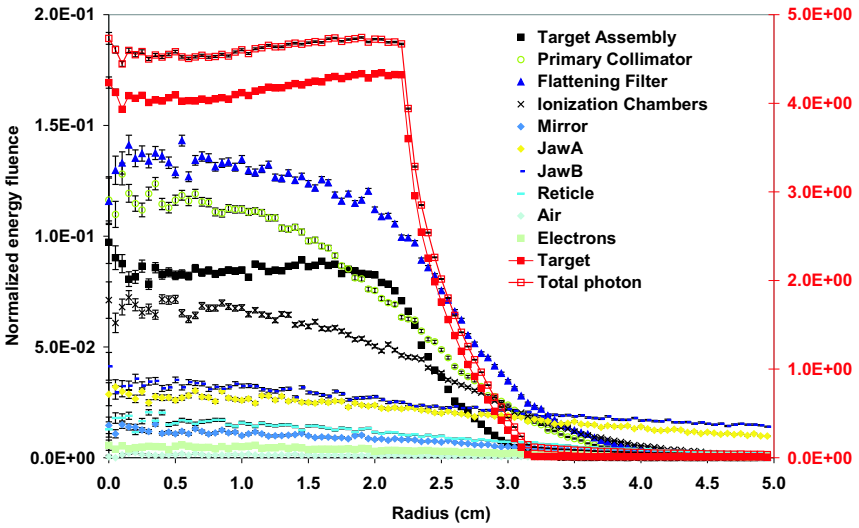

Figure 4.13: Radial energy fluence distributions for particles coming from the accelerator head components. Results are normalized to the total energy fluence.

The polar angle of a particle is defined as the angle of the trajectory of the particle with the z-axis. Figure 4.14 shows the distributions of the particles according to their angles in the scoring plane and Table 4.1 indicates the average angle of the particles at the scoring plane coming from each component. Figure 4.14 shows that most of the photons with small polar angles (<3.5 degrees) come from the target. Between 5 and 15 degrees, most of the photons are coming from the primary collimator, the flattening filter and the ionization chambers. For polar angles from 15 to 30 degrees, most of the photons come from the jaws. Finally, most of the photons with the higher polar angle (>40 degrees) are coming from the reticle. The total photon average angle presented in Table 4.1 is very close from the geometrical divergence angle calculated for this accelerator which is $2.86° \pm 0.5°$ for the 10×10 cm^2 field size. The spread of the distributions is linked to a defined component, more precisely with the distance between that component and the scoring plane. As this distance increases, the spread decreases. This is simply due to the maximum solid angle between a component and the scoring plane. For all the components, the number of particles increases until reaching a maximum value and then decreases. For photons, the polar angle at the scoring plane is of course the angle of emission at a defined component assuming straight line propagation. If we consider at first approximation that the photons are emitted from a point source defining a component, it is obvious that as the number of photons increases with the radius at the scoring plane, the number of photons must increase as the polar angle increases. The polar angle of maximum number of particles for each component is di-

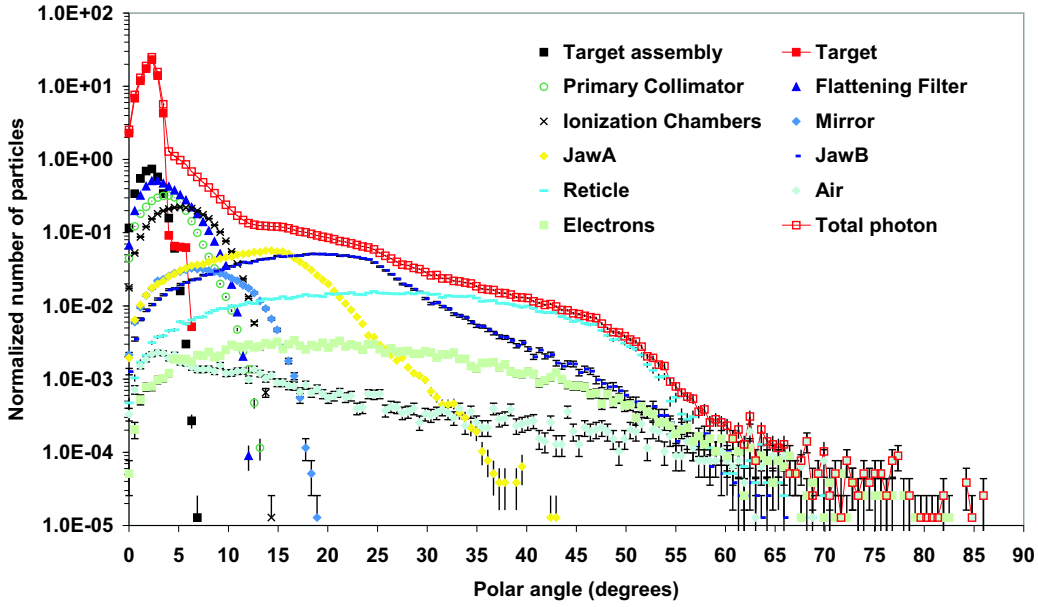

Figure 4.14: Angle distributions for particles in the scoring plane coming from the various accelerator head components. Results were normalized to the total number of particles in the scoring plane inside a radius ≤ 5 cm.

rectly linked to the jaws aperture. That is, a photon from one component with an angle of emission whose trajectory intercepts the jaws can be absorbed. In this study, we consider that the light field has a radius equal to 2.2 cm. Outside this region, particles emitted from the components above the jaws are most of them absorbed by the jaws. If we consider that photons are emitted from a single point corresponding to a defined component, a simple calculus gives us the maximum allowed emission angle for these photons without intercepting the jaws. For example, for the target component, the distance between the scoring plane and the point source is 45 cm, then the maximum polar angle is $\theta_{max} = \text{atan}(2.2/45) = 2.8°$. In Fig. 4.14, the value of the polar angle of maximum number of photons is 2.3°, very close to 2.8° which is calculated with the simple point source model. That is, most of the photons with angle of emission larger than 2.3° are absorbed by the jaws and then decreases the number of photons reaching the scoring plane. For photons from the primary collimator, the flattening filter and the ionizations chambers, the value of θ_{max} calculated with the point source model are closed to the values presented in Fig. 4.14. For the other components, there are larger differences because the source point approximation is no longer valid but the rational is the same.

The average polar angle at the scoring plane was calculated for photons and electrons coming from accelerator head components (see Fig. 4.15). For all components, the

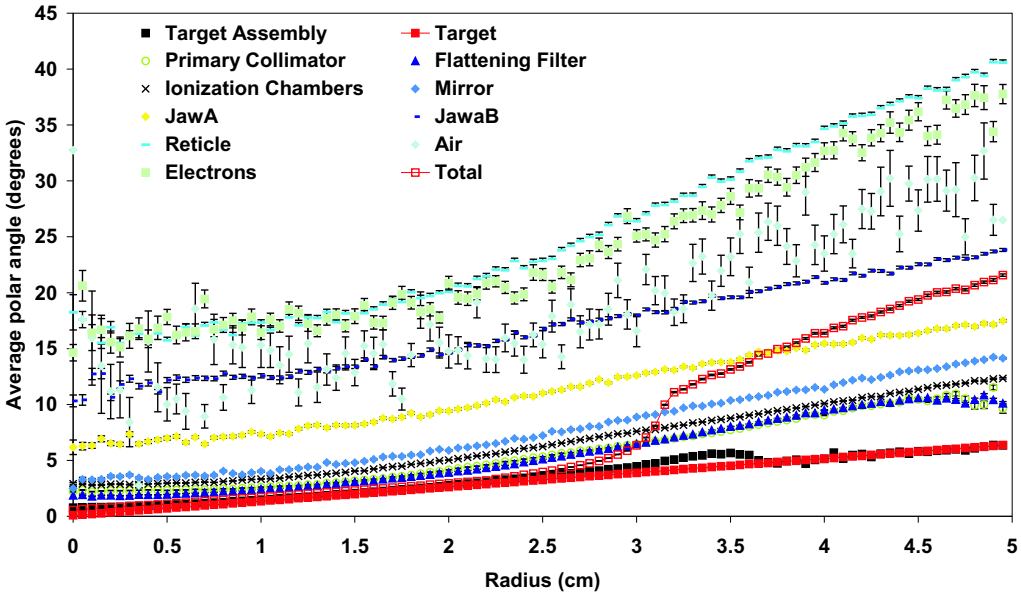

Figure 4.15: Radial average angle for particles coming from the accelerator head components.

average polar angle increases as the radius increases. This is of course essentially due to geometrical reasons. Figure 4.15 also shows that for a given position in the scoring plane, the average polar angle of the photons increases according to the component where the photon was emitted. In fact, the distance between the scoring plane and a point of origin (or last interaction) in a component defines a solid angle which becomes smaller as the component is located at larger distances from the scoring plane. This phenomena is also shown in Fig. 4.14 where the maximum photon polar angle increases as the distance between the components and the scoring plane decreases and, in Table 4.1 where also the average angle increases as the distance between the components and the scoring plane decreases. The discontinuity in the curve representing the radial average angle of all the photons in Fig. 4.14 is explained by the fact that inside the light field most of the photons are coming from the target. Outside the light field, the jaws become predominant explaining why the values of the average polar angle for all the photons are close to the values representing the photons from the jaws.

Finally, Fig. 4.16 shows how average energy of the particles varies when the polar angle increases. The behavior of the different curves cannot just be explained by the

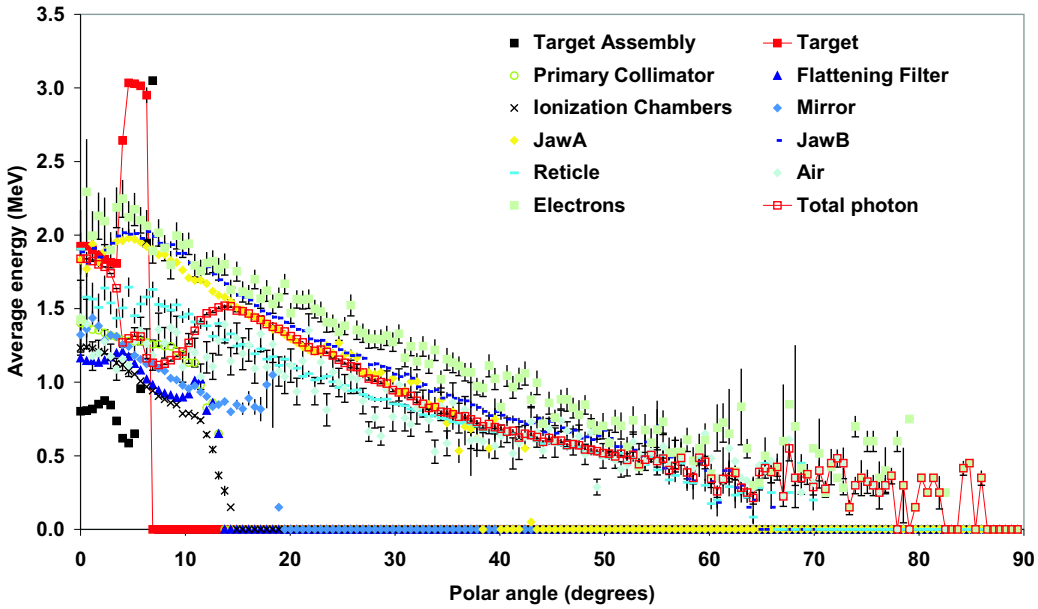

Figure 4.16: Radial average energy vs. polar angle for particles coming from the accelerator head components.

physical process occurring in the various components. In fact, according to the present processes (mostly bremsstrahlung and Compton processes), it is expected that as the polar angle increases, the average photon energy decreases. It should be remembered that photons that reach the scoring plane are essentially primary photons from the target component and secondary photons from the other components produced initially by processes involving the primary photons. All these photons passed through the flattening filter. It means that the energy of photons reaching the scoring plane not only depends on the angle of emission, but also depends on the thickness crossed at the flattening filter. It must also be pointed out that the thickness crossed at the flattening filter depends also on the point of emission of the photon. For example, for the same angle of emission for photons coming from the primary collimator, the thickness of crossed flattening filter depends strongly on the point of origin. That is, the relation between the angle and energy at the scoring plane is complex and depends basically of the type of interaction at origin, the point of origin and the thickness of crossed flattening filter. This can explain for example why for the small polar angles, the average energy does not decrease. This rational is also valid for photons coming from components below the flattening filter because as explained above, these particles were

originally produced by primary particles. In the simple case of photons coming from the target, it can be considered that these photons are emitted from a point source. According to the results presented in Fig. 4.4, most of these photons are produced by bremsstrahlung effect. The energy of these photons is strongly dependent on their angle of emission [KM59]: the larger is the angle of emission, the lower is the energy of the emitted photon. These photons cross the flattening filter. Due to the shape of this component, photons with larger angle of emission (from the point source) cross a smaller thickness of the flattening filter, being so less absorbed and decreasing the average energy. The two effects (energy-angle dependence in bremsstrahlung process and shape of the flattening filter) combine in such a way that, the average energy of the photons coming from the target decreases as the angle increases as shown in Fig. 4.16. The effect of the point of origin is negligible since the photon source can be considered a point. The abrupt increase of the energy of photons coming from the target and the target components is due to high energy photons with large angles of emission crossing the jaws without being absorbed. Only particles inside a radius $\leq$ 5 cm were taken into account, this explains the abrupt decrease in the curves for the target and target assembly.

4.3 Phase Space Data validation

4.3.1 Dosimetric methods

In order to validate the PSD, the common approach is to compare the calculated dose distributions for each additional collimator with the results obtained from measurements [LSM99]. There are several dosimetric methodologies, supports, that may be used to perform measurements for narrow photon beams. Detectors available at IPOFG-CROC, S.A., for this kind of measurements are ionization chambers, film and diode. Other systems such as diamond detector, MOSFETs detectors, TLDs and polymer gels coupled with magnetic resonance imaging have been used by other authors [RF95, HHB96, WAN$^+$00, HFL$^+$02, FCC$^+$98, PSA$^+$01].

There are basically two types of ionizations chambers: the parallel-plate and the thimble chambers. The PTW Markus parallel plate ionization chamber was designed for conventional radiotherapy dosimetry but can be used for radiosurgery dosimetry since its sensitive volume is small (0.05 cm^3, diameter 5 mm). Two thimble chambers are

available at IPOFG-CROC, S.A., for narrow photon beam dosimetry: the PTW 0.125 cm^3 thimble chamber type 31002 and the PTW PinPoint thimble chamber type 31006. The last one was specially developed for dosimetry of small fields. It is a waterproof 0.015 cm^3 cylindrical air chamber with a central electrode made of steel. The wall consists of PMMA covered with a graphite layer. The sensitive volume is 2 mm in diameter and 5 mm in length. Two orientations are possible: one with the chamber axis parallel to the beam axis (vertical) and one with the chamber axis perpendicular to the beam axis (horizontal). In the case of the 0.125 cm^3 chamber, it is recommended to use this chamber with its longitudinal axis parallel to the beam [AAP95].

The great advantage of the film dosimetry is its high spatial resolution. Unfortunately, its practical implementation is not an easy task. In fact, several parameters can influence the image quality and thus the measured results. The most important of these parameters is the film development process. The dose is obtained from the film using the calibration curve which transforms the optical density (OD) into absorbed dose in water. This calibration curve is very dependent of the characteristics of the development (temperature, chemical compositions, development time) [Nun95]. The films used at IPOFG-CROC, S.A., are the Kodak X-Omat V. To measure the optical density, an high intensity spot light, derived from a He-Ne laser, is scanned across the film plane as the film is moved perpendicular to the laser scan Lumiscan 50. The obtained spatial accuracy is 250 μm.

Finally, the PTW diode type 60008 (area of 1 mm^2 and thickness of 2.5 μm) was used to obtain basic dosimetric data. This detector is a single p-type Si diode. Although diodes suffer principally from energy, angular and dose rate dependence [VM94], their high spatial resolution and reproducibility turn them suitable for dosimetry of narrow photon beams.

The diode, PinPoint (vertical and horizontal orientations) and Markus detectors are used to obtained $DDCs$ and are connected to the motorized PTW MP3 40×40×50 cm^3 water phantom. All the measurements are performed for a $SSD = 100$ cm. For OAR, measurements are performed in MP3 water phantom using the diode detector, PinPoint chamber (in its two orientations). Films are also used and placed perpendicular to the beam axis, in a water equivalent phantom (SOLID WATER^{TM} phantom from RMI). The experimental setup is $SSD = 95$ cm and depth of measurement 5

cm. This is the setup used for basic dosimetric data measurement for STP3. Finally, OFs are measured in the MP3 water phantom using the Markus and the 0.125 cm^3 chambers linked to the PTW SN4 electrometer, the diode and the PinPoint detectors linked to the PTW Unidos electrometer. The PinPoint chamber was irradiated in its two possible orientations and the 0.125 cm^3 with its longitudinal axis parallel to the beam central axis. Measurements with the detectors in the MP3 water phantom were performed for a $SSD = 100$ cm and at 50 mm depth and values were reported to d_{max} using the DDC for each detector. Film, at different d_{max} in the solid water phantom for each additional collimator and the reference 10×10 cm^2 field, are also used to measure OF.

4.3.2 Patient-dependent simulation

For each additional collimator, the simulation of block 2 (see Fig. 4.1 (b)) was performed. In fact, two simulations were done for each additional collimator, one for calculating the depth dose distribution, and one for calculating the off axis dose distribution. In MCNP4C, the energy deposited in a cell is scored using the modified pulse height tally (*F8). Jeraj *et al.* [JKO99] have shown that, if the number of scoring cells increases, the calculation running time necessary to achieve a good accuracy dramatically increases keeping the default dose algorithm of MCNP code unchanged. They also have shown that this increase starts with a number of scoring cells particulary low (100 scoring cells). This is a great limitation if we want to calculate dose distributions in small cells in a large region of interest like a water phantom. In this study, we want to validate the PSD through comparisons between calculated and measured dose distributions. We choose that these dose distributions are, for each additional collimator, a DDC and an OAR. That is, it is just necessary to score dose in the beam central axis (for DDC) and in the x- or y-axis at various depths (for OAR). In order to keep the number of scoring cells below 100 and consequently not increasing dramatically the running time, it was decided to perform two different simulations.

In each simulation, specific cells to score dose must be built. It is clear that the spatial accuracy will be linked to the cell size. However, the calculation time needed to obtain results with a good accuracy can becomes very long. Another limitation in MCNP4C was found by Schaart *et al.* [SJZ+02]. They have shown that if the *F8 tally is used, a high spatial resolution cannot be achieved without compromising the accu-

racy of the calculation. They have shown that the repeated interruption of electron tracks at cell boundaries may significantly affect the calculated dose distribution if the voxel dimensions are smaller than about 10% of the electron range. Thus, the dimensions of the cells must be chosen according to a balance between the required spatial, the dose accuracy and the running time. The critical dimension of such narrow photon beams is obviously the diameter of the field. It is why, the dimension of the cells in the x-y plane must be chosen as small as possible to achieve the required spatial accuracy particulary for off axis dose calculations. For depth dose calculations, 80 scoring cells are placed along the beam central axis and their dimensions are: diameter = 1.5 mm, height = 5 mm (the volume of each cell is 0.009 cm^3 which is lower than the volume of the PinPoint chamber, 0.015 cm^3). Due to the possible poor statistics and because the problem presents a cylindrical symmetry, 39 cells corresponding to circular annuli are used for off axis dose calculations. These annuli are built in a such way that the distance between the internal and external radii is equal to 1 mm and the height equal to 5 mm (the cell in the beam central axis is a cylinder of 0.5 mm diameter and 5 mm height). The same setups for depth dose and OAR calculations defined earlier for measurements are used. Figures 4.17 (a) and (b) show the two different cell geometry configurations.

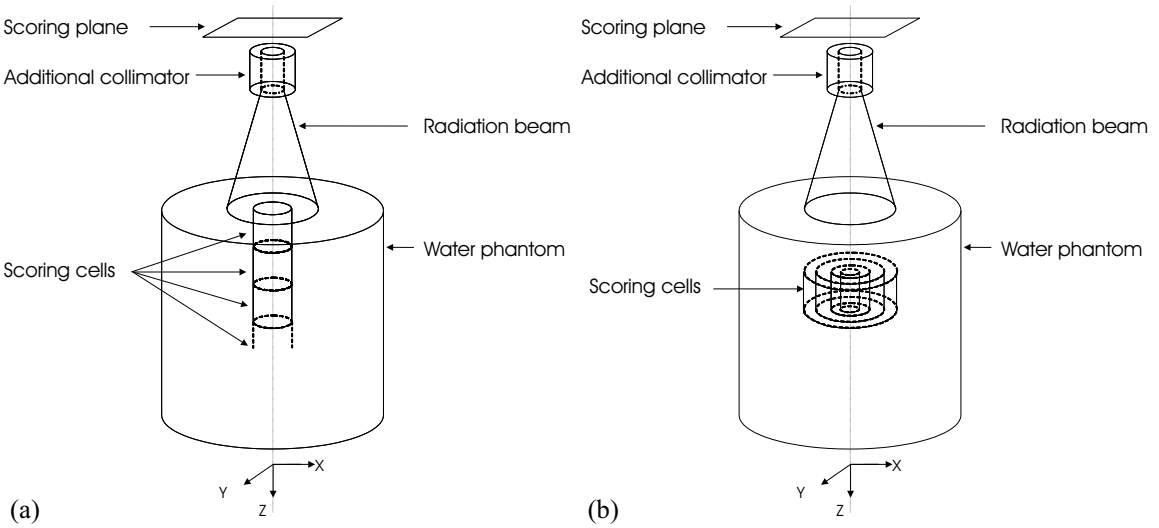

Figure 4.17: Simplified schematic view of the scoring cells for two different setups: (a) depth dose calculation, (b) off-axis dose calculation. The different geometrical components are not properly scaled.

In order to improve the statistics, the particle splitting mechanism was used in the

patient-dependent simulation block. In order to optimize the calculation running time, the importance in the cell is different depending if the cell will be used for scoring dose or not. Adjusting the importance of the cell can be very long time consuming particulary if the geometry is complex. A thumb rule is to try to keep the population of tracks travelling in the desired direction more or less constant [Bri00]. Splitting particles is of course directly linked to the associated error of the desired scored quantity. This error is roughly reduced by a factor of 2 when the number of particles is multiplied by a factor of 4. Thus, determining the level of error which gives reliable results is fundamental. Simulations with various combinations of cell importance were performed. In MCNP4C simulations, it is recommended to keep the ratio of adjacent importances small because a larger ratio places a greater burden on reliable sampling. The recommended value is a factor 4 in the importance ratio of adjacent cells. We found that the combination of cell importance for photons between importance=4 in the cell where particles are sampled from the PSD, and a value of 1024 in the scoring cells, enables the convergence of the results with associated error lower than 1.5% for depth and off axis dose calculations. For electrons, the value of importance has been kept equal to 1 (0 for void regions), because no significant improvement in the accuracy of the results was found with an associated substantial increase in the calculation running time.

4.3.3 Validation criteria

The quantitative evaluation of the calculated dose distributions is performed by direct comparison with measured dose distributions. In the past few years, with the increase of the use of CT-based treatment planning systems (TPSs), a great effort has been made to try to develop some quality assurance procedures to test the results given by the different TPSs [ICR87, BCL88, FDH$^+$98]. These procedures can be applied to results given by MC codes since they can also constitute a class of TPS. Van Dyke *et al.* [VBC$^+$93] have subdivided the dose distribution comparisons into regions of high and low dose gradients, each with a different acceptance criterion. In the low gradient regions, calculated and measured dose are directly compared using the dose-difference concept, whereas in the high gradient region, they used the concept of *distance-to-agreement* (DTA) to determine the acceptability of dose calculations. The DTA is the distance between a measured data point and the nearest point in the calculated dose distribution that exhibits the same dose. Several authors have suggested values for the acceptability criteria in low and high dose gradient regions [VBC$^+$93, FDH$^+$98, VWM01]. Most of them agree that, the dose-difference in the

low gradient region of high dose region cannot exceed 5%. This value depends on the complexity of the geometry (homogeneous, wedged, inhomogeneity, asymmetry, etc...) and also depends on the location of the point dose (central axis, outside beam edges, buildup region, etc...). In our case (radiosurgery application), the tolerance value of dose-difference $\triangle D_M$=2% is commonly used [DMH$^+$03]. In high gradient regions, values of DTA also differ according to the complexity of the geometry and the point dose location. For radiosurgery applications, the recommended value of DTA is $\triangle d_M$=1 mm [AAP95]. In the buildup region, because of the measurement difficulties, we will choose $\triangle d_M$=2 mm and $\triangle D_M$=10% [VWM01].

The evaluation images displaying the dose difference and DTA are complementary in determining the acceptability of dose calculation versus dose measurement. In order to merge both evaluation criteria into a single image, a composite analysis used by Harms *et al.* [HLW$^+$98] has been developed and uses a pass-fail criterion of both dose-difference and DTA. However, this method does not provide any quantitative measure of the magnitude of disagreement. Low *et al.* [LHM$^+$98] developed a method that simultaneously incorporate the dose and distance criteria. This method provides a numerical quality index: the gamma value (γ), that serves as the measure of disagreement in the regions that fail the acceptance criteria and indicates the calculation quality in the regions that pass.

In this section, we will briefly present the gamma method developed by Low *et al.* [LHM$^+$98]. In the gamma method, two dose distributions are compared: one defines the reference information $D_m(r)$ and the other is the queried for evaluation $D_c(r)$. The dose-difference criterion is $\triangle D_M$, and the DTA criterion is $\triangle d_M$. Figure 4.18 shows the representation of the method for determining an acceptance criterion that simultaneously considers the dose-difference and DTA.

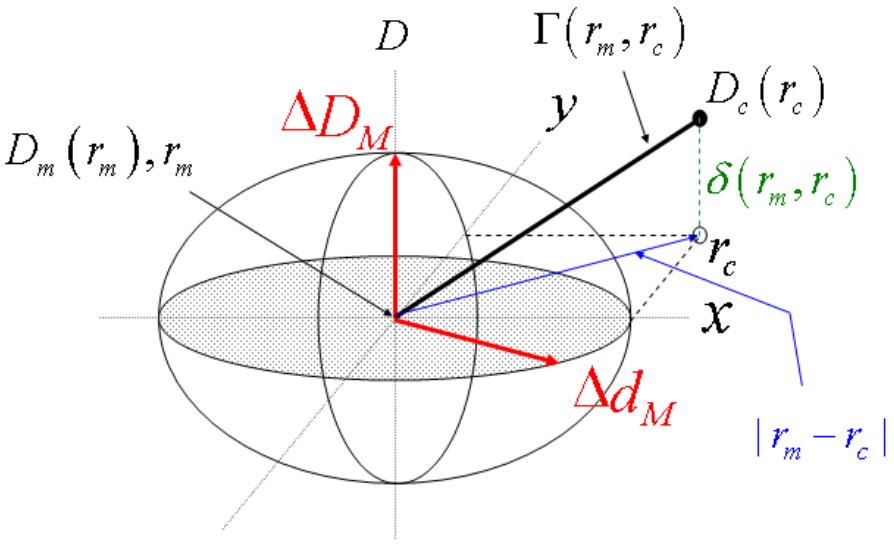

Figure 4.18: Geometric representation of dose distribution evaluation criterion using the combined ellipsoidal dose-difference and distance-to-agreement test.

An ellipsoid is selected as the surface representing the acceptance criterion. The equation defining the surface is:

$$1 = \sqrt{\frac{r^2(r_m, r)}{\triangle d_M^2} + \frac{\delta^2(r_m, r)}{\triangle D_M^2}}, \tag{4.7}$$

where

$$r(r_m, r) = |r - r_m|, \tag{4.8}$$

and

$$\delta(r_m, r) = D(r) - D_m(r_m) \tag{4.9}$$

is the dose difference at the position r_m. If any portion of the $D_c(r_c)$ surface intersects the ellipsoid defined in Eq. 4.7, the calculation passes at r_m. Defining the acceptance criteria not just along the δ-axis and in the $r_c - r_m$ plane allows for a more general comparison between calculation and measurement than does the composite evaluation developed by Harms *et al.* [HLW+98]. The quantity on the right-hand side of Eq. 4.7 is defined as the *quality index* γ at each point in the evaluation plane $r_c - r_m$ for the

measurement point r_m. That is:

$$\gamma(r_m) = min\{\Gamma(r_m, r_c)\}\forall\{r_c\}, \tag{4.10}$$

where

$$\Gamma(r_m, r_c) = \sqrt{\frac{r^2(r_m, r_c)}{\triangle d_M^2} + \frac{\delta^2(r_m, r_c)}{\triangle D_M^2}}, \tag{4.11}$$

$$r(r_m, r_c) = |r_c - r_m|, \tag{4.12}$$

and

$$\delta(r_m, r_c) = D_c(r_c) - D_m(r_m) \tag{4.13}$$

is the difference between dose value on the calculated and measured dose distributions, respectively. The pass-fail criteria therefore become:

$$\gamma(r_m) \leqslant 1, \text{ calculation passes,}$$

$$\gamma(r_m) > 1, \text{ calculation fails.} \tag{4.14}$$

Althouth the gamma method is a powerful tool for comparison of dose distributions, practical considerations must be done. The theory developed by Low *et al.* [LHM$^+$98] is directly applicable to continuous functions. In clinical cases, the dose distributions are discrete with possible different grid sizes for the two distributions (calculated and measured). Depuydt *et al.* [DEH02] have shown that $\gamma(r_m)$ remains dependent on the discretisation of the dose distributions and in most cases will not be the analytical minimum one would obtain if both dose distributions were presented as continuous functions. They have also pointed out that in regions of high dose gradients, even with a highly intensified calculation grid, gamma indices can be unjustly concluded to be larger than one. This is illustrated by Figs. 4.19 (a) and (b): calculation passes in (a) because calculated points are within the ellipsoid, calculation unjustly fails in (b) because no calculated points are within the ellipsoid. It is clear that the calculation does not fail in case (b) because the line that passes through the two closest calculated points from the reference point intercepts the ellipsoid of tolerances. To overcome this problem, a linear interpolation is performed between two calculated points. Thus, the interpolated points are compared with the reference point (see Fig. 4.19 (c)).

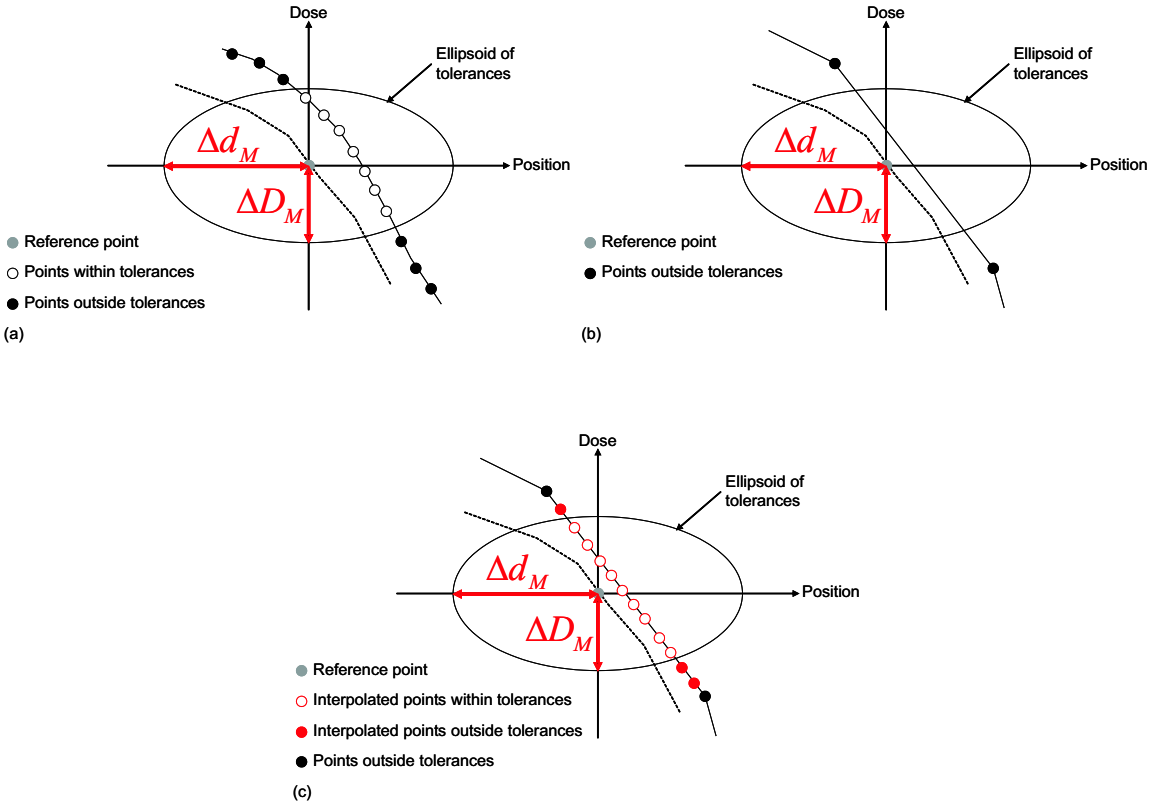

Figure 4.19: Geometric representation, for one-dimensional case, of the gamma criterion for discrete dose distributions. (a) Some calculated points are within the ellipsoid of tolerances. (b) No calculated points in the ellipsoid of tolerances. (c) Representation of interpolated points between two calculated points that are not within the ellipsoid of tolerances.

4.3.4 Percent depth dose

The IAEA TR398 protocol [IAE00] has been followed to setup the effective point of measurement [1] for the 0.125 cm^3 chamber with its axis perpendicular to the beam. The effective point of measurement of the PinPoint chamber in its two orientations has been found comparing measured PDD for a 10×10 cm^2 square field with PDD obtained with the 0.125 cm^3 chamber as reference (see Fig. 4.20). $PDDs$ were calculated

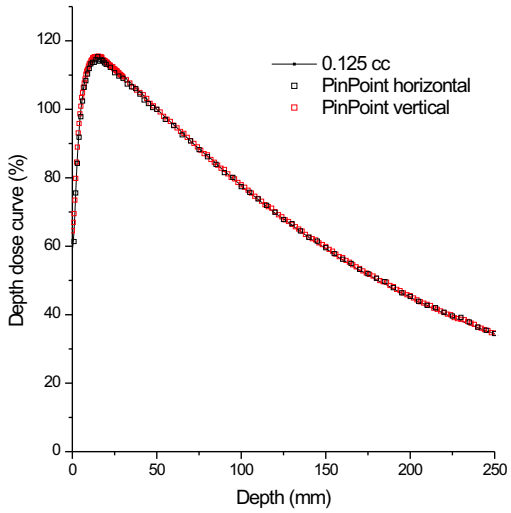

Figure 4.20: Measured percent depth dose for the 10×10 cm^2 square field. Results are normalized at 50 mm depth.

for all the additional collimators. Table 4.2 resumes the calculation times needed in a PC Pentium III (800 MHz) with 256 Mb of RAM to achieve a calculation error level lower than 1.5% in each scoring cell. Figures 4.21 (a)-(i) show the calculated $PDDs$

Additional collimator	Col5	Col7	Col9	Col11	Col13	Col15	Col17	Col20	Col23
CPU Time (hour)	15.9	20.0	24.1	29.5	36.0	43.5	52.2	67.3	84.9

Table 4.2: Calculation time needed to achieve an uncertainty of 1.5% in all calculated points for depth dose simulations.

and compare them with the $PDDs$ measured with the different detectors. In the same graph, the results of the γ-index quality criterion, taking into account as reference the results obtained by the diode, are also presented. All $DDCs$ are normalized at 50 mm depth.

[1] The effective point of measurement is used to correct the reading of the ionization chamber due to its non-water equivalence.

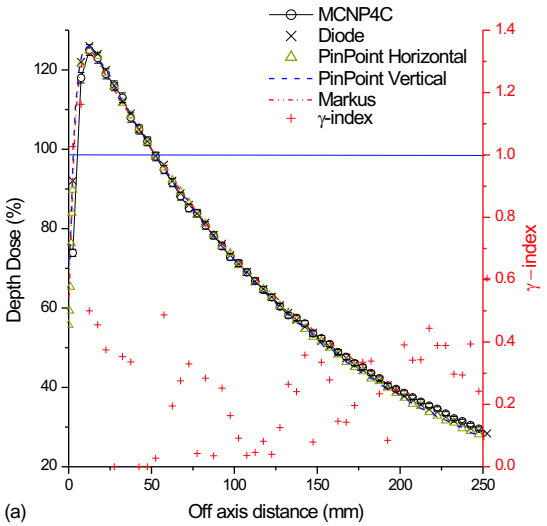
MCNP4C
Diode
PinPoint Horizontal
PinPoint Vertical
Markus
γ-index
Depth Dose (%)
γ−index
Off axis distance (mm)
(a)

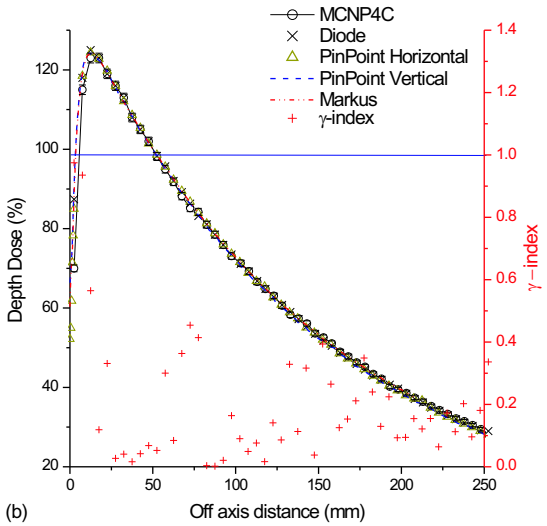
MCNP4C
Diode
PinPoint Horizontal
PinPoint Vertical
Markus
γ-index
Depth Dose (%)
γ−index
Off axis distance (mm)
(b)

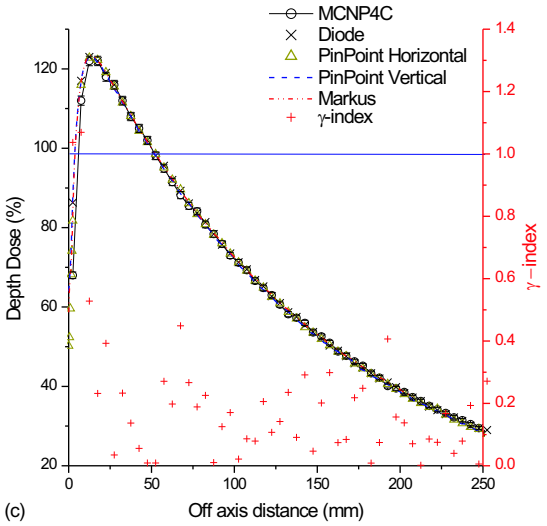
MCNP4C
Diode
PinPoint Horizontal
PinPoint Vertical
Markus
γ-index
Depth Dose (%)
γ−index
Off axis distance (mm)
(c)

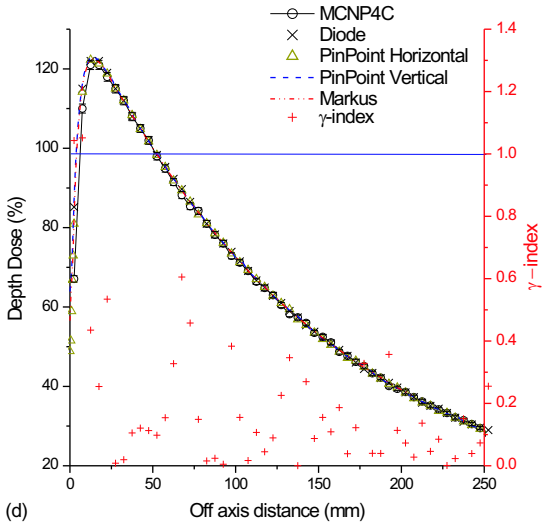
MCNP4C
Diode
PinPoint Horizontal
PinPoint Vertical
Markus
γ-index
Depth Dose (%)
γ−index
Off axis distance (mm)
(d)

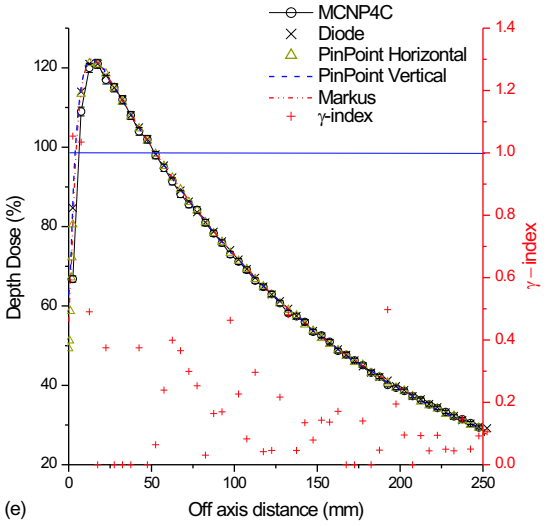
MCNP4C
Diode
PinPoint Horizontal
PinPoint Vertical
Markus
γ-index
Depth Dose (%)
γ−index
Off axis distance (mm)
(e)

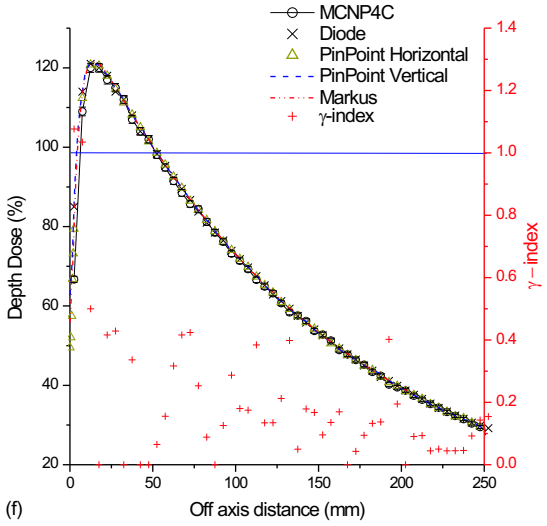
MCNP4C
Diode
PinPoint Horizontal
PinPoint Vertical
Markus
γ-index
Depth Dose (%)
γ−index
Off axis distance (mm)
(f)

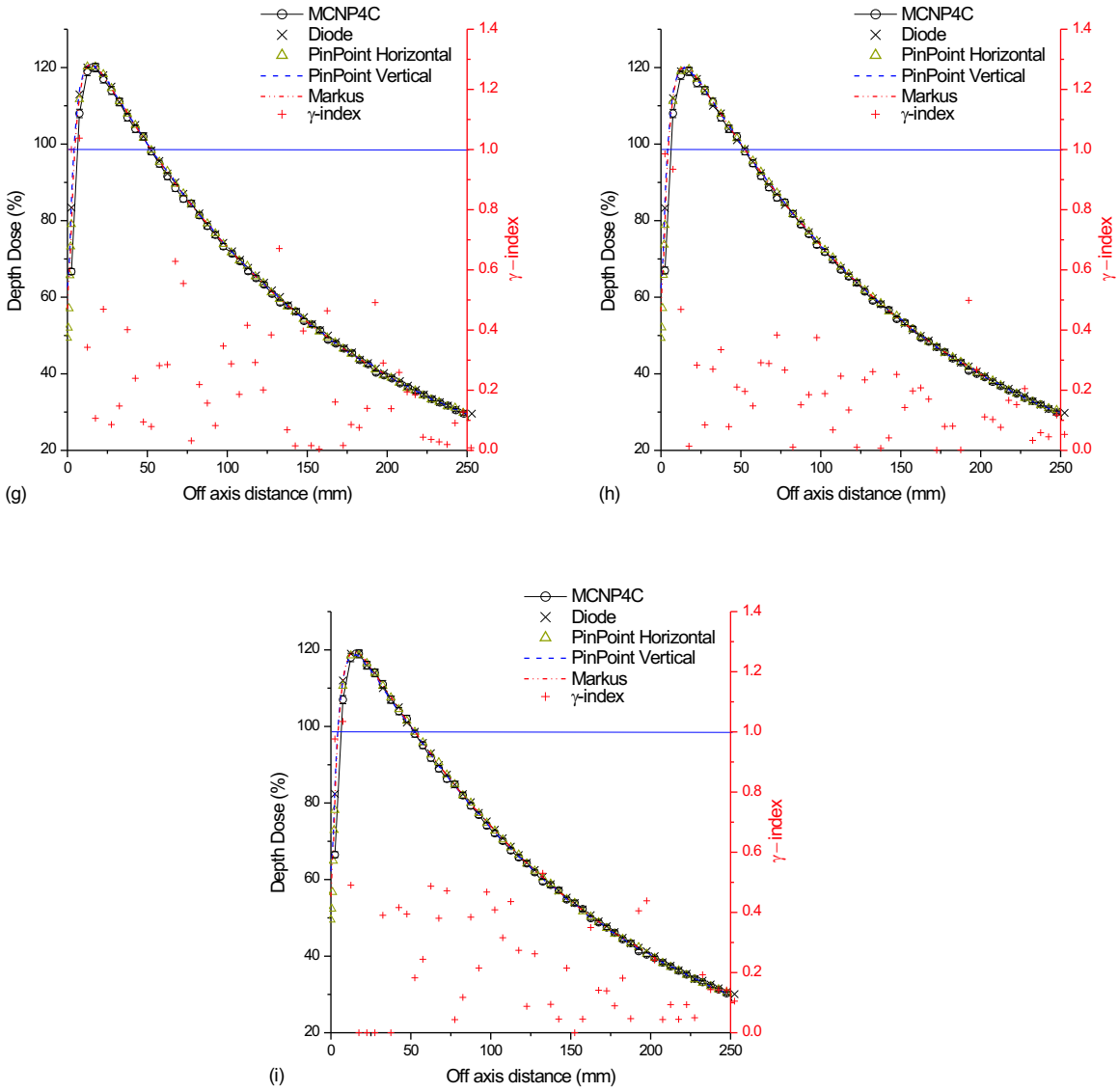

Figure 4.21: A comparison between calculated and measured percent depth dose (Source Surface Distance 100 cm). Each graphic represents the results for one additional collimator: (a) col5, (b) col7, (c) col9, (d) col11, (e) col 13, (f) col15, (g) col17, (h) col20, (i) col23. Results are normalized to value of dose at 50 mm depth for each additional collimator. The γ quality index is also plotted for each measurement point with the diode.

For depths higher than 10 mm, a good agreement between the calculated and measured, with the diode, $PDDs$ was found since the γ-index is always lower than 1. For the ionizations chambers, results show that, for the smallest additional collimators and at large depths, there is a tendency of over-response of the Markus detector and under-response of the PinPoint detector. Because the beams are divergent and PDD is defined as a ratio of dose measured at two different depths, the volume effect of the Markus chamber (more precisely the effect of the diameter) can explain the over-response. For the PinPoint chamber, the volume effect is not responsible of the under-response. It can be explained by the no water-equivalence of the PinPoint chamber for very small fields found by Haryanto *et al.* [HFL+02]. Despite these tendencies, for depths higher than 10 mm, results given by the PinPoint and Markus chambers can be considered in good agreement with calculations since γ-index of each detector is always lower than 1 even for the smallest additional collimators. Results also show that the PinPoint chamber can be used indifferently in its two orientations since the behavior of the curves remains unchanged for depths larger than d_{max}. For depths $\leqslant$ 10 mm, most of the γ-indexes for the diode are larger than 1. In the buildup, the dose gradient is very high and the size of the scoring cells along the z-axis can bias the calculated results. Although the diode detector is very suitable for measuring narrow photon beams dose, it overestimates the dose in the buildup region due to its high-Z component. It is well known that, due to non electron equilibrium condition in the buildup region, the used detectors are not able to give accurate results in this region; the detector of choice to measure surface dose is the extrapolation chamber [GK90].

In accordance with other authors [RHS+87, SP93], we found that d_{max} increases as the size of the additional collimator increases as shown in Fig. 4.22. As Sixel *et al.* [SP93] demonstrated, changes in d_{max} for small fields are essentially due to water phantom events and not changes induced by head scatter conditions. This effect is the opposite of the effect observed in conventional radiotherapy beams (field sizes $>$ 4×4 cm^2) where contributions of head scatter are much more important and produce a decrease in the depth of d_{max} as the field size increases [BL79, SP94]. In Chapter 5, this phenomena will be analyzed in more detail.

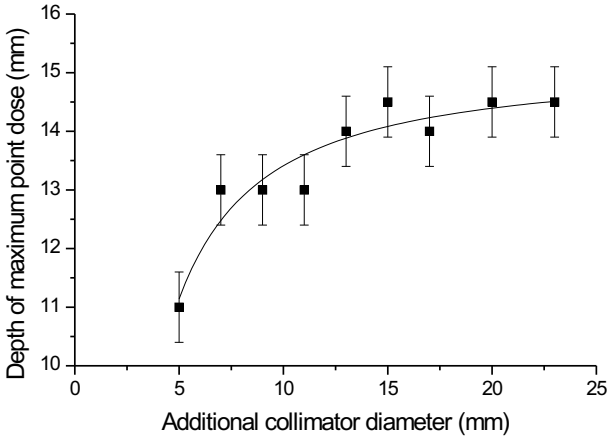

Figure 4.22: Measured depth of the maximum point dose d_{max} for each additional collimator. A trendline was added to show easier the shift of d_{max} as the size of the additional collimator increases.

4.3.5 Off-axis ratio

All the distributions are normalized to the maximum dose point at the depth of measurement or calculation. Normalization to the integral dose was not chosen because, in one hand, the current practice in clinical cases is to normalize the dose distributions to a single point or to an isodose and in the other hand, it is expected that the statistical uncertainties will be small enabling a good accuracy in the calculated results. Finally, the γ-index is a good indicator to show if data are well normalized or not. For example, for a normalization point chosen in a high dose region with a low dose gradient, if the γ-indexes of some the measured points (in this particular region) are greater than 1, that means the calculated points contain not negligible statistical fluctuations and are not accurate. Finally, Tab. 4.3 shows the running time of each simulation in order to reach an uncertainty lower than 1.5% in each calculated point.

According to the results presented in Figs. 4.23 (a)-(i), there are no significant differences between OAR measured with the PinPoint chamber in its two orientations. McKerracher *et al.* [MT99] have shown that the PinPoint chamber was not adequate to resolve accurately the dose in the penumbra which is confirmed by our results since the results of the PinPoint chambers are slightly different from results of the diode chamber in this region. This is of course due to the volume size effect of the PinPoint chamber compared to the diode. The film is better than the PinPoint chamber to resolve the dose in the penumbra but worst than the diode in this region. Identical result was found by McKerracher *et al.* [MT99]. Film overestimates the dose in the low-dose region outside

Additional collimator	Col5	Col7	Col9	Col11	Col13	Col15	Col17	Col20	Col23
CPU Time (hour)	16.7	20.4	25.3	31.4	38.9	47.7	57.1	75.1	95.5

Table 4.3: Calculation time needed to achieve an uncertainty of 1.5% in all calculated points for off axis dose simulations.

the field. This is due to the difficulty in calibrating the films at low doses (background substraction, processor inconstancy). Results of MC calculations are also presented in Figs. 4.23 (a)-(i) for all the additional collimators. As done for depth dose calculations, the γ-index is also presented for each measurement point in the graphics. The diode has been chosen as reference because some authors have performed OAR measurements with a diamond chamber, which is the most appropriate detector for radiosurgery measurements [Har95], and found that results given by the diode detector are very similar to those given by the diamond detector [RF95, HHB96, WAN$^+$00, HFL$^+$02]. For all the additional collimators, the calculated data are in good agreement with the measured data with the diode since the γ-indexes are lower than 1, except in only one point (col17 for $r = 0$ mm).

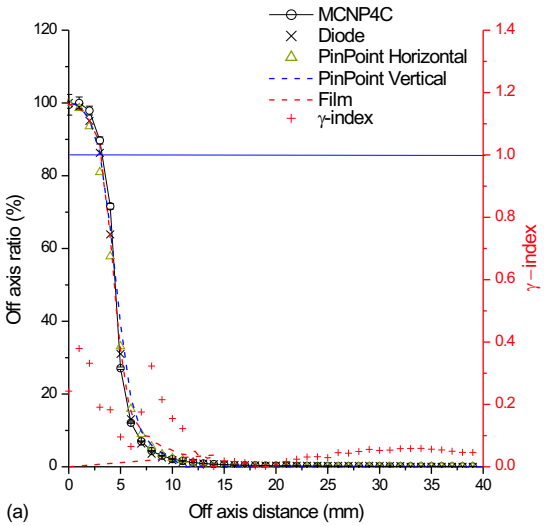
MCNP4C
Diode
PinPoint Horizontal
PinPoint Vertical
Film
γ-index
Off axis ratio (%)
γ−index
Off axis distance (mm)
(a)

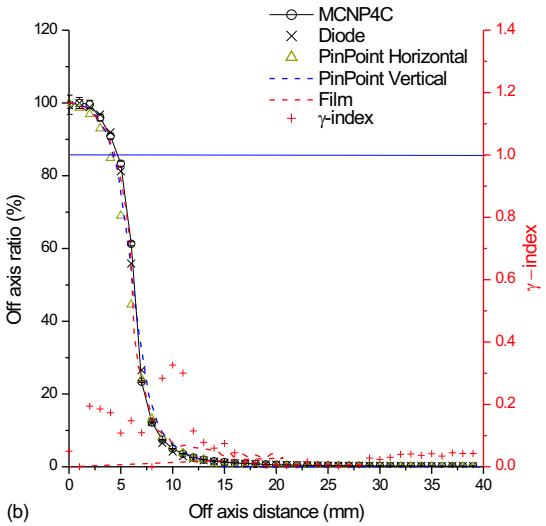
MCNP4C
Diode
PinPoint Horizontal
PinPoint Vertical
Film
γ-index
Off axis ratio (%)
γ−index
Off axis distance (mm)
(b)

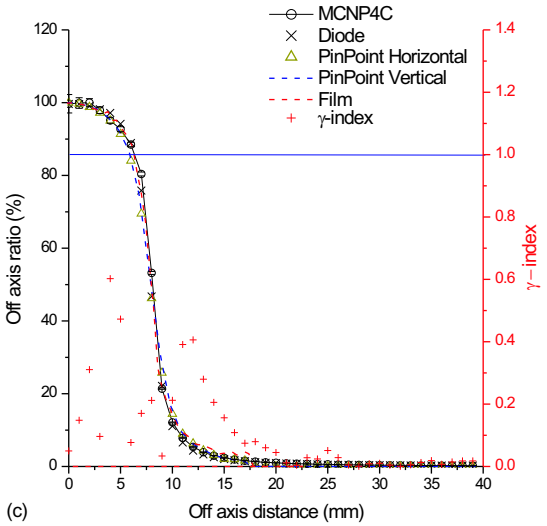
MCNP4C
Diode
PinPoint Horizontal
PinPoint Vertical
Film
γ-index
Off axis ratio (%)
γ−index
Off axis distance (mm)
(c)

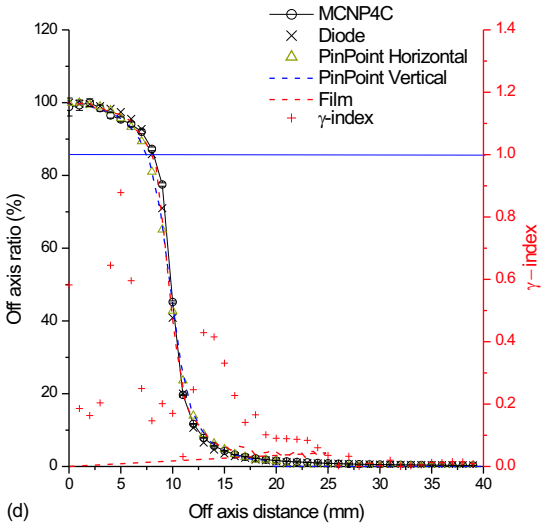
MCNP4C
Diode
PinPoint Horizontal
PinPoint Vertical
Film
γ-index
Off axis ratio (%)
γ−index
Off axis distance (mm)
(d)

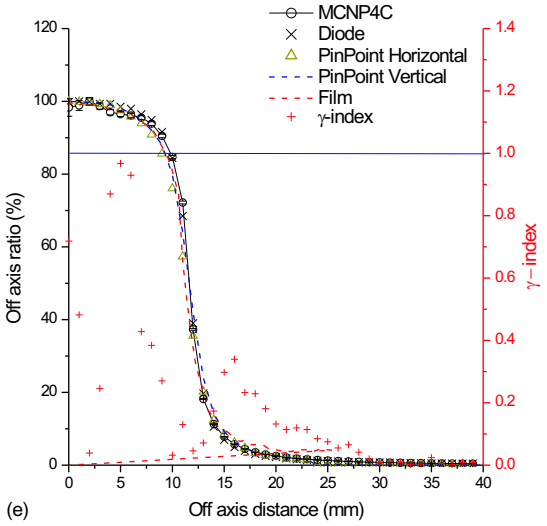
MCNP4C
Diode
PinPoint Horizontal
PinPoint Vertical
Film
γ-index
Off axis ratio (%)
γ−index
Off axis distance (mm)
(e)

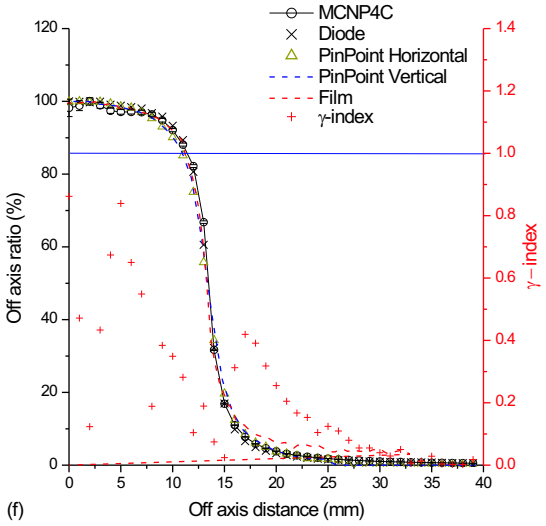
MCNP4C
Diode
PinPoint Horizontal
PinPoint Vertical
Film
γ-index
Off axis ratio (%)
γ−index
Off axis distance (mm)
(f)

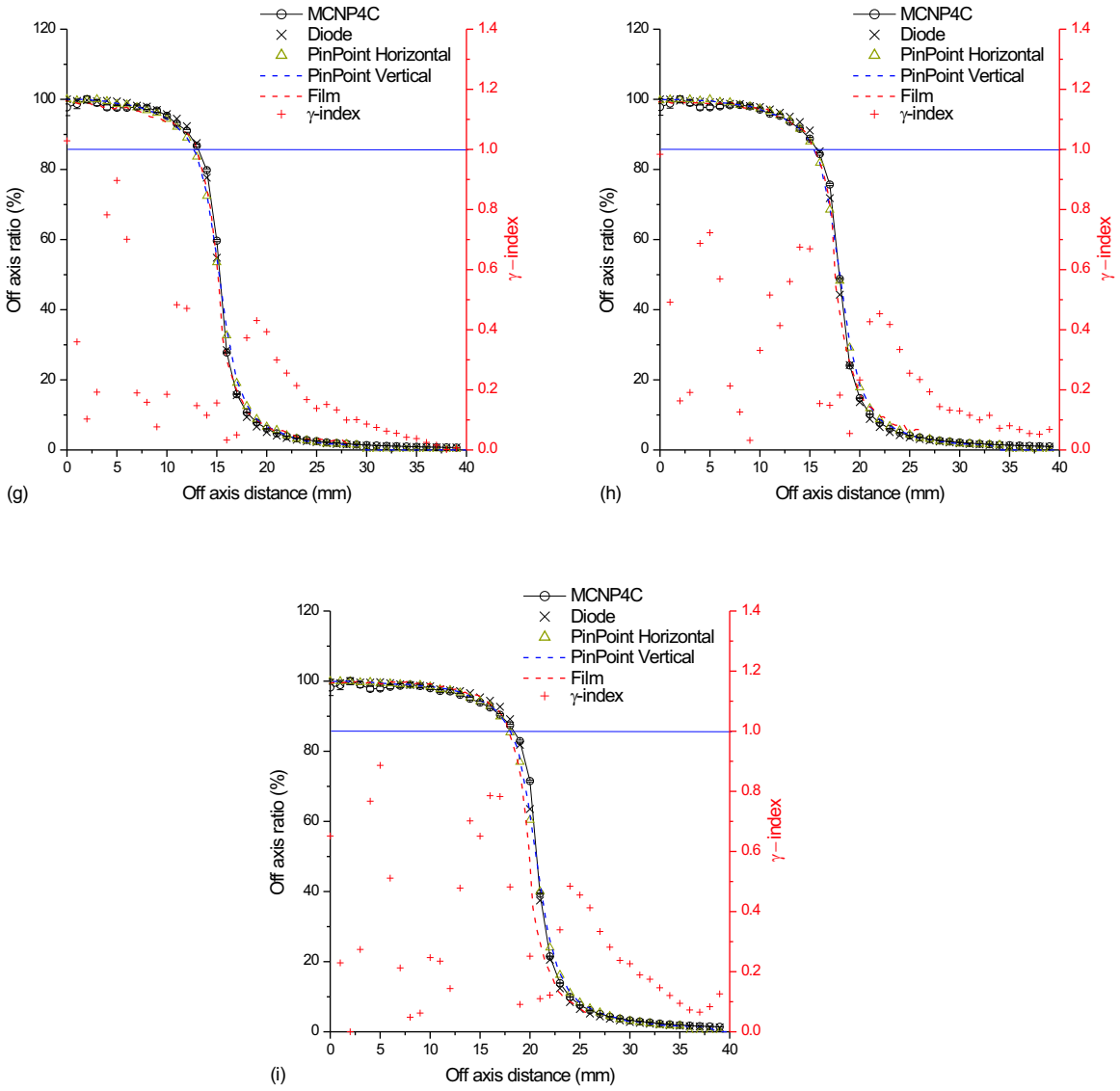

Figure 4.23: A comparison between calculated and measured off-axis ratios. The setup is the following: Source Surface Distance 95 cm, depth of calculation and measurement 5 cm. Each graphic represents the results for one additional collimator: (a) col5, (b) col7, (c) col9, (d) col11, (e) col 13, (f) col15, (g) col17, (h) col20, (i) col23. For each additional collimator, the results to the value of maximum dose. The γ quality index is also plotted for each measurement point.

4.3.6 Output factor

Due to the lack of lateral electron equilibrium, the type and size of the detectors have a great influence in the correct determination of the dose especially for the smallest narrow photon beams. For example, Fig. 4.24 shows how can the size of the detector (in this case a cylindrical ionization chamber with its longitudinal axis parallel to the beam central axis) influence the reading.

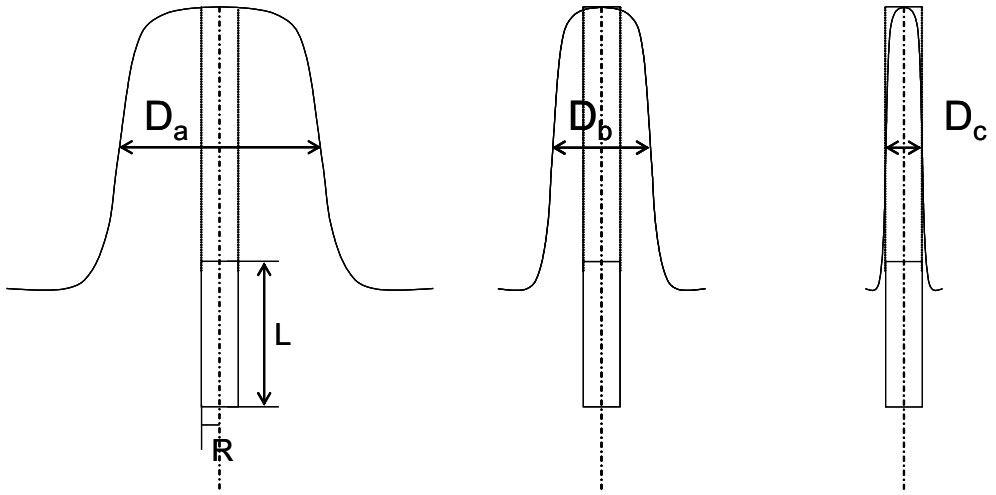

Figure 4.24: A relationship between the beam profiles of three additional collimators (D_a>D_b>D_c) with the cylindrical chamber dimension.

According to the definition of the OF, Fig. 4.24 shows that it is expected to measure (for the smallest beam) an OF lower than the true OF value. Some authors have proposed different correction factors for ionization chamber measurements. These corrections mainly consist of different methods of beam profile averaging throughout the chamber volume [EJ84, RHS$^+$87] or in the determination of dose value by extrapolation [RHS$^+$87] or interpolation techniques [HVF83]. In the frame of the Concerted Action DYNARAD project, we have developed within the so-called *Small Field Dosimetry Task Group* a method to correct the reading of the ionization chambers [LST$^+$00]. The ionization chamber is irradiated with its longitudinal axis parallel to the beam central axis to optimize the symmetry and maximizes the volume exposed to the beam. Our proposal assumes that the deficit of cumulated charge is proportional to the quotient between the effective volume of the chamber V_{ef} and actual one V_c. The correction factor F_c is then defined as:

$$F_c = \frac{V_c}{V_{ef}} = \frac{R^2}{2\int_0^R rp(r)dr}, \tag{4.15}$$

where R is the cylindrical chamber radius and $p(r)$ is the beam profile curve included within the chamber volume for every additional collimator, normalized to 1 and measured with the film. The corrected OF for an additional collimator c is thus given by:

$$OF_{corr}(c) = OF(c) \times F_c. \tag{4.16}$$

The correction factor will be applied to the 0.125 cm^3 ionization chamber.

The results of calculations and measurements are presented in Fig. 4.25. Table 4.4 shows the relative differences between the calculated OFs and the measured OFs with different detectors. According to the results, calculated OFs are in good agreement

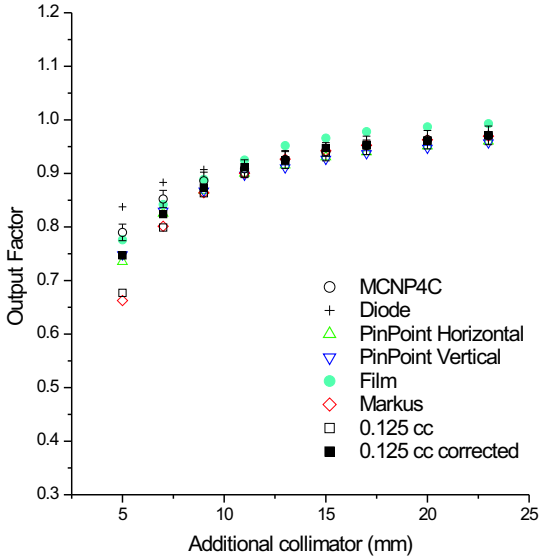

Figure 4.25: A comparison between calculated and measured output factors for all the additional collimators.

(within 3%) with the film measured OFs for all the additional collimators. For the other detectors, the agreement between calculated and measured OF is reached for additional collimators larger than 7 mm. For the 5 and 7 mm additional collimators, large differences are observed between calculated and measured OF values as shown in Table 4.4 particularly for OFs obtained with the Markus and the 0.125 cm^3 (uncorrected) ionization chambers. McKerracher *et al.* [MT99] have reported that OFs measured with the Markus chamber for the smallest beams are under-estimated possibly due to the non-tissue equivalent material surrounding the sensitive volume. The volume correction factor applied to the 0.125 cm^3 ionization chamber has an important effect

Additional Collimator	Calculated OF_c (MCNP4C)	δ_{diode}	$\delta_{PinPoint}$ (Horizontal)	$\delta_{PinPoint}$ (Vertical)	δ_{film}	δ_{Markus}	$\delta_{0.125cc}$ (Uncorrected)	$\delta_{0.125cc}$ (Corrected)
Col5	0.790 ± 0.015	-5.70	7.44	5.52	1.80	19.23	16.60	5.75
Col7	0.852 ± 0.016	-3.52	3.27	2.68	1.22	6.34	6.61	3.42
Col9	0.886 ± 0.016	-2.32	2.10	2.14	-0.32	2.58	2.65	1.43
Col11	0.909 ± 0.017	-1.65	0.98	1.28	-1.75	0.94	0.99	-0.33
Col13	0.926 ± 0.017	-1.58	1.13	1.65	-2.75	-0.09	0.19	0.13
Col15	0.941 ± 0.017	-1.20	1.07	1.47	-2.64	-0.18	0.18	-0.72
Col17	0.952 ± 0.017	-1.03	1.33	1.61	-2.62	-0.03	0.07	-0.11
Col20	0.963 ± 0.017	-0.48	1.28	1.64	-2.43	0.02	0.24	0.19
Col23	0.971 ± 0.017	-0.44	1.15	1.42	-2.21	0.14	0.03	-0.06

Table 4.4: Value of calculated output factor for all the additional collimators. δ is the relative difference between the calculated output factor OF_c and the measured output factor OF_m: $\delta_m = (OF_c - OF_m)/OF_m$ in %.

for field size lower than 13 mm [LST$^+$00]. For the 5 mm additional collimator, the difference between corrected and not corrected OF reaches up to 9%. For additional collimators greater than 13 mm, corrected and uncorrected OF values for the 0.125 cm^3 chamber are similar since F_c is almost equal to 1. Also due to the volume effect, the PinPoint chamber in its vertical position has a higher response for the smallest fields compared to the PinPoint chamber in the horizontal position. The differences between the OF values for the two orientations of the PinPoint chamber becomes very small as the size of the additional collimator increases (less than 0.5% for additional collimators greater than 9 mm). Values of corrected OFs for the 0.125 cm^3 are very closed from OF values for the PinPoint chamber in its vertical position as show in Fig. 4.25 for the smallest beams (relative difference lower than 0.7%). For the greatest additional collimators (>15 mm) there is a tendency of under-estimation of OFs measured by the PinPoint chamber (in its two orientations) compared to calculations and other detectors. It has been reported that the response of this chamber is slightly lower due to the over-response to low-energy Compton scatter for the 10×10 cm^2 field [MDD00]. It has to be noticed that, although the 0.125 cm^3 chamber was corrected and values obtained with this chamber are very close from values obtained with the PinPoint chamber in the vertical position, OFs measured with these two detectors are lower than calculated OFs for the smallest field sizes. This suggests that the volume effect is not the only responsible for this under-estimation. In fact, Haryanto *et al.* [HFL$^+$02] have shown that, for very small fields, there is no water-equivalence of the PinPoint chamber. They found a good agreement between calculated and measured OFs taking into account the air cavity of the PinPoint chamber. They have also shown that the size of the voxel where dose is scored for OF calculations, must describe as well as possible the volume of the detector. Finally, the diode detector over-estimates the OF for field sizes lower

than 11 mm. This is due to the short range of the electrons in silicon compared to water and thus creating a false electron equilibrium in these small fields. As done with the PinPoint chamber, a good agreement between calculated and measured OFs was found by Haryanto *et al.* [HFL$^+$02] if the material of the diode is taken into account in the simulation. They finally concluded that "MC methods give results that can be seen as the results for an ideal linear accelerator and can be significant in determining the correct OF for small fields".

Chapter 5

Detailed study of depth of maximum dose

One of the most interesting phenomena occurring when the size of the secondary collimators increases is that d_{max} also increases becoming deeper in a water phantom [SP93]. This is exactly the opposite of what is observed in conventional radiotherapy photon beams where as the size of the photon beam increases, d_{max} becomes closer to the surface of a water phantom [BL79]. The quite different size of photon beams in the two cases leads to different causes for the different behavior of d_{max}. According to Sixel *et al.* [SP93], the behavior of d_{max} in narrow photon beams is linked to water phantom scattering processes whereas it is well known that the shift in d_{max} in conventional beams is due to head scattered processes [SP94]. But the details of such phenomenon regarding narrow photon beams still remain quite unknown. The purpose of this chapter is to fully understand the behavior of d_{max} for narrow photon beams using MC simulations.

5.1 Experimental setup

The Siemens Mevatron KD2 linear accelerator in 6 MV photon mode was used. The aperture defined by the jaws was set to 10×10 cm^2 (at the isocentre). The 5, 7, 9, 11, 13, 15, 17, 20 and 23 mm additional collimators were used. The distance between the source and the bottom of the additional collimator is 56.5 cm. The PTW-Freiburg PinPoint chamber was used to obtain $DDCs$ in the buildup region for all the additional collimators. The chamber was irradiated with its maximum dimension perpendicular to the beam central axis and connected to a PTW-Freiburg MP3-motorized water

phantom. The SSD was set up at 100 cm.

5.2 Monte Carlo Simulation

In this study, MCNP4C was used with ITS-style energy-indexing algorithm [HKM$^+$92]. The *ptrac*-option of MCNP4C is used to track and record in an output file all the history of each source particle. MCNP4C can calculate dose in a medium allowing to separate this dose into two components (primary dose and scattered dose) using the *col*-option. Finally, MCNP4C can record in a *wssa*-file all the particles that reach a defined scoring plane. This *wssa*-file becomes a *rssa*-file that is the source of the following simulations. All the calculations were performed in a PC with a Pentium III (800 MHz) processor and 128 Mb of RAM.

In this work, the PSD generated in Chapter 4 was used since, once again, the geometry of the accelerator head remains unchanged. This PSD became the source of the next simulation block constituted by the additional collimator. For each additional collimator, a second PSD (PSD_2) was generated at a scoring plane placed just below it (cote 56.6 cm). This PSD_2 became the source for the last simulation block constituted by the $50 \times 50 \times 50$ cm^3 water phantom and the air column between the additional collimator and the water phantom. For simulations in water, electron kinetic energy cutoff was set to 50 keV whereas the photon energy cutoff remained unchanged. The number of particles recorded in PSD_2 varies from 4.7×10^4 for the 5 mm additional collimator to 9.7×10^5 for the 23 mm additional collimator.

The *ptrac*-option included in the MCNP4C code allows recording in a file called *ptrac*-file, all the events in the history of a particle. These events can be a source, bank, crossing surface, collision or terminated event. The way *ptrac*-option writes the type of event, the characteristics of a particle and its branch is not obvious. Although some commercial software allows extracting all the needed information [KV02], it was developed an in-house *ptrac*-file analyzing tool called *ptrac*-package based on the specific cards used in the simulations. Because the size of a *ptrac*-file can become very large, only the histories that contributed to the dose in the chosen scoring cells in the water phantom were recorded. For each particle that contributes to the dose in the scoring cells, *ptrac*-package records in an ascii-output file the following data:

1. type, position, energy and direction of the source particle on the scoring plane;

2. type, position, energy and direction of the particle in the water phantom before and after the interaction that originates the electron contributing to the dose at the chosen scoring cell;

3. origin, energy, direction of the electron that contributes to the dose;

4. energy of the electron entering the scoring cell;

5. energy of the electron leaving the scoring cell;

6. the scoring cell in the water phantom;

7. the number of photon interactions that proceeded the electron energy deposition in the scoring cell.

This output file was transformed in a PAW Ntuple [BCC$^+$00] file for a more straightforward analysis.

In order to study the region where d_{max} is included, 14 scoring cylindrical water cells were defined along the beam central axis (CAX). To describe this region, the distance along the CAX between the centers of two adjacent cells was set to 2 mm (equal to the diameter of the PinPoint chamber). As already stated, the size of the *ptrac*-file can be very large. To optimize the size of these files, the scoring cells in the water phantom should be chosen according to a balance between statistics and spatial resolution. Taking into account these conditions affecting the statistics of dose calculation, the diameter of the scoring cells was set to 5 mm. The volume of a scoring cell was thus 0.039 cm^3 which is roughly the double of the PinPoint chamber volume used to measure the dose although the critical dimensions along the beam central axis central axis are similar (both chamber length and diameter). In non-electron equilibrium situations (buildup region and lateral disequilibrium), the dose measured or calculated along the beam central axis can be underestimated because of the size of the chamber or the size of the scoring cell. A method to correct the dose was proposed by the Small Field Dosimetry Task Group of the European Concerted Action DYNARAD [LST$^+$00]. A correction factor based on the beam profile averaging was then used to obtain output factors for the different additional collimators. In the case of measuring or calculating percent depth dose curves, if the beam profiles, included in the chamber length or scoring cell diameter (5 mm) at the depth of measurement and at the depth of normalization, present a similar shape (see Fig. 5.1), leading to the same profile

averaging, there is no underestimation of the relative value of the dose at the point of measurement or calculation. It should be stressed that even for the smallest collima-

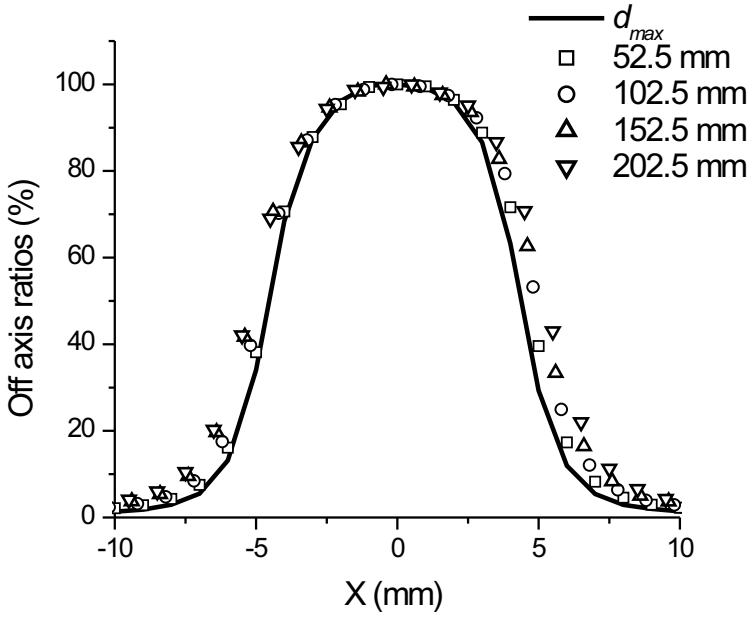

Figure 5.1: Measured off-axis ratios at different depths for the 5 mm additional collimators. Measurements were performed with a PTW-Freiburg diode (type TM60008) in the PTW-MP3 water phantom. Normalization was performed at the maximum dose at each depth.

tor, the beam diameter at the isocenter is 9 mm. For the same reason, having different scoring geometries for measurements and calculations do not affect the comparisons between the two sets of obtained values. A real comparison between measured and calculated values can only be performed if the ionization chamber is explicitly simulated especially for the smaller fields [HFL+02]. In addition, changes in water/air stopping power ratios can affect the ionization chamber readings [SKN+00] which is the case in non-equilibrium conditions. These are the reasons why corrections should be performed in the chamber outputs. Nevertheless, the goal of this study is not to compare directly results from measurements with Monte Carlo simulations in the buildup region but to try to understand the behavior of d_{max} in water using MC methods, in terms of the details of energy deposition.

5.3 Water dose components

The different contributions of phantom dose have been defined by Ahnesjö *et al.* [AA99] according to all possible origins both upstream and in-phantom processes. In our study, two dose components were taken into account: the primary and the scatter dose components. The primary dose component was defined as the deposited dose due to photons or electrons coming from the accelerator head that suffered no interactions in the additional collimators before entering the water. The scatter dose component was defined as the deposited dose due to particles that suffered their last interaction in the additional collimator before entering the water; this component was called the additional collimator scatter dose component. Sixel *et al.* [SP93] has demonstrated that the primary dose component is the responsible for the increase of d_{max} with the size of the additional collimators. This was confirmed by full MC simulations where depth dose curves for each PSD_2 were calculated as shown in Figs. 5.2 (a) and 5.2 (b) for the 5 mm and 23 mm additional collimators. The contribution of the additional collimator scatter dose component to the total dose is roughly 3% and 10% in the d_{max} region for the 5 mm and 23 mm additional collimators, respectively. However, the behavior of the two dose components is different. While for the additional collimator scatter dose component, its d_{max} seems the same (around 9 mm), presenting no variation between the 5 mm and the 23 mm additional collimator, for the primary dose component the variation in d_{max} is visible. It is clear that d_{max} for the primary beam increases from around 11 mm (5 mm additional collimator) to approximately 17 mm (23 mm additional collimator).

Experimentally, the shift of d_{max} was observed as shown in Fig. 5.3 where d_{max} increases with the size of the additional collimator which is in agreement with other authors [SP93, VDP98]. The experimental value of d_{max} varies from 11.0 ± 0.6 mm for the 5 mm collimator to 14.5 ± 0.6 mm for the 23 mm collimator. The error associated to measurements was evaluated according to the experimental uncertainty in positioning the PinPoint chamber (0.3 mm) and the measurement scanning step that was 1 mm (uncertainty equal to half value of the step). These values of measured d_{max} are compatible with MC calculated d_{max} values considering both primary and additional collimator scattered beams. It has to be noticed that the 2 mm height dimension of the scoring cells is sufficiently small to enable showing the behavior of d_{max} between the 5 mm and the 23 mm additional collimator.

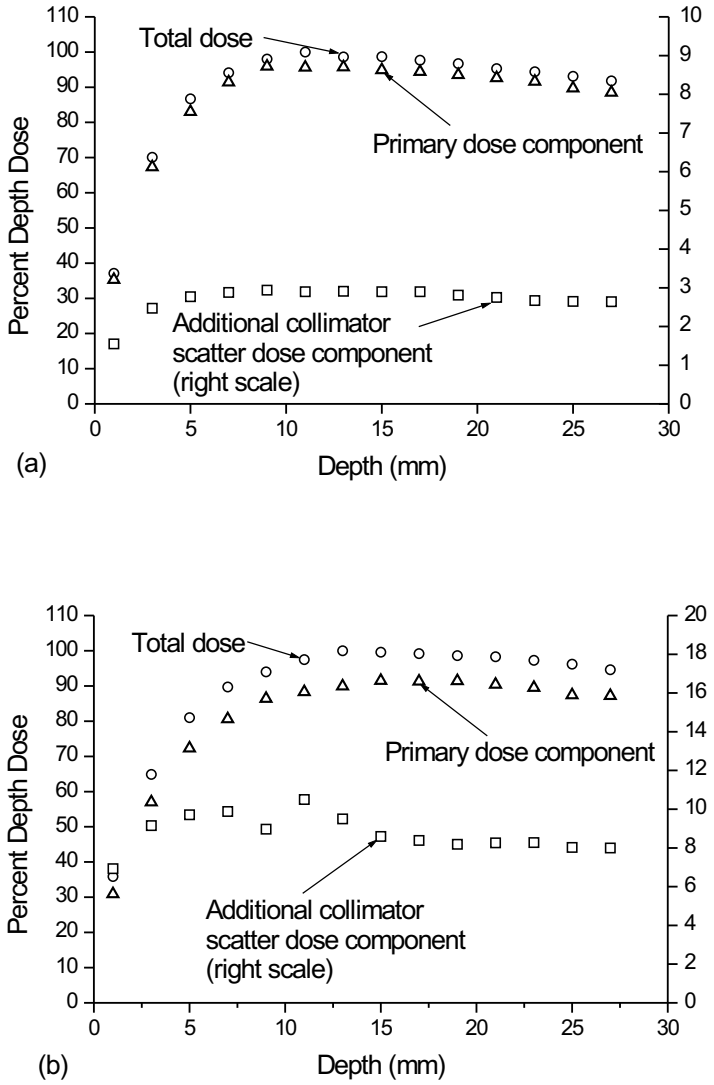

Figure 5.2: Calculated from full Monte Carlo simulations 5 mm (a) and 23 mm (b) additional collimator depth doses in the buildup region in water. Primary dose, additional collimator scatter dose components and total dose are obtained using the MCNP4C col-option. Relative errors calculated by MCNP4C associated to simulation results are less than 1.5% for the total dose, less than 2% for the primary dose, and less than 5% for the scattered dose.

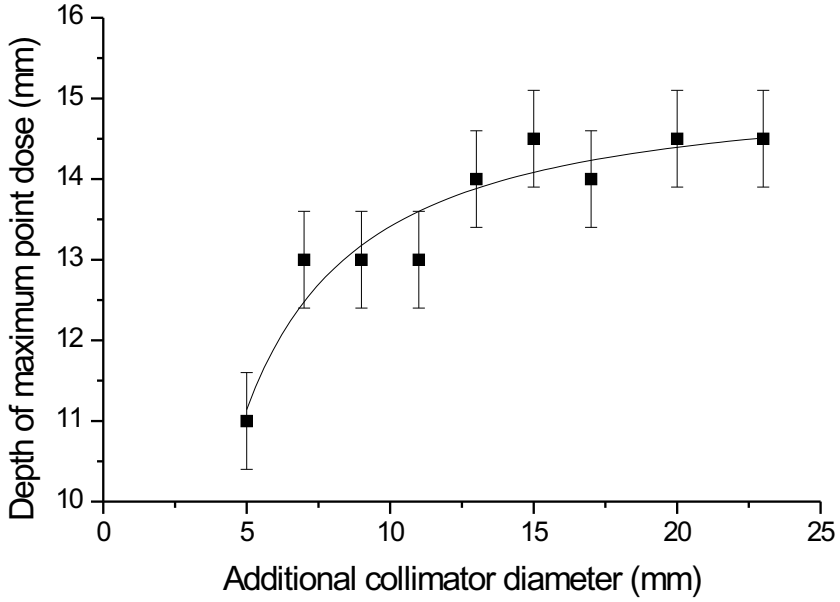

Figure 5.3: Measured depth of the maximum point dose d_{max} for each additional collimator. A trendline was added to show easier the shift of d_{max} as the size of the additional collimator increases.

Simulations have also shown that deposited dose due to electrons from the primary beam, additional collimator scattered beam and electrons originated in the air column between the additional collimator and the water phantom surface is negligible for all the additional collimators as shown in Fig. 5.4 for the 23 mm additional collimator. The percentage of electrons in the primary beam varies from 0.005% for the 5 mm additional collimator to 0.033% for the 23 mm additional collimator and is even smaller for electrons from the scattered components. It appears that the electron contamination is negligible for this kind of irradiation beams. So that in the further analysis only the photon primary beam will be taken into account.

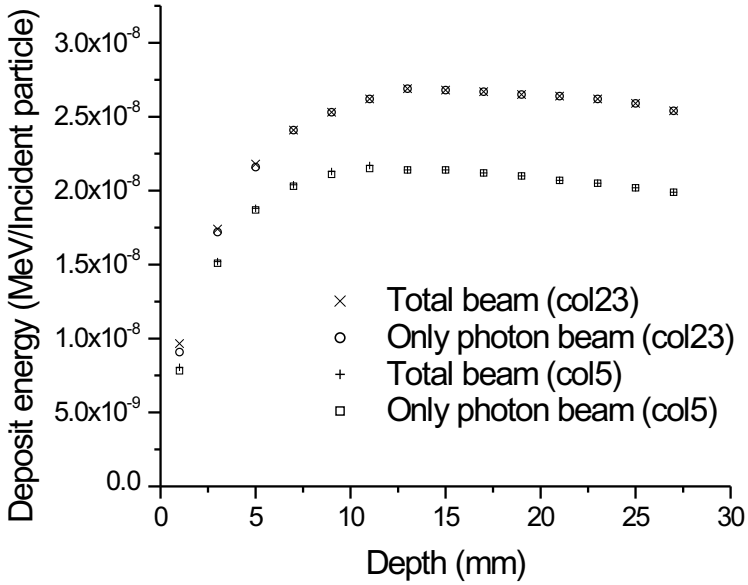

Figure 5.4: Calculated deposited energy from full Monte Carlo simulations. The total beam is composed by both scattered and unscattered photons and electrons. Relative errors associated to Monte Carlo calculations are lower than 1%.

5.4 Simplified source model

To understand the behavior of d_{max}, the knowledge of the energy deposition changes in the scoring cells as the size of the additional collimator increases is needed. In full MC simulations, each additional collimator has its own PSD_2 which represents the particle source for the simulation in the water phantom. A simplified source model was considered where all the PSD_2s of the additional collimators can be extracted from a single PSD_2. To apply such simplified source model some conditions should be fulfilled. The most important is that the characteristics of the particles (type, spatial distribution, spectrum, direction) for the various additional collimators on the scoring plane are similar. The analysis of the various PSD_2 showed that the unscattered photon radial distributions are similar for all the additional collimators except, of course, in the penumbra region. Figure 5.5 shows an example of such distributions.

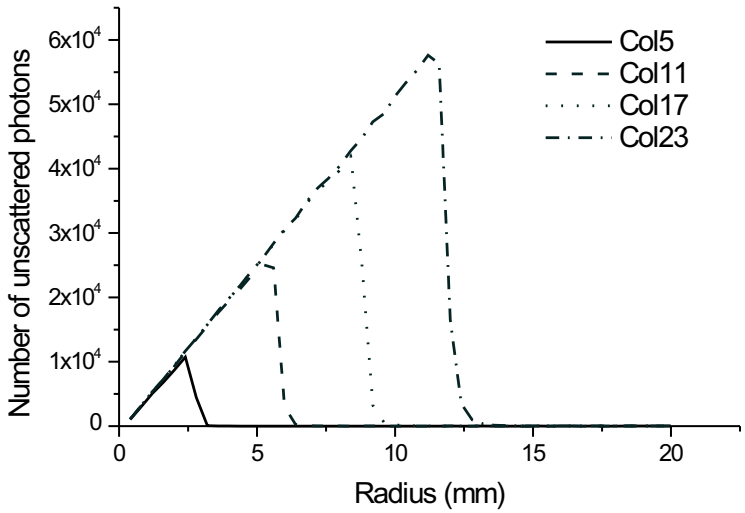

Figure 5.5: Radial spatial distributions of the unscattered photons in air.

Also the direction of the unscattered photons is roughly the same for all the additional collimators. In fact, the maximum unscattered photon angular spread between the 5 mm and the 23 mm additional collimator is less than 1.5 degrees (see Fig 5.6). This

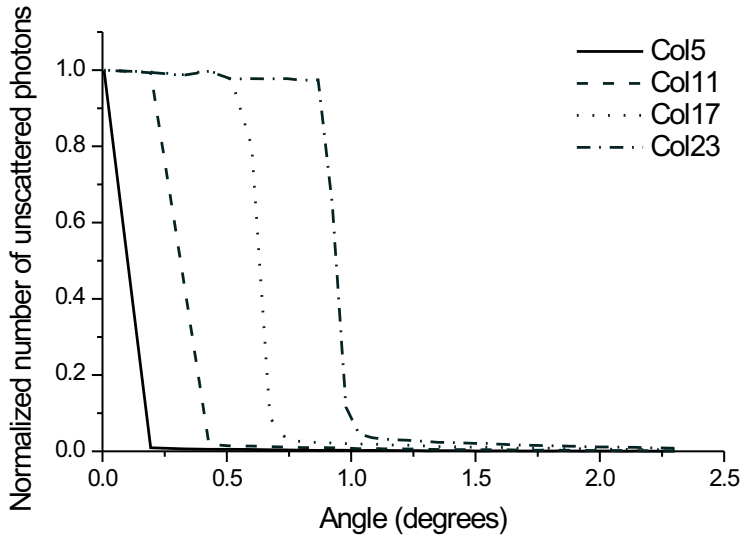

Figure 5.6: Radial average angle distributions of the unscattered photons in air.

means that all beams are very peaked forward and that it can be considered at a first approximation that the direction of the unscattered photons for the different additional

collimators is the same. Finally, full MC simulations have shown that the unscattered photon energy spectra, extracted from each PSD_2, are almost identical for all additional collimators. Figure 5.7 shows an example of such calculations for the 5 and 23 mm addtional collimators. The variation of the average energy from the 5 mm and the 23 mm additional collimators is less than 5%.

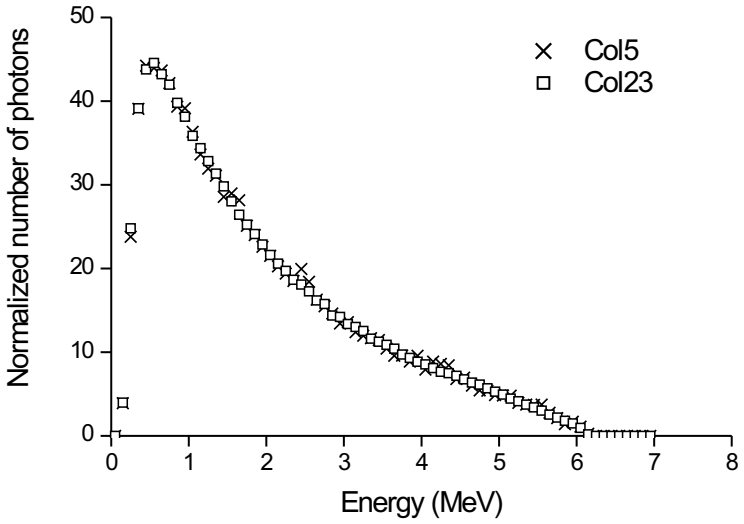

Figure 5.7: Energy distributions of the unscattered photons in air for the 5 and 23 mm additional collimators.

Once the conditions were fulfilled, the simplified additional collimator PSD source model could then be used for the unscattered photons: the 23 mm additional collimator PSD_2 was chosen and data for any smaller additional collimator were extracted from this additional collimator using *ptrac*-file with cylindrical geometrical cuts. For example, results for the 5 mm additional collimator were extracted only if unscattered photons inside a radius of 2.5 mm were taken into account, i.e, the coordinates x and y of the unscattered photons on the scoring plane must satisfy the criterion $(x^2 + y^2)^{1/2} \leq 2.5$ mm. An additional advantage of using just one PSD is that the analysis for successive increasing additional collimators can be done starting with the equivalent 5 mm additional collimator plus increasing annuli representing each additional larger collimator (see Fig. 5.8). It will then be easier to observe energy deposition changes in the scoring cells using only geometric cuts representing any additional collimator in the 23 mm output *ptrac*-file. Thus, only one simulation in water was

performed: simulation of the 23 mm additional collimator based on its PSD_2 source.

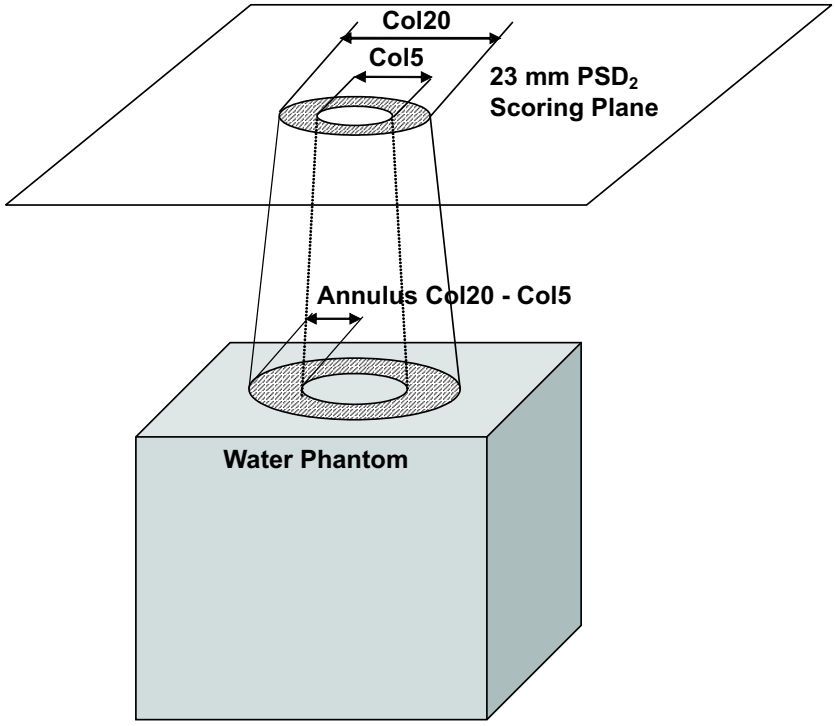

Figure 5.8: Equivalent 5 mm and 20 mm additional collimator fields in the 23 mm additional collimator PSD_2. The 20 mm additional collimator can be represented by the 5 mm additional collimator plus the annulus of internal diameter 5 mm and external diameter 20 mm.

5.5 Results and discussion

Full MC simulations have shown that most of the electrons originated in the water phantom were Compton electrons (more than 98.2% of the total originated electrons for the 5 mm and 23 mm additional collimators). Electrons from pair production collisions represent from 1.6 to 1.4% for the 5 mm and the 23 mm additional collimators respectively and are negligible for all the additional collimators (less than 0.3%). According to these results, only electrons from Compton collisions were taken into account for further analysis.

The deposited energy in a scoring cell will be considered at a first approximation as the kinetic energy of the electron entering the scoring cell minus the kinetic energy of the electron leaving the scoring cell. This approximation can be performed because the

contribution of bremsstrahlung photons to the deposited dose in the water phantom has been shown to be negligible for a 6 MeV electron beam [Tri02]. In fact, for the considered electron energy range, the total mass stopping power is almost equal to the collision mass stopping power. If the electron does not leave the scoring cell because of the imposed electron energy cutoff, the deposited energy is the kinetic energy of the electron entering the scoring cell.

According to the MC simulation results, most of the ejected electrons (Compton process) reaching the scoring cells were originated from one photon collision in water. These electrons represent 97% of the total number of Compton electrons that reached all scoring cells for the equivalent 5 mm additional collimator and 93% for the 23 mm additional collimator. In further calculations, electrons reaching the scoring cells will be separated into two groups: those originated from one photon collision and those originated from more than one photon collision.

Applying the simplified source model, the deposited energy due to electrons reaching the scoring cells that were produced by unscattered photons was analyzed. All errors associated to deposited energy values were calculated at 1SD.

Figure 5.9 (a) shows the deposited energy due to electrons from one photon collision for the 5 mm and the 23 mm additional collimators. A fit for the MC calculated dose values was performed based on the χ^2 test. For the application of this test, it was considered as null hypothesis, H_0, that the calculated distribution from the fit is compatible with the distribution of calculated values from MC results. The minimum level of significance P for rejection of the null hypothesis for the evaluation of the quality of the fit was chosen as 0.05 [Lyo89]. The chosen empiric fitting function was:

$$f(x) = a_1(e^{a_2x+a_3x^2}) + a_4(1 - e^{a_5x}). \tag{5.1}$$

The same function was chosen for the two sets of results (5 mm and 23 mm additional collimator). Once the parameters of the fitting function were calculated, χ^2=8.62 and P=0.473 for the 5 mm additional collimator and χ^2=10.31 and P=0.326 for the 23 mm additional collimator. The χ^2 test indicates that the levels of significance P are compatible with the hypothesis that calculated fitted values do not differ significantly from MC results ($P > 0.05$). The depth of dose maximum calculated from the empiric fitting functions are 12.2 mm for the 5 mm additional collimator while for the 23 mm additional collimator the maximum is around 15.8 mm. This shift is due to the increase

with depth of the deposited energy from the successive annuli as shown in Fig. 5.9 (b). The dose contributions at the scoring cells for the different annuli decrease although the number of unscattered photons increases as the size of the annuli increases. This is of course due to the electron range in water.

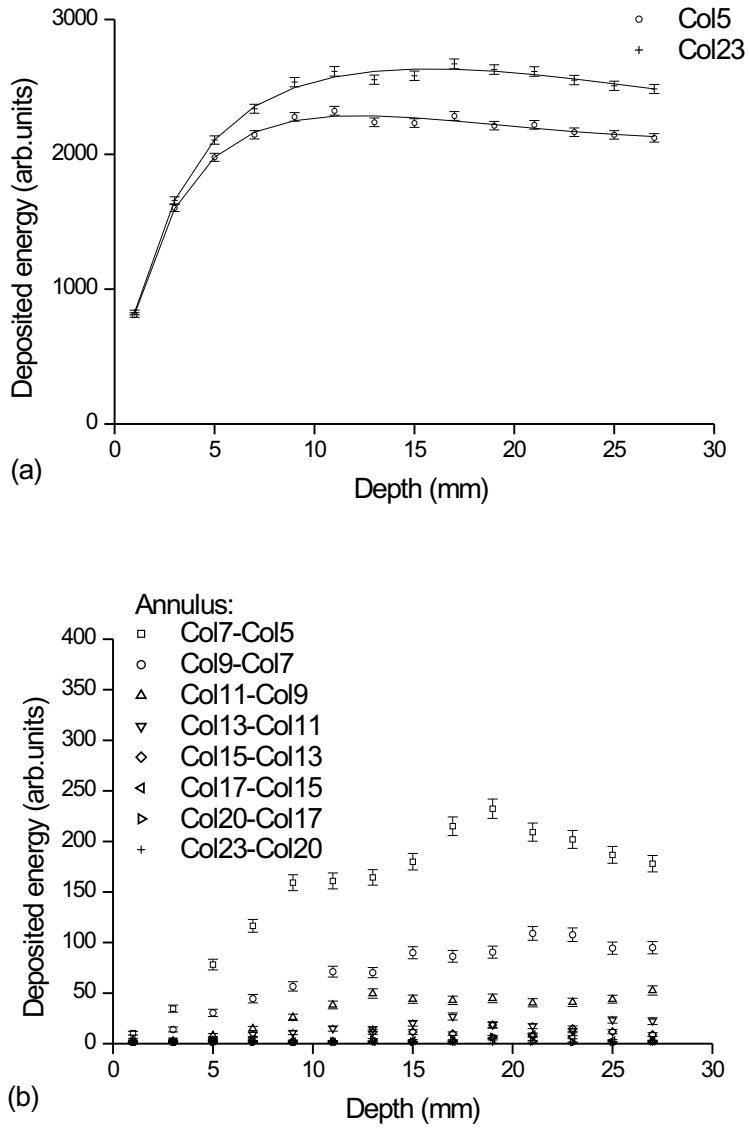

Figure 5.9: Deposited energy versus depth (a) due to electrons from one photon collision for the 5 mm and the 23 mm additional collimator. (b) Contribution of electrons from one photon collision for each annulus. Errors bars were added.

Figure 5.10 (a) shows the deposited energy due to the electrons originated from more

than one photon collision for the 5 mm and the 23 mm additional collimators. Also in this case, the shift in depth of dose maximum is clear. This shift is also due to the increasing with depth of the deposited energy from the successive annuli as shown in Fig. 5.10 (b).

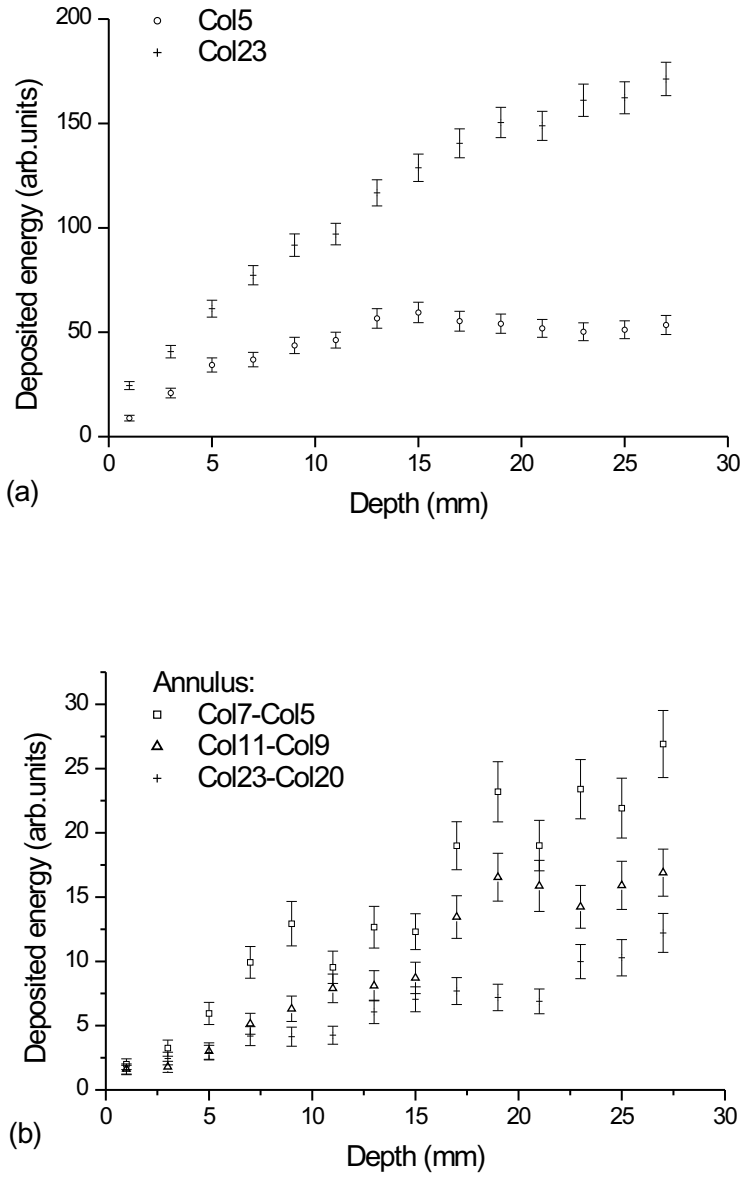

Figure 5.10: Deposited energy due to electrons from more one photon collision as a function of depth (a) for the 5 mm and the 23 mm additional collimator. (b) Contribution of electrons from more one photon collision for 3 different annuli.

Using the simplified source model, four curves are shown in Fig. 5.11: (1) the deposited energy for the 5 mm additional collimator (lower curve); (2) the deposited energy for the 23 mm additional collimator (upper curve); (3) the deposited energy of the 5 mm additional collimator added with the electron contribution of the 23 mm annulus for one photon collision; (4) the deposited energy of the 5 mm additional collimator added with the electron contribution of the 23 mm annulus for more than one photon collision. Using the same fitting procedure described earlier, all the curves passed the χ^2 test. Once more, the shift of d_{max} is clear. Results from fitting functions show that d_{max}=12.5 mm for curve 1, d_{max}=17.3 mm for curve 2, d_{max}=5.9 mm for curve 3 and d_{max}=3.6 mm for curve 4. Calculated values of d_{max} for curves 1 and 2 are compatible with results from full MC simulations for the primary dose component (11 mm and 17 mm for 5 mm and 23 mm additional collimators respectively).

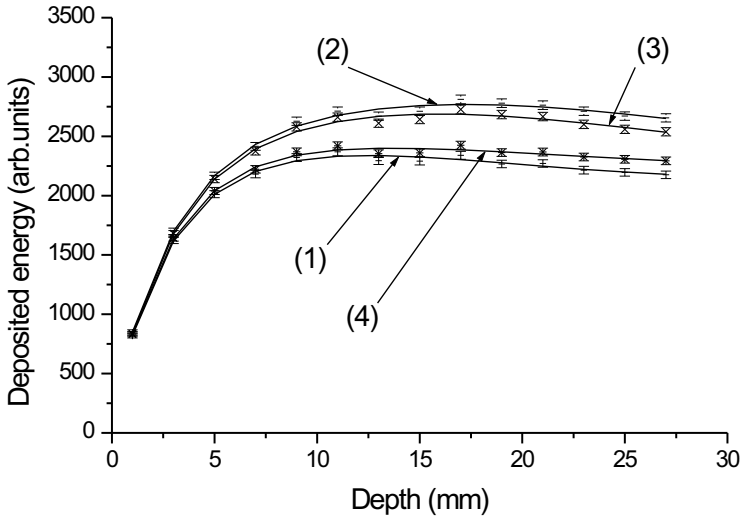

Figure 5.11: Deposited energy as a function of depth in four cases. Results of χ^2 test are the following: (1) χ^2=7.36 and P=0.599; (2) χ^2=9.46 and P=0.396; (3) χ^2=9.07 and P=0.431; (4) χ^2=7.26 and P=0.478.

Another interesting qualitative result is that the gradients of the deposited energy in the buildup region for the 5 mm and the 23 mm additional collimators are different. This is due to the contribution of the electrons from one photon collision as shown in Fig. 5.11. This contribution is in fact responsible for the behavior of the curves in the buildup region.

Finally, to complete this study, the initial average kinetic energies of the electrons reaching all scoring cells from one and more than one photon collision produced by the unscattered photons from annuli were calculated and are plotted in Fig. 5.12. The two

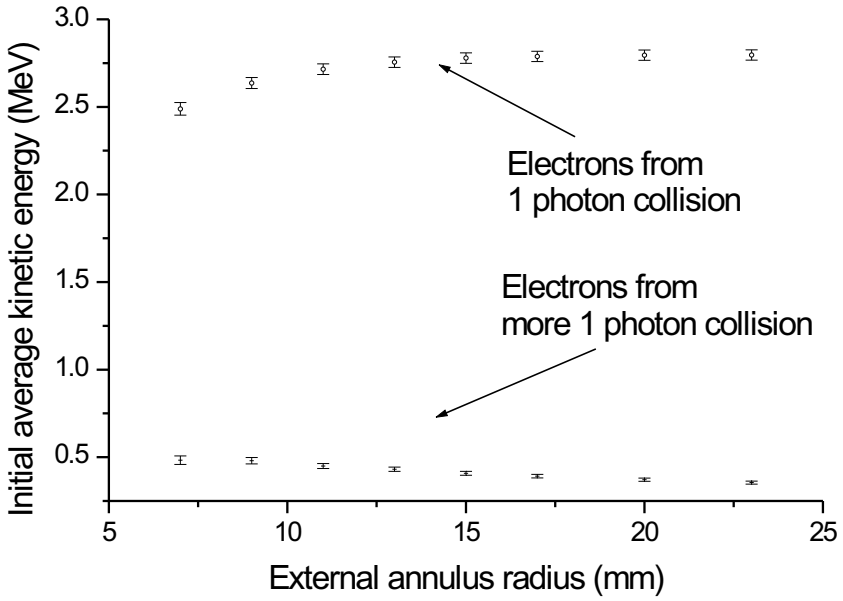

Figure 5.12: Initial average kinetic energy for electrons that reach all the scoring cells for one and more than one photon collisions. The unscattered photons are coming from annuli representing each additional collimator. The inner diameter of the annuli was fixed to 5 mm and the outer diameter was increased from 7 mm (7 mm additional collimator) to 23 mm (23 mm additional collimator).

curves have different behaviors. The initial average kinetic energy for electrons from one photon collision increases as the external radius of the annulus increases whereas the initial average kinetic energy for electrons from more than one photon collision slightly decreases as the external radius of the annulus increases. The increase of the initial kinetic electron energy from one photon collision can be explained by the fact that because the photon beams for the different additional collimators are very peaked forward, as the distance between the central axis and the point of photon collision increases, the kinetic energy of the electron from that collision should increase in order for it to reach the scoring cell. It is why these electrons can deposit dose relatively far way from their point of origin because of their ranges (for kinetic energy around 2.6 MeV electron range in water is about 20 mm). The slightly decrease of the initial kinetic electron energy from more than one photon collisions arises from localized processes of photon scattering in water near the scoring cells. As shown in Fig. 5.12,

the initial average kinetic energies of electrons from more than one photon collision are lower than 0.5 MeV and so the energy of these electrons is deposited locally (ranges in water lower than 1.8 mm) regarding the size of the scoring cells.

The behavior of d_{max} for the narrow photon beams used in radiosurgery was fully understood using Monte Carlo simulations. Photons that had no interactions in the additional collimators, contributing more than 90 % to the total dose in water, were responsible for the shift in d_{max}. Electrons originated from these photons and contributing to the dose deposit in water in the beam central axis could be divided in two groups: those that deposit energy far away from their point of origin and those that deposit energy locally. Finally, the changes in the initial gradients of the depth dose curves for these narrow photon beams were mainly due to electrons originated from the first photon collision in water.

Chapter 6

Multiple source model for narrow photon beams

Accurate dose distribution calculations are fundamental in the field of radiotherapy in order to reach expected outcomes in tumor control free of complications [ABL+97, ICR93, ICR99]. Unfortunately, in some complex setups (irregular fields, air/bone interfaces, heterogeneities), current commercial TPSs do not calculate dose distributions accurately [PWL01]. To overcome these problems, MC methods appeared as a powerful tool.

In radiosurgery, a high degree of both geometrical and dosimetrical accuracy must be achieved in this kind of treatment. The American Association of Physicist in Medicine (AAPM) [AAP95] suggests that the spatial accuracy should be about 1 mm and the uncertainty in the dose delivery up to 5% in order to fulfill the expected treatment outcome. For radiosurgery applications, the standard approach has the advantage of requiring the patient-independent component to be simulated only once, followed by the simulation of each additional collimator. Nevertheless some major problems limit the use of this approach. The geometry of a phantom or a reconstructed CT-image is divided in voxels. The size of these voxels must be small enough in order to achieve the required accuracy. When the size of the voxels decreases, the number of particles needed to achieve the same statistical uncertainty increases. In conventional radiotherapy applications, accurate results are achieved because the number of particles in the PSD is statistically relevant; this might not be the case in radiosurgery applications. The main technique for increasing the number of particles that reach the voxels is to increase, in the patient-independent simulations, the number of original histories which

is extremely time consuming and produces very large PSD files. Other option is to recycle several times the source PSD in the patient-dependent simulations. A typical radiosurgery treatment is composed of six arcs. Each arc, for calculation purposes, is divided at least into eight fixed photon beams. That means, in a typical radiosurgery treatment, forty eight photon beams must be simulated for the patient-dependent component. Time and storage capacity are thus strong limitation factors.

In the past few years, a new approach appeared concerning patient-independent beam models based on MC simulations. This approach uses virtual sources, single or multiple with different shapes (point, planar, annular, ...) which produce the same dosimetric effect than a full MC simulation. The first model for megavoltage photon beams was presented by Liu *et al.* [LMM97]. In this model, three different virtual sources were defined, one representing the primary photons coming from the target, one representing the scattered photons and finally one describing the electron contamination. Chetty *et al.* [CDS00] have developed a virtual source model which consists of a photon fluence grid composed of a matrix of square elements. In this model, all the photons are assumed to be originated in the target and a Gaussian blurring kernel is convolved with the photon fluence to match measured and calculated dose penumbrae. An electron virtual source was also added to take into account the electron contamination. This model is capable of accurately simulating arbitrary MLC fields. Recently, Deng *et al.* [DMH$^+$03] have developed a source model composed by two annular photon sources representing the primary and scattered photons to model their Cyberknife stereotactic radiosurgery system. They developed a method to define the two virtual sources from a standard set of measurements in water. They implemented this model in a MC-based TPS and obtained excellent agreement between the source model and the original phase space in homogeneous and heterogeneous simulated geometries [DGM$^+$04]. More complex source models were developed through extensive photon beam characterizations. In conventional radiotherapy, this detailed study has originated the so-called multiple source model [SCB$^+$99, DJK$^+$00, FSM$^+$01]. This model is based on the fact that particles originated in the same component of the accelerator head have similar characteristics: type, position, direction, energy. These radiation beam properties allow the assumption that particles originated in the same component can be viewed as emitted by the same virtual source. The representation of the virtual source depends on the type of component. A reconstructed radiation beam is then composed of various virtual sources representing each relevant component of the accelerator head. For some

cases in conventional radiotherapy studies, the optimization of this kind of model has reduced the data storage requirement by a factor of 10000 or more and the simulation time by a factor of 10 or more for the same accuracy in the results compared to full MC simulations [DJK+00]. The application of this model to radiosurgery appears to be attractive since the reduction both in time and data storage is very important. On the other hand, the additional collimator can coherently be considered as another virtual source to be added to those representing relevant accelerator head structures.

The purpose of this chapter is to develop and validate, through comparisons with measurements in a water phantom, a multiple source model for radiosurgery narrow photon beams that calculates dose distributions in small voxels with a good accuracy.

6.1 The multiple source model

Three major steps are necessary to develop a multiple source model (MSM). The first step is the full characterization of the beam, the second one, the choice of the different relevant virtual sources and finally the beam reconstruction. Following the classical approach, the geometry of the Siemens KD2, in 6 MV photon mode, was modelled using the MC code MCNP4C (see Chapter 4). A schematic view of the accelerator head in photon mode is displayed in Fig. 6.1. The choice of the scoring plane is important. Since the geometry of the accelerator head remains unchanged for radiosurgery treatment, only one simulation was performed and a scoring plane was placed just below the reticle of the accelerator (scoring plane 1 see Fig. 6.1). In this stage, the additional collimator is not simulated. A total of 8.3×10^9 tracks were stored in a PSD file at scoring plane 1. The second stage is the simulation of the 5, 7, 9, 11, 13, 15, 17, 20 and 23 mm additional collimators. The 10×10 cm^2 PSD is the source of the following simulations. At scoring plane 2 (see Fig. 6.1), a PSD was recorded for each additional collimator. This PSD becomes the source for direct patient-dependent simulations and the basis for the development of the Radiosurgery Multiple Source Model (RMSM).

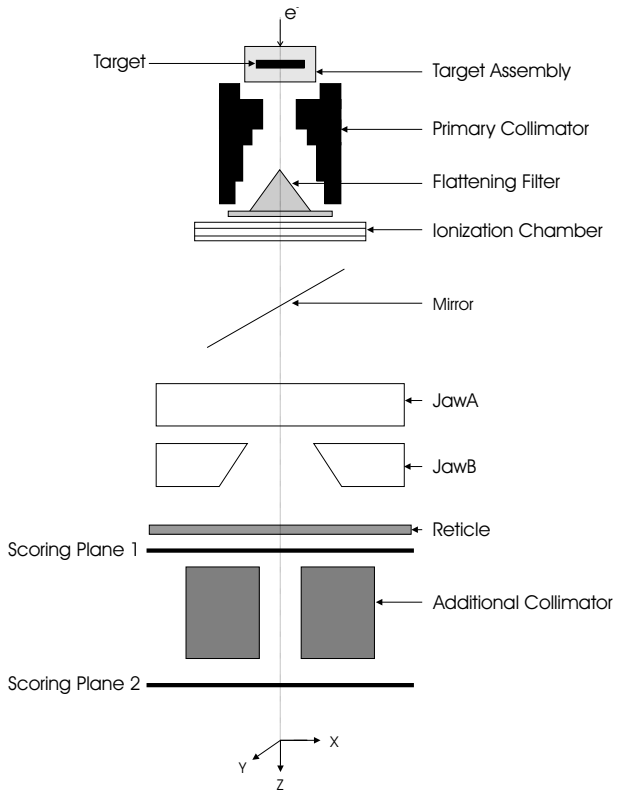

Figure 6.1: Simplified diagram of the Mevatron KD2 accelerator head components plus the additional collimator.

6.1.1 Beam characterization

MCNP4C code creates at a scoring plane a PSD file called *wssa*-file. The dedicated program MCNP-STRIP [Sie] reads the binary *wssa*-file and writes an ascii-file where any particle can be expressed by [DJK+00]:

$$P_i = (x_i, y_i, z_i, u_i, v_i, w_i, energy_i, zl_i, wt_i, itype_i). \tag{6.1}$$

P_i is a ten-dimensional vector where (x_i, y_i, z_i) are the coordinates of the particle at the scoring plane z_0; (u_i, v_i, w_i) are the direction cosines of the particles at scoring plane 2; $energy_i$ represents the energy of a photon or kinetic energy for an electron at scoring plane 2; zl_i represents the cote along the z-axis of the last interaction point or origin of the particle; wt_i the weight of the particle and finally $itype_i$ represents the type of particle (photon or electron). Using the HBOOK routines from the Cernlib, the PSD ascii file is transformed in a Ntuple PAW [BCC+00] readable file for an easier analysis.

The full characterization of the beam starts with the determination of the type of the particle that reaches the scoring plane 2 for each additional collimator, which will

define each different setup. In our study, particles that suffered no interactions between scoring planes 1 and 2 are called unscattered particles and those that suffered at least one interaction are called scattered particles. For each setup, particles from a component arriving at scoring plane 2 with an energy fluence less than 1% of the total energy fluence will be discarded. Simulations show that particles reaching the scoring plane 2 are almost unscattered photons (88.1% for the 5 mm to 94.5% for the 23 mm additional collimator). Scattered photons vary between 11.4% for the 5 mm additional collimator and 4.9% for the 23 mm additional collimator. Unscattered and scattered photons are taken into account in further analysis because they fulfill the criterion defined earlier. The fraction of electrons that reach scoring plane 2 is very small and their energy fluence is less than 1% of the total energy fluence for each additional collimator. Electrons are thus neglected and in all further characterization only photons (unscattered and scattered) will be taken into account. The ratio between the total number of particles that reach scoring plane 2 for an additional collimator and the total number of particle in the $10\times10\times$ cm^2 PSD source varies from 0.006 for the 5 mm additional collimator to 0.117 for the 23 mm additional collimator. This shows the dramatic reduction of the beam intensity and consequently the remarkably poor efficiency in simulating radiosurgery narrow beams.

Unscattered photons

Using MCNP4C, the only available information about the last interaction point or origin of the particle i recorded at scoring plane 2, is the coordinate along the z-axis given by zl_i. For photons, the point (xl_i, yl_i, zl_i) is easy to calculate assuming straight line propagation. If (u_i, v_i, w_i) are the direction cosines of the photon i, then the vectorial straight line equation yields:

$$xl_i = x_i + \frac{u_i}{w_i}\left(zl_i - z_0\right), \tag{6.2}$$

$$yl_i = y_i + \frac{v_i}{w_i}\left(zl_i - z_0\right), \tag{6.3}$$

where (x_i, y_i, z_0) are the coordinates of the particle i at a scoring plane. Once the point (xl_i, yl_i, zl_i) is calculated, an in-house program called XYZLAST calculates if the point is or is not inside a simulated component and then determines from which component of the accelerator head the photon has suffered its last interaction or has been generated. Figure 6.2 shows the relative number of unscattered photons reaching the scoring plane 2 for each accelerator head component and for each additional collimator. According

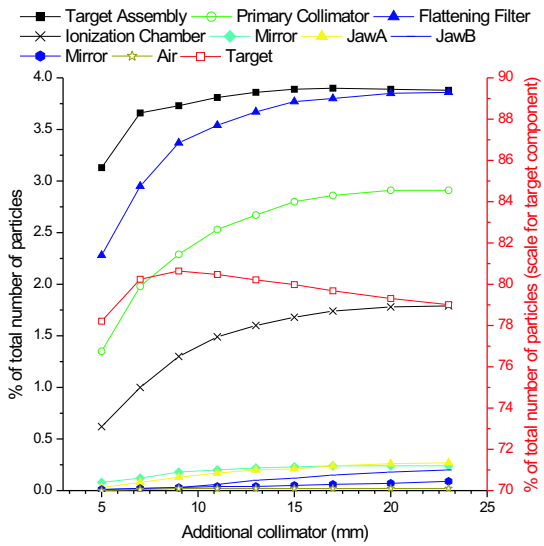

Figure 6.2: Relative number of unscattered photons that reach the scoring plane 2 for all the components of the accelerator head and for each additional collimator. The right scale is only applied to the target component. Normalization was performed to the total number of particles that reach the scoring plane 2 for each additional collimator.

to the results presented in Fig. 6.2, the main accelerator head components from which photons are coming from are the target (around 80% of the total number of particles reaching scoring plane 2 depending on the additional collimator), the target assembly, the flattening filter, the primary collimator and the ionizations chambers. They represent from 85.6% for the 5 mm to 91.4% for the 23 mm additional collimator of the total of particles reaching scoring plane 2. The energy fluence of these components fulfills the criterion defined earlier. The sum of the energy fluence contributions of all the other components (mirror, jaws, reticle and air) represents less than 1% of the total energy fluence for each additional collimator, so these components will not be taken into account in further calculations.

Taking advantage of the radial symmetry of the beams (the jaws components were excluded), radial spatial distributions of the unscattered photons for each additional collimator and for each head accelerator component were calculated. Figure 6.3 shows radial photon fluence distributions for the target component for 4 different additional collimators.

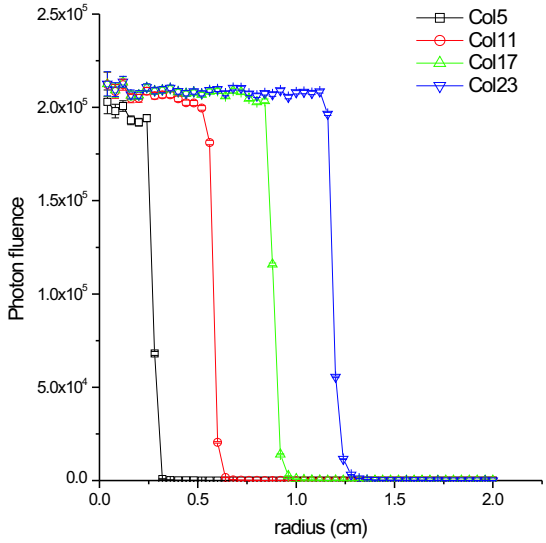

Figure 6.3: Radial fluence distributions of the unscattered photons from target component of the accelerator head at the scoring plane 2 for the 5, 11, 17 and 23 mm additional collimators.

Radial distributions of the photons at origin were also calculated. Figure 6.4 shows the results for photons coming from the primary collimator component. As the linear accelerator was simulated as a 3D object, photons are created along its z-axis. Nevertheless, a mean value of zl_i distribution along z-axis is considered for each component because the distance between scoring plane 2 and the point of origin of these photons is large compared to the dimension of that component. Table 6.1 shows the values of $\overline{zl}$ for the different accelerator head components.

Component	Target	Target Assembly	Primary collimator	Flattening Filter	Ionization chambers
$\overline{zl}$**(cm)**	0	0.908	4.635	9.368	10.910

Table 6.1: Values of $\overline{zl}$ for the different accelerator head components. $\overline{zl}$ represents the average cote along the z-axis of the point of origin of the unscattered photons for different accelerator head components.

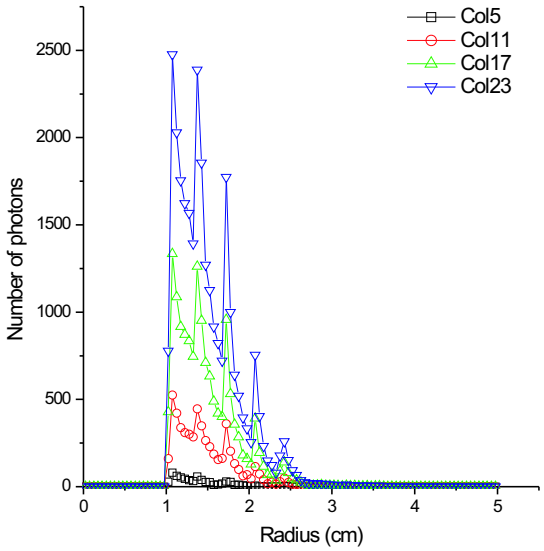

Figure 6.4: Radial distributions of the unscattered photons at origin for the primary collimator component of the accelerator head for the 5, 11, 17 and 23 mm additional collimator. The peaks in the curves are simply due to the geometry of the primary collimator.

In order to analyze the direction of the particle, the polar angle distributions of the unscattered photons were calculated for all the additional collimators and for the five accelerator head components previously considered. Simulations show that the average angle of the unscattered photons can be considered roughly constant for all additional collimators (see Fig. 6.5). As expected for photons coming from each component, when the size of the additional collimator increases, more photons with greater angles can reach scoring plane 2 and increase consequently the average angle of these photons, as shown in Fig. 6.5. This increase is nevertheless very small: less than 0.6 degrees between the 5 mm and the 23 mm additional collimator in the worst case (ionization chambers component). Finally, results show that the beams are very peaked forward (the angles of the photons that reach the scoring plane 2 varies from near 0 to less than 2.5 degrees for photons coming from the ionization chambers).

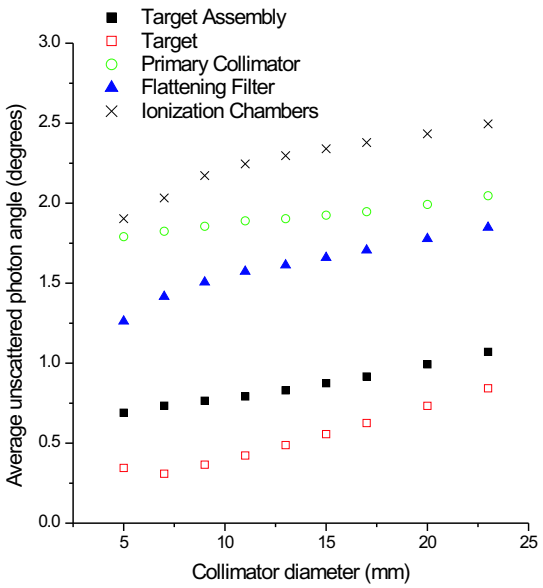

Figure 6.5: Average unscattered photon angle in air for the most relevant accelerator head components and for all additional collimators. For all the additional collimators, calculated relative errors at 1σ are lower than 0.4% for the target component, 1.5% for the primary collimator and target assembly components, 2% for the flattening filter component and finally 3% for the flattening filter component.

The unscattered photons average energy was calculated for each additional collimator and for the five relevant accelerator head components. Figure 6.6 shows the results of such calculations. For the target component, the average energy is roughly constant, from 1.971±0.007 MeV for the 5 mm to 1.941±0.002 MeV for the 23 mm additional collimator. For other components, the average energy decreases as the size of the additional collimator increases from the 5 mm to the 7 mm additional collimators and is roughly constant from the 9 mm to the 23 mm additional collimators. A careful analysis based on radial average energy distributions of unscattered photons for the five components showed that, except in the penumbra region, these distributions for each component are similar for all the additional collimators. Figure 6.7 shows the radial average energy distributions of each component for 23 mm additional collimator: the radial variation of the average energy is very weak for each component except in the penumbra region (where large statistical fluctuations occur due to the few particles present in this region).

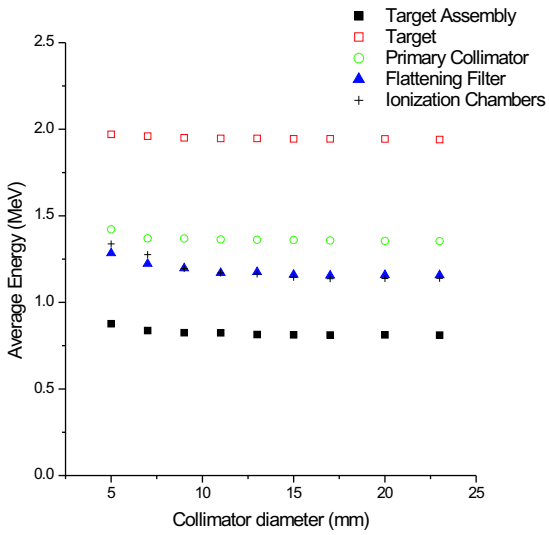

Figure 6.6: Average energy of the unscattered photons that reach the scoring plane 2 from each the relevant accelerator head component. For all the additional collimators, calculated relative errors at 1σ are lower than 0.4% for the target component, 2.5% for the primary collimator and target assembly components, 3% for the flattening filter component and finally 5% for the flattening filter component.

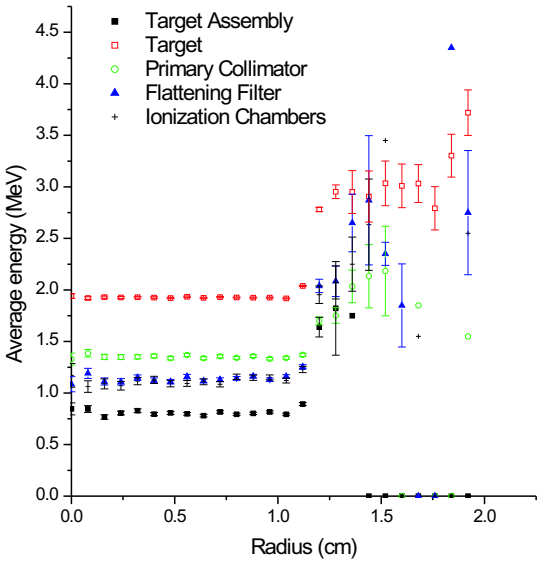

Figure 6.7: Radial average energy distributions of each accelerator head component for photons reaching the scoring plane 2 and for the 23 mm additional collimator.

Also, the simulation results showed that when the number of particles is statistically relevant, energy spectrum for each component does not change significantly for all the

additional collimators (Fig. 6.8 shows energy spectra results for the flattening filter component). According to these energy results, it is reasonable to assume that, for each component and each setup, the energy of the unscattered photons is not correlated with their position. In the penumbra region, because the statistics is very poor (especially

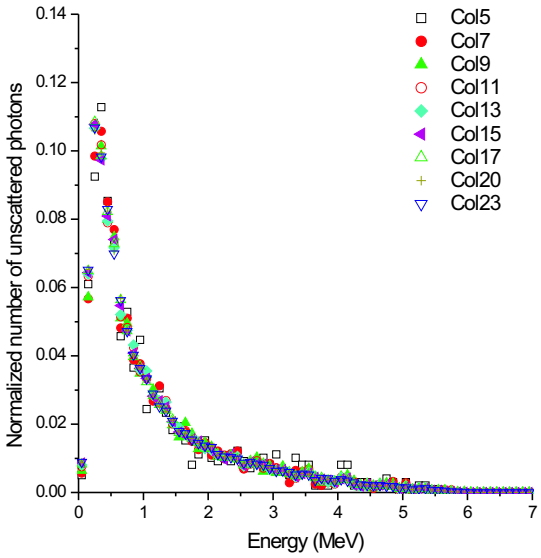

Figure 6.8: Energy spectra for unscattered photons from the flattening filter component for all the additional collimators (the penumbra region was excluded). Normalization was performed to the total number of unscattered photons for this component and for each additional collimator.

for the smallest additional collimators), it is difficult to calculate radial average energy distributions. Nevertheless, unscattered photons average energy can be calculated. Except for unscattered photons coming from the primary collimator component where their average energy is roughly constant as the size of the additional collimator increases (from 1.59±0.06 MeV to 1.54±0.02 MeV), for all the other components, the unscattered photons average energy decreases as the size of the additional collimator increases (from 1.34±0.12 MeV to 1.16±0.03 MeV for the target assembly, from 2.64±0.03 MeV to 2.34±0.01 MeV for the target, from 2.09±0.14 MeV to 1.69±0.03 MeV for the flattening filter and finally from 1.94±0.14 MeV to 1.61±0.04 MeV for the ionization chambers).

Scattered photons

In the case of scattered photons, a distinction must be made between photons that have suffered interactions in the additional collimators or in the air between scoring planes 1 and 2. Photons that have suffered their last interaction in air represent less than 0.01% of the total energy fluence of the particles that reach scoring plane 2, whatever the size of the additional collimator. These photons will not be taken into account. Photons that have their last interaction in the additional collimators must be separated into two components: those that reach scoring plane 2 through the hole of the additional collimator and those that reach scoring plane 2 due to transmission in the additional collimator. In our study these two components will be called the photon additional collimator net component (PAC_net) and the photon additional collimator transmitted component (PAC_trans). The PAC_net and PAC_trans components of the radiation beam can be considered as the contamination part of the beam in the sense of conventional radiotherapy. The contribution to the total energy fluence of particles that reach the scoring plane 2 varies for the PAC_net component between 2.5% and 4.5% for the 5 mm and the 23 mm additional collimators respectively and for the PAC_trans component varies from 8.9% to 0.4% for the same additional collimators.

It is valid to consider just an average coordinate $\overline{zl}$ for all the upward components. However, this assumption is not valid for the additional collimator because the distance between this additional collimator and scoring plane 2 is too short for that approximation. Additional collimators are thus arbitrary subdivided into four equal layers (see Fig. 6.9) where the average angles of the photon directions were calculated. Other quantities such as the photon average energy and radial spatial distributions were also calculated for each layer. According to the criterion that defines if particles from one component must be kept or not for future analysis, only photons coming from layer 4 for the PAC_net component and photons from layers 3 and 4 for the PAC_trans component are taken into account for all the additional collimators. These scattered photons represent, for layer 4 of the PAC_net component, 1.7% to 2.0% of the total energy fluence of particles reaching the scoring plane 2, represent, for layer 3 of the PAC_trans component, from 2.1% to 0.1% of the total energy fluence and, for layer 4 of the PAC_trans component, from 4.7% to 0.2%. For each layer and each component, radial spatial distributions of scattered photons at scoring plane 2 were calculated for all the additional collimators.

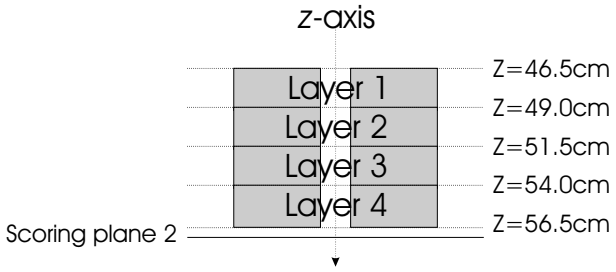

Figure 6.9: Additional collimator subdivided into four equal layers.

The scattered photon average angles for layer 4 of the PAC_net component and for layers 3 and 4 of the PAC_trans component were calculated and results are presented in Fig. 6.10. It is clear that for the PAC_trans component, the average angle is the same

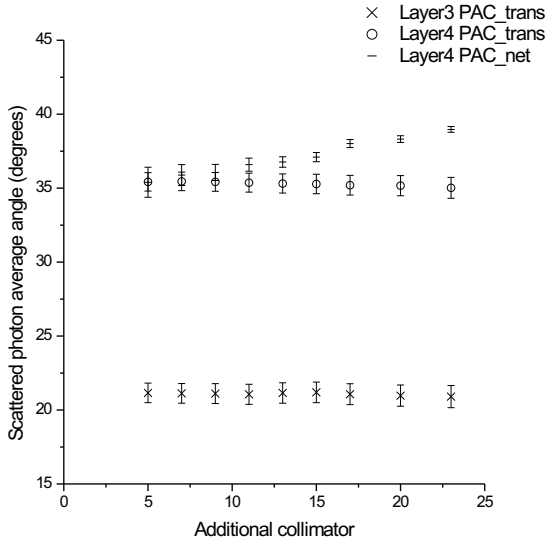

Figure 6.10: Average scattered photon angle in air for the PAC_net and PAC_trans components and for all the additional collimators. Errors bars were added.

for all additional collimators. This is of course due to the nature of this component (transmitted photons). The average angle of the PAC_net component slightly increases as the size of the additional collimators increases. Photons from this component, as defined earlier, reach scoring plane 2 through the hole of the additional collimator. It is clear that as the size of the additional collimator increases, photons originated with larger angles can reach scoring plane 2, then increasing the average angle. But this increase is small, less than 4 degrees. It can be considered in a first approximation that the average angle of photons from the PAC_net component remains constant as the size of the additional collimators increases. The effect of the PAC_net and PAC_trans

components in the radiation beam is clearly a spreading effect. Angles for these photons exceed those of the very peaked forward unscattered photons by 20 degrees.

The average energy of scattered photons coming from layer 4 of the PAC_net component and from layers 3 and 4 of the PAC_trans component was calculated and Fig. 6.11 shows the results as the size of the additional collimator increases. The average

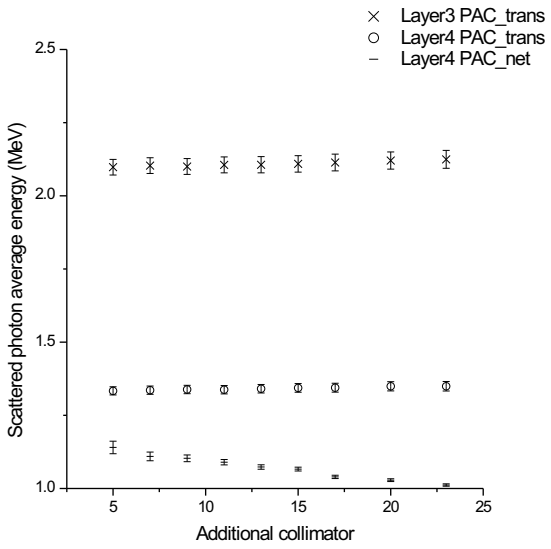

Figure 6.11: Average scattered photon energy in air for the PAC_net and PAC_trans components and for all the additional collimators. Errors bars were added.

photon energy remains constant for the scattered photons from layers 3 and 4 of the PAC_trans component whereas the average energy decreases slightly as the size of the additional collimator increases for photons of layer 4 of the PAC_net component. The behavior of the different curves can be explained by the two main interaction processes occurring in the additional collimators as shown by Monte Carlo simulations: bremsstrahlung and Compton processes. The direction of the created photon (bremsstrahlung) or scattered photon (Compton) is related with its energy: photons with larger angles of emission have lower energies [KM59, Kha84]. This is confirmed in Fig. 6.11 for the PAC_net component, when the size of the additional collimators increases, the scattered photon average energy decreases slightly whereas the scattered photon average angle increases slightly. In the case of the PAC_trans component, photons created near the top of the additional collimator must have a larger energy than those created at the bottom in order to reach scoring plane 2. This is confirmed in Fig. 6.11 where the average energy of scattered photons from layer 3 is larger than average

energy of scattered photons from layer 4.

Finally, spectra for each of the chosen layers of the additional collimator and the two scattered components are calculated. Results from the simulations show that for each photon component (PAC_net and PAC_trans) and for the same layer, scattered photon spectra for all the additional collimators are roughly the same. Figure 6.12 shows an example of such simulation for layer 4 of the PAC_net component.

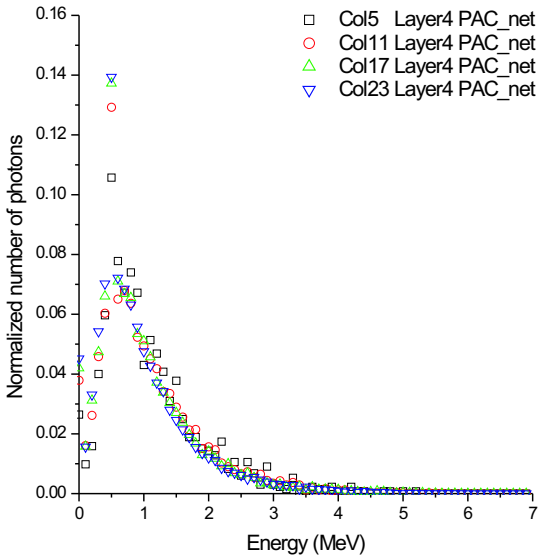

Figure 6.12: Scattered photon energy spectra for the PAC_net component. For each additional collimator, the energy spectrum is normalized to the total number of photons from this component.

6.1.2 Definition of the relevant virtual sources

Multiple source models are based on the assumption that all the particles originated in one accelerator component have the same characteristics and can be treated as if they were coming from a virtual source representing that accelerator component [MFR+97]. These models are also based on the fact that the energy ranges and incident directions of particles from a specific component are almost independent from the position of the particles in the scoring plane. According to the results of the full characterization of the PSDs of all the additional collimators at the scoring plane 2, the energy of the unscattered photons is not correlated to their position for $r_i = (x_i^2 + y_i^2)^{1/2} \leqslant Rc$ (Rc equal to the radius of the additional collimator). In the penumbra region ($r_i > Rc$),

the calculation of radial average energy distributions was not possible due to the poor statistics. In order to apply the multiple source model, it will be considered that the position of these photons is not correlated with their energies. Then the model proposed by Deng *et al.* [DJK+00] can be applied for the unscattered photons and using this model, the representation of a beam, ϕ_c^u, takes the following form for each additional collimator:

$$\phi_c^u\left(x_i, y_i, u_i, v_i, E_i\right) = \sum I_{j,i}^c f_j^c\left(E_i, r_i\right) \phi_j^c\left(x_i, y_i, xl_i, yl_i\right), \tag{6.4}$$

where for each additional collimator c, $I_{j,i}^c$ is the relative source intensity for source j of the photon i, (x_i, y_i) the coordinates of the photon i at scoring plane 2, (xl_i, yl_i) the coordinates of the photon i at its origin. $f_j^c\left(E_i, r_i\right)$ and $\phi_j^c\left(x_i, y_i, xl_i, yl_i\right)$ are respectively, the energy and fluence photon distributions with $r_i = (x_i^2 + y_i^2)^{1/2}$. In our multiple source model, for unscattered photons, $f_j^c\left(E_i, r_i\right)$ take two forms: $f_j^{c,1}\left(E_i, r_i\right)$ and $f_j^{c,2}\left(E_i, r_i\right)$ representing energy distributions with $r_i \leqslant Rc$ and $r_i > Rc$ respectively. In this model (x_i, y_i) and (xl_i, yl_i) are assumed not to be correlated. Then the direction of the photon at scoring plane 2 can be calculated and:

$$u_i^2 + v_i^2 + w_i^2 = 1. \tag{6.5}$$

As stated earlier, the scoring plane 2 is placed just below the additional collimator. We have developed, in our study, a simple model to calculate the direction of the scattered photons. We assume that for each additional collimator and for each layer, the scattered photons at scoring plane 2 have the same (u, v) distribution independently of their position in this scoring plane.

Due to the poor statistics, it is not possible to calculate, with a good accuracy, the values of average energy as a radial function. In that way, it is difficult to find if it exists or not a correlation between the position of the photons at scoring plane 2 and their average energy, enabling the separation between the energy and position. As done for unscattered photons with $r_i > Rc$, scattered photon position and energy must be considered uncorrelated in order to apply the multiple source model. Thus, for scattered photons, the beam representation ϕ_c^s for each additional collimator c is given by:

$$\phi_c^s\left(x_i, y_i, u_i, v_i, E_i\right) = \sum I_{j,i}^c g_j^c\left(E_i\right) \phi_j^c\left(x_i, y_i\right) \mu_j^c\left(u_i, v_i\right), \tag{6.6}$$

where $g_j^c\left(E_i\right)$ is the photon energy distribution, $\phi_j^c\left(x_i, y_i\right)$ is the photon spatial distribution at scoring plane 2 and $\mu_j^c\left(u_i, v_i\right)$ the (u, v) distribution at the same scoring

plane. Vector w_i is calculated using Eq. 6.5.

Some simplifications can be performed in Eqs 6.4 and 6.6. The first simplification comes from the radial symmetry of the beams: the coordinates (x_i, y_i) and (xl_i, yl_i) of the photons can be represented by the radial values r_i and rl_i (in the case of unscattered photons). The second simplification deals with the energy of the photons at the scoring plane 2. In this work, it was demonstrated for unscattered photons with $r_i \leqslant Rc$ and for scattered photons that all the photons at scoring plane 2 from each component have similar energy distributions for all additional collimators. So just one energy distribution for each component is necessary to build a multiple source model. For statistical reasons, the energy distributions of the 23 mm additional collimator were chosen. For unscattered photons with $r_i > Rc$, it will be considered that the energy distributions will be the same and equal (for statistical reasons) to the energy distributions of the 23 mm additional collimator. This approximation can be justified because the energy fluence of these photons is small compared to the total energy fluence: it represents from 7.5% for the 5 mm to 4.5% for the 23 mm additional collimator of the total energy fluence of the particles reaching scoring plane 2. With all these considerations, Eqs. 6.4 and 6.6 become for each additional collimator:
for unscattered photons:

$$\phi_c^u\left(x_i, y_i, u_i, v_i, E_i\right) = \sum I_{j,i}^c f_j^{23}\left(E_i, r_i\right) \phi_j^c\left(r_i, rl_i\right), \tag{6.7}$$

for scattered photons:

$$\phi_c^s\left(x_i, y_i, u_i, v_i, E_i\right) = \sum I_{j,i}^c g_j^{23}\left(E_i\right) \phi_j^c\left(r_i\right) \mu_j^c\left(u_i, v_i\right). \tag{6.8}$$

Finally, Table 6.2 shows the intensity of the eight chosen relevant virtual sources to build our RMSM.

Component	col5	col7	col9	col11	col13	col15	col17	col20	col23
Target	80.87	82.60	83.05	83.10	83.04	82.98	82.94	82.89	82.89
Target Assembly	3.24	3.77	3.84	3.93	3.99	4.04	4.05	4.07	4.07
Primary Collimator	1.40	2.03	2.35	2.61	2.77	2.90	2.97	3.05	3.05
Flattening Filter	2.36	3.04	3.47	3.65	3.80	3.91	3.96	4.03	4.05
Ionization Chambers	0.64	1.03	1.34	1.54	1.66	1.74	1.81	1.86	1.88
Layer 4 PACnet	2.87	3.06	3.26	3.40	3.51	3.52	3.58	3.64	3.74
Layer 3 PACtrans	1.94	1.01	0.61	0.40	0.28	0.21	0.16	0.11	0.08
Layer 4 PACtrans	6.69	3.46	2.07	1.36	0.95	0.69	0.52	0.36	0.25

Table 6.2: Percentage intensities of the relevant virtual sources representing the accelerator head plus the additional collimator.

6.1.3 Beam reconstruction

In order to simplify data manipulation, the HBOOK routines from the Cernlib were used [Bru94]. All the distributions are 1D or 2D histograms from where samplings were performed. The choice of the histogram bins is important. For each relevant virtual source, the bins of the histograms were chosen according to the size of the voxels in the patient-dependent simulation block and also to the statistics of each distribution.

The first step in beam reconstruction is the choice of the virtual relevant source from where all the photon characteristics will be calculated. A sampling is performed according to the intensity of each virtual source for a predefined additional collimator.

The next step in beam reconstruction is the determination of the photon position. All the sources are defined at scoring plane 2. Using cylindrical symmetry, each source is a circular disc with a finite radius R_{max} which depends on the virtual source. Then, for one source, the Cartesian coordinates of a photon i are defined at scoring plane 2 as follows:

$$x_i = r_i \cos(\theta_i), \tag{6.9}$$

$$y_i = r_i \cos(\theta_i), \tag{6.10}$$

with $0 \leq r_i \leq R_{max}$ and $0 \leq \theta_i \leq 2\pi$. However, just for unscattered photons, and for each source, the spatial photon distributions at origin $(\overline{zl})$ are used to calculate the photon direction: the coordinates at photon origin (xl_i, yl_i) are defined as $xl_i = r_i \cos(\theta_i')$ and $yl_i = r_i \sin(\theta_i')$ with $0 \leq r_i \leq Rl_{max}$ and $0 \leq \theta_i' \leq 2\pi$, where Rl_{max} is the maximum radius of the circular surface at the cote $\overline{zl}$ of origin of the photons for that

component. The coordinates of the photon (x'_i, y'_i) at scoring plane 2 for the considered source is then calculated using the following procedure:

1. r_i is sampled from the distribution of the virtual source,
2. θ_i is sampled uniformly from 0 to 2π,
3. x'_i and y'_i are calculated from Eqs. 6.9 and 6.10.

This procedure is also used to calculate (xl'_i, yl'_i) for unscattered photons for the determination of the direction. Using radial distributions increase the quality of the distributions. In fact because of the poor statistics associated with this kind of simulation, the initial (x_i, y_i) distribution (results from simulation) presents large statistical variations between adjacent bins as shown in Fig. 6.13 where the spatial distribution at scoring plane 2 of photons coming from target for the 23 mm additional collimator is presented. Using a radial distribution allows calculating an average number of photons in an annulus $r + dr$ increasing the statistics and then enhancing the quality of the reconstructed (x'_i, yi') distribution as shown in Fig. 6.14.

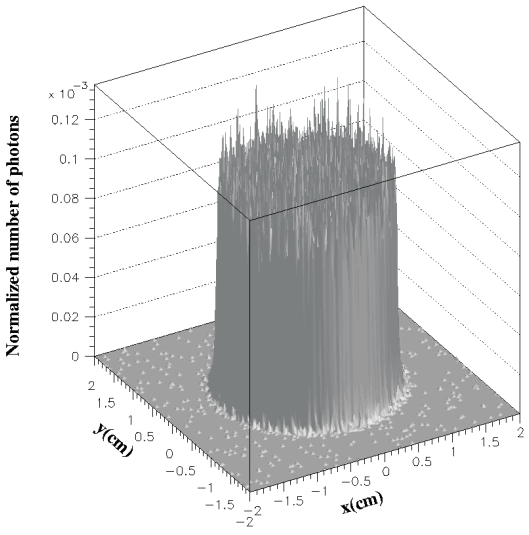

Figure 6.13: Spatial distribution for unscattered photons coming from the target component reaching the scoring plane 2 for the 23 mm additional collimator.

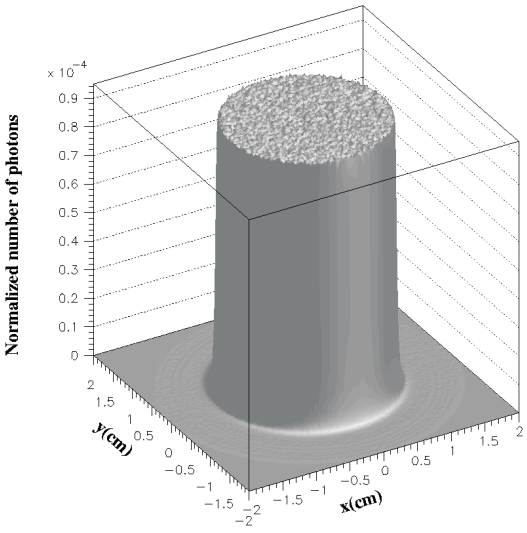

Figure 6.14: Reconstructed spatial distribution for target unscattered photons at scoring plane 2 for the 23 mm additional collimator after applying the circular symmetry optimization.

The third step in the beam reconstruction is the photon direction calculation. For an unscattered photon, a sampling is performed in the (rl_i) distribution in order to calculate (xl'_i, yl'_i). Once (x'_i, y'_i) and (xl'_i, yl'_i) are determined, the direction of the unscattered photon is given by:

$$u'_i = \frac{x'_i - xl'_i}{d'_i}, \tag{6.11}$$

$$v'_i = \frac{y'_i - yl'_i}{d'_i}, \tag{6.12}$$

where d'_i is the distance between (x'_i, y'_i) and (xl'_i, yl'_i) and w'_i is calculated from Eqs. 6.5. In the case of a scattered photon, a sampling is performed in the $\mu^c_j(u_i, v_i)$ distribution and w'_i is calculated from Eqs. 6.5.

The last step in the beam reconstruction is the determination of the energy of the photon. For an unscattered photon if $r'_i \leq Rc$ then a sampling is performed in the $f_j^{23,1}$ distribution otherwise a sampling is performed in the $f_j^{23,2}$ distribution. For a scattered photon, a sampling is performed in the g_j^{23} distribution. Figure 6.15 resumes all the beam reconstruction process.

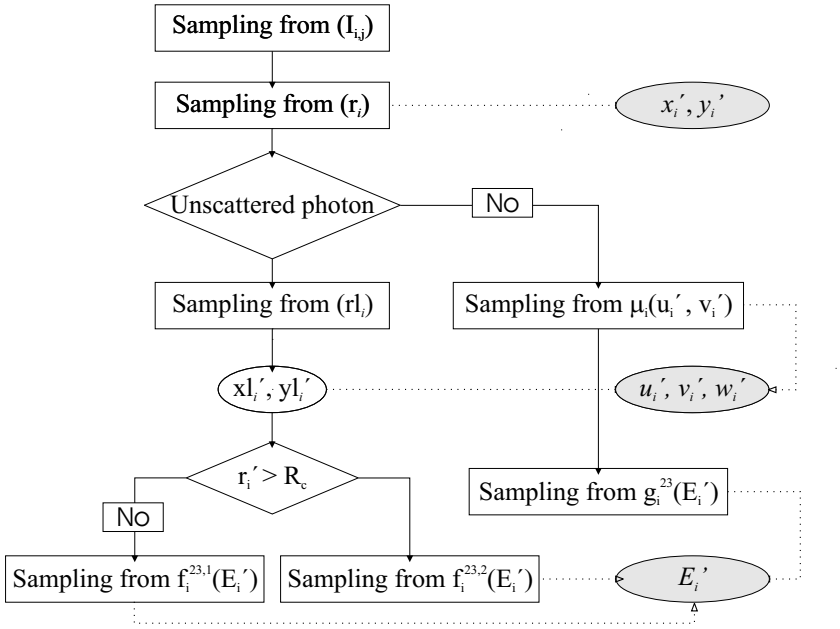

Figure 6.15: Beam reconstruction process.

6.2 Validation of RMSM

Measurements were performed in a PTW-Freiburg MP3 motorized water phantom. The PTW-Freiburg PinPoint chamber type 31006 (volume 0.015 cm^3) and the PTW-Freiburg diode type TM60008 were used to obtain depth dose curves but only the diode was used to obtain dose profiles. All calculations were performed in a PC with a Pentium III (800 Mhz) processor and 128 Mb of RAM.

The fast MC code DPM was used to simulate the patient-dependent block which in our study is a $20 \times 20 \times 50$ cm^3 water phantom divided into 20000 voxels of $1 \times 1 \times 5$ mm^3. The SSD was fixed at 100 cm. In all simulations, the electron absorption energy in water was fixed at 200 keV and the photon absorption at 50 keV. The minimum ($Emin$) and maximum ($Emax$) electron energy in look-up tables were fixed at 199 keV and 21 MeV. The minimum photon energy in look-up tables ($Emin\_ph$) was fixed at 49 keV. The cutoff energy for δ-ray production (Wcc) was fixed at 200 keV and the cutoff energy for bremsstrahlung production (Wcb) at 50 keV. And finally the step length parameters $shigh$, $slow$ and $ecross$ were fixed at 0.5 cm, 0.1 cm and 5 MeV. Because data are stored in 1D or 2D histograms, the HBOOK routines were included into DPM. The generator number RANLUX [MZ94, Jam94] was also included into DPM. Calculations for each additional collimator are performed in the entire simulated water phantom

but only results from a rectangular region of interest ($8 \times 8 \times 50$ cm^3) are analyzed.

6.2.1 Number of histories in DPM simulations

The number of histories in a simulation is a crucial parameter. It must be chosen according to a balance between the simulation running time and the values of the statistical errors associated with the simulated results. This number is of course different for each additional collimator. In order to optimize the simulation running time for each additional collimator, a relationship between the number of original histories and each additional collimator was established based on the correspondent output factor. The output factor $OF(Rc)$ of a collimator of diameter Rc is defined as [LST$^+$00]:

$$OF(Rc) = \frac{D_{max}(Rc)}{D_{max}(ref)}, \tag{6.13}$$

where $D_{max}(Rc)$ is the maximum absorbed dose in water in the beam central axis of a Rc additional collimator field and $D_{max}(ref)$ is the corresponding value for the reference field size. OF values have already been calculated from full MC simulations using MCNP4C (see Chapter 4) and results are presented in Table 6.3 (OF_{4C}) for a 10×10 cm^2 reference field size. In this study, the developed multiple source model can only be applied to the additional collimators. That is, $D_{max}(10 \times 10$ cm$^2)$ can not be calculated but using the previous OF_{4C} results, Eq. 6.13 can be rewritten as following:

$$OF(Rc) = OF_{4C}(23)\frac{D_{max}(Rc)}{D_{max}(23)}, \tag{6.14}$$

In DPM simulations, the calculated dose D_{max}^{RM} is normalized to the number of original histories n_{RM} for each setup. Taking the assumption that OF calculated by RMSM must be equal to OF calculated by MCNP4C, Eq. 6.14 becomes:

$$OF_{RM}(Rc) = OF_{4C}(Rc) = OF_{4C}(23)\frac{n_{RM}(Rc)D_{max}^{RM}(Rc)}{n_{RM}(23)D_{max}^{RM}(23)}. \tag{6.15}$$

It was established that the relative error associated to dose calculations for the 23 mm additional collimator at d_{max} (point of maximum dose along the beam central axis) should be lower than 2% at 2σ. According to this criterion, a simulation with the RMSM for the 23 mm additional collimator was performed for a number of original histories of 7.2×10^8. The calculated number of original histories for each additional collimator based on OF_{4C} simulation results and Eq. 6.15 is presented in Table 6.3. This rational will be useful for future beam additions which is the basis of a radiosurgery treatment and warrants that OF calculated by RMSM is accurate if the ratio $\frac{n_{RM}(Rc)}{n_{RM}(23)}$ presented in Table 6.3 for each additional collimator is used.

Additional Collimator (mm)	$\frac{n_{RM}(Rc)}{n_{RM}(23)}$	OF_{4C}	OF_{RM}
5	0.046	0.790±0.015	0.788±0.019
7	0.090	0.852±0.016	0.852±0.020
9	0.150	0.886±0.016	0.886 ±0.020
11	0.224	0.909±0.017	0.909±0.020
13	0.313	0.926±0.017	0.926±0.021
15	0.423	0.941±0.017	0.940±0.021
17	0.542	0.952±0.017	0.953±0.021
20	0.754	0.963±0.017	0.964±0.022
23	1.000	0.971±0.017	0.971±0.022

Table 6.3: Relative number of original histories for each additional collimator based on output factors calculated by MCNP4C (OF_{4C}). Results are normalized to the number of original histories $n_{RM}(23) = 7.2 \times 10^8$. OF calculated by RMSM are also presented.

6.2.2 Dose distributions

For each additional collimator, PDD along the beam central axis and $OARs$ at various depths along the x- and y-axis were calculated and compared with measurements. The tolerances used in these comparisons for γ quality index calculations are the same used in Chapter 4. An in-house analyzing tool was developed to extract the desired dosimetric data from the DPM output calculated 3D dose matrix. The chosen depths for dose profiles were 52.5 mm, 102.5 mm, 152.5 mm and 202.5 mm. A total of 7.2×10^8 initial photons were simulated for the 23 mm additional collimator and using results from Table 6.3, CPU running times varied from 0.60 h for the 5 mm to 11.43 h for the 23 mm additional collimator. Calculated associated errors from DPM at 2σ were lower than 2.5% until a depth of 202.5 mm for all the additional collimators.

Figures 6.16 (a)- (i) show the calculated PDDs and compare them with PDDs measured with the diode. Results are normalized at 50 mm depth. Results from RMSM are also compared with MCNP4C calculations (DDC simulations performed in Chapter 4). For depths lower than 10 mm, the γ-index are greater than 1. In the buildup region, the diode is not suitable (see Chapter 4). For depths higher than 10 mm, a good agreement between the calculated and measured, with the diode, depth dose curves was found since the γ-index is generally lower than 1. Large γ-indexes as shown for example for 11 mm additional collimator (Fig. 6.16 (d)) are mainly due to statistical

fluctuations.

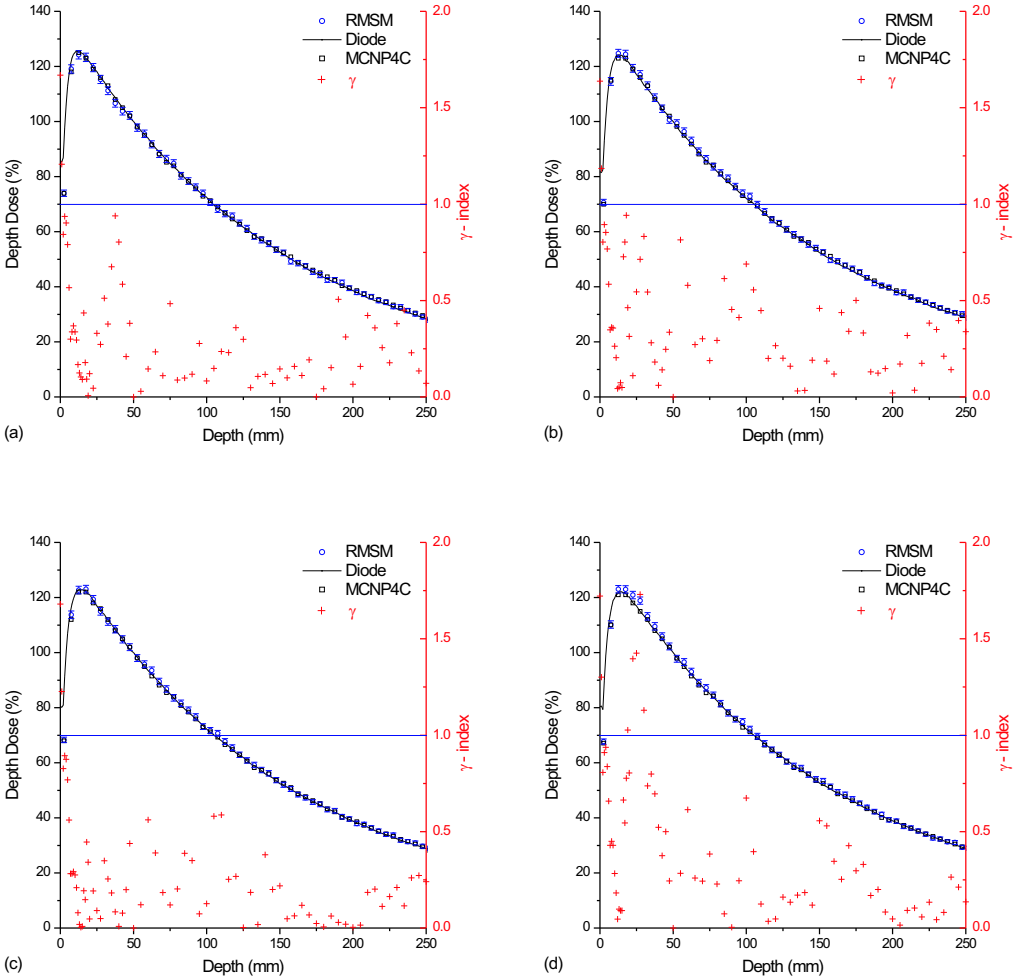

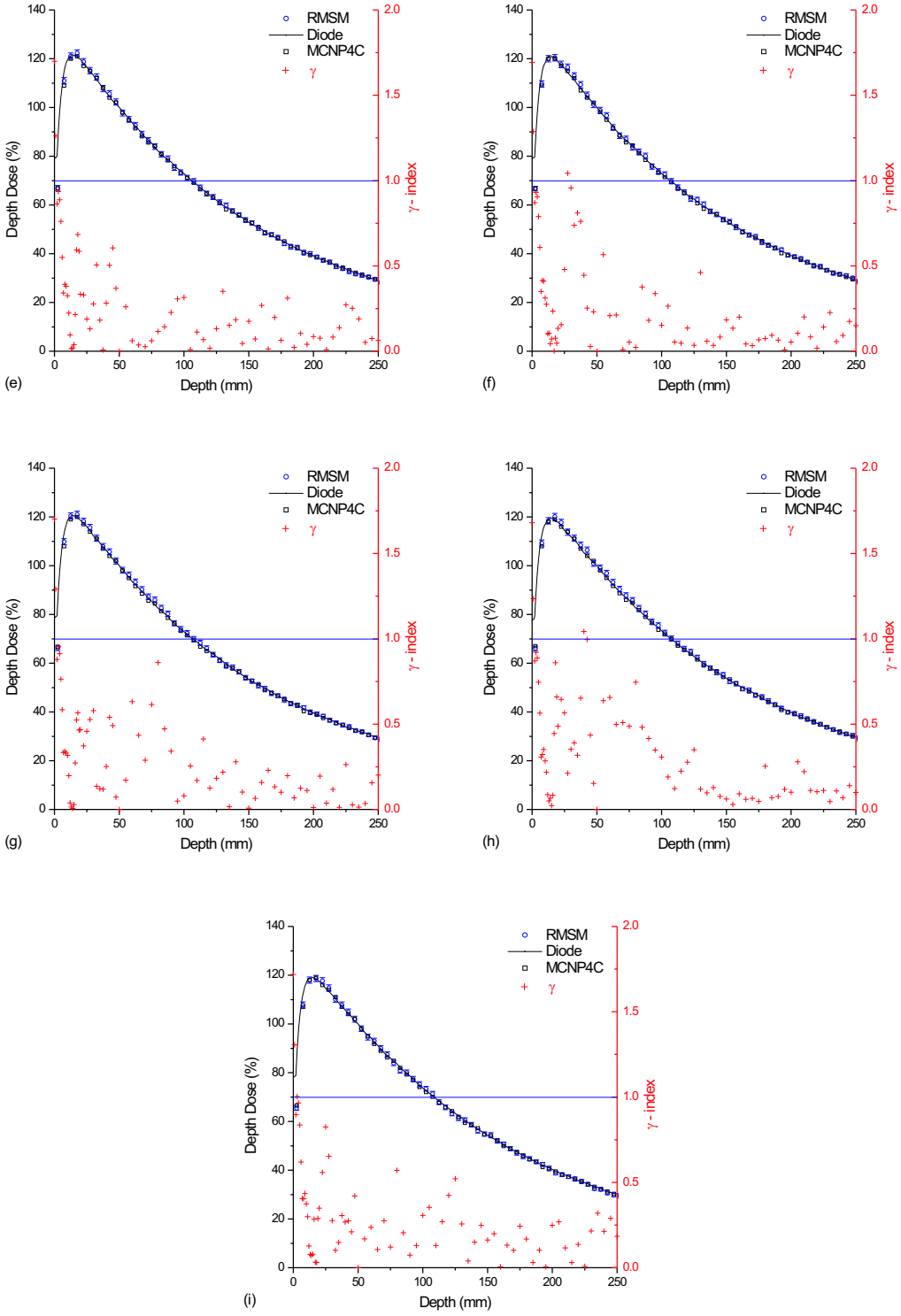

Figure 6.16: A comparison between calculated with RMSM and measured percent depth dose ($SSD = 100$ cm). Each graphic represents the results for one additional collimator: (a) col5, (b) col7, (c) col9, (d) col11, (e) col 13, (f) col15, (g) col17, (h) col20, (i) col23. Results are normalized to value of dose at 50 mm depth for each additional collimator. The γ quality index is plotted for each measurement point with the diode. Percent depth dose calculated with MCNP4C is also plotted.

Finally, Figs. 6.17-6.25 show the calculated $OARs$ compared with the measured $OARs$ in the x-axis and y-axis for all the additional collimators. Results are normalized at the maximum dose point along the beam central axis. A good agreement was found between measured and calculated $OARs$ since the calculated γ-indexes are lower than 1, except in only one case (7 mm additional collimator in the y-axis) due to a possible statistical fluctuation.

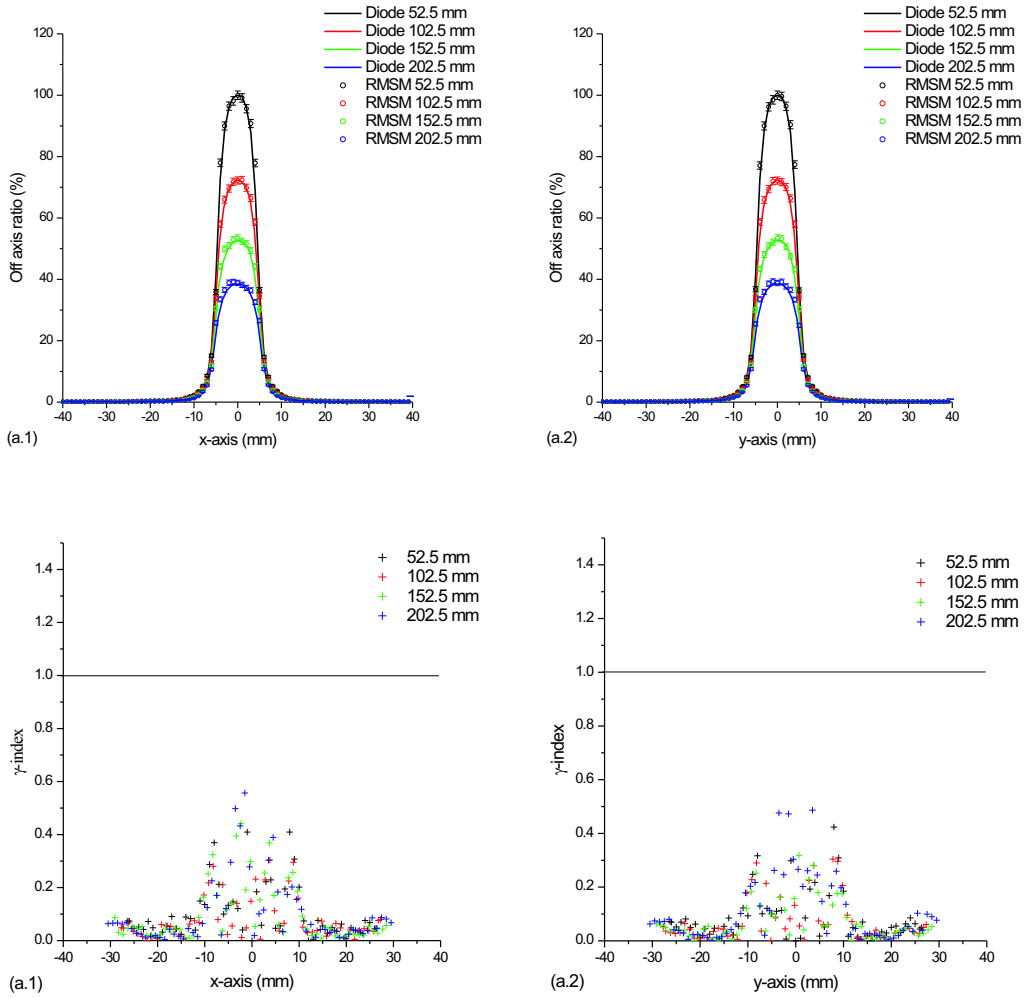

Figure 6.17: A comparison between calculated (RMSM) and measured (diode) off-axis ratios (OAR) at various depths in water along (1) the x-axis and (2) the y-axis for the 5 mm additional collimator. In each axis, the γ-index is calculated.

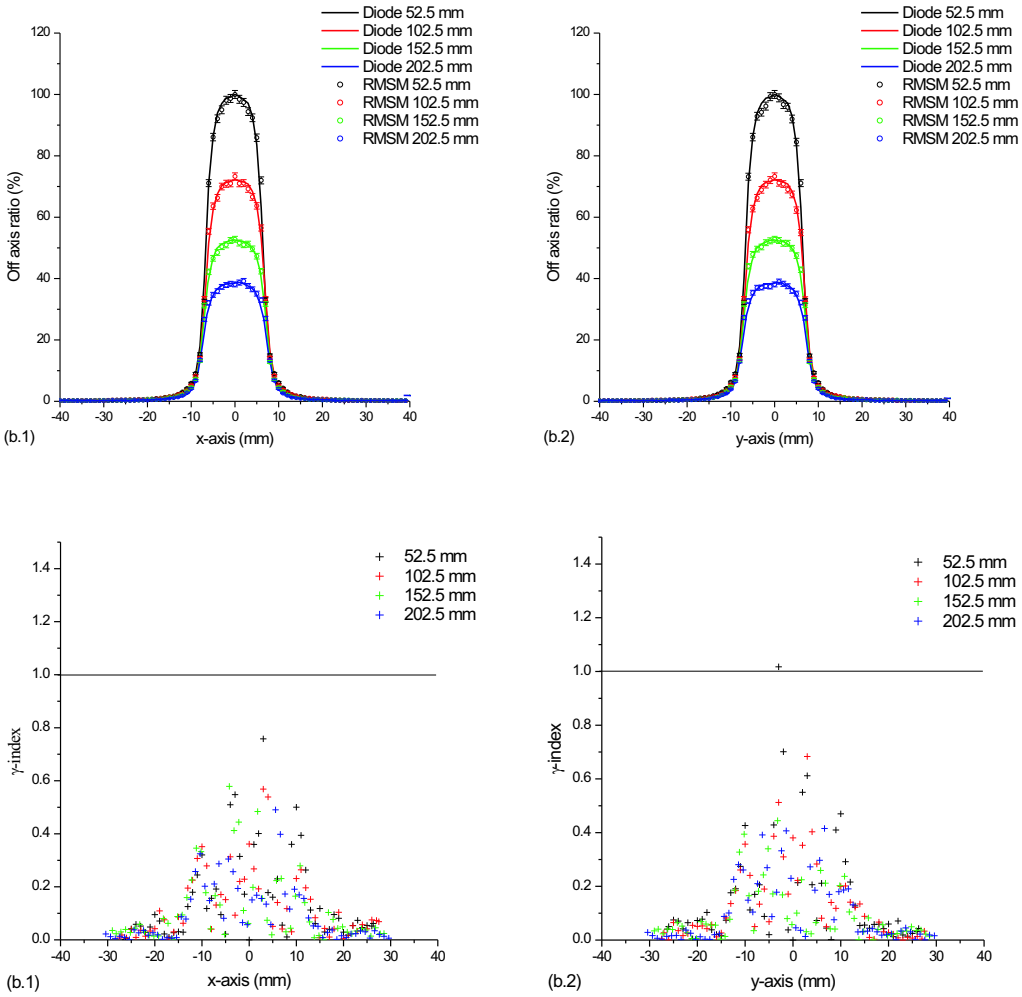

Figure 6.18: A comparison between calculated (RMSM) and measured (diode) off-axis ratios (OAR) at various depths in water along (1) the x-axis and (2) the y-axis for the 7 mm additional collimator. In each axis, the γ-index is calculated.

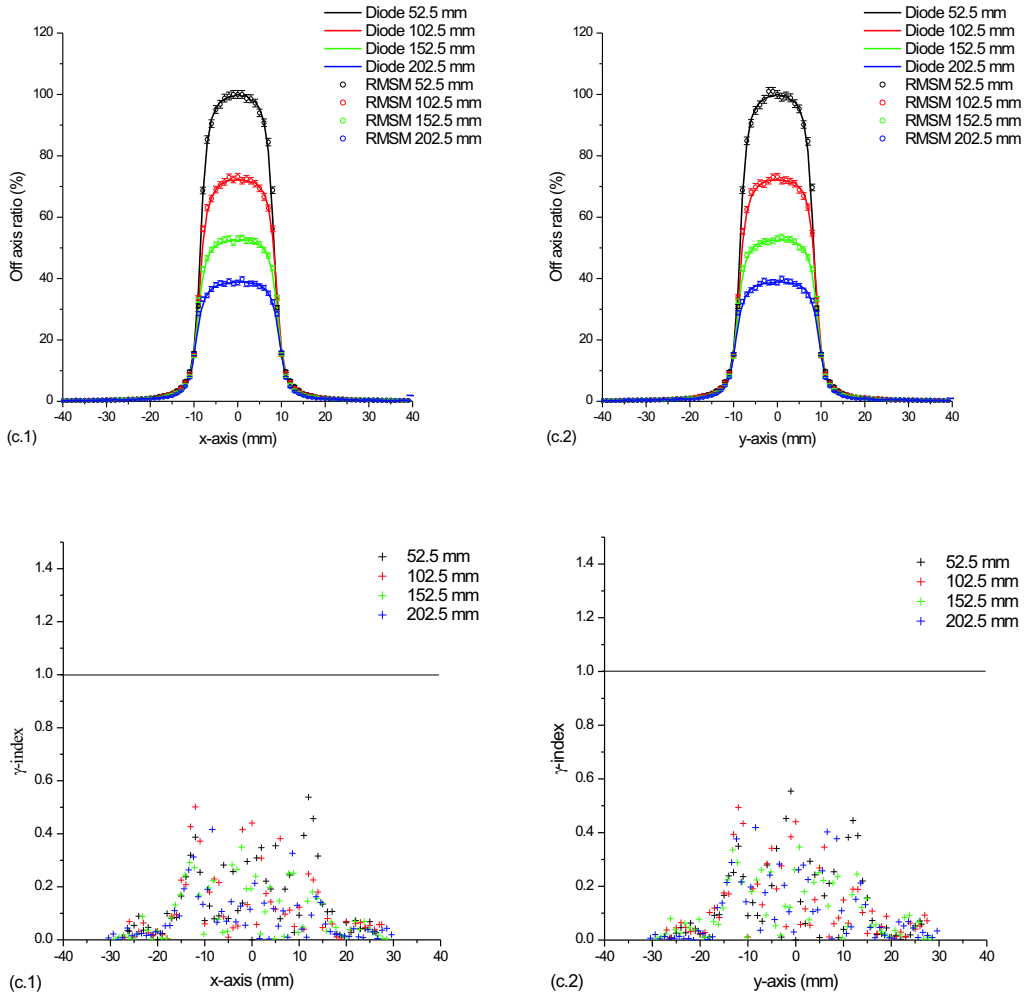

Figure 6.19: A comparison between calculated (RMSM) and measured (diode) off-axis ratios (OAR) at various depths in water along (1) the x-axis and (2) the y-axis for the 9 mm additional collimator. In each axis, the γ-index is calculated.

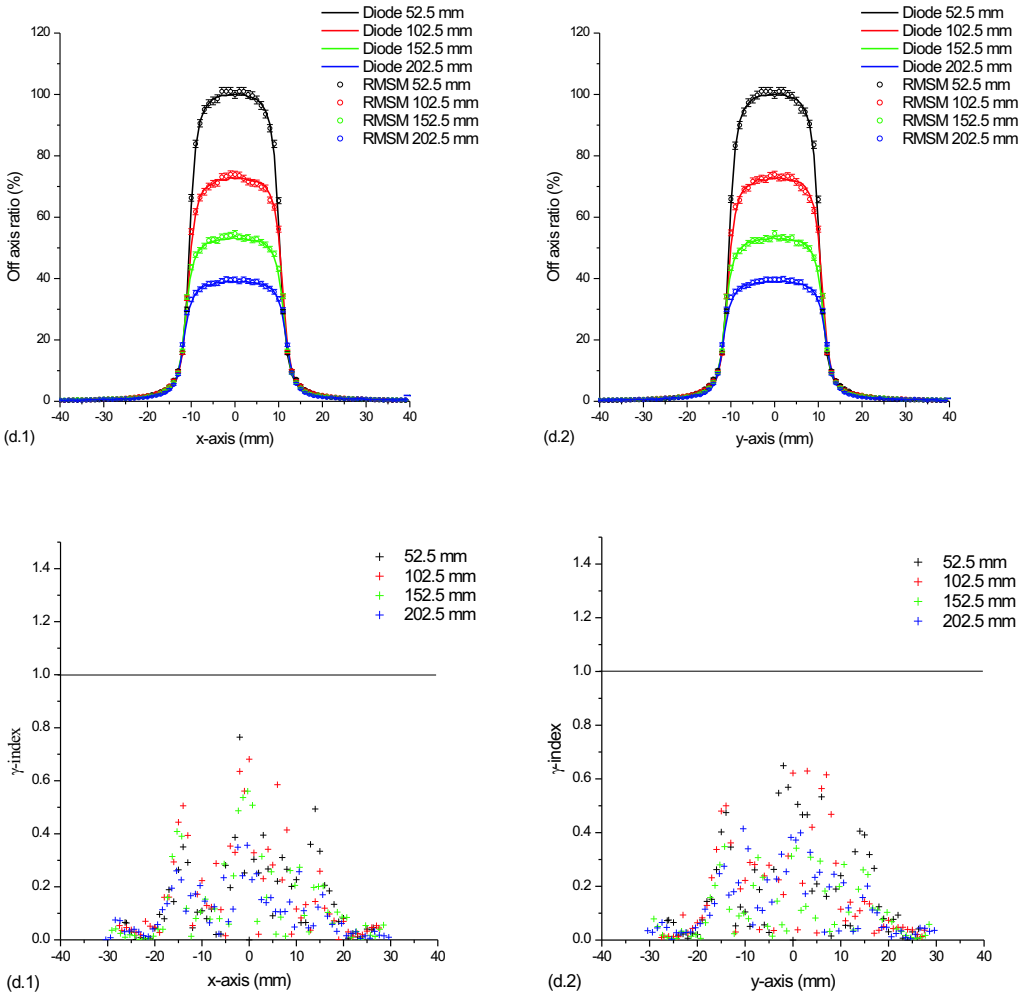

Figure 6.20: A comparison between calculated (RMSM) and measured (diode) off-axis ratios (OAR) at various depths in water along (1) the x-axis and (2) the y-axis for the 11 mm additional collimator. In each axis, the γ-index is calculated.

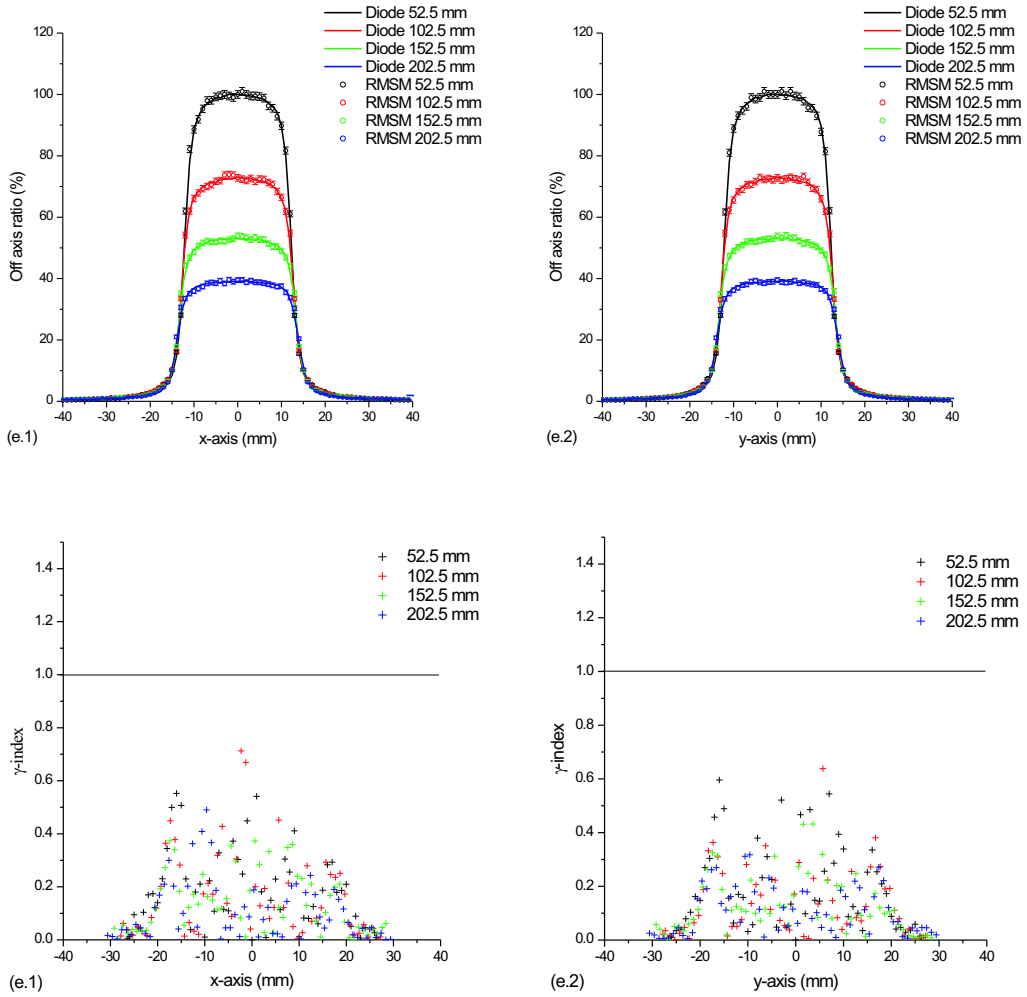

Figure 6.21: A comparison between calculated (RMSM) and measured (diode) off-axis ratios (OAR) at various depths in water along (1) the x-axis and (2) the y-axis for the 13 mm additional collimator. In each axis, the γ-index is calculated.

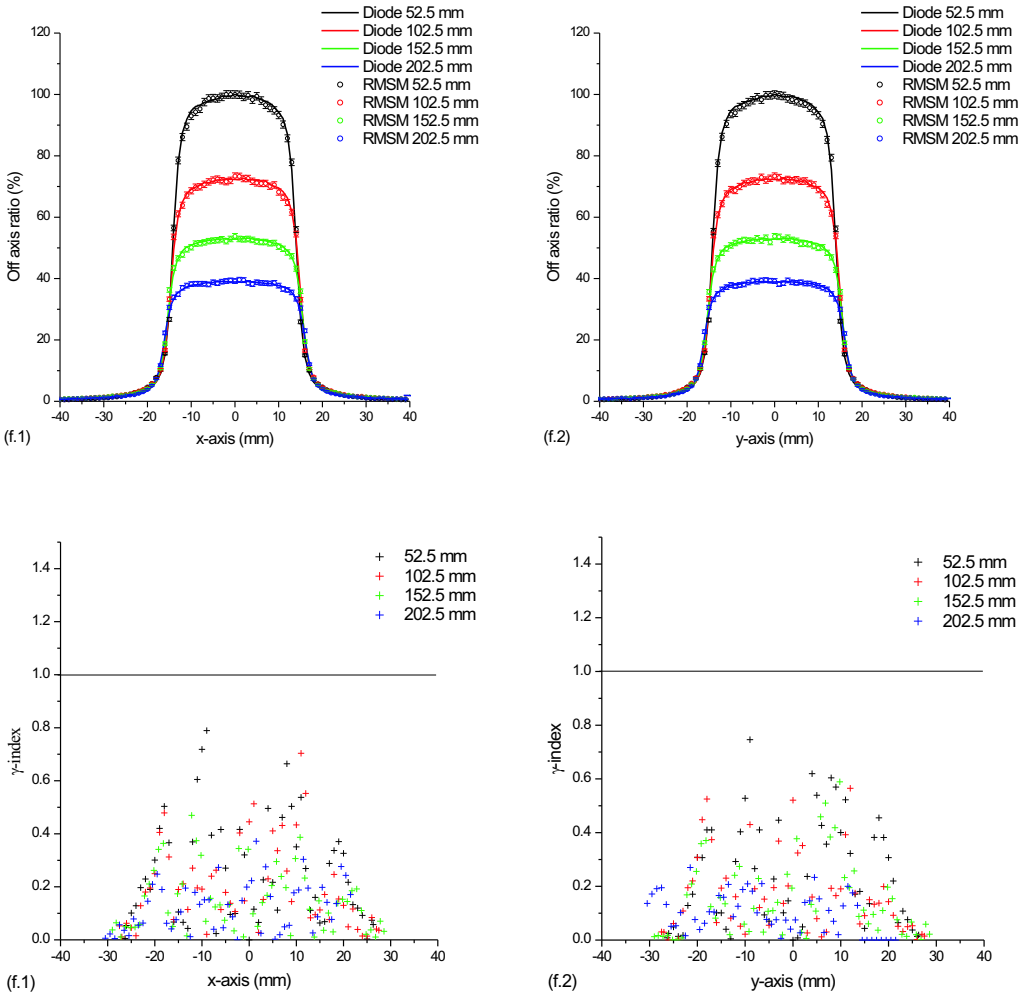

Figure 6.22: A comparison between calculated (RMSM) and measured (diode) off-axis ratios (OAR) at various depths in water along (1) the x-axis and (2) the y-axis for the 15 mm additional collimator. In each axis, the γ-index is calculated.

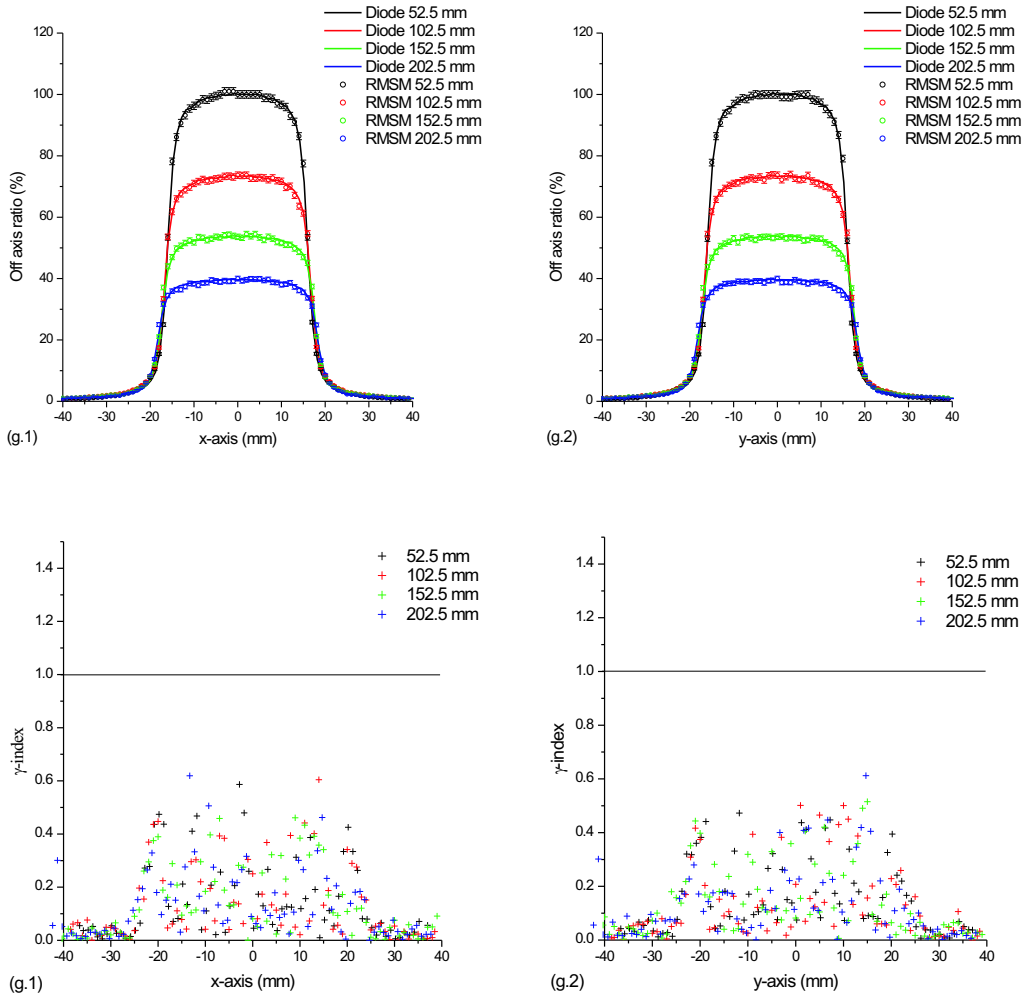

Figure 6.23: A comparison between calculated (RMSM) and measured (diode) off-axis ratios (OAR) at various depths in water along (1) the x-axis and (2) the y-axis the 17 mm additional collimator. In each axis, the γ-index is calculated.

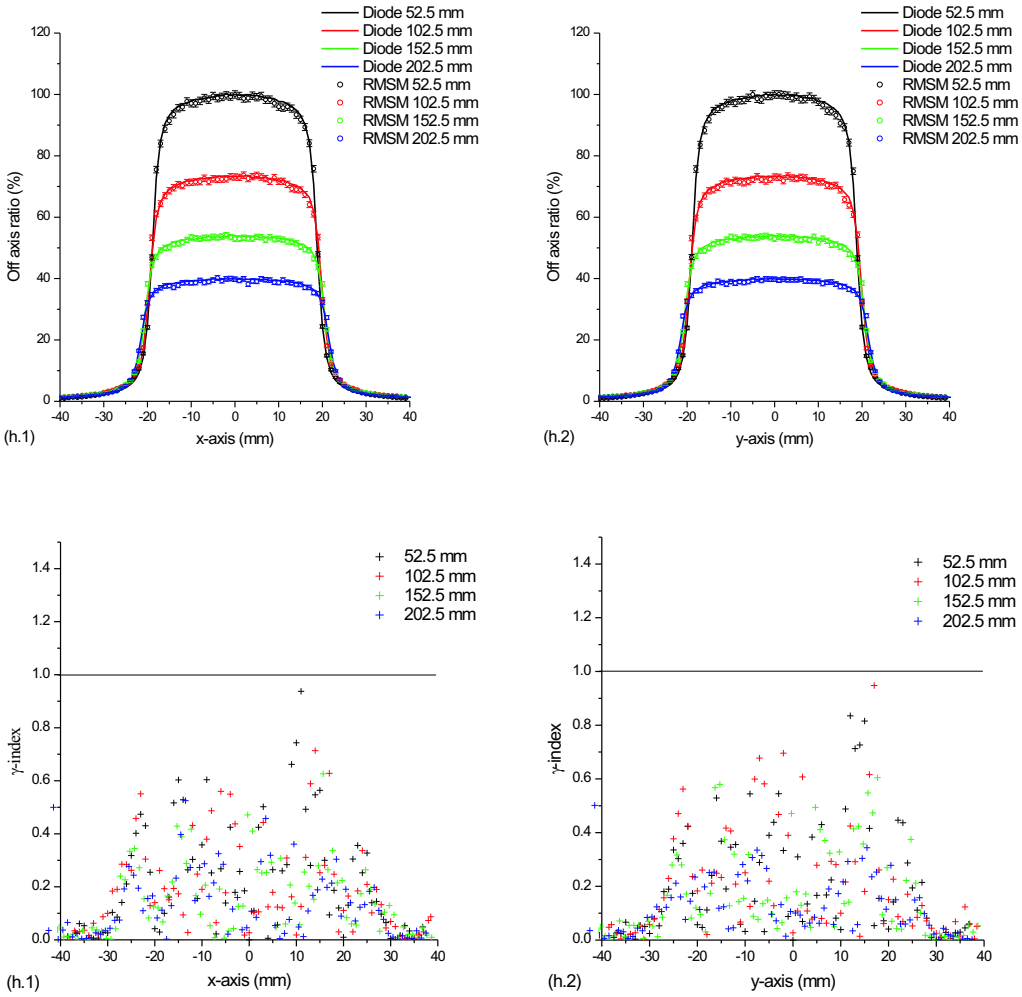

Figure 6.24: A comparison between calculated (RMSM) and measured (diode) off-axis ratios (OAR) at various depths in water along (1) the x-axis and (2) the y-axis for the 20 mm additional collimator. In each axis, the γ-index is calculated.

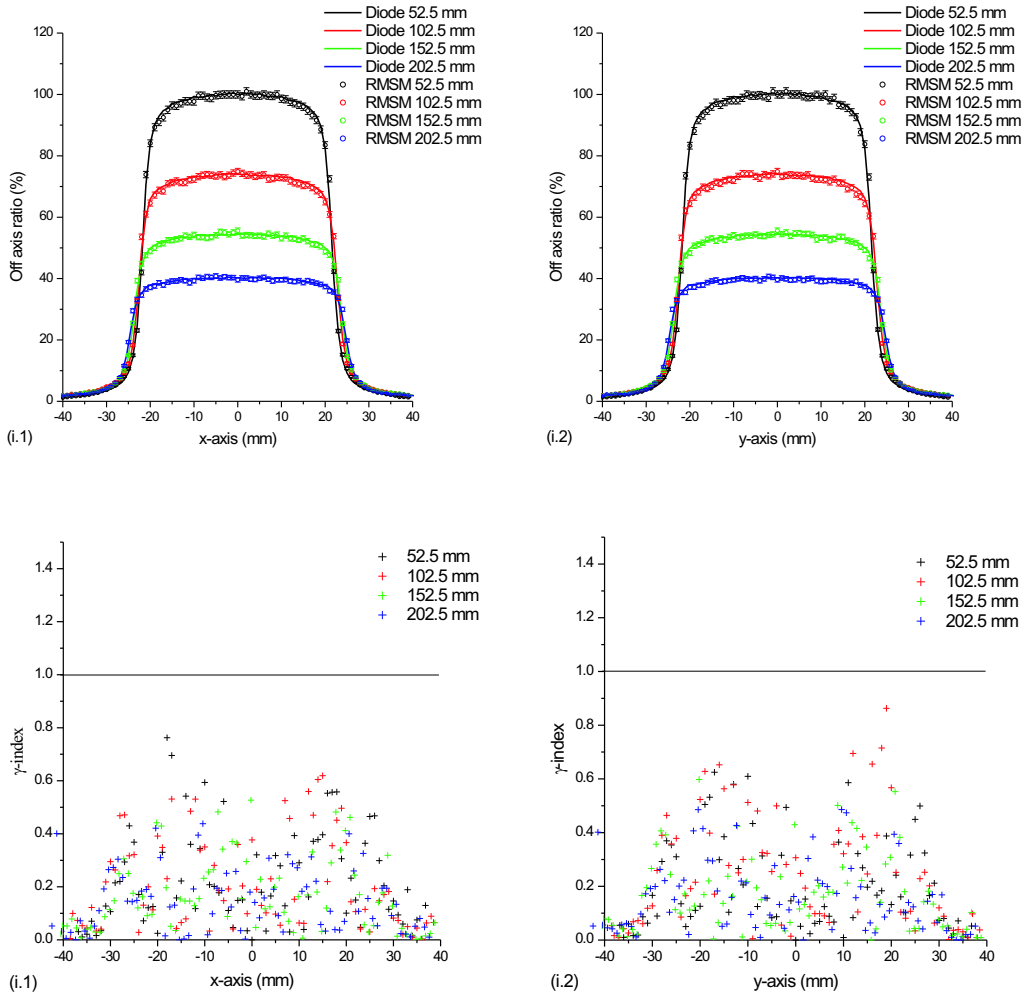

Figure 6.25: A comparison between calculated (RMSM) and measured (diode) off-axis ratios (OAR) at various depths in water along (1) the x-axis and (2) the y-axis for the 23 mm additional collimator. In each axis, the γ-index is calculated.

The poor efficiency in simulating the narrow photon beams producing PSDs whose quality prevented calculating dose with the required accuracy was a major problem. To overcome this difficulty, an accurate multiple source model was developed that enhanced the quality of the reconstructed PSDs, reducing also the time and storage capacities. Our model can now be the dose engine of a MC-based treatment planning system.

Chapter 7

Clinical implementation of RMSM

In the past few years, different treatment planning systems (TPS) for conventional radiotherapy have appeared having MC simulations as a basis [DSS98, MMK+99, LPD+00, YSS+00]. MC simulations have also been used to benchmark commercial TPS [FCR+00, LRS+00, PWL01]. For radiosurgery, only a few MC based TPS have been developed [SDH+98, DMH+03]. Due to the characteristics of radiosurgery treatments (multiple arcs, small field and scoring voxel dimensions), we have developed a multiple source model using the DPM MC code for dose calculation (see Chapter 6). The purpose of this chapter is to develop a MC-based TPS in order to have a post-planning dose calculation evaluation for radiosurgery treatments that are routinely calculated with a commercial TPS. Like any radiosurgery treatment planning, our TPS must include tools such as CT-image data conversion to human tissue, stereotactic geometrical transformation. A source transformation to simulate the arcs must also be included. Finally, a comparison with two real cases will be performed.

7.1 CT-Interface

The only available information contained in a pixel of a CT-image is called the CT-number. It is thus necessary to transform such number in density and chemical composition in order to calculate dose in real condition. In this section, we will briefly describe the methodology developed by Schneider *et al.* [SBS00] and implemented in the CT-Interface of our RMSM-based TPS.

7.1.1 CT-number parametrization

The CT-number of a pixel expressed in Hounsfield units H is given by:

$$H = \left(\frac{\overline{\mu}}{\overline{\mu}_{H2O}} - 1 \right) \times 1000, \tag{7.1}$$

where $\overline{\mu}$ is the mean linear attenuation coefficient at the pixel position along a tomographic projection. It has to be noticed that $\overline{\mu}$ depends on the x-rays spectra of the CT-machine. From theoretical calculated CT-numbers for our CT Siemens Somatom Plus 4 (120 kVp), Schneider *et al.* [SBS00] have found that the density ρ and the chemical composition w_i of a human tissue with an Hounsfield value H can be described by a mixture of two human tissues $(\rho_1, w_{1,i}, H_1)$ and $(\rho_2, w_{2,i}, H_2)$ and are expressed by:

$$\rho(H) = \frac{\rho_1 H_2 - \rho_2 H_1 + (\rho_2 - \rho_1)H}{H_2 - H_1} \qquad (\mathrm{gcm}^{-3}), \tag{7.2}$$

$$w_i(H) = \frac{\rho_1 (H_2 - H)}{(\rho_1 H_2 - \rho_2 H_1) + (\rho_2 - \rho_1)H} (w_{1,i} - w_{2,i}) + w_{2,i}, \tag{7.3}$$

where $H_1 \leq H \leq H_2$. These authors have divided the human tissues in various groups. For skeletal tissues where the Hounsfield values are in the interval:

$$-22 \leq H \leq 1524,$$

it was considered that these tissues are composed by skeleton cortical bone (cb) and red/yellow marrow (ma). Thus, Eqs. 7.2 and 7.3 become:

$$\rho(H) = (1.017 + 0.592 \times 10^{-3} H) \qquad (\mathrm{gcm}^{-3}), \tag{7.4}$$

$$w_i(H) = \frac{1524 - H}{1566 + 0.92H} (w_{ma,i} - w_{cb,i}) + w_{cb,i}. \tag{7.5}$$

In Eq. 7.5, $w_{ma,i}$ and $w_{cb,i}$ denote the elemental weights of red/yellow marrow and skeleton cortical bone. For the soft tissues, a sub-division was performed by the authors. For the interval of soft tissues 1 with CT-numbers:

$$-98 \leq H \leq 14,$$

it was considered that these tissues are composed by adipose tissue (at) and adrenal gland (ag). Equations 7.2 and 7.3 become:

$$\rho(H) = (1.018 + 0.893 \times 10^{-3} H) \qquad (\mathrm{gcm}^{-3}), \tag{7.6}$$

$$w_i(H) = \frac{0.93(14 - H)}{114 + 0.1H}(w_{at,i} - w_{ag,i}) + w_{ag,i}. \tag{7.7}$$

For the interval of soft tissues 2 with CT-numbers:

$$23 \leq H \leq 100,$$

it was considered that these tissues are composed by small intestine (wall) (si) and connective tissue (ct). Equations 7.2 and 7.3 become:

$$\rho(H) = (1.003 + 1.169 \times 10^{-3}H) \qquad (\text{gcm}^{-3}), \tag{7.8}$$

$$w_i(H) = \frac{1.03(100 - H)}{77 + 0.09H}(w_{si,i} - w_{ct,i}) + w_{ct,i}. \tag{7.9}$$

Finally, in the interval:

$$-1000 \leq H \leq -98,$$

the densities of the tissues with CT-numbers starting from the air ($H = -1000$, $\rho = 1.21 \times 10^{-3}$ gcm^{-3}) and adipose tissue ($H = -98$, $\rho = 0.93 \times 10^{-3}$ gcm^{-3}) are given by the following interpolation:

$$\rho(H) = \left(1.21 \times 10^{-3} + (H - 1000)\frac{-0.93 + 1.21 \times 10^{-3}}{98 - 1000}\right) \qquad (\text{gcm}^{-3}), \tag{7.10}$$

In this interval, the authors have considered three regions. For $-1000 \leq H \leq -950$ the composition of air was chosen, for $-950 \leq H \leq -120$ the composition of lung and finally for $-120 \leq H \leq -93$ the composition of adipose tissue.

7.1.2 Hounsfield units conversion into tissue parameters

The results of the CT-parametrization are not suitable yet for use in the Monte Carlo code DPM. This code uses the formatted material data employed in the MC code PENELOPE [SFB+96]. Each material must be defined in a separate *mat*-file. For a defined material, a *mat*-file must be generated for a given density and then preprocessed in order to calculate the different cross sectional data. Thus, the continuous functional relationship $w_i(H)$ must be transformed into step functions and in each step, one or more densities are calculated defining then one or more materials in this step.

The Hounsfield bin width is based on the deviations of theoretical and measured Hounsfield values for the phantom materials used for CT-scanner calibrations. For skeleton tissues $-22 \leq H \leq 1524$, Schneider *et al.* have found that the bin width must be 100 Hounsfield units. Although Eqs. 7.4 and 7.5 are defined for $H \geq -22$, these equations will only be applied for $H \geq 100$ because no skeletal tissue occurs below this value [SBS00]. For soft tissues 1, $-98 \leq H \leq 14$, they found a bin width of 20 Hounsfield units. Due to the weak correlation between elemental weights and CT-numbers for soft tissues 2, $23 \leq H \leq 100$, the parametrization 7.9 has been replaced by a mean composition. Because the values of the connective tissue ($H = 100$) are not close to the mean composition values, an interval of 40 Hounsfield units around $H = 100$ was defined for this tissue. Functions 7.6 and 7.9 are used between -98 and 100 Hounsfield units. Due to the discontinuity between soft tissues 1 and 2, a value of $\rho = 1.03$ gcm^{-3} is used [SBS00]. In the interval $-950 \leq H \leq -120$, 28 materials were defined corresponding to bins of 30 Hounsfield units [PWL98]. In each bin, the density was calculated according Eq. 7.10 but the chemical composition remained unchanged in the interval $-950 \leq H \leq -120$ using the composition of the lung. Only one bin is defined in the interval $-1000 \leq H \leq -950$ and the density and composition of the air were used. The stereotaxic ring is fixed to the patient head by titanium screws which $H > 2100$ for our CT-scan. Because beams arcs can intercept these screws, we have to include this material. In order to avoid a discontinuity between $H = 1524$ and $H = 2100$, 5 bins of 100 Hounsfield units are defined where the density and chemical composition for these 5 additional materials are calculated using Eq. 7.4 and 7.5.

According to the performed conversion of the Hounsfield values into tissue parameters, 61 materials were defined. Figure 7.1 shows the conversion curve H.vs.density of the different materials. Table 7.1 shows the conversion of the Hounsfield values to elemental weights for the 61 materials according to the defined Hounsfield values intervals.

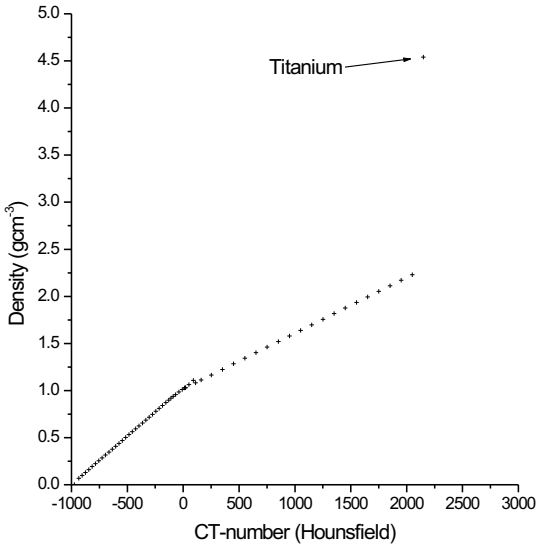

Figure 7.1: Conversion of CT-number into density of 61 defined materials for Siemens Somatom Plus 4.

		w_i(%)												
Hounsfield interval	Material	H	C	N	O	Na	Mg	P	S	Cl	Ar	K	Ca	Ti
−1000 - −950	1			75.5	23.2						1.3			
−950 - −120	2 - 29	10.3	10.5	3.1	74.9	0.2		0.2	0.3	0.3		0.2		
−120 - −83	30 - 31	11.6	68.1	0.2	19.8	0.1		0.0	0.1	0.1				
−82 - −53	32	11.3	56.7	0.9	30.8	0.1		0.0	0.1	0.1				
−52 - −23	33	11.0	45.8	1.5	41.1	0.1		0.1	0.2	0.2				
−22 - 7	34	10.8	35.6	2.2	50.9	0.0		0.1	0.2	0.2				
8 - 18	35 - 36	10.6	28.4	2.6	57.8	0.0		0.1	0.2	0.2		0.1		
19 - 80	37 - 38	10.3	13.4	3.0	72.3	0.2		0.2	0.2	0.2		0.2		
80 - 120	39 - 40	9.4	20.7	6.2	62.2	0.6		0.0	0.6	0.3				
120 - 200	41	9.5	45.5	2.5	35.5	0.1		2.1	0.1	0.1		0.1	4.5	
200 - 300	42	8.9	42.3	2.7	36.3	0.1		3.0	0.1	0.1		0.1	6.4	
300 - 400	43	8.2	39.1	2.9	37.2	0.1		3.9	0.1	0.1		0.1	8.3	
400 - 500	44	7.6	36.1	3.0	38.0	0.1	0.1	4.7	0.2	0.1			10.1	
500 - 600	45	7.1	33.5	3.2	38.7	0.1	0.1	5.4	0.2				11.7	
600 - 700	46	6.6	31.0	3.3	39.4	0.1	0.1	6.1	0.2				13.2	
700 - 800	47	6.1	28.7	3.5	40.0	0.1	0.1	6.7	0.2				14.6	
800 - 900	48	5.6	26.5	3.6	40.5	0.1	0.2	7.3	0.3				15.9	
900 - 1000	49	5.2	24.6	3.7	41.1	0.1	0.2	7.8	0.3				17.0	
1000 - 1100	50	4.9	22.7	3.8	41.6	0.1	0.2	8.3	0.3				18.1	
1100 - 1200	51	4.5	21.0	3.9	42.0	0.1	0.2	8.8	0.3				19.2	
1200 - 1300	52	4.2	19.4	4.0	42.5	0.1	0.2	9.2	0.3				20.1	
1300 - 1400	53	3.9	17.9	4.1	42.9	0.1	0.2	9.6	0.3				21.0	
1400 - 1500	54	3.6	16.5	4.2	43.2	0.1	0.2	10.0	0.3				21.9	
1500 - 1600	55	3.4	15.5	4.2	43.5	0.1	0.2	10.3	0.3				22.5	
1600 - 1700	56	3.1	14.0	4.3	43.9	0.1	0.2	10.7	0.3				23.4	
1700 - 1800	57	2.9	12.8	4.3	44.2	0.1	0.2	11.0	0.3				24.1	
1800 - 1900	58	2.6	11.8	4.4	44.5	0.1	0.2	11.3	0.3				24.7	
1900 - 2000	59	2.4	10.8	4.5	44.8	0.1	0.2	11.6	0.3				25.4	
2000 - 2100	60	2.2	9.8	4.5	45.0	0.1	0.2	11.9	0.3				25.9	
>2100	61												0.0	100.0

Table 7.1: Conversion of CT-number to elemental weights according to Schneider *et al.* [SBS00] of 61 defined materials for Siemens Somatom Plus 4.

7.1.3 Conversion of CT-pixel to DPM-voxel

Images from CT scanner Siemens Somaton Plus 4 have to be filled in a voxel-based phantom into the MC code DPM for dose calculation. One image is composed by 512×512 pixels. To reduce storage and computation time, this image is reduced to 256×256 pixels. For a pixel $P(i,j)$ in the reduced image, the Hounsfield value $H^{256}(i,j)$ is given by:

$$H^{256}(i,j) = \frac{\sum_{j'=0}^{1}\sum_{i'=0}^{1} H^{512}(2i-i', 2j-j')}{4}, \tag{7.11}$$

where H^{512} is the Hounsfield value in the 512×512 image.

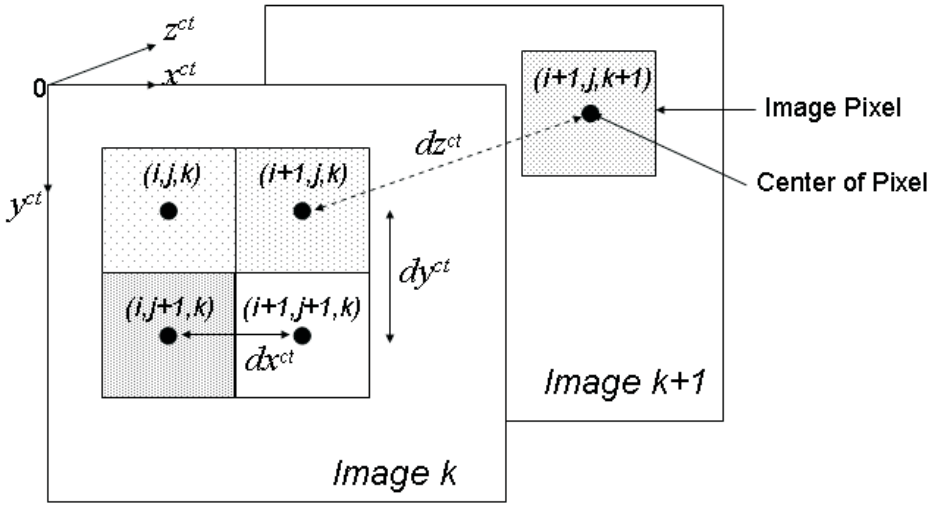

Figure 7.2: Representation of the pixels in two CT consecutive images.

During a radiosurgery CT examination, the patient is in supine position and images of the head are acquired from feet to head direction. Considering that the first acquired image ($k = 1$) is located at $z^{ct} = dz/2$, the coordinates of the center of a pixel $P(i,j,k)$,

where k represents the number of the image, are given by:

$$\begin{pmatrix} x_p^{ct} \\ y_p^{ct} \\ z_p^{ct} \\ 1 \end{pmatrix} = A_{ijk_{ct} \to p_{ct}} \begin{pmatrix} i \\ j \\ k \\ 1 \end{pmatrix}, \tag{7.12}$$

where

$$A_{ijk_{ct} \to p_{ct}} = \begin{pmatrix} dx^{ct} & 0 & 0 & \frac{-dx^{ct}}{2} \\ 0 & dy^{ct} & 0 & \frac{-dy^{ct}}{2} \\ 0 & 0 & dz^{ct} & \frac{-dz^{ct}}{2} \\ 0 & 0 & 0 & 1 \end{pmatrix}, \tag{7.13}$$

where dx^{ct} is the distance between pixels $P(i,j,k)$ and $P(i+1,j,k)$, dy^{ct} the distance between pixels $P(i,j,k)$ and $P(i,j+1,k)$ and dz^{ct} the distance between two consecutive images or pixels $P(i,j,k)$ and $P(i,j,k+1)$ (see Fig. 7.2). In order to transform CT-pixels in DPM-voxels, we have to find a relationship between DPM reference system and CT-reference system because they are different. Figure 7.3 shows the voxel-based phantom as DPM defines.

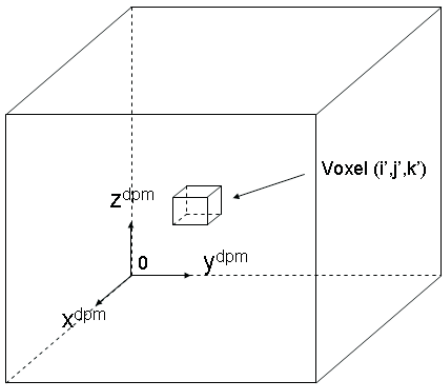

Figure 7.3: Representation of the voxel (i', j', k') in the DPM reference system.

The coordinates of a pixel $P(i,j,k)$ in DPM reference system are given by:

$$\begin{pmatrix} x_p^{dpm} \\ y_p^{dpm} \\ z_p^{dpm} \\ 1 \end{pmatrix} = A_{p_{ct}\rightarrow p_{dpm}} \begin{pmatrix} x_p^{ct} \\ y_p^{ct} \\ z_p^{ct} \\ 1 \end{pmatrix}, \tag{7.14}$$

where

$$A_{p_{ct}\rightarrow p_{dpm}} = \begin{pmatrix} 0 & 0 & -1 & Ndz^{ct} \\ 1 & 0 & 0 & 0 \\ 0 & -1 & 0 & N_y^{ct} dy^{ct} \\ 0 & 0 & 0 & 1 \end{pmatrix}, \tag{7.15}$$

where N is the total number of images and N_y^{ct} the total number of pixels in the y-axis of the CT-reference system. Combining Eqs. 7.12 and 7.14, a pixel $P(i,j,k)$ in the CT-image is transformed in a voxel in the DPM reference system which coordinates are given by:

$$\begin{pmatrix} x_p^{dpm} \\ y_p^{dpm} \\ z_p^{dpm} \\ 1 \end{pmatrix} = A_{ijk\rightarrow p_{dpm}} \begin{pmatrix} i \\ j \\ k \\ 1 \end{pmatrix}, \tag{7.16}$$

where

$$A_{ijk\rightarrow p_{dpm}} = A_{p_{ct}\rightarrow p_{dpm}} A_{ijk\rightarrow p_{ct}}, \tag{7.17}$$

and with

$$1 \leq i \leq N_x^{ct},$$
$$1 \leq j \leq N_y^{ct},$$
$$1 \leq k \leq N.$$

For our images, $N_x^{ct} = N_y^{ct} = 256$, $dx^{ct} = dy^{ct}$ =1.367 mm and dz^{ct} =2 mm. If N_x^{dpm}, N_y^{dpm}, N_z^{dpm} and d_x^{dpm}, d_y^{dpm}, d_z^{dpm} are respectively the numbers and dimensions of voxels in the x- y- and z-axis, then:

$$N_x^{dpm} = N, \qquad d_x^{dpm} = d_z^{ct};$$
$$N_y^{dpm} = N_x^{ct}, \qquad d_y^{dpm} = d_x^{ct};$$
$$N_z^{dpm} = N_y^{ct}, \qquad d_z^{dpm} = d_y^{ct}.$$

Finally, the conversion of the pixel indices (i, j, k) in the CT-reference system to voxel indices (i', j', k') in the DPM reference system is given by:

$$\begin{pmatrix} i' \\ j' \\ k' \\ 1 \end{pmatrix} = A_{ijk_{ct} \rightarrow i'j'k'_{dpm}} \begin{pmatrix} i \\ j \\ k \\ 1 \end{pmatrix}, \tag{7.18}$$

where

$$A_{ijk_{ct} \rightarrow i'j'k'_{dpm}} = \begin{pmatrix} 0 & 0 & -1 & N+1 \\ 1 & 0 & 0 & 0 \\ 0 & -1 & 0 & N_y^{ct}+1 \\ 0 & 0 & 0 & 1 \end{pmatrix}. \tag{7.19}$$

The coordinates of center of the voxel $V(i', j', k')$ are calculated using Eq. 7.16.

7.1.4 Implementation of the CT-Interface

Once the list of materials is determined (61 in our case), it is necessary to process the material data in order to pre-calculate all the cross-sections and energy losses for these materials before performing a DPM simulation. All the characteristics of a defined material (number of elemental elements, relative weight of each elemental element, density) are included in the $mat_i.in$ file where i is the number of the material. The routine MATERIAL will process all the $mat_i.in$ files using as input *penepN.tab* and *penphN.tab* files which are respectively electron/positron and photon elemental raw data files. The routine PREDPM reads data files that are generated by the pre-processor MATERIAL and generates series of output files which are the DPM material data inputs. Problem parameters such as cutoffs, list of materials are specified in a *predpm.in* input file. All the procedure described above must be repeated if the list of materials or a characteristic of a material has to be changed. Figure 7.4 shows a simplified diagram of material pre-process procedure.

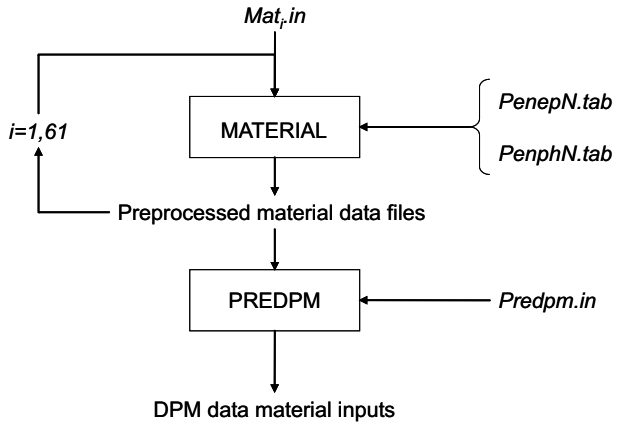

Figure 7.4: Simplified diagram of DPM material pre-process procedure.

The in-house routine GENVOXEL was developed in order to read CT-images from a *patient* and fills a file named *patient*.vox which contains all the information of a voxel-based phantom according to DPM specifications. GENVOXEL attributes at each CT-image pixel a material according to its Hounsfield value. Once the number of voxels in each axis and the voxel size were introduced in *patient*.vox, GENVOXEL writes in the same row the material number and density for each voxel. Each row represents a voxel which coordinates are not in fact explicitly introduced. The 1^{st} row refers to the voxel $(i' = 1, j' = 1, k' = 1)$ with one corner in the (0,0,0) position and the center at:

$$x_v^{dpm} = dx^{dpm}/2, \quad y_v^{dpm} = dy^{dpm}/2, \quad z_v^{dpm} = dz^{dpm}/2;$$

the 2^{nd} row refers to the voxel $(i' = 1, j' = 1, k' = 2)$ centered at:

$$x_v^{dpm} = dx^{dpm}/2, \quad y_v^{dpm} = dy^{dpm}/2, \quad z_v^{dpm} = 3dz^{dpm}/2,$$

and so on. Row $(N_z^{dpm} + 1)$ refers to the voxel $(i' = 1, j' = 2, k' = 1)$ centered at:

$$x_v^{dpm} = dx^{dpm}/2, \quad y_v^{dpm} = 3dy^{dpm}/2, \quad z_v^{dpm} = dz^{dpm}/2,$$

and finally, row $(N_z^{dpm} \times N_y^{dpm} + 1)$ refers to the voxel $(i' = 2, j' = 1, k' = 1)$ centered at:

$$x_v^{dpm} = 3dx^{dpm}/2, \quad y_v^{dpm} = dy^{dpm}/2, \quad z_v^{dpm} = dz^{dpm}/2.$$

The indices (i', j', k') are calculated from Eq. 7.18.

7.2 Stereotactic Transformation Interface

In order to perform stereotactic therapies based on the head frame, the planning data must be transferred onto the patient. This transfer can be achieved with a high precision only if the planning data contain a stereotactic localization system which allows stereotactic coordinates to be calculated. The stereotactic coordinate system is defined by the stereotactic ring as shown in Fig. 7.5. With the patient in the supine position, the stereotactic x-axis will point to the patient's right-hand side, the y-axis will point upwards from the head through the patient's nose, the z-axis will point along the patient's body axis towards the top of the head and finally, the origin of the axis is at the center of the stereotactic ring.

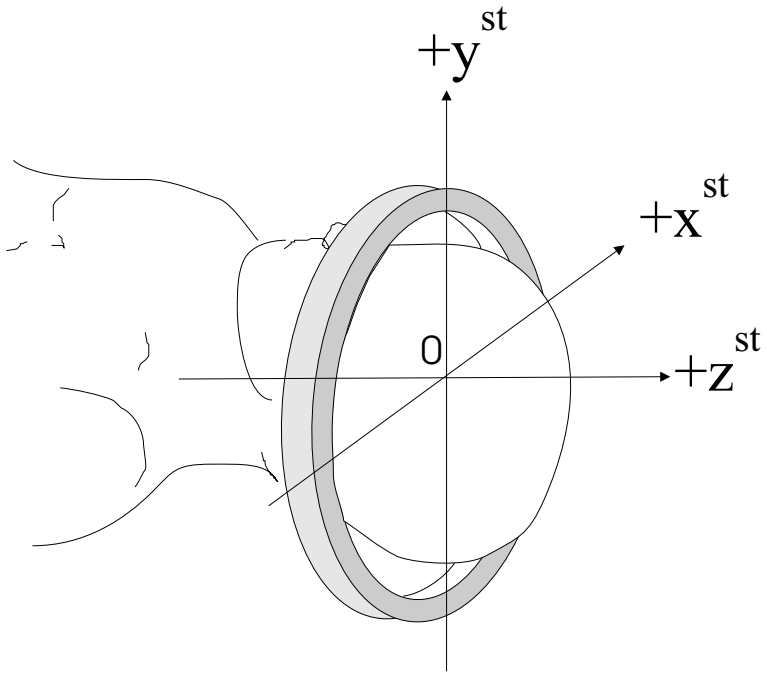

Figure 7.5: Coordinate system of the stereotactic head ring.

7.2.1 Fiducial points

In order to obtain stereotactic coordinates from the images data, special localizers attached to the head ring are used (see Fig. 7.6). Each localizer is constituted by 3 wires and the intersections of these wires with the image plane are called fiducial points shown in Fig. 7.7. Figure 7.8 shows the positions of the fiducial points 1-3 as seen on the CT-slice and in the anterior localizer.

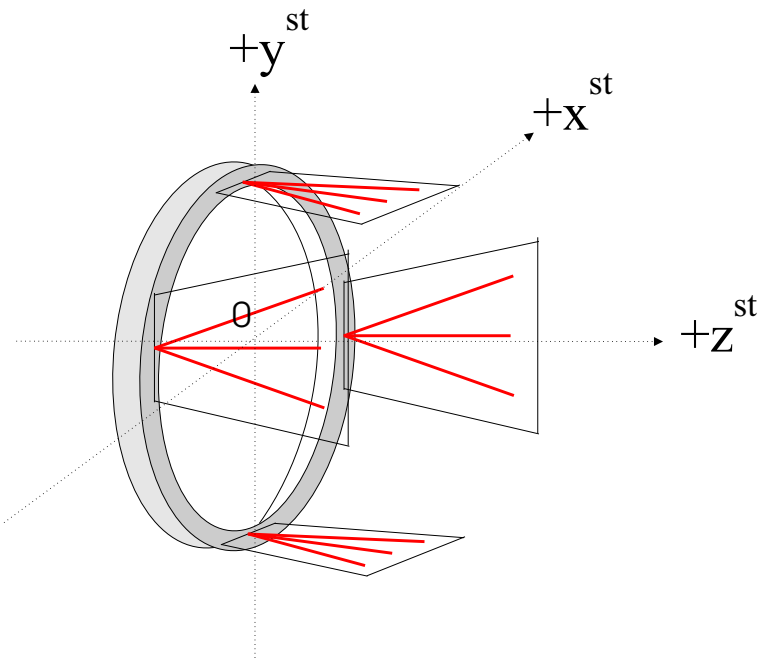

Figure 7.6: Stereotactic localizers mounted on the stereotactic head ring.

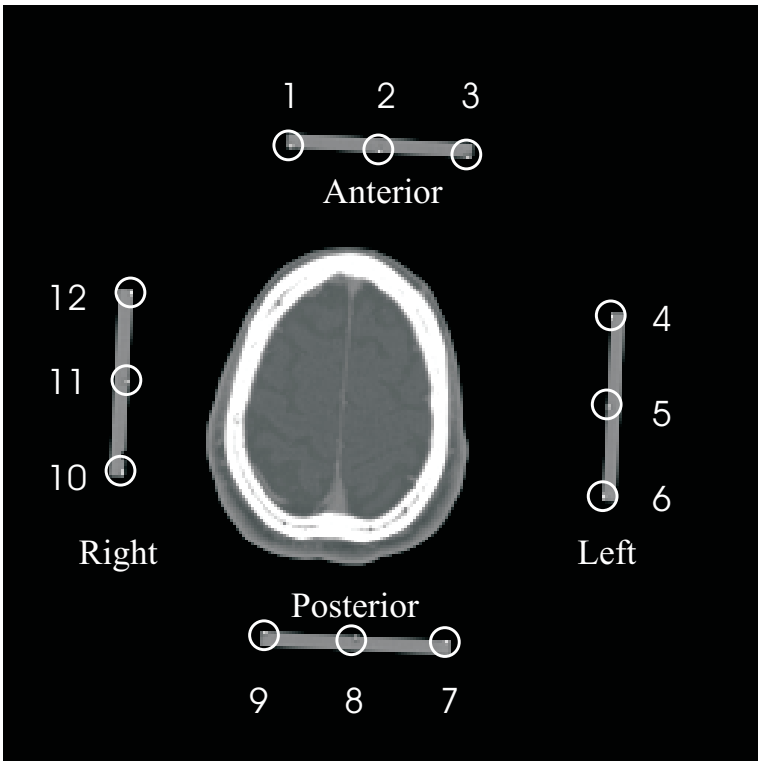

Figure 7.7: Fiducial points in a CT-image.

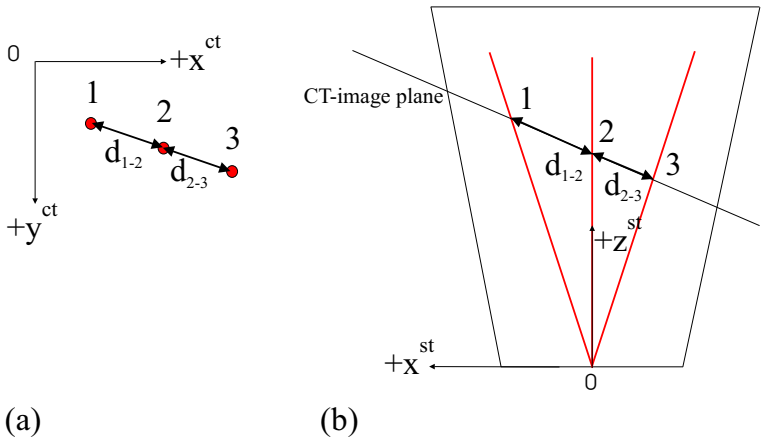

Figure 7.8: Positions of the fiducial points 1-3 as seen (a) on the CT-slice and (b) in the anterior localizer.

The stereotactic localizers are built in a such a way that the stereotactic coordinates x^{st} and y^{st} of the fiducial points are given by:

$$\begin{aligned}
P_1 \rightarrow \quad & x_1^{st} = \frac{z_1^{st}}{2}, && y_1^{st} = d_{ant};\\
P_2 \rightarrow \quad & x_2^{st} = 0, && y_2^{st} = d_{ant};\\
P_3 \rightarrow \quad & x_3^{st} = -\frac{z_3^{st}}{2}, && y_3^{st} = d_{ant};\\
P_4 \rightarrow \quad & x_4^{st} = -d_{left}, && y_4^{st} = \frac{z_3^{st}}{2};\\
P_5 \rightarrow \quad & x_5^{st} = -d_{left}, && y_5^{st} = 0;\\
P_6 \rightarrow \quad & x_6^{st} = -d_{left}, && y_6^{st} = -\frac{z_3^{st}}{2};\\
P_7 \rightarrow \quad & x_7^{st} = -\frac{z_7^{st}}{2}, && y_7^{st} = -d_{post};\\
P_8 \rightarrow \quad & x_8^{st} = 0, && y_8^{st} = -d_{post};\\
P_9 \rightarrow \quad & x_9^{st} = \frac{z_9^{st}}{2}, && y_9^{st} = -d_{post};\\
P_{10} \rightarrow \quad & x_{10}^{st} = d_{right}, && y_{10}^{st} = -\frac{z_{10}^{st}}{2};\\
P_{11} \rightarrow \quad & x_{11}^{st} = d_{right}, && y_{11}^{st} = 0;\\
P_{12} \rightarrow \quad & x_{12}^{st} = d_{right}, && y_{12}^{st} = \frac{z_{10}^{st}}{2};
\end{aligned} \tag{7.20}$$

where d_{ant}, d_{left}, d_{post} and d_{right} are the distances between the localizer plates *anterior, left, posterior* and *right* respectively and the z-axis. In our case:

$$d_{ant} = d_{left} = d_{post} = d_{right} = d_p = 111.3\,\text{mm}.$$

Using the distance between the fiducial points in each localizer, the coordinates (x^{st}, y^{st}, z^{st}) of each fiducial point can be calculated. To show how these points can be calculated, we will use the *anterior* localizer. For the other localizers, the rational is the same.

According to Fig. 7.8 (b), we have the following equations:

$$(d_{1-2} + d_{2-3})^2 = (x_1^{st} + |x_3^{st}|)^2 + (z_1^{st} - z_3^{st})^2, \tag{7.21}$$

$$\frac{x_1^{st}}{|x_3^{st}|} = \frac{d_{1-2}}{d_{2-3}}, \tag{7.22}$$

where d_{1-2} is the distance between points 1 and 2 and d_{2-3} the distance between points 2 and 3. According to the characteristics of the *anterior* localizer we have:

$$z_1^{st} = 2x_1^{st}, \tag{7.23}$$

$$z_3^{st} = 2|x_3^{st}|. \tag{7.24}$$

Combining Eqs. 7.21-7.24 we obtain:

$$x_1^{st} = \frac{d_{1-2} + d_{2-3}}{\sqrt{5 + 5\left(\frac{d_{2-3}}{d_{1-2}}\right)^2 - 6\frac{d_{2-3}}{d_{1-2}}}}. \tag{7.25}$$

The coordinate x_3^{st} is given by:

$$x_3^{st} = -x_1^{st}\frac{d_{2-3}}{d_{1-2}}. \tag{7.26}$$

Finally, the coordinate z_2^{st} is simply given by:

$$z_2^{st} = (z_1^{st} - z_3^{st})\frac{d_{2-3}}{d_{1-2} + d_{2-3}} + z_3^{st}. \tag{7.27}$$

Thus, for the points 1, 2 and 3 of the *anterior* localizer, we have:

$$P_1 \rightarrow \quad x_1^{st} = \frac{d_{1-2} + d_{2-3}}{\sqrt{5 + 5\left(\frac{d_{2-3}}{d_{1-2}}\right)^2 - 6\frac{d_{2-3}}{d_{1-2}}}}, \quad y_1^{st} = d_p, \quad z_1^{st} = 2x_1^{st};$$

$$P_2 \rightarrow \quad x_2^{st} = 0, \qquad\qquad y_2^{st} = d_p, \quad z_2^{st} = (z_1^{st} - z_3^{st})\frac{d_{2-3}}{d_{1-2} + d_{2-3}} + z_3^{st};$$

$$P_3 \rightarrow \quad x_3^{st} = -x_1^{st}\frac{d_{2-3}}{d_{1-2}}, \qquad y_3^{st} = d_p, \quad z_3^{st} = 2|x_3^{st}|.$$

For the points 4, 5 and 6 of the *left* localizer, we have:

$$P_4 \rightarrow \quad x_4^{st} = -d_p, \quad y_4^{st} = \frac{d_{4-5} + d_{5-6}}{\sqrt{5 + 5\left(\frac{d_{5-6}}{d_{4-5}}\right)^2 - 6\frac{d_{5-6}}{d_{4-5}}}}, \quad z_4^{st} = 2y_4^{st};$$

$$P_5 \rightarrow \quad x_5^{st} = -d_p, \quad y_5^{st} = 0, \qquad\qquad z_5^{st} = (z_4^{st} - z_6^{st})\frac{d_{5-6}}{d_{4-5} + d_{5-6}} + z_6^{st};$$

$$P_6 \rightarrow \quad x_6^{st} = -d_p, \quad y_6^{st} = -y_4^{st}\frac{d_{5-6}}{d_{4-5}}, \qquad z_6^{st} = 2|y_6^{st}|.$$

For the points 7, 8 and 9 of the *posterior* localizer, we have:

$$\begin{aligned}
P_7 \rightarrow \quad & x_7^{st} = -x_9^{st}\frac{d_{7-8}}{d_{8-9}}, && y_7^{st} = -d_p, \quad z_7^{st} = 2|x_7^{st}|; \\
P_8 \rightarrow \quad & x_8^{st} = 0, && y_8^{st} = -d_p, \quad z_8^{st} = (z_9^{st} - z_7^{st})\frac{d_{7-8}}{d_{7-8}+d_{8-9}} + z_7^{st}; \\
P_9 \rightarrow \quad & x_9^{st} = \frac{d_{7-8}+d_{8-9}}{\sqrt{5+5\left(\frac{d_{7-8}}{d_{8-9}}\right)^2 - 6\frac{d_{7-8}}{d_{8-9}}}}, && y_9^{st} = -d_p, \quad z_9^{st} = 2x_9^{st}.
\end{aligned}$$

Finally, for the points 10, 11 and 12 of the *right* localizer, we have:

$$\begin{aligned}
P_{10} \rightarrow \quad & x_{10}^{st} = d_p, \quad y_{10}^{st} = -y_{12}^{st}\frac{d_{10-11}}{d_{11-12}}, && z_{10}^{st} = 2|y_{10}^{st}|; \\
P_{11} \rightarrow \quad & x_{11}^{st} = d_p, \quad y_{11}^{st} = 0, && z_{11}^{st} = (z_{12}^{st} - z_{10}^{st})\frac{d_{10-11}}{d_{10-11}+d_{11-12}} + z_{10}^{st}; \\
P_{12} \rightarrow \quad & x_{12}^{st} = d_p, \quad y_{12}^{st} = \frac{d_{10-11}+d_{11-12}}{\sqrt{5+5\left(\frac{d_{10-11}}{d_{11-12}}\right)^2 - 6\frac{d_{10-11}}{d_{11-12}}}}, && z_{12}^{st} = 2y_{12}^{st}.
\end{aligned}$$

7.2.2 Transformation

In the last section, we have calculated the coordinates of the fiducial points in the stereotactic reference system. The coordinates of each fiducial point are also calculated in the CT-reference system. It is now necessary to have a single coordinate transformation between the CT-reference system and the stereotactic reference system. It is also possible to calculate a coordinate transformation for each CT-slice but the accuracy will be worst than using a global transformation including all the CT-slices [LKH+94]. Lemieux *et al.* have used a Volume Transformation Matrix (VTM), F_v, which is a 4-by-4 matrix that maps pixel coordinates onto stereotactic frame coordinates. The VTM is a homogeneous transformation matrix that can include rotations, translations and scaling. Geometrically, only four non-coplanar fiducial points are necessary to calculate VTM. However, since the localization of these fiducial points is subject to error, this will result in an inaccurate VTM. If we denote $(x_{f_i}^{ct}, y_{f_i}^{ct}, z_{f_i}^{ct})$ and $(x_{f_i}^{st}, y_{f_i}^{st}, z_{f_i}^{st})$ the coordinates of a fiducial point i in the CT-reference system and in the stereotactic reference system respectively, the mapping, for n fiducial points, is given by:

$$\begin{pmatrix} x_{f_1}^{st} & x_{f_2}^{st} & \ldots & x_{f_n}^{st} \\ y_{f_1}^{st} & y_{f_2}^{st} & \ldots & y_{f_n}^{st} \\ z_{f_1}^{st} & z_{f_2}^{st} & \ldots & z_{f_n}^{st} \\ 1 & 1 & \ldots & 1 \end{pmatrix} = F_v \begin{pmatrix} x_{f_1}^{ct} & x_{f_2}^{ct} & \ldots & x_{f_n}^{ct} \\ y_{f_1}^{ct} & y_{f_2}^{ct} & \ldots & y_{f_n}^{ct} \\ z_{f_1}^{ct} & z_{f_2}^{ct} & \ldots & z_{f_n}^{ct} \\ 1 & 1 & \ldots & 1 \end{pmatrix}, \tag{7.28}$$

or

$$X_f^{st} = F_v X_f^{ct}. \tag{7.29}$$

The relationship between the stereotactic reference system and the DPM reference system is given by:

$$X_f^{st} = G_v X_f^{dpm}, \tag{7.30}$$

where

$$G_v = F_v A^{-1}_{p_{ct} \rightarrow p_{dpm}}. \tag{7.31}$$

Using the formalism of Eq. 7.29, we can write for a fiducial point i:

$$x_{f_i}^{st} = F_{v1} X_{f_i}^{ct} = F_{v1} \begin{pmatrix} x_{f_i}^{ct} \\ y_{f_i}^{ct} \\ z_{f_i}^{ct} \\ 1 \end{pmatrix}, \tag{7.32}$$

$$y_{f_i}^{st} = F_{v2} X_{f_i}^{ct} = F_{v2} \begin{pmatrix} x_{f_i}^{ct} \\ y_{f_i}^{ct} \\ z_{f_i}^{ct} \\ 1 \end{pmatrix}, \tag{7.33}$$

$$z_{f_i}^{st} = F_{v3} X_{f_i}^{ct} = F_{v3} \begin{pmatrix} x_{f_i}^{ct} \\ y_{f_i}^{ct} \\ z_{f_i}^{ct} \\ 1 \end{pmatrix}, \tag{7.34}$$

where F_{v1}, F_{v2} and F_{v3} are 1-by-4 matrix representing respectively the 1^{st}, 2^{nd} and 3^{rd} row of the F_v matrix.

When $n > 3$, a least-squares solution that minimizes the residual, R^2 given by:

$$R^2 = \sum_{i=1}^{n} (x_{f_i}^{st} - F_{v_1} X_{f_i}^{ct})^2 + \sum_{i=1}^{n} (y_{f_i}^{st} - F_{v_2} X_{f_i}^{ct})^2 + \sum_{i=1}^{n} (z_{f_i}^{st} - F_{v_3} X_{f_i}^{ct})^2, \tag{7.35}$$

is obtained. Unfortunately, the solutions found F_{v_1}, F_{v_2} and F_{v_3} using the residual R^2 of Eq. 7.35 lead to inaccurate results. In fact, we have to guarantee that for example for point 1 of the *anterior* localizer (see Fig. 7.8), the relation $2|x'^{st}_{f_1}| = z'^{st}_{f_1}$ is still true

($x'^{st}_{f_1}$ and $z'^{st}_{f_1}$ are calculated with the solutions found F_{v_1} and F_{v_3}). Thus, Eq. 7.35 must be modified where, due to the characteristics of the localizers, some geometrical constraints must be imposed. Equation 7.35 can be rewritten as following:

$$R^2 = \sum_{i=1}^{n}(x^{st}_{f_i} - F_{v_1}X^{ct}_{f_i})^2 + \sum_{i=1}^{n}(y^{st}_{f_i} - F_{v_2}X^{ct}_{f_i})^2 + r_z^2, \tag{7.36}$$

where r_z^2 represents the imposed geometrical constraint.

Using the nomenclature of Fig. 7.8, for the n_1 points 1, 3, 7 and 9, we have:

$$r^2_{z_{1-3-7-9}} = \sum_{i=1}^{n_1}(2|F_{v1}X^{ct}_{f_i}| - F_{v3}X^{ct}_{f_i})^2. \tag{7.37}$$

For the n_2 points 4, 6, 10 and 12, the constraint is:

$$r^2_{z_{4-6-10-12}} = \sum_{i=1}^{n_2}(2|F_{v2}X^{ct}_{f_i}| - F_{v3}X^{ct}_{f_i})^2. \tag{7.38}$$

For the n_3 points 2 and n_4 points 8:

$$r^2_{z_2} = \sum_{i=1}^{n_3}\left(\frac{|F_{v1}X^{ct}_{1_i}|F_{v3}X^{ct}_{3_i} + |F_{v1}X^{ct}_{3_i}|F_{v3}X^{ct}_{1_i}}{|F_{v1}X^{ct}_{1_i}| + |F_{v1}X^{ct}_{3_i}|} - F_{v3}X^{ct}_{2_i}\right)^2, \tag{7.39}$$

$$r^2_{z_8} = \sum_{i=1}^{n_4}\left(\frac{|F_{v1}X^{ct}_{7_i}|F_{v3}X^{ct}_{9_i} + |F_{v1}X^{ct}_{9_i}|F_{v3}X^{ct}_{7_i}}{|F_{v1}X^{ct}_{7_i}| + |F_{v1}X^{ct}_{9_i}|} - F_{v3}X^{ct}_{8_i}\right)^2. \tag{7.40}$$

Finally, for the n_5 points 5 and n_6 points 11:

$$r^2_{z_5} = \sum_{i=1}^{n_5}\left(\frac{|F_{v2}X^{ct}_{4_i}|F_{v3}X^{ct}_{6_i} + |F_{v2}X^{ct}_{6_i}|F_{v3}X^{ct}_{4_i}}{|F_{v2}X^{ct}_{4_i}| + |F_{v2}X^{ct}_{6_i}|} - F_{v3}X^{ct}_{5_i}\right)^2, \tag{7.41}$$

$$r^2_{z_{11}} = \sum_{i=1}^{n_6}\left(\frac{|F_{v2}X^{ct}_{10_i}|F_{v3}X^{ct}_{12_i} + |F_{v2}X^{ct}_{12_i}|F_{v3}X^{ct}_{10_i}}{|F_{v2}X^{ct}_{10_i}| + |F_{v2}X^{ct}_{12_i}|} - F_{v3}X^{ct}_{11_i}\right)^2. \tag{7.42}$$

Thus:

$$r_z^2 = r^2_{z_{1-3-7-9}} + r^2_{z_{4-6-10-12}} + r^2_{z_2} + r^2_{z_5} + r^2_{z_8} + r^2_{z_{11}}, \tag{7.43}$$

with $n = n_1 + n_2 + n_3 + n_4 + n_5 + n_6$.

Once F_v is determined, it is possible to calculate the tilts of the stereotactic ring in the DPM reference system. This will be important in the future determination of the starting position and direction of a source particle. We will denote ψ^{ct}_x, ψ^{ct}_y and ψ^{ct}_z the tilt angles of the stereotactic ring around respectively, the x^{ct}-, y^{ct}- and z^{ct}-axis of

the CT-image reference system. Let us consider 2 points P_1 and P_2 whose coordinates are $(x_1^{st}, y_1^{st}, z_1^{st})$, $(x_2^{st}, y_2^{st}, z_2^{st})$ in the stereotactic reference system and $(x_1^{ct}, y_1^{ct}, z_1^{ct})$, $(x_2^{ct}, y_2^{ct}, z_2^{ct})$ in the CT-image reference system. According to CT-image and stereotactic reference system orientations, the tilt angles of the ring in the CT-reference system are given by:

$$\psi_x^{ct} = \arctan \frac{z_1^{ct} - z_2^{ct}}{y_2^{ct} - y_1^{ct}} = \frac{F_{v3}^{-1} \begin{pmatrix} x_1^{st} \\ y_1^{st} \\ z_1^{st} \\ 1 \end{pmatrix} - F_{v3}^{-1} \begin{pmatrix} x_1^{st} \\ 0 \\ z_1^{st} \\ 1 \end{pmatrix}}{F_{v2}^{-1} \begin{pmatrix} x_1^{st} \\ y_1^{st} \\ z_1^{st} \\ 1 \end{pmatrix} - F_{v2}^{-1} \begin{pmatrix} x_1^{st} \\ 0 \\ z_1^{st} \\ 1 \end{pmatrix}}, \tag{7.44}$$

$$\psi_y^{ct} = \arctan \frac{z_1^{ct} - z_2^{ct}}{x_2^{ct} - x_1^{ct}} = \frac{F_{v3}^{-1} \begin{pmatrix} x_1^{st} \\ y_1^{st} \\ z_1^{st} \\ 1 \end{pmatrix} - F_{v3}^{-1} \begin{pmatrix} 0 \\ y_1^{st} \\ z_1^{st} \\ 1 \end{pmatrix}}{F_{v1}^{-1} \begin{pmatrix} x_1^{st} \\ y_1^{st} \\ z_1^{st} \\ 1 \end{pmatrix} - F_{v1}^{-1} \begin{pmatrix} 0 \\ y_1^{st} \\ z_1^{st} \\ 1 \end{pmatrix}}, \tag{7.45}$$

$$\psi_z^{ct} = \arctan \frac{x_1^{ct} - x_2^{ct}}{y_2^{ct} - y_1^{ct}} = \frac{F_{v1}^{-1} \begin{pmatrix} x_1^{st} \\ y_1^{st} \\ z_1^{st} \\ 1 \end{pmatrix} - F_{v1}^{-1} \begin{pmatrix} x_1^{st} \\ 0 \\ z_1^{st} \\ 1 \end{pmatrix}}{F_{v2}^{-1} \begin{pmatrix} x_1^{st} \\ y_1^{st} \\ z_1^{st} \\ 1 \end{pmatrix} - F_{v2}^{-1} \begin{pmatrix} x_1^{st} \\ 0 \\ z_1^{st} \\ 1 \end{pmatrix}}, \tag{7.46}$$

where F_{v2}^{-1}, F_{v2}^{-1} and F_{v2}^{-1} are respectively the 1^{st}, 2^{nd} and 3^{rd} row of the F_v^{-1} matrix. In the stereotactic reference system, we have:

$$\psi_x^{st} = -\psi_x^{ct}, \psi_y^{st} = -\psi_y^{ct}, \psi_z^{st} = \psi_z^{ct}, \tag{7.47}$$

and in the DPM reference system:

$$\psi_x^{dpm} = -\psi_z^{ct}, \psi_y^{dpm} = \psi_x^{ct}, \psi_z^{dpm} = -\psi_y^{ct}. \tag{7.48}$$

7.2.3 Implementation and validation

In order not to reduce the accuracy of the transformation, F_v is calculated taking into account the original 512×512 CT-images. The in-house routine LOCATEGLOBALEV searches in each CT-images the fiducial points and calculates for these points the stereotactic coordinates. An output file *patient*.st is created. The routine Microsoft Excel^{TM} SOLVER based on the Generalized Reduced Gradient (GRG2) nonlinear optimization code [LWJ+78] reads *patient*.st and calculates F_v. Figure 7.9 shows the results of the stereotactic transformation and compares with the results given by the commercial TPS STP3 in two distinct patient cases. A very good agreement was found between the results thus indicating that our transformation is accurate. This accuracy is also confirmed by results of the ring tilts presented in Table 7.2.

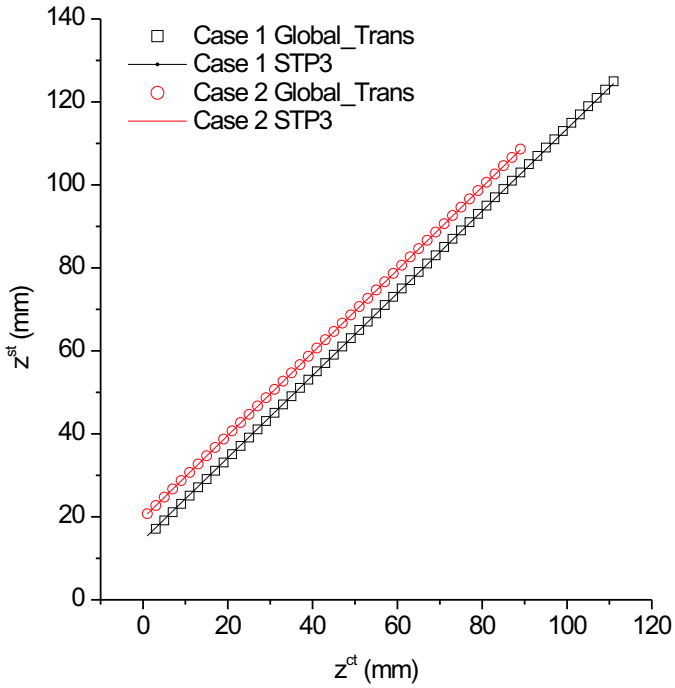

Figure 7.9: Stereotactic transformation results in two patient cases.

Angle (degrees)	Case 1		Case 2	
	GlobalTrans	STP3	GlobalTrans	STP3
ψ_x^{ct}	0.62	0.74	0.63	0.71
ψ_y^{ct}	0.14	0.09	0.20	0.09
ψ_z^{ct}	1.94	2.10	2.78	2.81

Table 7.2: Tilts of the ring in the CT-reference system for two cases compared with ones calculated by the commercial TPS STP3.

7.3 Source Interface

In Chapter 6, we have developed a multiple source model where the characteristics of the photons in scoring plane 2 were sampled from 1-D and 2-D histograms. Radiosurgery treatments are characterized by no-coplanar arcs. That is, we have to calculate the new position and direction of a sampled photon from the multiple source model, taking into account the positions of the gantry and the couch of the accelerator, but also the tilts of the ring. We will denote θ_g and φ_c the angles of the gantry and couch according to DIN-6847 standard norm (see Fig. 7.10).

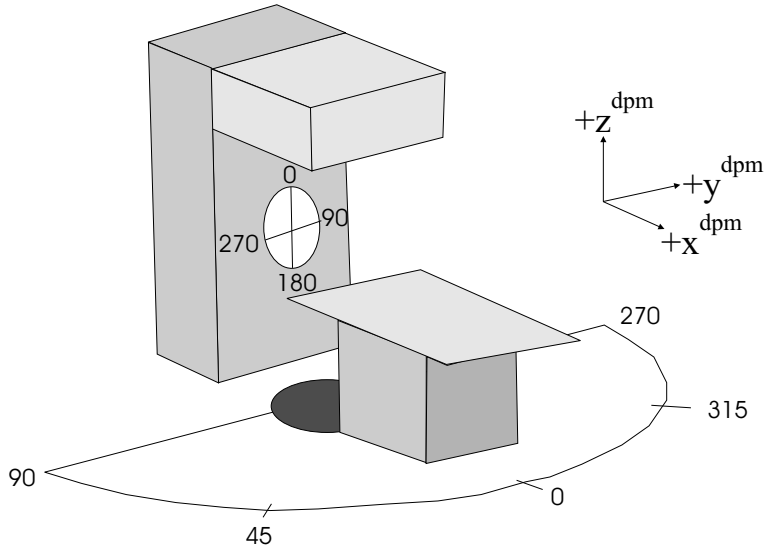

Figure 7.10: Angle definitions of the linear accelerator according to the DIN-6847 standard. The DPM reference system is also represented.

7.3.1 Rotation transformations

If we first consider that the isocenter of the accelerator is located at $(0, 0, 0)$ in the DPM reference system and (x^s, y^s, z^s) the coordinates of the sampled photon (from the multiple source model) in the DPM reference system, the new coordinates (x_1^s, y_1^s, z_1^s) of the photon, taking into account the rotations of the gantry and the couch (see Fig. 7.11), are given by:

$$\begin{pmatrix} x_1^s \\ y_1^s \\ z_1^s \end{pmatrix} = B_{\theta_g,\varphi_c} \begin{pmatrix} x^s \\ y^s \\ z^s \end{pmatrix}, \tag{7.49}$$

where

$$B_{\theta_g,\varphi_c} = \begin{pmatrix} \cos\varphi_c & -\cos\theta_g \sin\varphi_c & -\sin\theta_g \sin\varphi_c \\ \sin\varphi_c & \cos\theta_g \cos\varphi_c & \sin\theta_g \cos\varphi_c \\ 0 & -\sin\theta_g & \cos\theta_g \end{pmatrix}. \tag{7.50}$$

The new cosines vectors are thus simply given by:

$$\begin{pmatrix} u_1^s \\ v_1^s \\ w_1^s \end{pmatrix} = B_{\theta_g,\varphi_c} \begin{pmatrix} u^s \\ v^s \\ w^s \end{pmatrix}, \tag{7.51}$$

where (u^s, v^s, w^s) are the cosines vectors in the DPM reference system of the sampled photon in scoring plane 2. It must be reminded that (x^s, y^s, z^s) and (u^s, v^s, w^s) are given in the DPM reference system with of course $\theta_g = \varphi_c = 0$.

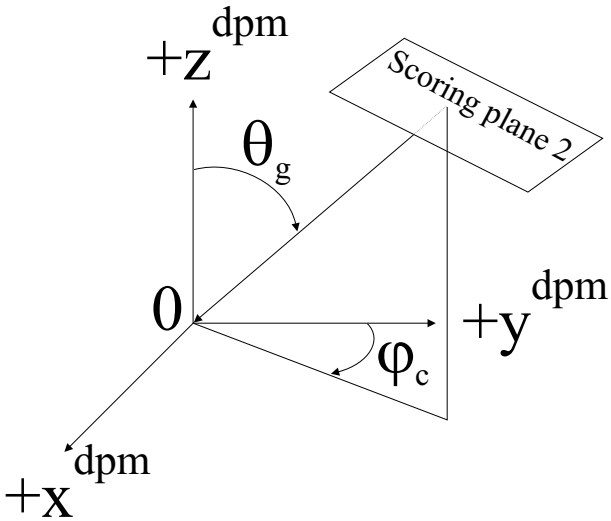

Figure 7.11: Angle definitions of the gantry (θ_g) and couch (φ_c) of the accelerator according to the DPM reference system.

Now, we have to take into account the tilts of the ring in the DPM reference system. The coordinates of the photon are then given by:

$$\begin{pmatrix} x_2^s \\ y_2^s \\ z_2^s \end{pmatrix} = B_\psi \begin{pmatrix} x_1^s \\ y_1^s \\ z_1^s \end{pmatrix}, \tag{7.52}$$

where

$$B_\psi = \begin{pmatrix} \cos\psi_x^{st}\cos\psi_y^{st} - \sin\psi_x^{st}\sin\psi_y^{st}\sin\psi_z^{st} & -\sin\psi_y^{st}\cos\psi_z^{st} & -\sin\psi_x^{st}\cos\psi_y^{st} - \cos\psi_x^{st}\sin\psi_y^{st}\sin\psi_z^{st} \\ \cos\psi_x^{st}\sin\psi_y^{st} + \sin\psi_x^{st}\cos\psi_y^{st}\sin\psi_z^{st} & \cos\psi_y^{st}\cos\psi_z^{st} & -\sin\psi_x^{st}\sin\psi_y^{st} + \cos\psi_x^{st}\cos\psi_y^{st}\sin\psi_z^{st} \\ \sin\psi_x^{st}\cos\psi_z^{st} & -\sin\psi_z^{st} & \cos\psi_x^{st}\cos\psi_z^{st} \end{pmatrix}. \tag{7.53}$$

The cosines vectors are also given by:

$$\begin{pmatrix} u_2^s \\ v_2^s \\ w_2^s \end{pmatrix} = B_\psi \begin{pmatrix} u_1^s \\ v_1^s \\ w_1^s \end{pmatrix}. \tag{7.54}$$

Combining Eqs. 7.49 with 7.52 and 7.51 with 7.54, the coordinates and cosines vectors of a photon sampled from the scoring plane taking into account the rotations of the gantry and the couch of the accelerator and also the tilts of the ring are given by:

$$\begin{pmatrix} x_2^s \\ y_2^s \\ z_2^s \end{pmatrix} = B_\psi B_{\theta_g,\varphi_c} \begin{pmatrix} x^s \\ y^s \\ z^s \end{pmatrix}, \tag{7.55}$$

and

$$\begin{pmatrix} u_2^s \\ v_2^s \\ w_2^s \end{pmatrix} = B_\psi B_{\theta_g,\varphi_c} \begin{pmatrix} u^s \\ v^s \\ w^s \end{pmatrix}. \tag{7.56}$$

Finally, all the calculations were performed taking into account that the coordinates of isocenter of the accelerator in the DPM reference system was $(0,0,0)$. If the coordinates of the isocenter are $(x_{iso}^{dpm}, y_{iso}^{dpm}, z_{iso}^{dpm})$, the final coordinates of the sampled photons are simply given by:

$$x_3^s = x_2^s + x_{iso}^{dpm}, \tag{7.57}$$

$$y_3^s = y_2^s + x_{iso}^{dpm}, \tag{7.58}$$

$$z_3^s = z_2^s + x_{iso}^{dpm}. \tag{7.59}$$

7.3.2 Implementation

The characteristics of the photon in the scoring plane 2 are given by the in-house routine SOURCE_GENERATOR which reads the 1-D and 2-D histograms where the multiple source model is recorded. Once the coordinates and direction of the starting photon were determined in the DPM reference system, the in-house routine ROTATION3D_TAC calculates the new coordinates and direction of the photon taking into account the gantry and couch rotations and also the ring tilts.

At this stage, any simulation can not be performed yet. This is simply due to the definition of the DPM voxel-based phantom. In our simulations, the DPM phantom is filled with the CT-images. Any starting particle from scoring plane 2 is thus located outside the cube, which defines the phantom. In DPM simulations, the starting point of the particles must be located inside the cube. The in-house routine CROSS_PLANES3D calculates the coordinates $(x^s_{dpm}, y^s_{dpm}, z^s_{dpm})$ of a point P^s_{dpm}, which is the intersection between the line passing through the point (x^s_3, y^s_3, z^s_3) which direction is defined by (u^s_2, v^s_2, w^s_3), and the nearest face of the DPM cube phantom. Thus, P^s_{dpm} is the starting point of the photon for simulation.

The purpose of our MC-based TPS is a post-planning dose calculation evaluation. That is why the coordinates of the isocenter $(x^{dpm}_{iso}, y^{dpm}_{iso}, z^{dpm}_{iso})$ are calculated by our stereotactic transformation using the stereotactic coordinates given by STP3. In STP3, the arcs are subdivided into fixed beams. Then, the same fixed beams will be used for the simulations. Figure 7.12 summarizes the implementation of the source interface.

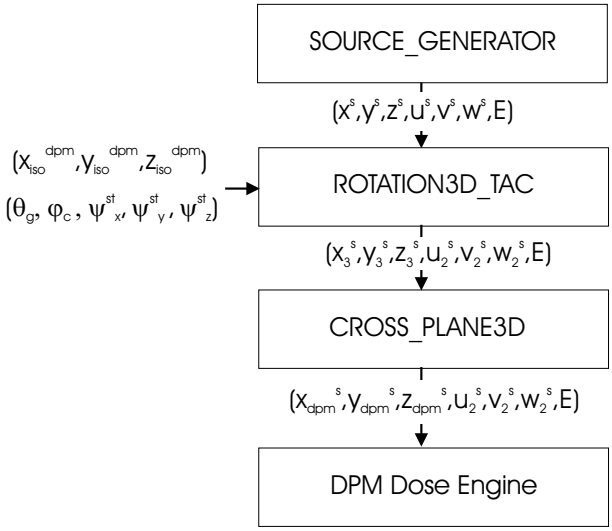

Figure 7.12: Simplified diagram of the Source Interface implementation.

7.4 Clinical cases

In this section, we will present results given by our simulations for two distinct cases. The two treated cases were arteriovenous malformation (AVM) localized in the brain. Table 7.3 shows the characteristics of each case. Calculations were performed using a Pentium IV processor (CPU=2.8 GHz) and 256 Mb RAM. For case 1, two sub-cases were simulated: the first one (Case 1.a) considering that all the materials are water, and the second (Case 2.a) taking into account the heterogeneities. For case 2, only one simulation was performed taking into account the heterogeneities. The number of histories for each fixed beam was 2.1×10^8. This number for the 11 mm additional collimator was fixed using the results presented in Table 6.3. Table 7.4 shows the average CPU time per fixed beam for each cases and the associated dose relative error at the isocenter.

	Case 1	**Case 2**
Target volume (cm^3)	2.4	1.7
Isocenter coordinates in stereotactic reference system (mm)	$(-44.9, -56.1, 57.1)$	$(-24.2, 8.4, 40.7)$
Tilts (degrees)		
ψ_x^{ct}	0.62	0.63
ψ_y^{ct}	0.14	0.20
ψ_z^{ct}	1.94	2.78
Additional collimator	11	11
Number of arcs	5	6
Couch positions φ_c (degrees according to IEC)	18,36,54,72,90	0,30,60,90,300,330
Gantry arc (degrees according to IEC)		
Start	100	20 (φ_c=0,30,60,90)
		340 (φ_c=300,330)
Stop	172	160 (φ_c=0,30,60,90)
		200 (φ_c=300,330)
Number of fixed beams	25	48
Dose at isocenter (Gy)	20 (100%)	18.8 (100%)
Reference isodose Pr in STP3 (Gy)	15 (75%)	15 (79.8%)

Table 7.3: Plan characterization for two patient cases. The reference isodose Pr is the isodose that involves at least 90% of the volume the target.

	Case 1.a	**Case 1.b**	**Case 2**
Average CPU time/Fixed beam (hours)	2.38	3.28	2.36
Dose error at isocenter	$\pm 0.22\%$	$\pm 0.22\%$	$\pm 0.17\%$

Table 7.4: Average CPU time per fixed beam and dose associated error at isocenter for simulations performed with 2.1×10^8 histories (per fixed beam) using the 11 mm additional collimator.

The first important result and shown in Tables 7.5 and 7.6 deals with the maximum dose value and its localization. MC simulations show that if the heterogeneities are taking into account, there is an increase of 1.9% for Case 1 and 1.8% for Case 2 of the value of the maximum dose compared with the values given by STP3. It is interesting to notice that this increase is of the same order as that found by Rugsti *et al.* [RRJ+98]. This increase can be clinically relevant. Also relevant can be the new localization found by MC simulations for the maximum dose. In the two cases with heterogeneities, it has been found that the maximum dose is located outside the target volume compared with STP3.

	STP3 Case 1	**RMSM Case 1.a**	**RMSM Case 1.b**
Value of maximum dose (%)	102.5	102.4	104.4
Stereotactic coordinates of maximum dose (mm)	$(-47.3, -61.4, 59.9)$	$(-48.2, -62.0, 61.9)$	$(-50.5, -64.5, 63.9)$
Localization of maximum dose	in target	in target	outside target (in cranial bone)

Table 7.5: Comparison between maximum dose points calculated by STP3 and RMSM for cases 1.a and 1.b.

	STP3 Case 2	**RMSM Case 2**
Value of maximum dose (%)	100.5	103.3
Stereotactic coordinates of maximum dose (mm)	$(-24.2, 8.6, 42.6)$	$(-27.81, 12.15, 42.7)$
Localization of maximum dose	in target	outside target

Table 7.6: Comparison between maximum dose points calculated by STP3 and RMSM for case 2.

Unfortunately, only qualitative dose distribution comparisons with the commercial TPS STP3 can be performed since STP3 does not allow exporting data such as volumes (for dose volume histogram representations), dose matrix distributions. Comparisons between STP3 and simulations results are obtained using the normalized dose distributions (100% at isocenter) in the axial, coronal and sagittal planes where the isocenter is localized. It is perfectly visible in Figs. 7.13-7.27 that, in all the cases, the 95% isodose given by MC simulations is smaller than that calculated by STP3. Also perfectly visible is that the 10% isodose calculated by MC is always larger than that calculated by STP3. For Case 1, it seems that there are no significant differences between STP3 and MC results for isodoses 90, Pr, 50% (Pr is the isodose that involves at least 90%

of the volume the target in STP3) even in case 1.b where the heterogeneities and the inferior pin and support are taken into account. This is probably due to the fact that, in this region, there is no large differences between material densities ($\backsim$ 1 for brain and from 1.2 to 2 for cranial bone region). When the target is located near a high region density, which is exactly Case 2, some important differences appear. The effect of the high density region is visible in the axial plane as shown in Figs. 7.22 and 7.23 where isodoses 95 and 90% calculated by STP3 are different from those calculated by MC. Figures 7.22 and 7.23 also show that due to this high density heterogeneity, the isodoses are stretched in the z^{dpm}-axis as well shown in the sagittal plane (see Figs. 7.26 and 7.27).

Figure 7.13: Dose distribution calculated by STP3 for case 1 in the axial plane.

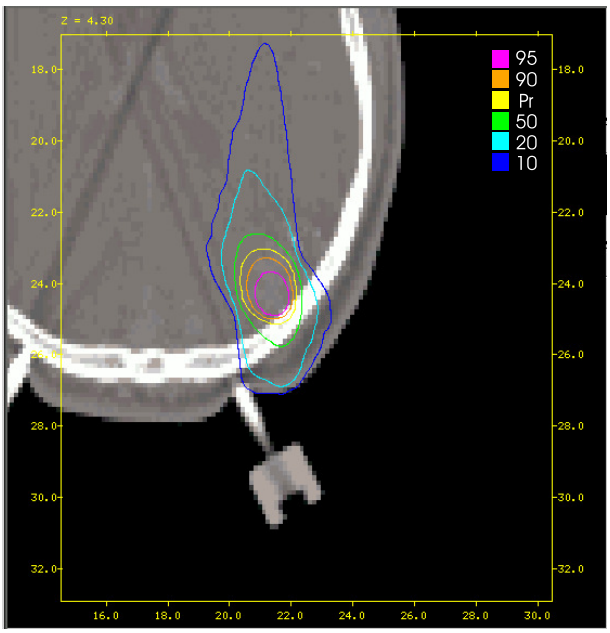

Figure 7.14: Dose distribution calculated without heterogeneities by RMSM for case 1.a in the axial plane.

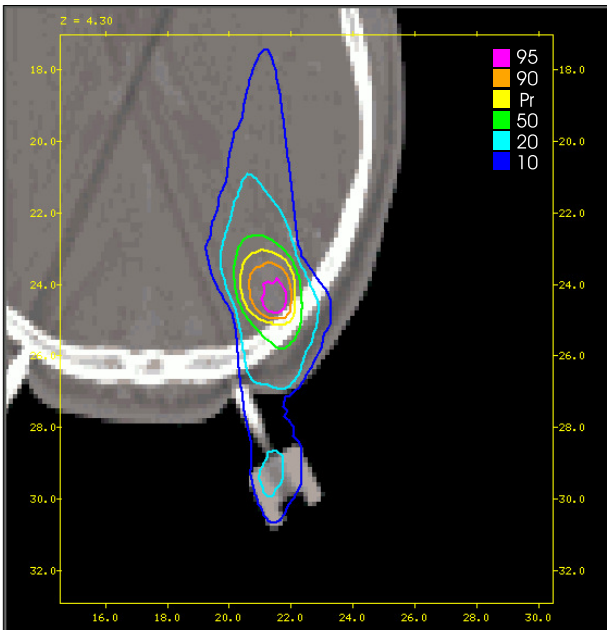

Figure 7.15: Dose distribution calculated with heterogeneities by RMSM for case 1.b in the axial plane.

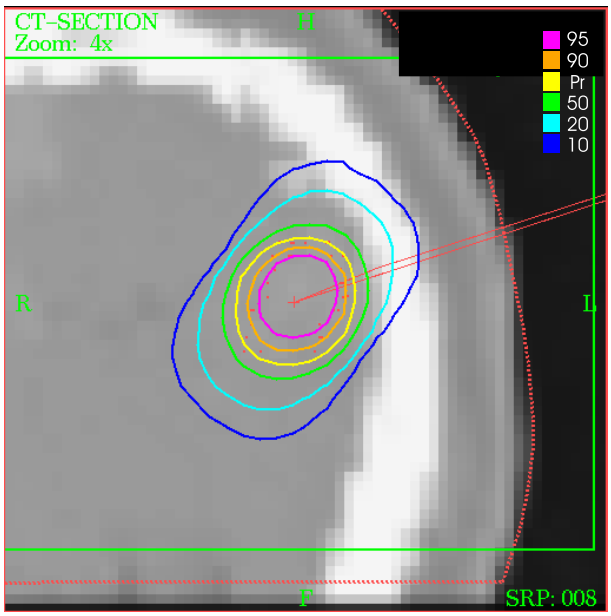

Figure 7.16: Dose distribution calculated by STP3 for case 1 in the coronal plane.

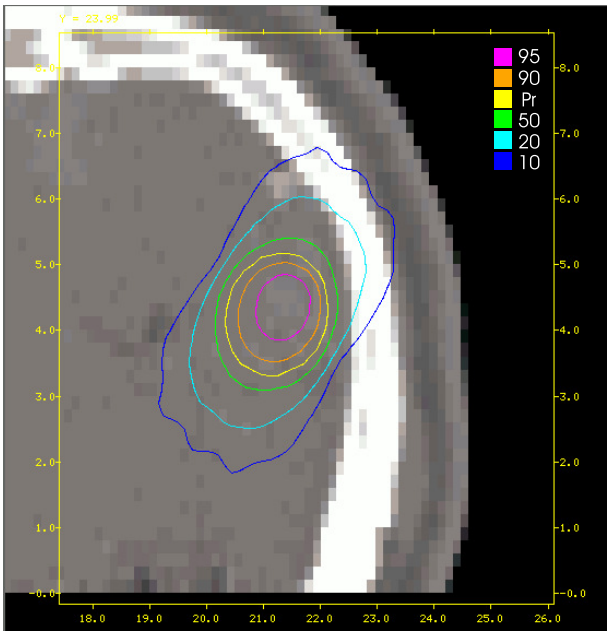

Figure 7.17: Dose distribution calculated without heterogeneities by RMSM for case 1.a in the coronal plane.

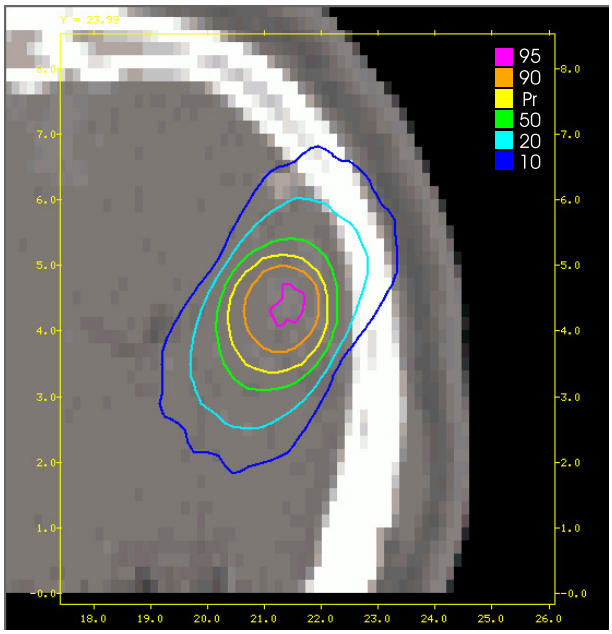

Figure 7.18: Dose distribution calculated with heterogeneities by RMSM for case 1.b in the coronal plane.

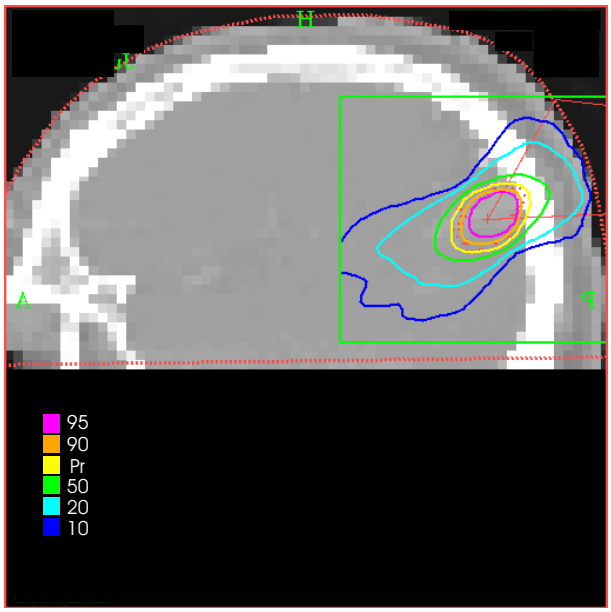

Figure 7.19: Dose distribution calculated by STP3 for case 1 in the sagittal plane.

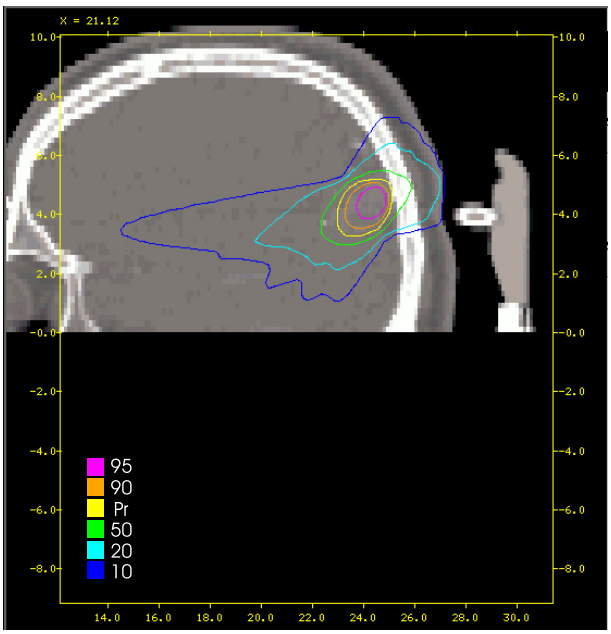

Figure 7.20: Dose distribution calculated without heterogeneities by RMSM for case 1.a in the sagittal plane.

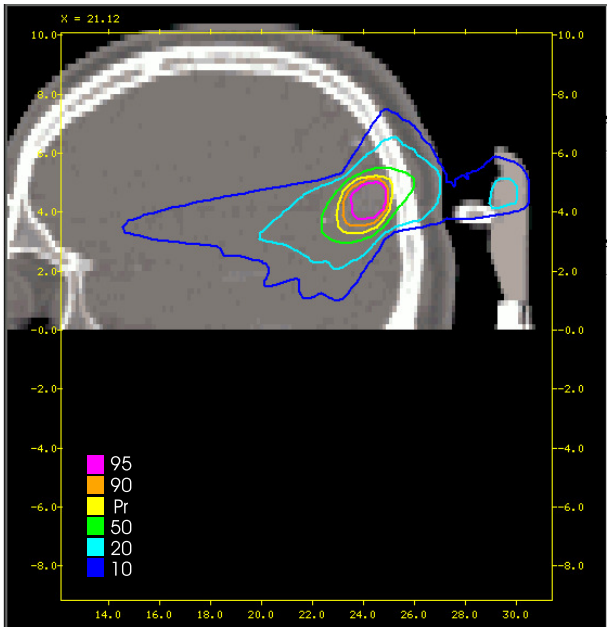

Figure 7.21: Dose distribution calculated with heterogeneities by RMSM for case 1.b in the sagittal plane.

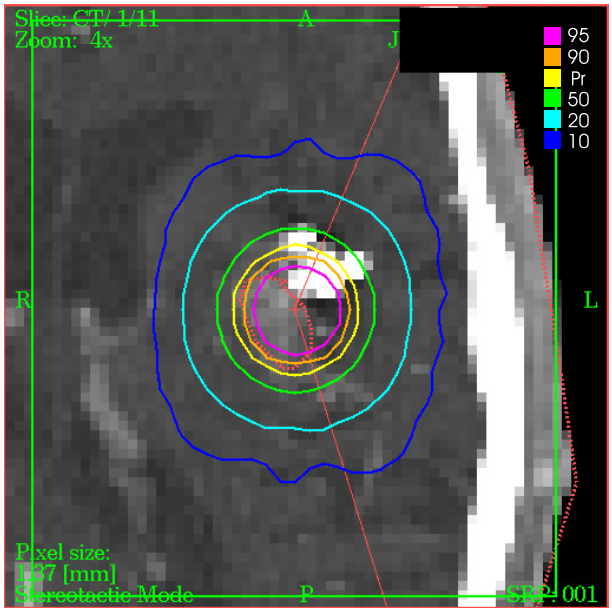

Figure 7.22: Dose distribution calculated by STP3 for case 2 in the axial plane.

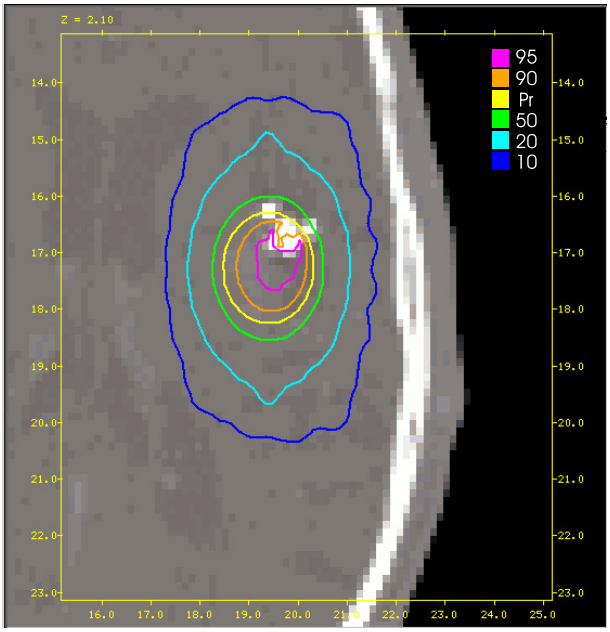

Figure 7.23: Dose distribution calculated with heterogeneities by RMSM for case 2 in the axial plane.

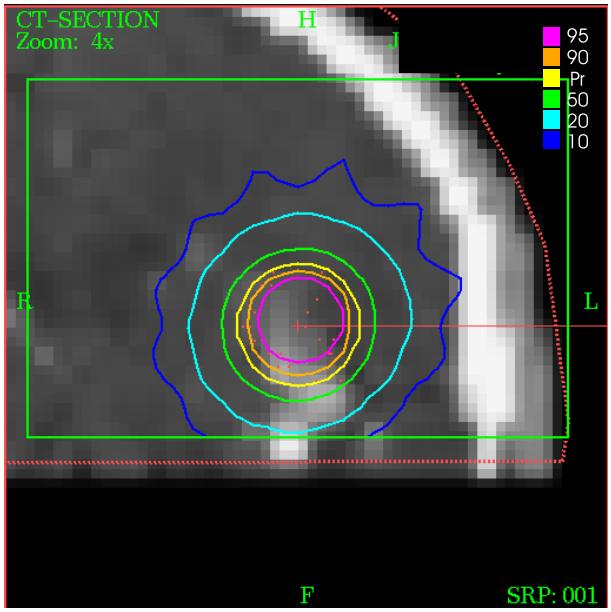

Figure 7.24: Dose distribution calculated by STP3 for case 2 in the coronal plane.

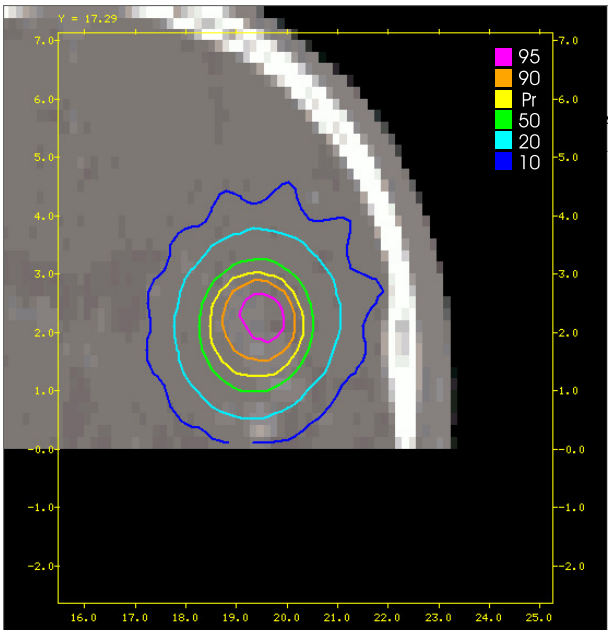

Figure 7.25: Dose distribution calculated with heterogeneities by RMSM for case 2 in the coronal plane.

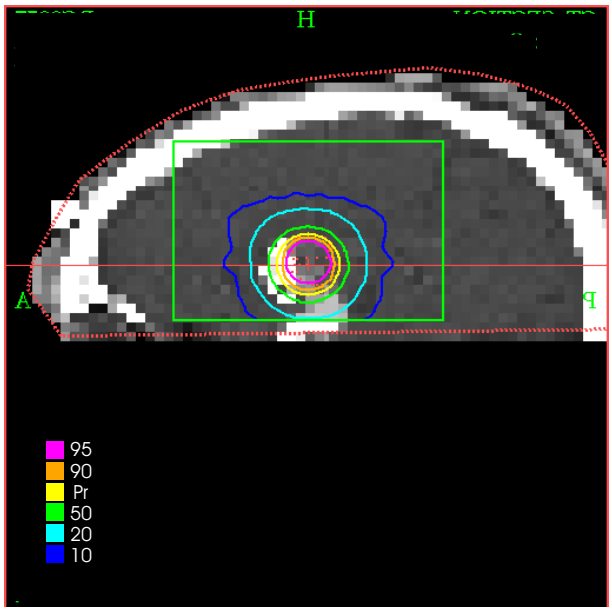

Figure 7.26: Dose distribution calculated by STP3 for case 2 in the sagittal plane.

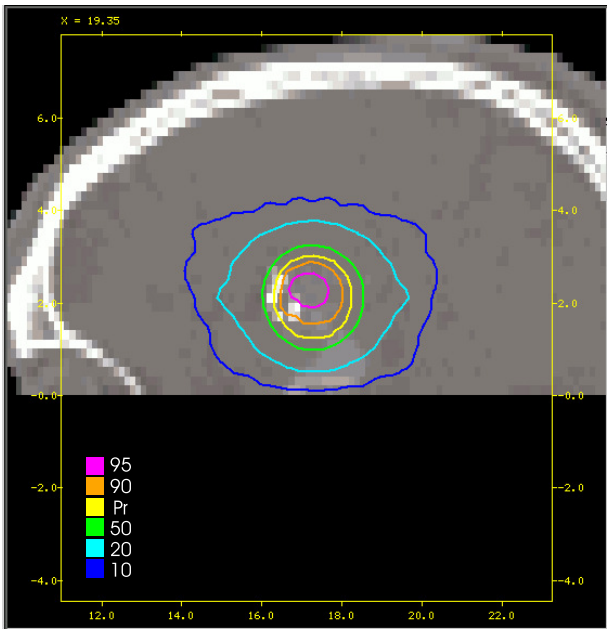

Figure 7.27: Dose distribution calculated with heterogeneities by RMSM for case 2 in the sagittal plane.

This study has shown that, when the target is localized in regions with low differences in material density, MC results are not so different than the results given by STP3. Great differences appear when the target is localized near a high density region. This last result is particularly important if we consider not only SRS treatments but also stereotactic radiotherapy treatments (SRT). For example, in head and neck treatments using SRT procedure, lesions are localized in regions with large density differences: bone, soft tissue, air cavities. In this region, Rodrigues [Rod02] has found differences between MC calculations and commercial TPS results of the order of 10% for conventional radiotherapy photon beams. Our model can be easily adapted to SRT procedures, using CBI techniques, modifying only the stereotactic transformation interface. This will, for sure, improve the accuracy of the calculated dose distributions in SRT procedures.

Conclusions

Two main objectives were delineated in the beginning of this work. The first one was to determine the most accurately as possible the absorbed dose delivered by narrow photon beams. Linked to this objective was the problematic of the behavior of the depth of maximum dose for such narrow photon beams. The second main objective was to develop a fast and as accurate as possible MC-based radiosurgery treatment planning for post-treatment verification.

A full MC simulation of the Siemens Mevatron KD2 linear accelerator head in 6 MV photon mode was performed. The resulting Phase Space Data was validated through a common approach which was to compare the calculated dose distributions for each additional collimator with the results obtained from different measurement methods and try to find a internal self-consistency. A good agreement between the calculated and depth dose curves measured with the diode, the Markus and the PinPoint detectors, for depths higher than 10 mm was found although it exists a tendency of over-response by the Markus detector and under-response by the PinPoint detector for the smallest additional collimators and at large depths. For off axis ratio, calculations were found to be in a good agreement with measurements performed with the diode. The PinPoint chamber is not adequate to resolve accurately the dose in the penumbra due to its volume effect. The film, although better than the PinPoint chamber in the penumbra region, overestimates the dose in the low-dose region due to calibration difficulties. Thus, it can be concluded that the diode detector is a good choice for depth dose and off axis ratio measurements for narrow photon beams. Due to the lack of lateral electron equilibrium, the type and size of the detectors were shown to have a great influence in the correct determination of the output factors for the smallest narrow photon beams. Great differences between calculated and measured OF were found for these smallest fields. MC calculations were shown to be the most accurate method for OF determination.

The behavior of d_{max} for narrow photon beams was fully understood studying the details of the scattered photon and electron processes in water. The depth of maximum dose d_{max} increases as the size of the additional collimator increases for narrow photons beams used in radiosurgery and that was confirmed by the MC simulations. This phenomenon is opposite to what happens in conventional radiotherapy photon beams. Although the additional collimator scatter dose component is not negligible, the d_{max} associated to this component remains unchanged as the size of the additional collimator increases. Photons that have no interactions in the additional collimators mainly determine the shift in d_{max} for narrow photon beams. MC simulations in water showed that secondary electrons contributing to the central axis dose could be divided in two groups. Electrons from one photon collision are originated far way from the central axis and can deposit dose deeper from their point of origin. However there are electrons from more than one photon collision originated very near the beam central axis that deposit dose locally. It was demonstrated that also these electrons contribute to the same effect in d_{max}. Finally, it was demonstrated that the changes in the initial gradient of the depth dose curves as the size of the additional collimators increases, are due to the contributions of electrons originated from one photon collision processes in water. The increasing use of small photon fields not only in radiosurgery but also, more and more often, in intensity modulated radiotherapy (IMRT) beam segments, raises the interest of this kind of detailed study.

Due to the great limitation in time and storage capacity in full MC simulations, a multiple source model applied to radiosurgery was developed. To achieve this goal, a full characterization of the narrow photons beams produced by radiosurgery additional collimators was performed. This full characterization showed that electron contributions could be neglected. Also, most of the photons in the radiation beam came from the accelerator head components, particularly form the target. Finally the photons originated in the additional collimators can be separated in two components. For each additional collimator simulation, eight relevant virtual sources were considered: five representing the accelerator head components and three representing the additional collimator. Beam reconstructions were performed sampling stored 1-D and 2-D distributions. For direction determination, a sampling was performed in the stored cosine direction distributions for virtual sources representing the additional collimators. Using the very fast code DPM, dose distributions were calculated in a water phantom and a very good agreement was found with measurements.

Our model, which is the dose engine of a MC-based treatment planning system, was applied to real complex clinical cases. Due to the particularity of the MC DPM, a CT-interface was developed to include the CT-images characteristics into voxel-based geometry. Using a developed stereotactic transformation interface, the positions of the virtual sources, simulating the arcs, were easily determined. In the two studied real cases, our MC based treatment planning has shown that, when the target is localized in regions with low differences in material density, results are not so different than results given by our commercial treatment planning. Great differences appear when the target is localized near a high density region. The relevance of such differences depends on the type of target (tumor, AVM), dimension and localization. This is why plan dose distributions are discussed by a multidisciplinary team to try to find the best compromise between what the Physician wants and what the Physicist can deliver.

Our treatment planning was developed to be a post-treatment verification tool. Further work has to be done to really substitute a conventional treatment planning. First, tools to delineate volumes have to be introduced in our system. This will allow the evaluation of plans using dose volume histograms. Second, the determination of the accelerator monitor units have to be included. Finally, using a CPU cluster and with the constant increase of CPU velocities, the overall calculation process will drastically decrease. This can be performed because our model calculates each fixed beam in separate runs.

In this thesis, we cared about radiosurgery treatments performed with conical additional collimators producing narrow photon beams. In the past few years, more and more sophisticated delivery techniques appeared. One of the most widely spread is the use of the micro multileaf. The shape of the irradiation beam is adjusted to the lesion volume. Treatment can be performed using a pre-determined number of static beams or using arcs where the beam shapes are dynamically adjusted to the lesion. The accurate determination of the absorbed dose in the patients is very problematic especially when plans are based on IMRT techniques. It will be, for sure, a great and enthusiastic challenge to apply the Monte Carlo methods to simulate such beams. The thorough examination and understanding of the details of basic dosimetry of such beams and associated microscopic processes of energy deposition phenomena will contribute to more accurate dose calculations in order to fulfill the ultimate aim of those demanding modern radiotherapy techniques.

References

[AA99] A.Ahnesjö and M.M.Aspradakis, "Dose calculations for external photon beams in radiotherapy", *Phys. Med. Biol.* **44**:R99–R155, 1999.

[AAP95] "Stereotactic Radiosurgery", AAPM Report 54, American Association of Physicists in Medicine, American Institute of Physics, New York, 1995.

[AB84] P.Andreo and A.Brahme, "Restricted energy-loss straggling and multiple scattering of electrons in mixed Monte Carlo procedure", *Radiat. Res.* **100**:16–29, 1984.

[ABL+97] P.Aaltonen, A.Brahme, I.Lax, S.Levernes, I.Naslund, J.B.Reitan, and I.Turesson, "Specification of dose delivery in radiation therapy", *Acta Oncol.* **36**:1–32, 1997.

[And92] P.Andreo, "Absorbed dose beam quality factors for dosimetry of high-energy photon beams", *Phys. Med. Biol.* **37**:2189–2211, 1992.

[Arn93] J.Arndt, "Focussed Gamma radiation - The Gamma Knife", *Chapter 3 in Physical Aspects of Stereotactic Radiosurgery,* pp 87-128, Edited by M.H.Philips, Plenum Press, New York, 1993.

[Att84] F.H.Attix, "A simple derivation of Ngas, a correction in Awall, and other comments on the AAPM Task Group 21 protocol", *Med. Phys.* **11**(5):725–728, 1984.

[Att86] F.H.Attix, "Introduction to Radiological Physics and Radiation Dosimetry", Wiley, New York, 1986.

[BCC+00] R.Brun, O.Couet, N.L.Cremel, C.Vandomi, and P.Zanarini, "PAW - Physics Analysis Workstation", program Library Long Writeup Q121, CERN, European Organization for Nuclear Research, Geneva, 2000.

[BCL88] A.Brahme, J.Chavaudra and T.Landberg, "Accuracy requirements and quality assurance of external beam therapy with photons and electrons", *Acta Oncol.* **1**:1–76, 1988.

[BD83] O.Betti and V.Derechinsky, "Irradiation stereotaxique multifaisceaux", *Neurochirurgie* **29**:295–298, 1983.

[Ber63] J.M.Berger, "Monte Carlo calculation of the penetration and diffusion of fast charged particles", *in Methods of Computational Physics*, Vol. I, pp 135-215, Edited by B.Alder, S.Fernbach and M.Rotenberg, Academic Press, New York, 1963.

[BHS+99] M.J.Berger, J.H.Hubbell, S.M.Seltzer, J.S.Coursey and D.S.Zucker, "XCOM: Photon Cross Sections Database - NIST Standard Reference Database 8 (XGAM)", National Institute of Standards and Tecnology, 1999.
http://physics.nist.gov/PhysRefData/Xcom/Text/XCOM.html

[Bie00] A.F.Bielajew. "Photon Monte Carlo simulation", *Chapter 12 in Fundamentals of the Monte Carlo Method for Neutral and Charged Particle Transport*, pp 161-178, University of Michigan, 2000.

[BL50] O.Blunck and S.Leisegang, "Zum Energieverlust schneller Elektronen in dünnen Schichten", *Z. Physik* **128**:500, 1950.

[BL79] P.J.Biggs and C.C.Ling, "Electrons as the cause of the observed d_{max} shift with field size in high energy photon beams", *Med. Phys.* **6**:291–295, 1979.

[BMO94] A.S.Beddar, D.J.Manson and P.F.O'Brien, "Absorbed dose perturbation caused by diodes for small field photon dosimetry", *Med. Phys.* **21**:1075–1079, 1994.

[BR87] A.F.Bielajew and D.W.O.Rogers, "PRESTA: The parameter reduced electron-step transport algorithm for electron Monte Carlo transport", *Nucl. Instrum. Methods Phys. B*, **18**:165–183, 1987.

[Bra10] W.H.Bragg, "Consequences of the corpuscular hypothesis of the gamma and x rays, and the ranges of the beta rays", *Phil. Mag.*, **20**:385, 1910.

[Bra88] A.Brahme, "Accuracy requirements and quality assurance of external beam therapy with photons and electrons", *Acta Oncol.* Suppl. 1, 1988.

[Bri00] J.Briesmeister, "MCNP-A General Monte Carlo N-particle transport code version 4C", Report LA-13709-M, Los Alamos National Laboratory, Los Alamos, 2000.

[Brj72] British Journal of Radiology, Suppl. 11, 1972.

[Bru94] R.Brun, "HBOOK - Statistical Analysis and Histogramming", program Library Long Writeup Y250, CERN, European Organization for Nuclear Research, Geneva, 1994.

[BS82] M.J.Berger and S.M.Seltzer, "Stopping Powers and Ranges of Electrons and Positrons", Report NBSIR 82-2550, National Bureau of Standards, Washington DC, 1982.

[BS01] A.F.Bielajew and F.Salvat, "Improved electron transport mechanics in PENELOPE Monte Carlo model", *Nucl. Instrum. Methods Phys. B*, **173**:332–343, 2001.

[BTR89] B.E.Bjärngard, J.-S.Tsai and R.K.Rice, "Attenuation in very narrow photon beams", *Rad. Research*, 118:195–200, 1989.

[BW51] O.Blunck and K.Westphal, "Zum Energieverlust energiereicher Elektronen in dünnen Schichten", *Z. Physik* **130**:641, 1951.

[CAF01] A.Chaves, C.Alves, M.Fragoso, M.C.Lopes, C.Oliveira, L.Peralta, P.Rodrigues, J.Seco, and A.Trindade, "EGS4 and MCNP4B MC Simulation of a Siemens KD2 Accelerator in 6 MV Photon Mode", Technical Report 01-01, LIP Preprint Note, 2001.
http://weblib.cern.ch/abstract?EXT-2001-008

[CCG94] E.L.Chaney, T.J.Cullip and T.A.Gabriel, "A Monte Carlo study of accelerator head scatter", *Med. Phys.* **21**:1383–1390, 1994.

[CDS00] I.Chetty, J.J.DeMarco and T.D.Solberg, "A virtual source model for Monte Carlo modeling of arbitrary intensity distributions", *Med. Phys.* **27**:166–172, 2000.

[CE76] V.A.Chechin and V.C.Ermilova, "The Ionization-Loss Distribution at Very Small Absorber Thickness", *Nucl. Instr. Meth.* **136**:551, 1976.

[CLO00] A.Chaves, M.C.Lopes and C.Oliveira, "Monte Carlo simulation applied to radiosurgery narrow beams using MCNP4C", *Radioproteção* **1**:149–157, 2000/2001.

[CLO+03] A.Chaves, M.C.Lopes, C.Oliveira, C.Alves, L.Peralta, P.Rodrigues and A.Trindade, "Basic dosimetry of radiosurgery narrow beams using Monte Carlo simulations - A detailed study of depth of maximum dose", *Med. Phys.* **30**:2904–2911, 2003.

[CPS91] D.E.Cullen, S.T.Perkins and S.M.Seltzer, "Tables and Graphs of Electron Interaction Cross Section 10 eV to 100 GeV Derived from the LLNL Evaluated Electron Data Library (EEDL), Z=1-100", Techical Report UCRL-50400, Vol. 31, Lawrence Livermore National Laboratory, 1991.

[DB85] A.Dutreix and A.Bridier, "The dosimetry of ionizing radiation", Vol. 1, Academic Pressm Inc., 1985.

[DEH02] T.Depuydt, A.Van Esch and D.P.Huyskens, "A quantitative evaluation of IMRT dose distributions: refinement and clinical assessment of the gamma evaluation", *Rad. and Onc.* **62**:309–319, 2002.

[DGM+04] J. Deng, T.Guerrero, C.-M.Ma and R.Nath., "Modelling 6 MV photon beams of a stereotactic radiosurgery system for Monte Carlo treatment planning", *Phys. Med. Biol.* **49:**1689–1704, 2004.

[DJK+00] J.Deng, S.B.Jiang, A.Kapur, J.Li, T.Pawlicki and C.-M.Ma, "Photon beam characterization and modeling for Monte Carlo treatment planning", *Phys. Med. Biol.* **45**:411–427, 2000.

[DMH+03] J.Deng, C.-M.Ma, J.Hai and R.Nath, "Commissioning 6 MV photon beams of a stereotactic radiosurgery system for Monte Carlo treatment planning", *Med. Phys.* **30**:3124–3134, 2003.

[DSC+98] J.J.De Marco, T.D.Solberg, I.Chetty and J.B.Smathers, "Efficient sampling algorithms for Monte Carlo based treatment planning", *Radiat. Phys. Chem.* **53**:229–234, 1998.

[DSS98] J.J.De Marco, T.D.Solberg and J.B.Smathers, "A CT-based Monte Carlo simulation tool for dosimetry planning and analysis", *Med. Phys.* **25**:1–11, 1998.

[EJ84] M.J.Engler and G.L.Jones, "Small beam calibration by 0.6 and 0.2 cm^3 ionization chambers", *Med. Phys.* **11**:822–826, 1984.

[Eva55] R.D.Evans, "The atomic nucleus", McGraw-Hill Book Company, Inc., New York, 1955.

[FCA+99] M.Fragoso, A.Chaves, C.Alves, M.C.Lopes, C.Oliveira, L.Peralta L and J.Seco, "MC simulation of a linear accelerator treatment head -EGS4 and MCNP-4B intercomparison", *in Proc. 8th Int. Conf. On Calorimetry in High Energy Physics*, pp 697–702, Edited by G.Barreira, B.Tomé, A.Gomes, A.Maio and M.J.Varanda, World Scientific, Singapore, 1999.

[FCC+98] P.Francescon, S.Cora, C.Cavedon, P.Scalchi and S.Reccanello, "Use of new type of radiochromic film, a new parallel-plate micro-chamber, MOSFETs, and TLD 800 microtubes in dosimetry of small beams", *Med. Phys.* **25**:503–511, 1998.

[FCR+00] P.Francescon, C.Cavedon, S.Reccanello and S.Cora, "Photon dose calculation of a three-dimensional treatment planning system compared to the Monte Carlo BEAM", *Med. Phys.* **27**:1579–1587, 2000.

[FDH+98] B.Fraass, K.Doppke, M.Hunt, G.Kutcher, G.Starkschallm, R.Stern and J.Van Dyke, "American Association of Physicist in Medicine - Radiation Therapy Committee Task Group 53: Quality assurance for clinical radiotherapy treatment planning", *Med. Phys.* **25**:1773–1829, 1998.

[FHD+03] M.Fippel, F.Haryanto, O.Dohm and F.Nüsslin, "A virtual photon energy fluence model for Monte Carlo dose calculation", *Med. Phys.* **30**:301–311, 2003.

[FKR00] M.K.Fix, H.Keller and P.Rüegsegger, "Simple beam models for Monte Carlo photon beam dose calculations in radiotherapy", *Med. Phys.* **27**:2739–2747, 2000.

[FMB+93] J.M.Fernández-Vare, R.Mayol, J.Baró and F.Salvat, "On the theory and simulation of multiple elastic scattering electrons", *Nucl. Instrum. Methods Phys. B* **73**:447–473, 1993.

[FSM+01] M.K.Fix, M.Stampanoni, P.Manser, E.J.Born, R.Mini and P.Rüegsegger, "A multiple source model for 6 MV photon beam dose calculations using Monte Carlo", *Phys. Med. Biol.* **46**:1407–1457, 2001.

[GH78] M.A.Gardner and R.J.Howerton, "ACTL: Evaluated Neutron Activation Cross-Section Library - Evaluation Techniques and Reaction Index", Report UCRL-50400, Vol. 18, Lawrence Livermore National Laboratory, 1978.

[GK90] B.J.Gerbi and F.M.Khan, "Measurements of dose in the buildup region using fixed-separation plane parallel ionization chambers", *Med. Phys.* **17**:17–25, 1990.

[Gra29] L.H.Gray, "Absorption of penetrating radiation", *in Proc. Roy. Soc. A (London)*, 122:647, 1929.

[Gre81] J.R.Greening, "Fundamentals of Radiation Dosimetry", Adam Higler, Bristol, 1981.

[GS40a] S.A.Goudsmit and J.L.Saunderson, "Multiple scattering of electrons", *Phys. Rev.* **57**:24–29, 1940.

[GS40b] S.A.Goudsmit and J.L.Saunderson, "Multiple scattering of electrons II", *Phys. Rev.* **58**:36–42, 1940.

[Har95] G.H.Hartmann, "Quality Assurance Program on Stereotactic Radiosurgery", Report from a Quality Assurance Task Group, Spinger, Heidelberg, 1995.

[HCH+75] R.J.Howerton, D.E.Cullen, R.C.Haight, M.H.MacGregor, S.T.Perkins and E.F.Plechaty, "The LLL Evaluated Nuclear Data Library (ENDL): Evaluation Techniques, Reaction Index, and Descriptions of Individual Reactions", Report UCRL-50400, Vol. 15, Part A, Lawrence Livermore National Laboratory, 1975.

[Hei54] W.Heitler, "The Quantum Theory of Radiation", Clarendon Press, Oxford, 1954.

[HFL+02] F.Haryanto, M.Fippel, W.Laub, O.Dohm and F.Nüsslin, "Investigation of photon beam output factors for conformal radiation therapy - Monte

Carlo simulations and measurements", *Phys. Med. Biol.* **47**:N133–N143, 2002.

[HHB+93] M.Heydarian, P.W.Hoban, W.A.Beckham, I.M:Borchardt and A.H.Beddoe, "Evaluation of a PTW diamond detector for electron beam measurements", *Phys. Med. Biol.* **38**:1035–1042, 1996.

[HHB96] M.Heydarian, P.W.Hoban and A.H.Beddoe, "A comparison of dosimetry techniques in stereotactic radiosurgery", *Phys. Med. Biol.* **41**:93–110, 1996.

[HKM+92] J.A.Halbleib, R.P.Kensek, T.A.Mehlhirn, G.D.Valdez, S.M.Seltzer and M.J.Berge, "ITS version 3.0: the integrated TIGER series of coupled electron/photon Monte Carlo transport codes", Report SAND91-1634, Sandia National Laboratories, Albuquerque, 1998.

[HLW+98] W.B.Harms Sr., D.A.Low, J.W.Wong and J.A.Purdy, "A software tool for the quantitative evaluation of 3D dose calculation algorithms", *Med. Phys.* **25**:1830–1836, 1998.

[HØ79] J. H. Hubbell and I. Øverbø, "Relativistic atomic form factors and photon coherent scattering cross sections", *J. Phys. Chem. Ref. Data* **9**:69, 1979.

[HSS+84] G.H.Hartmann, W.Schlegel, V.Sturm and W.J.Lorenz, "A fast algorithm to calculate 3-dimensional dose distributions for radiosurgery", *in Proc. 8th Int. Conf. in the Use of Computers in Radiation Therapy*, pp 99-102, IEEE Computer Society Press, Silver Spring, 1984.

[HVF83] P.V.Houdek, J.M.Van Buren and J.V.Fayos, "Dosimetry of small radiation fields for 10 MV X-Rays", *Med. Phys.* **10**:333–336, 1984.

[IAE87] "Absorbed dose determination in photon and electron beam. An International code of practice", Technical Report Series 277, International Atomic Energy Agency, Vienna, 1987.

[IAE00] "Absorbed Dose Determination in External Beam Radiotherapy: An International Code of Practice for Dosimetry based on Standards of Absorbed Dose to Water", Technical Report Series 398, International Atomic Energy Agency, Vienna, 2000.

[ICR70] "Linear Energy Transfer", ICRU Report 16, International Commission On Radiation Units and Measurements, Bethesda, MD, 1970.

[ICR84] "Stopping Powers for Electrons and Positrons", ICRU Report 37, International Commission On Radiation Units and Measurements, Bethesda, MD, 1984.

[ICR87] "Use of computers in external beam radiotherapy procedures with high-energy photons and electrons", ICRU Report 42, International Commission On Radiation Units and Measurements, Bethesda, MD, 1987.

[ICR93] "Prescribing, Recording and Reporting Photon Beam Therapy", ICRU Report 50, International Commission On Radiation Units and Measurements, Bethesda, MD, 1993.

[ICR98] "Fundamental Quantities and Units for Ionizing Radiation", ICRU Report 60, International Commission On Radiation Units and Measurements, Bethesda, MD, 1998.

[ICR99] "Prescribing, Recording and Reporting Photon Beam Therapy", ICRU Report 62, Supplement to ICRU Report 50, International Commission On Radiation Units and Measurements, Bethesda, MD, 1999.

[Jam94] F.James, "RANLUX: A FORTRAN implementation of the high-quality pseudorandom number generator of Luscher", *Computer Physics Communications* **79**:111–114, 1994.

[JBF+93] D.A.Jaffray, J.J.Battista, A.Fenster and P.Munro, "X-ray sources of medical linear accelerators: focal and extra-focal radiation", *Med. Phys.* **20**:1417–1427, 1993.

[JKM00] S.B.Jiang, A.Kapur and C.-M.Ma, "Electron beam modeling and commissioning for Monte Carlo treatment planning", *Med. Phys.* **27**:180–191, 2000.

[JKO99] R.Jeraj, P.J.Keall and P.M.Ostwald, "Comparisons between MCNP, EGS4 and experiment for clinical electron beams", *Phys. Med. Biol.* **44**:705–717, 1999.

[KB98] I.Kawrakow and A.F.Bielajew, "On the representation of electron multiple scattering distributions for Monte Carlo calculations", *Nucl. Instrum. Methods Phys. B* **134**:325–336, 1998.

[KFF96] I.Kawrakow, M.Fippel and K.Friedrich, "3D electron dose calculation using a Voxel based Monte Carlo algorithm (VMC)", *Med. Phys.* **23**:445–457, 1996.

[Kha84] F.M.Khan, "The Physics of Radiation Therapy", Edited by G. Stamathis, J. W. Pine and L. Jadlos, Williams & Wilkins, Baltimore, 1984.

[Kin79] R.Kinsey, "Data Formats and Procedures for Evaluated Nuclear Data File, ENDF", Report BNL-NCS-5096 (ENDF 102) 2nd Edition (ENDF/B-V), Brookhaven National Laboratory, 1979.

[Kle84] S.C.Klevenhagen, "Electron Interactions with Matter", *Chapter 2 in Physics of Electron Beam Therapy*, pp 37-66. Adam Hilher Ltd., 1984.

[KM59] W.H.Koch and J.W.Motz, "Bremsstrahlung Cross-Section Formulas and related data", *Reviews of Modern Physics* **31**:920–943, 1959.

[KN29] O.Klein and Y.Nishina, "Über die Streuung von Strahlung durch freie Elektronen nach der neuen relativistischen Quantendynamik von Dirac", *Z. für Physik* **52**:853–868, 1929.

[Kno89] G.F.Knoll, "Radiation interactions", *Chapter 2 in Radiation Detection and Measurement,*, pp 30-64, John Wiley & Sons, second edition, 1989.

[KR00] I.Kawrakow and D.W.O.Rogers, "The EGSnrc code system: Monte Carlo simulation of electron and photon transport", Report PIRS-701, National Research Council of Canada, Ottawa, 2000.

[KV02] A.Kenneth and S.Van Ripper, "Sabrina-Visualization in support of MCNP, Version 3.63", White Rock Science, Los Alamos, 2002.

[Lan44] L.Landau, "On the Energy Loss of Fast Particles by Ionization", *J. Phy. USSR* **8**:201, 1944.

[LCL01] S-Y.Lin, T-C.Chu and J-P.Lin, "Monte Carlo simulation of a clinical linear accelerator", *Appl. Radiat. Isot.* **55**:759–765, 2001.

[LCM95] D.M.Lovelock, C.S.Chui and R.Mohan, "A Monte Carlo model of photon beams used in radiation therapy", *Med. Phys.* **22**:1387–1394, 1995.

[Lek51] L.Leksell, "The stereotaxic method and radiosurgery of the brain", *Acta Chir. Scand.* **102**:316–319, 1951.

[Leo86] W.R.Leo, "Passage of Radiation Through Matter", *Chapter 2 in Techniques for Nuclear and Particles Physics Experiments*, pp 17-63, Springer-Verlag, 1986.

[Lew50] H.W.Lewis, "Multiple scattering in an infinite medium", *Phys. Rev.* **78**:526–529, 1950.

[LHM+98] D.A.Low, W.B.Harms, S.Mutic and J.A.Purdy, "A technique for the quantitative evaluation of dose distributions", *Med. Phys.* **25**:656–661, 1998.

[LKH+94] L.Lemieux, N.D.Kitchen, S.W.Hughes and D.G.T.Thomas, "Voxel-based localization in frame-based and frameless stereotaxy and its accuracy", *Med. Phys.* **21**:1301–1310, 1994.

[LLB+92] E.Loewenthal, E.Loewinger, E.Bar-Avraham and G.Barnea, "Measurement of the source size of a 6- and 18-MV radiotherapy linac", *Med. Phys.* **19**:687–690, 1988.

[LMB88] W.R.Lutz, N.Maleki and B.E.Bjärngardt, "Evaluation of a beam-spot camera for megavoltage x rays", *Med. Phys.* **15**:614–617, 1988.

[LMM97] H.H.Liu, T.RMackie and E.C.McCullough, "A dual photon beam model used in convolution/superposition dose calculations for clinical x-ray beams", *Med. Phys.* **24**:1960–1974, 1997.

[LPD+00] J.S.Li, T.Pawalicki, J.Deng, S.B.Jiang, E.Mok and C.-M.Ma, "Validation of a Monte Carlo dose calculation tool for radiotherapy treatment planning", *Phys. Med. Biol.* **45**:2969–2985, 2000.

[LRS+00] R.D.Lewis, S.J.S.Ryde, A.W.Seaby, D.A.Hancock and C.J.Evans, "Use of Monte Carlo computation in benchmarking radiotherapy treatment planning system algorithms", *Phys. Med. Biol.* **45**:1755–1764, 2000.

[LSM99] B.Libby, J.Siebers and R.Mohan, "Validation of Monte Carlo generated phase-space descriptions of medical linear accelerators", *Med. Phys.* **26**:1476–1483, 1999.

[LST+00] M.C.Lopes, F.Sánchez-Doblado, K.Theodorou, A.Mazal, L.Nuñez, A.Chaves, C.Kappas, M.Bazioglou and P.Lassalete, "A proposed method for beam measurements in stereotactic radiotherapy", *Phys. Medica* **16**:91–94, 2000.

[LWJ+78] L.S.Lasdon, A.D.Warren, A.Jain and M.Ratner, "Design and testing of a generalized reduced gradient code for nonlinear programming", *ACM Trans. Math. Software* **4**:34–50, 1978.

[Lyo89] L.Lyon, "Statistics for Nuclear and Particle Physicists", pp 111–119, University Press, Cambridge, 1989.

[Maz90] D.A.Mazal, "Radiotherapie Stereotaxique Par Petits Faisceaux de Rayons X De Haute Energie: Développement Des Moyens Techniques Et Dosimetriques", PhD thesis, Université Paul Sabatier, Toulouse, 1990.

[MDD00] C.Martens, C.De Wagter and W.De Neve, "The value of the PinPoint ion chamber for characterization of small field segments used in intensity-modulated radiotherapy", *Phys. Med. Biol.* **44**:2519–2530, 2000.

[MFR+97] C.-M.Ma, B.A.Faddegon, D.W.O.Rogers and T.R.Mackie, "Accurate characterization of Monte Carlo calculated electron beams for radiotherapy", *Med. Phys.* **24**:401–416, 1997.

[MMK+99] C.-M.Ma, E.Mok, A.Kapur, T.Pawlicki, D.Findley, S.Brain, K.Forster and A.L.Boyer, "Clinical implementation of a Monte Carlo treatment planning system", *Med. Phys.* **26**:2133–2134, 1999.

[Mol47] G.Molière, "Theorie der streuung schnelller geladener teilchen I. Einzelstreuung am abgeschirmten Coulomb field Z", *Naturforsch* **2a**:133–145, 1947.

[Mol48] G.Molière, "Theorie der streuung schnelller geladener teilchen I. Mehrfach- und Vielfachstreuung Z", *Naturforsch* **3a**:78–97, 1948.

[Mot29] N.F.Mott, "The Scattering of Fast Electrons by Atomic Nuclei", *in Proc. Roy. Soc (London)*, A124:425, 1929.

[MR88] P.Minro and J.A.Rawlinson, "Therapy imaging: Source sizes of radiotherapy beams", *Med. Phys.* **15**:517–524, 1988.

[MRW00] C.-M.Ma, D.W.O.Rogers and B.Walters, "DOSXYZ00 Users Manual", NRC Report PIRS -0509B(revE), National Research Council of Canada, Ottawa, 2000.

[MT99] C.McKerracher and D.I.Thwaites, "Assessment of new small field detectors against standard-field detectors for practical stereotactic beam data acquisition", *Phys. Med. Biol.* **44**:2143–2160, 1999.

[MZ94] G.Marsaglia and A.Zaman, "Some portable very-long-period random number generators Computers", *Physics* **8**:117–121, 1994.

[Nah78] A.E.Nahum, "Water/air mass stopping-power ratios for megavoltage photon and electron beams", *Phys. Med. Biol.* **23**:24–38, 1978.

[Nah85] A.E.Nahum, "The interactions of Electrons with Matter: I. Energy Losses, Stopping Power and Range", *in The Computation of Dose Distributions in Electron Beam Radiotherapy*, pp 27-55, edited by A.E.Nahum, Medical Physics Publishing, Madison, Wisconsin, 1985.

[Nah88] A.E.Nahum, "Extension of the Spencer-Attix Cavity Theory to the 3 media situation for Electron beams", *in Dosimetry in Radiotherapy*, , Vol. 1, pp 87-115, edited by IAEA, Vienna, 1988.

[Nun95] L.M.Nuñez, "Modelo para la verificacion dosimetrica en radiocirugia", PhD thesis, Universidad de Sevilla, 1995.

[Phi93] J.Arndt, "Stereotactic Radiosurgery - Introduction to Physical Principles", *Chapter 1 in Physical Aspects of Stereotactic Radiosurgery*, pp 1-44, Edited by M.H.Philips, Plenum Press, New York, 1993.

[PSA+01] E.Pappas, I.Seimenis, A.Angelopoulos, P.Georgolopoulou, M.Kamariotaki-Paparigopoulou, T.Maris, P.Sandilos and L.Vlachos, "Narrow stereotactic beam profile measurements using N-vinylpyrrolidone based polymer gels and magnetic resonance imaging", *Phys. Med. Biol.* **46**:783–797, 2001.

[PWL98] F.C.P.du Plessis, C.A.Willemse and M.G.Lötter, "The indirect use of CT numbers to establish material properties needed for Monte Carlo calculation of dose distributions in patients", *Med. Phys.* **25**:1195–1201, 1998.

[PWL01] F.C.P.du Plessis, C.A.Willemse and M.G.Lötter, "Comparison of Batho, ETAR and Monte Carlo dose calculation methods in CT based patients models", *Med. Phys.* **28**:582–589, 2001.

[RBM+90] D.W.O.Rogers, A.F.Bielajew, T.R.Mackie and S.S.Kubsad, "The OMEGA project: treatment planning for electron-beam radiotherapy using Monte Carlo simulation", *Phys. Med. Biol.* **25**:285, 1990.

[RC99] J.L.Robar and B.G.Clark, "The use of radiographic film for linear accelerator stereotactic radiosurgical dosimetry", *Med. Phys.* **26**:2144–2150, 1999.

[RF95] S.N.Rustgi and D.Frye, "Dosimetric characterization of radiosurgical beams with a diamond detector", *Med. Phys.* **22**:567–570, 1995.

[RFD+95] D.W.O.Rogers, B.A.Faddegon, G.X.Ding, C.-M.Ma, J.We and R.Mackie, "BEAM: a Monte Carlo code to simulate radiotherapy treatment units", *Med. Phys.* **22**:503–524, 1995.

[RHS+87] R.K.Rice, J.L.Hansen, G.K.Svensson and R.L.Siddon, "Measurement of dose distributions in small beams of 6MV x-rays", *Phys. Med. Biol.* **32**:1087–1099, 1987.

[RMB75] M.E.Riley, C.J.MacCallum and F.Biggs, "Theoretical Electron-Atom Elastic Scattering Cross Sections. Selected Elements, 1 keV to 256 keV", *Atom. Data and Nucl. Data Tables* **15**:443, 1975.

[Rod02] P.Rodrigues, "Verificação de Cálculo de Dose em Radioterapia Externa por Simulação de Monte Carlo", Master's thesis, Faculdade de Ciências, Universidade de Lisboa, 2002.
http://www.lip.pt

[RRJ+98] S.N.Rusthi, A.K.Rustgi, S.B.Jiang and K.M.Ayyangar, "Dose perturbation caused by high-density inhomogeneities in small beams in stereotactic radiosurgery", *Phys. Med. Biol.* **43**:3509–3518, 1998.

[Rut11] E.Rutherford, "The Scattering of α and β Particles by Matter and the Structure of the Atom", *Philos. Mag.* **21**:669, 1911.

[SA55] L.V.Spencer and F.H.Attix, "A theory of cavity ionization", *Radiat. Res.* **3**:239–254, 1955.

[SAB+97] J.Sempau, E.Acosta, J.Baró, J.M.Fernández-Varea and F.Salvat, "An algorithm for Monte Carlo simulation of coupled electron-photon transport", *Nucl. Instrum. Methods Phys. B* **132**:377–390, 1997.

[SB85] S.M.Seltzer and M.J.Berger, "Bremsstrahlung spectra from electron interactions with screened atomic nuclei and orbital electrons", *Nucl. Instrum. Methods Phys. B* **12**:95–134, 1985.

[SBC00] A.E.Schach von Wittenau, P.M.Bergstrom Jr and L.J.Cox, "Patient-dependent beam-modifier physics in Monte Carlo photon dose calculations", *Med. Phys.* **27**:935–947, 2000.

[SBS00] W.Schneider, T.Bortfeld and W.Schlegel, "Correlation between CT numbers and tissue parameters needed for Monte Carlo simulations of clinical dose distributions", *Phys. Med. Biol.* **45**:459–478, 2000.

[SCB+99] A.E.Schach von Wittenau, L.J.Cox, P.M.Bergstrom Jr and W.P.Chandler, "Correlated histogram representation of Monte Carlo derived medical accelerator photon-output phase space", *Med. Phys.* **26**:1196–1211, 1999.

[SDH+98] T.D.Solberg, J.J. De Marco, F-E-Holly. J.B.Smathers and A.F.DeSalles, "Monte Carlo treatment planning for stereotactic radiosurgery", *Rad. and Oncol.* **49**:73–84, 1999.

[Sel88] S.M.Seltzer, "Monte Carlo Transport of Electrons and Photons", *in An overview of ETRAN Monte Carlo Methods*, pp 153–181, Edited by T.M.Jenkins, W.R.Nelson and A.Rindi, Plenum Press, New York, 1998.

[Sel91] S.M.Seltzer, "Electron-Photon Monte Carlo Calculations: The ETRAN Code", *Appl. Radiat. Isot.* **42**(10):917–941, 1991.

[SFB+96] F.Salvat, J.M.Fernandez-Vera, J.Baro and J.Sempau, "PENELOPE, an algorithm and computer code for Monte Carlo simulation of electron-photon showers", Technical Report 799, Ciemat-Centro de Investigaciones Energéticas, Medioambiantales y Tecnológicas, 1996.

[Sie] J.V.Siebers, "Mcnp-strip", Private communication.

[SJZ+02] D.R.Schaart, J.T.M.Jansen, J.Zoetelief and P.de Leege, "A comparison of MCNP4C electron transport with ITS 3.0 and experiment at energies

between 100 keV and 200 MeV: Influence of voxel size, substeps and energy indexing algorithm", *Phys. Med. Biol.* **47**:1459–1484, 2002.

[SK96] R.Sjögren and M.Karlson, "Electron contamination in clinical high energy photon beams", *Med. Phys.* **23**:1873–1881, 1996.

[SKG+93] E.Shaw, R.Kline, M.Gillin, L.Jouham, A.Hirschfeld, R.Dinapoli, and L.Martin, "Radiation Therapy Oncology Group: Radiosurgery Quality Assurances Guidelines", *Int. J. Rad. Onc. Biol. Phys.* **27**(5):1231–1239, 1993.

[SKL+99] J.V.Siebers, P.J.Keall, B.Libby and R.Mohan, "Comparison of EGS4 and MCNP4b Monte Carlo codes for generation of photon phase space distributions for a Varian 2100C", *Phys. Med. Biol.* **44**:3009–3026, 1999.

[SKN+00] J.V.Siebers, P.J.Keall, A.E.Nahum and R.Mohan, "Converting absorbed dose to medium to absorbed dose to water for Monte Carlo based photon beam dose calculations", *Phys. Med. Biol.* **44**:983–995, 2000.

[SLG+72] L.Steiner, L.Leksell, T.Greitz, D.M.C.Foster and E.O.Backlung, "Stereotaxic radiosurgery for cerebral arteriovenous malformations. Report of a case", *Acta Cir. Scand.* **138**:459–464, 1972.

[SLR02] A.E.Sach von Wittenaum C.M.Logan and R.D.Rikard, "Using a tungsten rollbar to characterize the source spot of a megavoltage bremsstrahlung linac", *Med. Phys.* **29**:1797–1806, 2002.

[SMH+98] T.D.Solberg, J.J.DeMarco, F.E.Holly, J.B.Smathers and A.F.DeSalles, "Monte Carlo treatment planning for stereotactic radiosurgery", *Rad. and Onc.* **49**:73–74, 1998.

[SP93] E.K.Sixel and E.V.Podgorsak, "Buildup region of high-energy x-ray beams in radiosurgery", *Med. Phys.* **20**:761–764, 1993.

[SP94] E.K.Sixel and E.V.Podgorsak, "Buildup region and depth of maximum of megavoltage x-ray beams", *Med. Phys.* **21**:411–416, 1994.

[SR02] R.Sheik-Bagheri and D.W.O.Rogers, "Monte Carlo calculation of nine megavoltagem photon beam spectra using the BEAM code", *Med. Phys.* **29**:391–402, 2002.

[SRR+00] R.Sheik-Bagheri, D.W.O.Rogers, C.K.Ross and J.P.Seuntjens, "Comparison of measured and Monte Carlo calculated dose distributions from the NRC linac", *Med. Phys.* **27**:2256–2266, 2000.

[Ste97] G.G.Steel, "Basic Clinical Radiobiology", Second Edition, Edited by G.G.Stell, Arnold, London, 1997.

[STP96] STP3 User Manual V3.3x, Howmedica Leibinger GmbH, 1996

[SWB00] J.Sempau, S.J.Wilderman and A.F.Bielajew, "DPM, a fast, accurate Monte Carlo code optimized for photon and electron radiotherapy planning dose calculations", *Phys. Med. Biol.* **45**:2263–2291, 2000.

[SWD+01] C.L.H.Siantar, R.S.Walling, T.P.Daly, B.Faddegon, N.Albright, P.Bergstrom, A.F.Bielajew, C.Chung, D.Garrett, R.K.House, D.Knapp, D.J.Wieczorek and L.J.Verhey, "Description and dosimetric verification of PEREGRINE Monte Carlo dose calculation system for photon beams incident on a water phantom", *Med. Phys.* **28**:1322–1337, 2001.

[Tri02] A.Trindade, "Optimização do cálculo de dose por simulação Monte Carlo em radioterapia externa com feixes de electrões", Master's thesis, Faculdade de Ciências, Universidade de Lisboa, 2002.
http://www.lip.pt

[VBC+93] J.Van Dyke, R.B.Barnett, J.E.Cygler and P.C.Shragge, "Commissioning and quality assurance of treatment planning computers", *Int. J. Radiat. Oncol. Biol. Phys.* **26**:261–273, 1993.

[VDP98] F.Verhaegen, I.J.Das and H.Palmans, "Monte Carlo dosimetry study of a 6MV stereotactic radiosurgery unit", *Phys. Med. Biol.* **43**:2755–2768, 1998.

[VM94] J.Van Dam and G.Marinello, "Methods for in vivo Dosimetry in External Radiotherapy", ESTRO booklet 1, Garant, Leuven, 1994.

[VWM01] J.Venselaar, H.Welleweerd and B.Mijnheer, "Tolerances for accuracy oh photon beam dose calculations of treatment planning systems", *Rad. and Onc.* **60**:191–201, 2001.

[WAN+00] M.Westermark, J.Arndt, B.Nilsson and A.Brahme, "Comparative dosimetry in narrow high-energy photon beams", *Phys. Med. Biol.* **45**:685–702, 2000.

[WM84] M.S.Weinhous and J.A.Meli, "Determination P_{ion}, the correction factor for recombination losses in an ionization chamber", *Med. Phys.* **11**:846–849, 1984.

[WMH+65] E.Woodcock, T.Murphy, P.Hemmings and S.Longworth, "Techniques used in the GEM code for Monte Carlo neutronics calculation in reactors and other systems of complex geometry", *in Proc. Conf. on Applications of Computing Methods to Reactor Problems*, p. 557, 1965.

[WZK+93] A.Wu, R.D.Zwicker, A.M.Kalend adn Z.Zeng, "Comments on dose measurements for narrow beam in radiosurgery", *Med. Phys.* **20**:777–779, 1993.

[YSS+00] H.Yoriyaz, A. dos Santos, M.G.Stabin and R.Cabezas, "Absorbed fractions in a voxel-based phantom calculated with MCNP-4B code", *Med. Phys.* **27**:1555–1562, 2000.

[YSS01] H.Yoriyaz, M.G.Stabin and A.dos Santos, "Monte Carlo MCNP-4b-based absorbed dose distribution estimates for patient-specific dosimetry", *J. Nucl. Med* **42**:662–669, 2001.

[ZP98] T.C.Zhu and J.R.Palta, "Electron contamination in 8 and 18 MV photon beams", *Med. Phys.* **25**:13–19, 1998.

[ZW99] W.Van der Zee and J.Welleweerd, "Calculating photon beam characteristics with Monte Carlo techniques", *Med. Phys.* **26**:1883–1892, 1999.